

TR diss 2719S

# STELLINGEN

behorende bij het proefschrift

*Computational strategies for masonry structures*

van

*P.B. Lourenço*

1. About one-third of the world's population still lives in primitive earth houses because modern western technology has failed to satisfy the local increasing demand of better low-cost housing.

*Ongeveer eenderde van de wereldbevolking woont nog steeds in leemhuten omdat de westerse technologie niet in staat is geweest in de behoefte aan betere goedkope woningen te voorzien.*

J. Dethier, Down to Earth: Mud architecture, an old idea, a new future. Thames and Hudson, London, UK (1982).

2. The decline of masonry as a structural material in developed nations is not merely an economical issue. Rather, it reflects the shortcomings in our knowledge and the inability to transfer the knowledge into field practice, according to the actual safety concepts.

*Metselwerk als constructiemateriaal in de geïndustrialiseerde landen gaat niet alleen achteruit om economische redenen. Het reflecteert ook de tekortkomingen in onze expertise en de onmogelijkheid om de expertise, met inachtneming van de huidige veiligheidsconcepten, naar de praktijk te vertalen.*

3. The lack of communication between masonry experimentalists and analysts is so severe that most test results are of no use for the purpose of development and validation of numerical tools.

*Het gebrek aan communicatie tussen experimentele en numerieke deskundigen op het gebied van metselwerk is zo groot dat de meeste meetresultaten onmogelijk voor ontwikkeling en validatie van numeriek gereedschap gebruikt kunnen worden.*

4. It is misleading to validate numerical tools against experimental results solely by means of load-displacement diagrams.

*Het is misleidend om numeriek gereedschap alleen met last-verplaatsingsdiagrammen te valideren.*

5. It is not possible to fully assess the safety of a structure only by its limit load. The nature of the post-peak behavior (brittle/ductile) must also be known.

*Het is niet mogelijk om de veiligheid van een constructie volledig aan de hand van alleen zijn bezwijklast te karakteriseren. Het na-bezwijkgedrag (bros/taai) dient ook te worden onderzocht.*

6. The term consistent tangent is a pleonasm because the Jacobian of a given nonlinear problem is unique.

*De uitdrukking consistente tangent is een pleonasme omdat de Jacobiaan van een gegeven nietlineair probleem eenduidig vastligt.*

7. In the presence of complex yield surfaces attention must be given to the selected material parameters in order to ensure convexity. This can become a challenge for orthotropic materials. In particular, the requirements of Tsai and Wu to keep the ellipsoidal shape of their  $\mathbb{R}^6$  surface are erroneous.

*Bij complexe vloeifuncties dient aandacht te worden besteed aan de geselecteerde materiaalparameters in verband met convexiteit. Dit kan een uitdaging worden voor orthotrope materialen. Zo zijn bijvoorbeeld de voorwaarden van Tsai en Wu om hun  $\mathbb{R}^6$  vloeiooppervlak ellipsoidal te houden beslist fout.*

S.W. Tsai and E.M. Wu, A general theory of strength of anisotropic materials. J. Composite Mat., 5, p. 58-80 (1971).

8. The value of strut-and-tie models for concrete structures is mainly pedagogical. In the case of nontrivial structures, more questions than answers are likely to arise. It is striking that the two strut-and-tie models adopted by Schlaich *et al.* for the well-known deep beam with an opening fail to capture the structure's behavior.

*De waarde van staafwerkmodellen voor betonconstructies is voornamelijk educatief. Bij complexe constructies komen hieruit waarschijnlijk meer vragen dan antwoorden voort. Zo valt op dat de twee staafwerkmodellen van Schlaich c.s. voor de bekende wandligger met opening niet in staat zijn om het constructiegedrag te beschrijven.*

J. Schlaich *et al.*, Toward a consistent design of structural concrete. PCI Journal, 32(3), p. 74-150 (1987).

P.B. Lourenço *et al.*, Compared study of nonlinear finite element analysis and the strut-and-tie model for concrete structures. A designer perspective. EPMESC IV, Dalian, P.R. China, p. 660-667 (1992).

9. The design of reinforced concrete walls, slabs and shells based on the linear elastic internal force distribution should be taught in any civil engineering graduation. In combination with sound engineering judgment, this is a fundamental tool of today's structural concrete designer.

*Het ontwerp van gewapend betonnen wanden, platen en schalen op basis van de lineair-elastische interne krachtsverdeling dient onderwezen te worden in elke opleiding voor civiele techniek. Samen met het ingenieursinzicht vormt dit een fundamenteel stuk gereedschap voor de moderne betonconstructeur.*

P.B. Lourenço and J.A. Figueiras, Solution for the design of reinforced concrete plates and shells. J. Struc. Engrg, ASCE, 121(5), p. 815-823 (1995).

10. One of the most important consequences of nonlinear analysis is that today's safety concept based on partial safety factors cannot be adopted. In particular, the use of design values for the material parameters is completely inappropriate. Incomprehensibly, very little attention is given to this fact.

*Een van de belangrijkste gevolgen van nietlineaire berekeningen is dat het huidige veiligheidsconcept, gebaseerd op partiële veiligheidsfactoren, niet gebruikt kan worden. In het bijzonder is het gebruik van ontwerpwaarden voor materiaalparameters volkomen ongeschikt. Het is onbegrijpelijk dat hieraan zo weinig aandacht wordt geschonken.*

J. Eibl, Safety considerations for nonlinear analysis. IABSE, 62, Stuttgart, p. 337-342 (1991).

11. The difficulties inherent to the theories arising in the last decade for the description of cohesive-frictional materials, which resort to nonstandard continua, increase the division between practitioners and academics.

*De hogere-orde continuümtheorieën, in het laatste decennium gebruikt voor de beschrijving van cohesieve wrijvingsmaterialen, vergroten de afstand tussen de wetenschap en de praktijk.*

12. Researchers spend too much time and effort reporting good results and too little reporting bad results.

*Onderzoekers besteden te veel tijd aan het rapporteren van goede resultaten en te weinig aan dat van slechte.*

13. The "stop-and-green" traffic lights system adopted in the Netherlands causes a waste of time and money because the existence of "green waves" is fundamental for a proper flow of traffic.

*Omdat het bestaan van "groene golven" essentieel is voor een vlotte verkeersafwikkeling, is het Nederlandse systeem van verkeerslichten ("stop-en-groen") een verspilling van tijd en geld.*

644300

3190349

TR diss 2719

**TR diss  
2719**

COMPUTATIONAL STRATEGIES

FOR

MASONRY STRUCTURES

COMPUTATIONAL STRATEGIES

FOR

MASONRY STRUCTURES

PROEFSCHRIFT

ter verkrijging van de graad van doctor  
aan de Technische Universiteit Delft,  
op gezag van de Rector Magnificus, Prof. ir. K. F. Wakker,  
in het openbaar te verdedigen ten overstaan van een commissie,  
door het College van Dekanen aangewezen,  
op maandag 19 februari 1996 te 16.00 uur

door

PAULO JOSÉ BRANDÃO BARBOSA LOURENÇO

engenheiro civil,  
Faculdade de Engenharia da Universidade do Porto,  
geboren te Porto, Portugal



Dit proefschrift is goedgekeurd door de promotor:

Prof. dr. ir. J. Blaauwendraad

Toegevoegd promotor:

Dr. ir. J.G. Rots

Samenstelling promotiecommissie:

Rector Magnificus, voorzitter

Prof. dr. ir. J. Blaauwendraad, TU Delft, promotor

Dr. ir. J.G. Rots, TU Delft, toegevoegd promotor

Prof. dr. ir. R. de Borst, TU Delft

Prof. dr. J.A. Figueiras, Univ. Porto

Prof. dr. ir. H.S. Rutten, TU Eindhoven

Prof. dr. ir. J.C. Walraven, TU Delft

Published and distributed by:

Delft University Press

Stevinweg 1

2628 CN Delft

The Netherlands

Telephone +31 15 2783254

Fax +31 15 2781661

CIP-GEGEVENS KONINKLIJKE BIBLIOTHEEK, DEN HAAG

Lourenço, Paulo José Brandão Barbosa

Computational strategies for masonry structures /

Paulo José Brandão Barbosa Lourenço. - Delft :

Delft University Press. - Ill.

Thesis Delft University of Technology. -

With ref. - With summary in Dutch.

ISBN 90-407-1221-2

NUGI 841

Subject headings: masonry / plasticity.

Copyright © 1996 by P.B. Lourenço

All rights reserved.

No part of the material protected by this copyright notice may be reproduced or utilized in any form or by any means, electronic or mechanical, including photocopying, recording or by any information storage and retrieval system, without permission from the publisher:

Delft University Press, Stevinweg 1, 2628 CN Delft, The Netherlands.

Printed in the Netherlands.

## ACKNOWLEDGEMENTS

The research reported in this thesis has been carried out at the Civil Engineering Department of Delft University of Technology since November 1992, on leave from the University of Minho. The algorithms have been implemented in pilot versions of the DIANA code. The calculations have been performed on a Silicon Graphics Workstation. This research was supported by the Netherlands Technology Foundation (STW) under grant DCT 33.3052, since January 1994. Additional financial support by TNO Building and Construction Research is gratefully acknowledged.

The work was performed under the direct guidance of Dr. Jan Rots and the supervision of Prof. Johan Blaauwendraad.

I am grateful to all my colleagues from the Computational Mechanics Group, especially to Peter Feenstra, Arend Groen and Jerzy Pamin, for their support and interesting discussions, and Harold Thung, for keeping all the computers running smoothly. I would like to express also my deep gratitude to Prof. René de Borst, head of the Computational Mechanics Group, for his interest and care.

I would like to record my thanks to Prof. Joaquim Figueiras from the University of Porto, for making the first contacts leading to my stay in Delft and for the fruitful discussions and care since the first time we met, back in 1989, to apply for a young researcher grant. I would also like to thank the Civil Engineering Department of the University of Minho for making my stay in Delft possible.

Finally, I would like to thank all my family, for their love and support, and my wife Lúcia, for the love, the patience and the courage to embark on this trip to the Netherlands.

# CONTENTS

1. Introduction .....	1
1.1 Masonry: Past and present .....	1
1.2 The role of research on structural masonry .....	6
1.3 Overview of computational modeling of masonry structures .....	7
1.4 Objectives and scope of this study .....	8
2. Modeling masonry: A material description .....	11
2.1 Micro- and macro-modeling .....	11
2.2 Aspects of softening behavior .....	13
2.3 Properties of unit and mortar .....	15
2.4 Properties of the unit-mortar interface .....	16
2.4.1 Mode I failure .....	16
2.4.2 Mode II failure .....	17
2.5 Properties of the composite material .....	20
2.5.1 Uniaxial compressive behavior of masonry .....	20
2.5.2 Uniaxial tensile behavior of masonry .....	21
2.5.3 Biaxial behavior .....	23
2.6 Summary .....	25
3. Finite elements and plasticity .....	27
3.1 Nonlinear finite elements .....	28
3.1.1 Iterative techniques for the solution of nonlinear problems .....	29
3.1.2 Softening behavior: constrained Newton-Raphson method .....	31
3.2 Numerical implementation of plasticity theory .....	33
3.2.1 Integration of the elastoplastic equations .....	36
3.2.2 Evaluation of the tangent operator .....	40
3.3 Summary .....	42
4. Micro-modeling: A composite interface model for masonry .....	43
4.1 Adopted modeling strategy .....	43
4.2 Formulation of the composite interface model .....	48
4.2.1 The tension cut-off criterion .....	49
4.2.2 The Coulomb friction criterion .....	51
4.2.3 The compressive cap criterion .....	53
4.2.4 A composite yield criterion .....	56
4.3 Validation .....	59
4.3.1 TU Eindhoven shear walls .....	60
4.3.2 Deep beam .....	73
4.4 Reflections on the modeling strategy .....	77
4.4.1 Modeling cracking of the units .....	77

4.4.2	Modeling compressive failure .....	79
4.4.3	Influence of dilatancy .....	80
4.4.4	Mesh sensitivity of the composite interface model .....	82
4.5	Summary .....	83
5.	From micro to macro: Homogenization techniques .....	85
5.1	The elastoplastic homogenization of layered materials .....	86
5.1.1	Elastic formulation .....	88
5.1.2	Elastoplastic formulation .....	92
5.1.3	Validation .....	95
5.2	Derivation of the elastic characteristics of masonry .....	106
5.2.1	Accuracy of the methodology for different stiffness ratios .....	107
5.2.2	Results of a masonry shear wall .....	111
5.3	Tensile behavior parallel to the bed joints .....	113
5.4	Summary .....	121
6.	Macro-modeling: An anisotropic continuum model for masonry .....	123
6.1	Formulation of the anisotropic continuum model .....	124
6.1.1	Discretization aspects .....	126
6.1.2	A Rankine type criterion .....	127
6.1.3	A Hill type criterion .....	133
6.1.4	A composite yield criterion .....	137
6.1.5	The orientation of the material axes .....	137
6.2	Definition of the model parameters from experimental results .....	138
6.2.1	Required information to define the yield criterion .....	138
6.2.2	Comparison with experimental data of masonry strength .....	140
6.3	The inelastic behavior of the model. Elementary tests .....	145
6.3.1	Orthotropic behavior in uniaxial tension .....	145
6.3.2	Orthotropic behavior in uniaxial compression .....	146
6.3.3	The definition of a mesh independent compressive fracture energy .....	149
6.4	Validation .....	151
6.4.1	ETH Zurich clay brick masonry shear walls .....	152
6.4.2	ETH Zurich concrete block masonry shear walls .....	163
6.4.3	Discussion of the results .....	165
6.5	Reflections about the modeling strategy .....	166
6.5.1	Limitations of macro-models .....	166
6.5.2	Mesh sensitivity of the anisotropic continuum model .....	171
6.6	Summary .....	172
7.	Applications .....	175
7.1	The step towards fracture mechanics based design rules: Movement-joint spacing in masonry walls .....	175

7.2	Assessment of damage in old masonry buildings caused by tunneling induced settlements .....	183
7.3	Assessment of residual strength in damaged structures .....	192
7.4	Summary .....	194
8.	Summary and conclusions .....	195
	References .....	199
	Samenvatting .....	209

## 1. INTRODUCTION

Masonry is the oldest building material that still finds wide use in today's building industries. Important new developments in masonry materials and applications occurred in the last decades but the techniques to assemble bricks and blocks are essentially the same as the ones developed some thousand years ago. Naturally, innumerable variations of masonry materials, techniques and applications occurred during the course of time. The influence factors were mainly the local culture and wealth, the knowledge of materials and tools, the availability of material and architectural reasons.

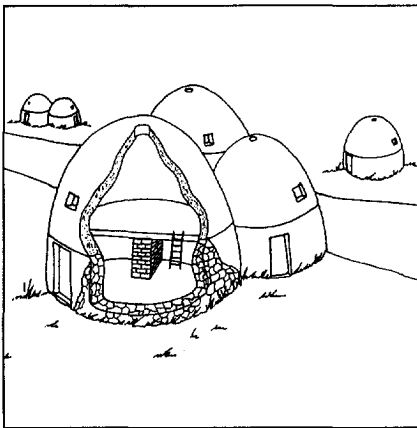
The most important characteristic of masonry construction is its simplicity. Laying pieces of stone or bricks on top of each other, either with or without cohesion via mortar, is a simple, though adequate technique that has been successful ever since remote ages. Other important characteristics are the aesthetics, solidity, durability and low maintenance, versatility, sound absorption and fire protection. Loadbearing walls, infill panels to resist seismic and wind loads, prestressed masonry cores and low-rise buildings are examples of constructions where the use of structural masonry is presently competitive. However, innovative applications of structural masonry are hindered by the fact that the development of design rules has not kept pace with the developments for concrete and steel. The underlying reason is the lack of insight and models for the complex behavior of units, mortar, joints and masonry as a composite material. Existing calculation methods are mainly of empirical and traditional nature and the use of numerical tools for the analysis or design of masonry structures is rather incipient. Another important drawback is the education of engineers. Design and field knowledge of masonry is absent or minimal in the programs of most graduations in structural engineering. It seems thus that the present situation is not so much a shortcoming of the product but rather the shortcomings are in our knowledge, and in the ability to transfer this knowledge into field practice.

### 1.1 Masonry: Past and present

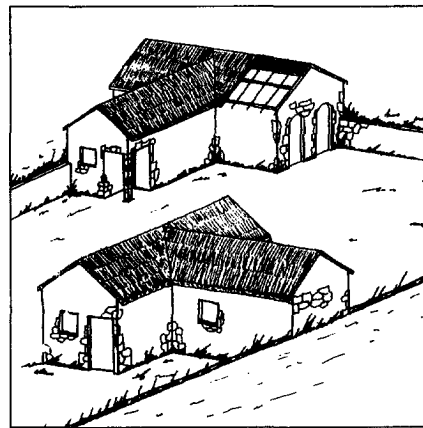
Archaeologists recognize three main stages in the cultural evolution of mankind, respectively known as the Stone, Bronze and Iron Ages, according to the use made of these materials for tools and weapons. Successively too, man passed through phases in the means of gaining subsistence. In the savage state, livelihood came from hunting, fishing and food gathering; in the barbarian state, roughly according to the late Stone Age, crop and cattle-rearing had been learnt and men could enjoy a settled life. True civilization was only reached when economic and social developments had advanced sufficiently to allow the building of towns and cities, wherein a part of the population could engage in trade, industry and professional pursuits. It is about ten thousand years ago, with the earliest civilization, that the history of architecture really begins and simultaneously masonry arises as a building technique. The primitive savage endeavors of mankind to

secure protection against the elements and from attack included seeking shelter in rock caves, learning how to build tents of bark, skins, turves or brushwood and huts of wattle-and-daub. Some of such types crystallized into houses of stone, clay or timber. The evolution of mankind is thus linked to the history of architecture, see e.g. Musgrove and Fletcher (1987), and the history of building materials, see e.g. Davey (1961).

The first masonry material to be used was probably stone. In the ancient Near East, evolution of housing was from huts, to apsidal houses (Figure 1.1a), and finally to rectangular houses (Figure 1.1b).



(a)



(b)

*Figure 1.1* Examples of prehistoric architecture of masonry in the ancient Near East: (a) beehive houses from a village in Cyprus (c. 5650 BC); (b) rectangular dwellings from a village in Iraq (c. 5500-5000 BC).

The earliest examples of the first permanent stone masonry houses can be found near Lake Hullen, Israel (c. 9000-8000 BC), where dry-stone huts, circular and semi-subterranean, from 3 [m] to 9 [m] in diameter were found. Several other legacies of stone masonry survived until present as testimonies of ancient and medieval cultures, for instance, the Egyptian architecture with its pharaonic pyramids (c. 2800-2000 BC), the Roman and Romanesque architecture (c. AD 0-1200) with its temples, palaces, arches, columns, churches, bridges and aqueducts, see e.g. Figure 1.2, the Gothic architecture (c. AD 1200-1600) with its magnificent cathedrals and many others. It is with the Gothic masons that the art of cutting stone reached its splendor. The Gothic cathedrals consisted of a skeleton of piers, buttresses, arches and ribbed vaulting, see Figure 1.3. The walls enclosed, but did not support, the structure and, indeed, they consisted, mainly, of glazed windows.

Presently, however, stone has received a new role in the building industry because quarrying, transporting and placing such a heavy and expensive material became prohibitive. Better and more economical materials can be used for structural applications and stone has become mostly a facing material.

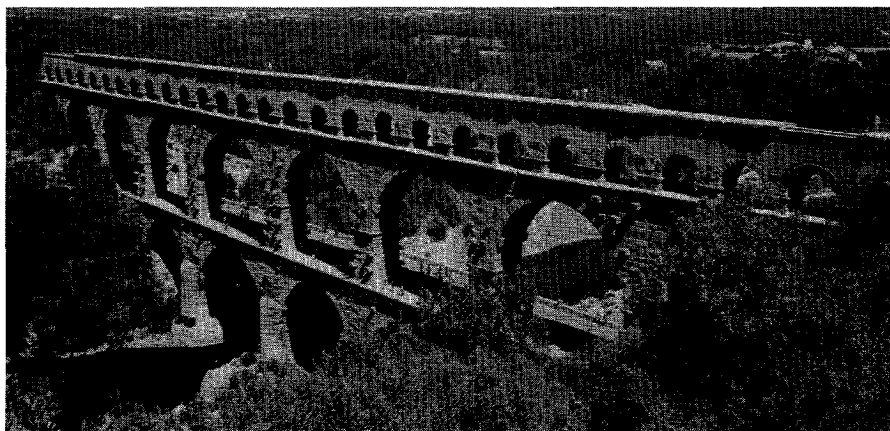


*Figure 1.2* The 290 [m] long aqueduct Pont du Gard, Nîmes, France (c. AD 14) is well preserved and formed of three tiers of arches, crossing the valley 50 [m] above the river. Except for the top tier, the masonry was laid dry.

In addition to the use of stone also mud brick started to be used as a masonry material. It was the populated areas of the ancient times that witnessed the emergence of sun dried bricks. The demand of building materials combined with the abundance of clay<sup>†</sup>, the hot dry climate necessary to cure the brick and the shortage of timber and building stones that did not require cutting, led to the development of the brick. At Jericho, Palestine (c. 8350-7350 BC), many round and oval houses were found. Each was about 5 [m] in diameter and built of loaf-shaped mud-bricks with indentations on the convex face to give a key to the clay mortar. The reasons for the use of brick as a building material were well established. It was a product that could be easily produced. It was lighter than stone, easy to mould and formed a wall that was fire resistant and durable. In Egypt, from pre-dynastic times (5000 BC) until the Roman occupation (AD 50) the chief material for building houses was sun dried brick, commonly of Nile mud. The pure Nile mud shrinks over 30 % in the drying process but the addition of chopped straw and sand to the mud prevented the formation of cracks. The manner of making bricks at Thebes, the capital of the Upper Egypt is illustrated in the wall painting discovered in the tomb of Rekhmara (c. 1500 BC), see Figure 1.4.

The practice of burning brick probably started with the observation that the brick near a cooking fire or the brick remaining after a thatch roof burnt seemed to be stronger and more durable. To make burnt bricks, an adequate supply of fuel was necessary, which may have partially accounted for the continued use of sun dried bricks in the near East. A very early example of burnt brick mass production is given by a up-draught kiln excavated in Khafaje, Iraq, dating from the third millennium BC. It was circular in plan

---

<sup>†</sup> Clay and lateritic soil suitable for use as building material constitute 74 % of the world's crust, Dethier (1982).

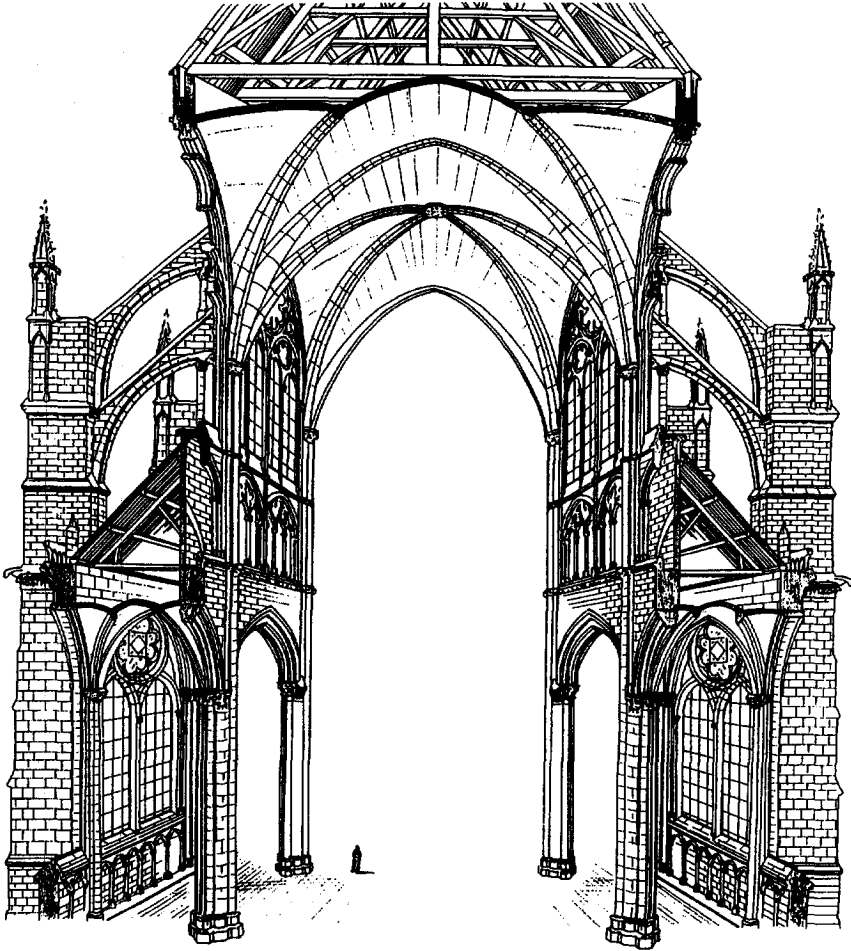


*Figure 1.3* Transverse section of a typical Gothic cathedral, Amiens, France (1220-1288). The collected load of the nave vaulting has a downward component due to its own weight and a horizontal component due to the arched form of the vault, which are carried, respectively, by a system of columns and massive buttresses weighted by pinnacles.

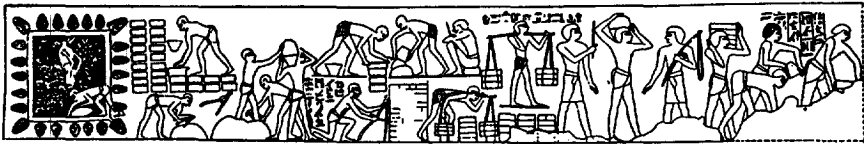


*Figure 1.4* Brick making in Egypt, as depicted in a wall painting in the tomb of Rekhmara at Thebes (c. 1500 BC).

with four holes beneath the oven floor, and it was very similar in construction to the up-draught kilns used by the Romans two thousand years later. The earliest recorded reference to burnt brick is possibly from a papyrus of the Nineteenth Dynasty in Egypt (c. 1300 BC), Spencer (1979), but the most famous reference is found in the Bible, Genesis XI, 3-4, when the inhabitants of Babylonia "said to one another 'Come, let us make bricks and bake them'. They used brick for stone and bitumen for mortar. Then they said 'Let us build ourselves a city and tower with its top in the heavens'". And they built probably the first ever skyscraper as it is estimated that the seventh level of the Tower of Babel topped a height of 90 [m]. In fact, by c. 900-600 BC, the Babylonians completely mastered burning brick and produced patterned bricks and wall tiles with polychrome glazes. But, it is only in the Roman times that a large, strong and centralized Empire fulfil the conditions to the wide spread of brick. There were many kinds of clayey materials suitable for making bricks and tiles readily available in all the areas of the Roman Empire and the desire to obtain domination and homogenization of architecture and building techniques made the rest. The size of bricks became more standardized, different shapes were manufactured for special purposes, and seals, trademarks or decorative motifs began to be impressed in the brick.

The next milestone in the history of masonry is the era of the Industrial Revolution as described by Elliot (1992). Due to the expansion of the industrial activity, traditional handwork procedures were replaced by machinery. The turning point of the brick industry came, finally, in 1858 with the introduction of the Hoffman kiln which enabled all the stages of firing to be carried out concurrently and continuously. Since then, further research and developments led to the creation of efficient brick making industries.

Presently, in the building industry, it is possible to find units of different materials and shapes, different types of mortar and different techniques. Ancient and new coexist in a, sometimes indiscernible, mixture of tradition and novelty. Modern units of concrete, lightweight concrete with expanded clay aggregate, aerated concrete, calcium-silicate or polystyrene, coexist with the traditional brick units of mud or clay. Recent and revived techniques as grouted masonry, reinforced masonry, prestressed masonry, prefabricated masonry panels, mortarless masonry or masonry with very large blocks coexist with the oldest technique of putting small bricks on top of each other. Recent mortars with admixtures, cement mortars and (retarded) ready-mix mortars coexist with the ancient clay, gypsum, lime and bitumen mortar.

Some of the recent developments, e.g. a low dimensional variation of the units combined with improved building tools or large calcium-silicate units combined with modern stacking techniques resorting to machinery, have led to increasing labor productivity and reduced costs. However, in developed countries, masonry seems to have lost, almost completely, its structural function because reinforced concrete and steel structures became more competitive. In Europe and North America, masonry is used nowadays primarily as a cladding system or infill non-loadbearing walls. Exceptions are loadbearing reinforced masonry in North America and structural masonry used in low-rise buildings. The situation in Developing and Third World countries in Latin

America, Asia and Africa is quite different as structural masonry is still widely used, see e.g. Dajun (1994) and Suter (1982). It is remarkable that over one-third of the world's population still lives in earth houses today, Dethier (1982), for modern western technology has failed, both financially and socially, to satisfy the local increasing demand of cheap housing. Thus, it is believed that the decline of masonry as a structural material is not only due to economical reasons but also to underdeveloped masonry codes and lack of insight in the behavior of this type of structures.

## 1.2 The role of research on structural masonry

In the past masonry structures were erected by the time-honored method of trial and error. The traditional methods and rules-of-thumb were passed, sometimes in secrecy, from one generation to the other. Without mathematical or predictive methods, but with experience and great skill, an impressive empirical wisdom was obtained. A typical example was given before with the ability of Gothic builders to fashion stone into ribs and vaults that suggests some understanding of the action of forces within the structure. The evolution of the old techniques into new and modern applications occurred unsuccessfully. Presently, prejudices persist against structural masonry, based on the claim that it is expensive, fragile, unable to withstand earthquakes and dependent on unreliable workmanship and unknown quality. As a consequence, only few resources have been put in structural masonry research, the current codes of practice are underdeveloped and there is a lack of knowledge about the behavior of this composite material. The fundamental point of today's research in structural masonry is thus to *rationalize the engineering design of structural masonry*. Considerable research effort has been made in the last two decades but progress has been hindered by the lack of communication between analysts and "experimentalists". A good example of an integrated research program is given by CUR (1994). A combined experimental/numerical basis is the key to validate, extend and improve existing methods. At the present stage of knowledge, numerical simulations are fundamental to provide insight into the structural behavior and support the derivation of rational design rules. Nevertheless, the step towards the development of reliable and accurate numerical models cannot be performed without a thorough material description and a proper validation by comparison with a significant number of experimental results. This means that carefully, deformation controlled, experiments in large-scale masonry tests, small masonry samples and masonry components are necessary. Recently discovered properties, like softening and dilatancy, being virtually absent in the masonry literature, play a crucial role in the nonlinear processes. Nonlinear finite element analyses will always be helpful for the *validation of the design of complex masonry structures under complex loading conditions*. In particular computations beyond the limit load down to a possibly lower residual load are needed to assess the safety of the structure. Aside from failure analysis, also the serviceability limit states can be successfully validated with numerical analyses, e.g. crack control and prevention for restrained shrinkage and differential movements.

Another important aspect is the safety of existing structures under actual or new loading conditions, with an emphasis in the preservation of historical structures. Reliable numerical models are necessary to *assess and strengthen existing masonry structures*. Recent examples of the danger of assuming that ancient structures last forever are given by the Civic Tower of Pavia, Italy, and the Campanile of San Marco in Venice, Italy. Both millenary structures were the love and pride of the locals and failed without previous warning. A less dramatic, but trendy example is given by the damage caused by tunneling in historical city centers, e.g. Amsterdam, in the Netherlands.

The final point is the need to *improve the performance of masonry buildings in Third World countries*. Research must be carried out on techniques that use local materials, are kept as simple as possible and do not increase significantly the cost. This is not merely a question of transferring existing technology. An example of bad performance of traditional masonry is given by the catastrophic earthquake in Guatemala (1976) where complete towns made of masonry totally collapsed. The houses were made of thick walls of dried mud brick and heavy roofs. The ground-shaking of the 200 [km] long fault moved so much that these buildings were shaken down. The strength-weight ratio of the dried mud bricks was very poor and, most likely, the cause that killed so many people. An increase of the strength-weight ratio or the use of natural reinforcement, bamboo for example, could have saved many lives, see also Kok (1995).

### 1.3 Overview of computational modeling of masonry structures

The previous Section introduced the importance of sophisticated numerical tools, capable of predicting the behavior of the structure from the linear stage, through cracking and degradation until complete loss of strength. It is then possible to control the serviceability limit states, fully understand failure mechanisms and reliably assess the structural safety. This objective can only be achieved if accurate and robust constitutive models are complemented with advanced solution procedures of the system of equations which results from the finite element discretization (it is tacitly assumed that the finite element method is adopted to simulate the structural behavior). Only recently did the masonry research community begin to show interest in sophisticated numerical tools as an opposition to the prevailing tradition of rules-of-thumb and empirical formulae. The fact that little importance has been attached to numerical aspects is confirmed by the absence of any well established models. The difficulties in adopting existing numerical tools from more advanced research fields, namely the mechanics of concrete, rock and composite materials, are hindered by the particular characteristics of masonry.

Masonry is a composite material that consists of units and mortar joints. A detailed analysis of masonry, hereby denoted *micro-modeling*, must then include a representation of units, mortar and the unit/mortar interface. This approach is suited for small structural elements with particular interest in strongly heterogeneous states of stress and strain. The primary aim of micro-modeling is to closely represent masonry from the knowledge of the properties of each constituent and the interface. The necessary

experimental data must be obtained from laboratory tests in the constituents and small masonry samples. Several attempts to use interfaces for the modeling of masonry were carried out in the last decade with reasonably simple models, see Anthoine (1992) and Lourenço (1994) for references. In particular, gradual softening behavior and all failure mechanisms, namely tensile, shear and compressive failure, have not been fully included.

In large and practice-oriented analysis the knowledge of the interaction between units and mortar is, generally, negligible for the global structural behavior. In these cases a different approach can be used, hereby denoted *macro-modeling*, where the material is regarded as an anisotropic composite and a relation is established between average masonry strains and average masonry stresses. This is clearly a phenomenological approach, meaning that the material parameters must be performed in masonry tests of sufficiently large size under homogeneous states of stress. A complete macro-model must reproduce an orthotropic material with different tensile and compressive strengths along the material axes as well as different inelastic behavior for each material axis. A reduced number of orthotropic material models specific for masonry has been proposed, see Anthoine (1992) and Lourenço (1995b) for references. It is not surprising that so few macro-models have been implemented due to the intrinsic complexity of introducing orthotropic behavior. The models proposed in the past failed to be widely accepted due to the difficulties of formulating robust numerical algorithms and representing satisfactorily the inelastic behavior.

To the knowledge of the author, previous numerical micro- and macro-analyses of unreinforced masonry structures are limited to the structural pre-peak regime. However, it is believed that computations beyond the limit load down to a possibly lower residual load are essential to assess the structural safety.

## 1.4 Objectives and scope of this study

This study focuses on the nonlinear analysis of unreinforced masonry structures which can be approximated as being in a state of plane stress, such as panels and shear walls. The structures under consideration are subjected to short time static loads, which are not necessarily proportional but, in essence, monotonical. The primary aim of this study is the development and evaluation of robust and accurate numerical tools, both at the micro- and macro-level. The objectives of this study are:

- to adopt solution techniques and develop constitutive models which are stable and economical in the entire loading regime of the structure;
- to develop a constitutive micro-model for unreinforced masonry which includes softening and incorporates all failure mechanisms, viz. tensile, shear and compressive failure;
- to discuss the adequacy of using homogenization techniques, in which the macro-behavior of the composite is predicted from the micro-properties of masonry constituents;

- to develop a constitutive macro-model for unreinforced masonry that includes anisotropic elastic as well as anisotropic inelastic behavior and incorporates the knowledge of nonlinear fracture mechanics used in crack propagation problems;
- to verify the developed models by comparing the predicted behavior with the behavior observed in experiments on different types of structures. The developed models should be able to predict the failure mode and the ultimate load with reasonable agreement with the experimental values. It is noted, however, that masonry experimental results show typically a wide scatter, not only in large structures but also in small tests. The main concern of this work is, thus, to demonstrate the ability of the models to capture the behavior observed in the experiments and not a sharp reproduction of the experimental results in the form of a load-displacement curve;
- demonstration of the applicability of the models in engineering practice.

It is further noted that the models developed and the discussion carried out in this study have a much broader applicability than masonry structures. It is expected that the proposed micro-model can spin-off to other areas such as adhesives, joints in rock and stone works, contact problems between bodies and, in general, all types of interface behavior where bonding, cohesion and friction between constituents form the basic mechanical actions. The macro-model can be utilized for most anisotropic materials such as glass, plastics or wood as well as any composite.

Chapter 2 characterizes masonry and the modeling strategies for masonry structures. In particular, it addresses the need of a thorough material description in order to develop accurate numerical models. It is noted that deformation controlled tests are generally lacking, especially with respect to the composite behavior of masonry. An overview of testing apparatus and results relevant for numerical purposes is presented.

Chapter 3 deals with the solution procedures to solve the equilibrium of a body and reviews the general formulation of a plasticity based constitutive model. The nonlinear system of equations which follows from the finite element discretization will be solved with an incremental-iterative globally convergent Newton-Raphson method with arc-length control and line search technique. A general formulation for the numerical implementation of the theory of multisurface plasticity is presented in modern concepts, including an implicit Euler backward return mapping solved with a regular Newton-Raphson method and consistent tangential operators for all modes of the composite yield surface.

Chapter 4 introduces an interface failure criterion for the micro-modeling of masonry. The multisurface plasticity model comprehends a straight tension cut-off, the Coulomb friction law and an elliptical cap. The inelastic behavior includes tensile strength softening, cohesion softening, compressive strength hardening and softening, friction softening or hardening, dilatancy softening and coupling between tensile and shear failure. Validation of the model is performed by means of a comparison between the calculated numerical results and experimental results available in the literature.

Chapter 5 deals with two perspectives of the homogenization techniques. A first approach aims at describing the composite behavior of masonry in a simplified manner.

The process resorts to the constitutive laws of the masonry components and the geometrical arrangement of units and mortar but does not actually discretize the geometry. This simplified homogenization technique is based in the assumption of layered materials, for which a novel matrix formulation for elastoplastic behavior is presented. A second approach aims at predicting macro-properties of masonry resorting to the discretization of masonry components. Two examples are given, namely, the calculation of the composite elastic constants and the calculation of the composite tensile fracture energy in the direction parallel to the bed joints.

Chapter 6 presents an anisotropic continuum model for the macro-modeling of masonry. The multisurface plasticity model comprehends a Rankine type yield surface for tension and a Hill type yield surface for compression. Anisotropic elasticity is combined with anisotropic plasticity, in such a way that totally different behavior can be predicted along the material axes, both in tension and compression. Validation of the model is performed by means of a comparison between the calculated numerical results and experimental results available in the literature.

Chapter 7 presents engineering applications of the models developed in this study. One application concerns the spacing of movement-joints in masonry walls, as an example of how the developed models can be used to obtain ready-to-use design rules. Another application concerns the prediction of damage in existing masonry buildings due to settlements caused by tunneling, as an example of the assessment of complex structures under new loading conditions. The last application concerns the safety of damaged historical buildings, as an example of the assessment of existing structures under current loading conditions.

Chapter 8 presents an extended summary and final conclusions which can be derived from this study.

## 2. MODELING MASONRY: A MATERIAL DESCRIPTION

This Chapter deals with micro- and macro-modeling of masonry and the connection with the corresponding micro- and macro-material descriptions. The aspects of softening in quasi-brittle materials are introduced before a brief review of the material properties necessary for a complete numerical description is presented. A material description for micro-modeling must be obtained from tests in the masonry constituents and small masonry samples whereas, for macro-modeling, tests must be performed in masonry specimens of sufficient size under homogeneous states of stress and strain. Importance is given to deformation controlled test configurations capable of capturing the entire load-displacement diagram. In particular, attention is given to an integrated analytical, experimental and numerical research program completed in the Netherlands and reported by CUR (1994). A complete description of the material is not pursued in this study and the reader is referred to Drysdale *et al.* (1994) and Hendry (1990) for this purpose.

### 2.1 Micro- and macro-modeling

Masonry is a material which exhibits distinct directional properties due to the mortar joints which act as planes of weakness. In general, the approach towards its numerical representation can focus on the micro-modeling of the individual components, viz. unit (brick, block, etc.) and mortar, or the macro-modeling of masonry as a composite, see also Rots (1991). Depending on the level of accuracy and the simplicity desired, it is possible to use the following modeling strategies, see Figure 2.1:

- Detailed micro-modeling - units and mortar in the joints are represented by continuum elements whereas the unit-mortar interface is represented by discontinuous elements;
- Simplified micro-modeling - expanded units are represented by continuum elements whereas the behavior of the mortar joints and unit-mortar interface is lumped in discontinuous elements;
- Macro-modeling - units, mortar and unit-mortar interface are smeared out in the continuum.

In the first approach, Young's modulus, Poisson's ratio and, optionally, inelastic properties of both unit and mortar are taken into account. The interface represents a potential crack/slip plane with initial dummy stiffness to avoid interpenetration of the continuum. This enables the combined action of unit, mortar and interface to be studied under a magnifying glass. In the second approach, each joint, consisting of mortar and the two unit-mortar interfaces, is lumped into an "average" interface while the units are expanded in order to keep the geometry unchanged. Masonry is thus considered as a set

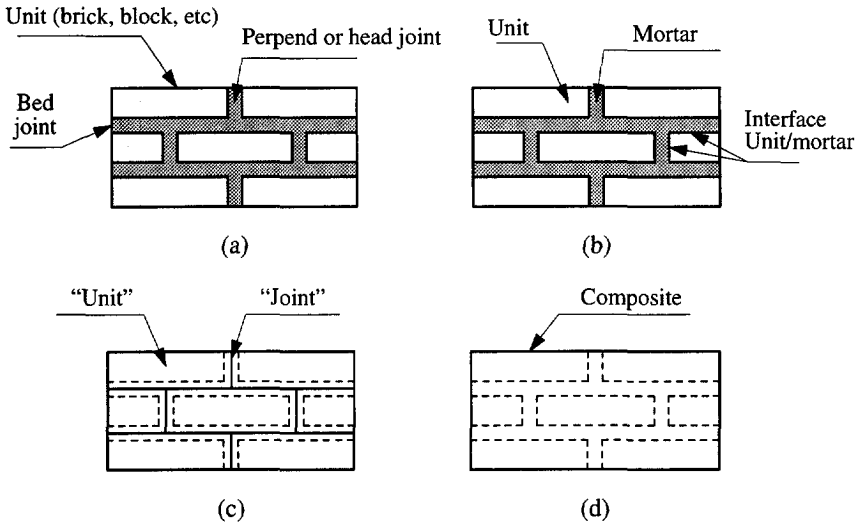


*Figure 2.1* Modeling strategies for masonry structures: (a) masonry sample; (b) detailed micro-modeling; (c) simplified micro-modeling; (d) macro-modeling.

of elastic blocks bonded by potential fracture/slip lines at the joints. Accuracy is lost since Poisson's effect of the mortar is not included. The third approach does not make a distinction between individual units and joints but treats masonry as a homogeneous anisotropic continuum. One modeling strategy cannot be preferred over the other because different application fields exist for micro- and macro-models. Micro-modeling studies are necessary to give a better understanding about the local behavior of masonry structures. This type of modeling applies notably to structural details, but also to modern building systems like those of concrete or calcium-silicate blocks, where window and door openings often result in piers that are only a few block units in length. These piers are likely to determine the behavior of the entire wall and individual modeling of the blocks and joints is then to be preferred. Macro-models are applicable when the structure is composed of solid walls with sufficiently large dimensions so that the stresses across or along a macro-length will be essentially uniform. Clearly, macro-modeling is more practice oriented due to the reduced time and memory requirements as well as a user-friendly mesh generation. This type of modeling is most valuable when a compromise between accuracy and efficiency is needed.

Accurate micro- or macro-modeling of masonry structures requires a thorough experimental description of the material. However, the properties of masonry are influenced by a large number of factors, such as material properties of the units and mortar, arrangement of bed and head joints, anisotropy of units, dimension of units, joint width, quality of workmanship, degree of curing, environment and age. Due to this diversity, only recently the masonry research community began to show interest in sophisticated numerical models as an opposition to the prevailing tradition of rules-of-thumb or

empirical formulae. Moreover, obtaining experimental data, which is reliable and useful for numerical models, has been hindered by the lack of communication between analysts and experimentalists. The use of different testing methods, test parameters and materials preclude comparisons and conclusions between most experimental results. It is also current practice to report and measure only strength values and to disregard deformation characteristics. In particular, for the post-peak or softening regime almost no relevant information was available in the literature.

## 2.2 Aspects of softening behavior

Softening is a gradual decrease of mechanical resistance under a continuous increase of deformation forced upon a material specimen or structure. It is a salient feature of quasi-brittle materials like clay brick, mortar, ceramics, rock or concrete, which fail due to a process of progressive internal crack growth. Such mechanical behavior is commonly attributed to the heterogeneity of the material, due to the presence of different phases and material defects, like flaws and voids. Even prior to loading, mortar contains microcracks due to the shrinkage during curing and the presence of the aggregate. The clay brick contains inclusions and microcracks due to the shrinkage during the burning process. The initial stresses and cracks as well as variations of internal stiffness and strength cause progressive crack growth when the material is subjected to progressive deformation. Initially, the microcracks are stable which means that they grow only when the load is increased. Around peak load an acceleration of crack formation takes place and the formation of macrocracks starts. The macrocracks are unstable, which means that the load has to decrease to avoid an uncontrolled growth. In a deformation controlled test the macrocrack growth results in softening and localization of cracking in a small zone while the rest of the specimen unloads.

For tensile failure this phenomenon has been well identified, see e.g. Hordijk (1991). For shear failure, a softening process is also observed as degradation of the cohesion in Coulomb friction models. For compressive failure, softening behavior is highly dependent upon the boundary conditions in the experiments and the size of the specimen, Van Mier (1984) and Vonk (1992). Experimental concrete data provided by Vonk (1992) indicated that the behavior in uniaxial compression is governed by both local and continuum fracturing processes.

Figure 2.2 shows characteristic stress-displacement diagrams for quasi-brittle materials in uniaxial tension and compression. In the present study, it is assumed that the inelastic behavior both in tension and compression can be described by the integral of the  $\sigma - \delta$  diagram. These quantities, denoted respectively as fracture energy  $G_f$  and compressive fracture energy  $G_c$ , are assumed to be material properties. With this energy-based approach tensile and compressive softening can be described within the same context which is plausible, because the underlying failure mechanisms are identical, viz. continuous crack growth at micro-level. It is noted that masonry presents other type of failure mechanism, generally identified as mode II, that consists of slip of

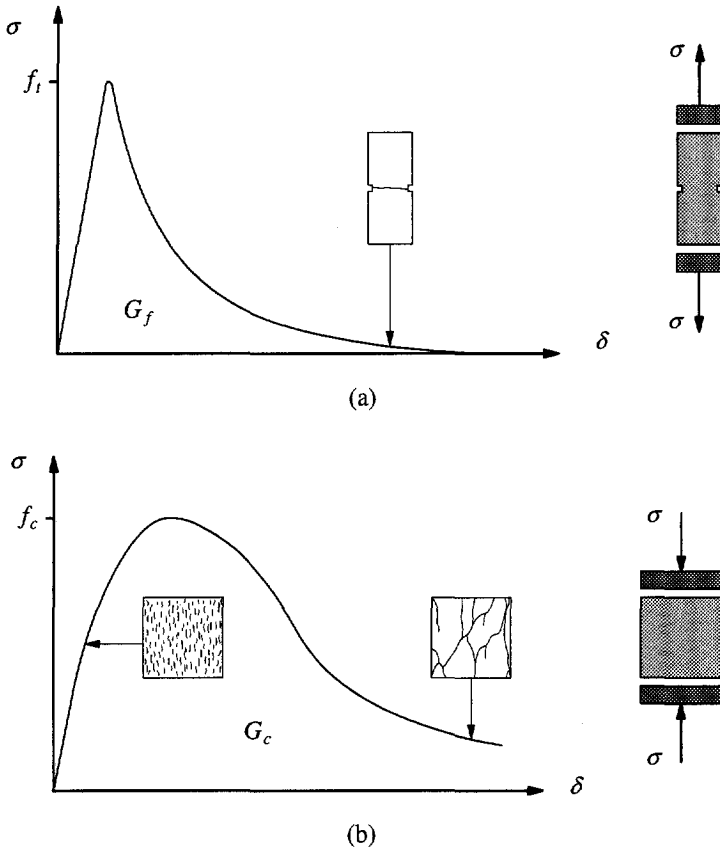


Figure 2.2 Typical behavior of quasi-brittle materials under uniaxial loading and definition of fracture energy: (a) tensile loading ( $f_t$  denotes the tensile strength); (b) compressive loading ( $f_c$  denotes the compressive strength).

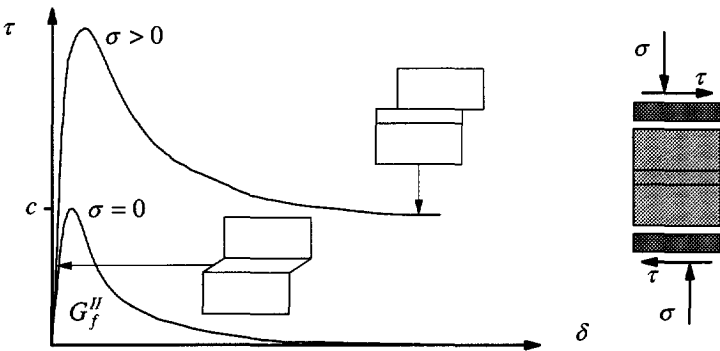


Figure 2.3 Behavior of masonry under shear and definition of mode II fracture energy  $G_f^{II}$  ( $c$  denotes the cohesion).

the unit-mortar interface under shear loading, see Figure 2.3. Again, it is assumed that the inelastic behavior in shear can be described by the mode II fracture energy  $G_f^II$ , defined by the integral of the  $\tau - \delta$  diagram in the absence of normal confining load. Shear failure is a salient feature of masonry behavior which must be incorporated in a micro-modeling strategy. However, for continuum models, this failure cannot be directly included because the unit and mortar geometries are not discretized. Failure is then associated with tension and compression modes in a principal stress space.

### 2.3 Properties of unit and mortar

The properties of masonry are strongly dependent upon the properties of its constituents. Compressive strength tests are easy to perform and give a good indication of the general quality of the materials used. The CEN Eurocode 6 (1995) uses the compressive strength of the components to determine the strength of masonry even if a true indication of those values is not simple.

For the masonry units, standard tests with solid platens result in an artificial compressive strength due to the restraint effect of the platens. The CEN Eurocode 6 (1995) minimizes this effect by considering a normalized compressive strength  $f_b$ , which results from the standard compressive strength, in the relevant direction of loading, multiplied by an appropriate shape/size factor. The normalized compressive strength refers to a cubic specimen with  $100 \times 100 \times 100$  [mm<sup>3</sup>] and cannot be considered representative of the true strength. Experiments in the uniaxial post-peak behavior of compressed bricks and blocks are virtually non-existent and no recommendations about the compressive fracture energy  $G_c$  can be made.

It is difficult to relate the tensile strength of the masonry unit to its compressive strength due to the different shapes, materials, manufacture processes and volume of perforations. For the longitudinal tensile strength of clay, calcium-silicate and concrete units, Schubert (1988a) carried out an extensive testing program and obtained a ratio between the tensile and compressive strength that ranges from 0.03 to 0.10. For the fracture energy  $G_f$  of solid clay and calcium-silicate units, both in the longitudinal and normal directions, Van der Pluijm (1992) found values ranging from 0.06 to 0.13 [Nmm/mm<sup>2</sup>] for tensile strength values ranging from 1.5 to 3.5 [N/mm<sup>2</sup>].

Experiments on the biaxial behavior of bricks and blocks are also lacking in the literature. This aspect gains relevance due to the usual orthotropy of the units due to perforations. As a consequence, the biaxial behavior of a brick or block with a given shape is likely to be unknown, even if the behavior of the material from which the unit is made, e.g. concrete or clay, is known.

For the mortar, the compressive strength  $f_{mo}$  is obtained from standard tests carried out in the two halves of the  $40 \times 40 \times 160$  [mm<sup>3</sup>] prisms used for the flexural test. The specimens are casted in steel molds and the water absorption effect of the unit is ignored, being thus non-representative of the mortar inside the composite. Currently, investigations in mortar disks extracted from the masonry joints are being carried out to

fully characterize the mortar behavior, Bierwirth *et al.* (1993), Schubert and Hoffman (1994) and Stöckl *et al.* (1994). Nevertheless, there is still a lack of knowledge about the complete mortar uniaxial behavior, both in compression and tension.

## 2.4 Properties of the unit-mortar interface

The bond between the unit and mortar is often the weakest link in masonry assemblages. The nonlinear response of the joints, which is then controlled by the unit-mortar interface, is one of the most relevant features of masonry behavior. Two different phenomena occur in the unit-mortar interface, one associated with tensile failure (mode I) and the other associated with shear failure (mode II).

### 2.4.1 Mode I failure

Van der Pluijm (1992) carried out deformation controlled tests in small masonry specimens of solid clay and calcium-silicate units, see Figure 2.4. These tests resulted in an exponential tension softening curve with a mode I fracture energy  $G_f^I$  ranging from 0.005 to 0.02 [ $Nmm/mm^2$ ] for a tensile bond strength ranging from 0.3 to 0.9 [ $N/mm^2$ ], according to the unit-mortar combination. This fracture energy is defined as the amount of energy to create a unitary area of a crack along the unit-mortar interface. A close observation of the cracked specimens revealed that the bond area was smaller than the cross sectional area of the specimen, see Figure 2.5a. This so-called net bond surface seems to concentrate in the inner part of the specimen, which can be a combined result from shrinkage of the mortar and the process of laying units in the mortar bed. For a

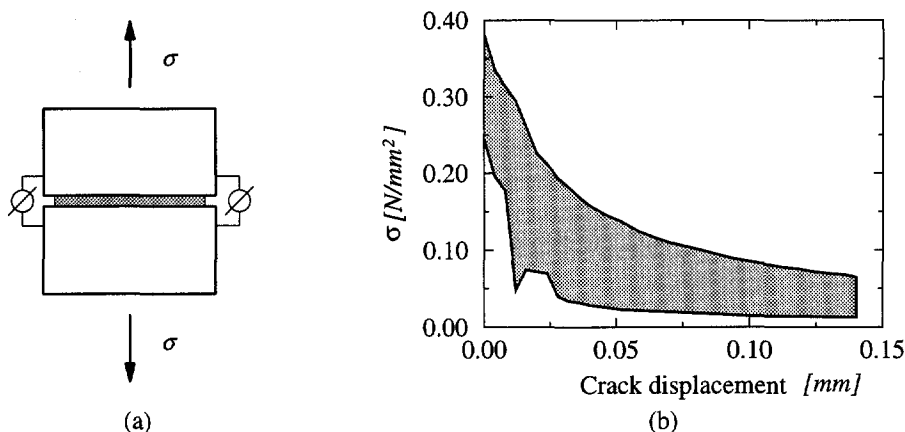
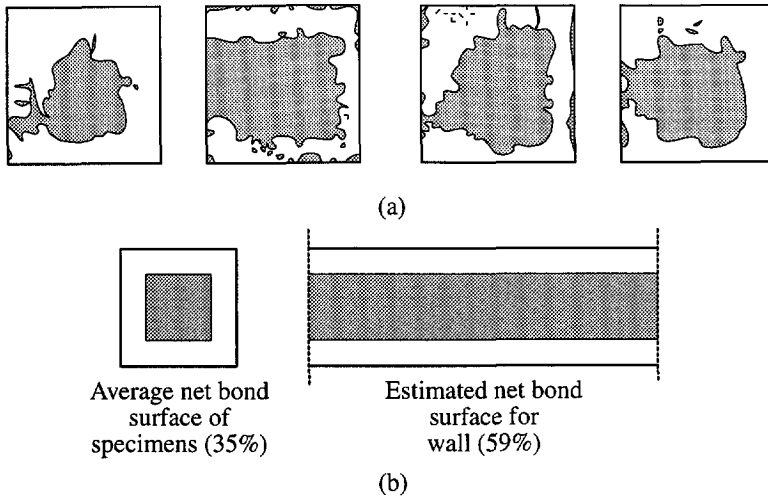


Figure 2.4 Tensile bond behavior of masonry, Van der Pluijm (1992): (a) test specimen; (b) typical experimental stress-crack displacement results for solid clay brick masonry (the shaded area represents the envelope of three tests).



**Figure 2.5** Tensile bond surface, Van der Pluijm (1992): (a) typical net bond surface for tensile specimens of solid clay units; (b) extrapolation of net bond surface from specimen to wall.

wall the net bond surface must be corrected according to a smaller number of edges, see Figure 2.5b. The values given above refer to the real cross section of a wall and result from an extrapolation of the measured net bond surface of the specimen to the assumed net bond surface of the wall, neglecting any influence of the vertical joints.

## 2.4.2 Mode II failure

An important aspect in the determination of the shear response of masonry joints is the ability of the test set-up to generate a uniform state of stress in the joints. This objective is difficult because the equilibrium constraints introduce non-uniform normal stresses in the joint. A discussion about the adequacy of different test configurations will not be given here and the reader is referred to Van der Pluijm (1993) and Atkinson *et al.* (1989) for this purpose.

Van der Pluijm (1993) presents the most complete characterization of the masonry shear behavior, for solid clay and calcium-silicate units. The test set-up shown in Figure 2.6 permits to keep a constant normal confining pressure upon shearing. Confining (compressive) stresses were applied with three different levels: 0.1, 0.5 and 1.0 [ $N/mm^2$ ]. The test apparatus did not allow for application of tensile stresses and even for low confining stresses extremely brittle results are found with potential instability of the test set-up. Noteworthy, for several specimens with higher confining stresses shearing of the unit-mortar interface was accompanied by diagonal cracking in the unit.

The experimental results yield an exponential shear softening diagram with a residual dry friction level, see Figure 2.7a. The area defined by the stress-displacement

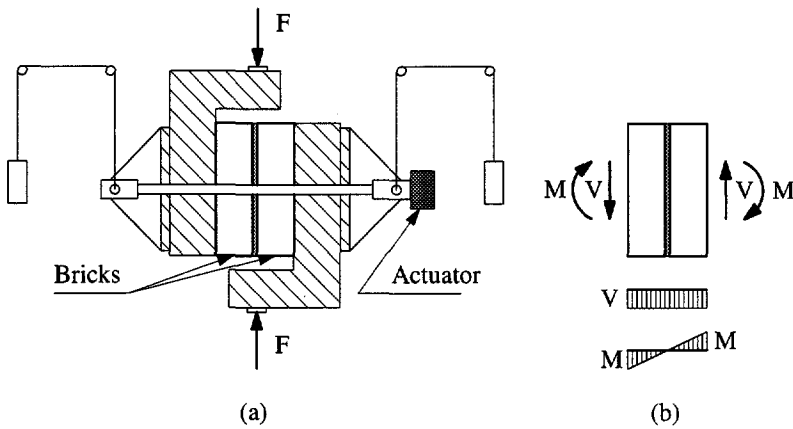


Figure 2.6 Test set-up to obtain shear bond behavior, Van der Pluijm (1993): (a) test specimen ready for testing; (b) forces applied to the test specimen during testing.

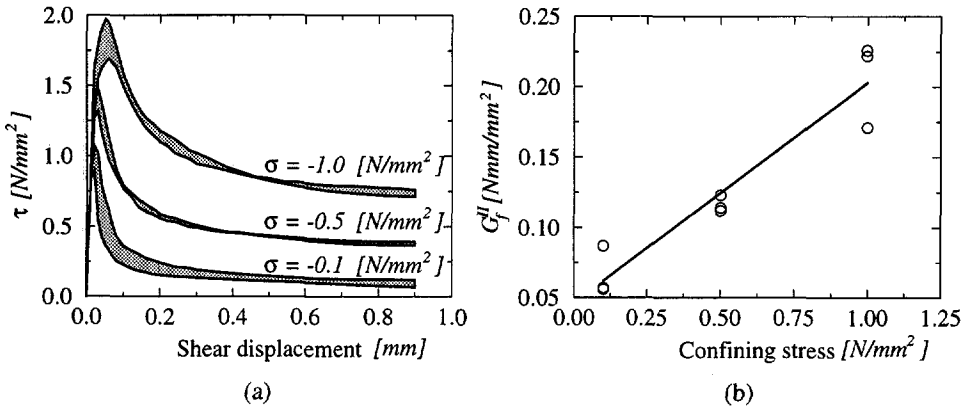


Figure 2.7 Typical shear bond behavior of the joints for solid clay units, Van der Pluijm (1993): (a) stress-displacement diagram for different normal stress levels (the shaded area represents the envelope of three tests); (b) mode II fracture energy  $G_f^{II}$  as a function of the normal stress level.

diagram and the residual dry friction shear level is named mode II fracture energy  $G_f^{II}$ , with values ranging from 0.01 to 0.25 [Nmm/mm<sup>2</sup>] for initial cohesion  $c$  values ranging from 0.1 to 1.8 [N/mm<sup>2</sup>]. The value for the fracture energy depends also on the level of the confining stress, see Figure 2.7b. Evaluation of the net bond surface of the specimens is no longer possible but the values measured for tensile bond strength can be assumed to hold. Additional material parameters can be obtained from such an experiment, see Figure 2.8. The initial internal friction angle  $\phi_0$ , associated with a Coulomb friction model, is measured by  $\tan \phi_0$ , which ranges from 0.7 to 1.2, for different unit-mortar combinations. The residual internal friction angle  $\phi_r$  is measured by  $\tan \phi_r$ ,

which seems to be approximately constant and to equal 0.75. The dilatancy angle  $\psi$  measures the uplift of one unit over the other upon shearing, see Figure 2.8b. Note that the dilatancy angle depends on the level of the confining stress, see Figure 2.9a. For low confining pressures, the average value of  $\tan \psi$  falls in the range from 0.2 to 0.7, depending on the roughness of the unit surface. For high confining pressures,  $\tan \psi$  decreases to zero. With increasing slip,  $\tan \psi$  also decreases to zero due to the smoothing of the sheared surfaces, see Figure 2.9b.

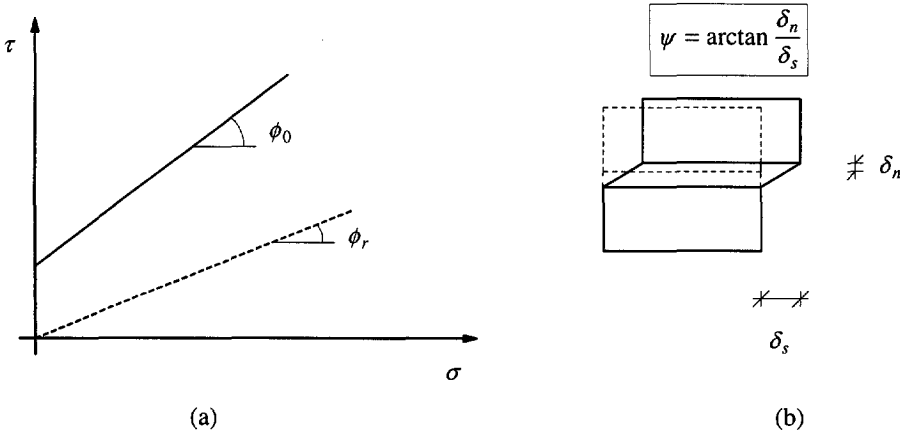


Figure 2.8 Definition of friction and dilatancy angles: (a) Coulomb friction law, with initial and residual friction angle; (b) dilatancy angle as the uplift of neighboring units upon shearing.

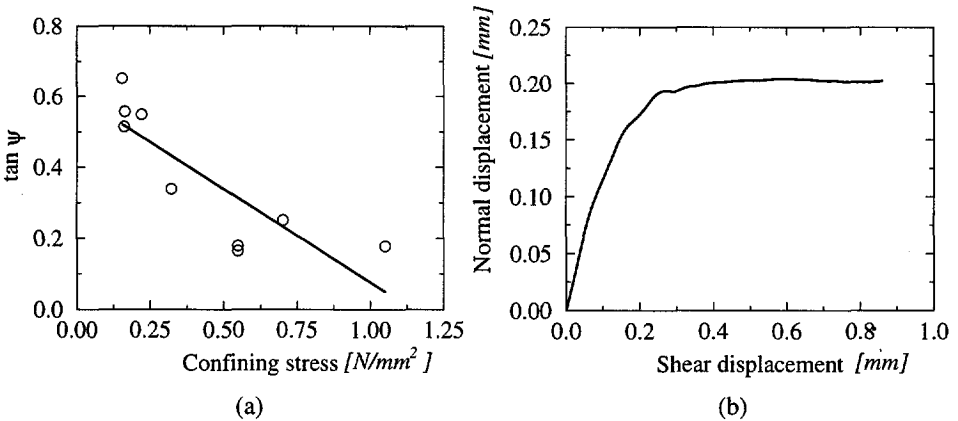


Figure 2.9 Typical shear bond behavior of the joints for solid clay units, Van der Pluijm (1993): (a) tangent of the dilatancy angle  $\psi$  as a function of the normal stress level; (b) relation between the normal and the shear displacement upon loading.

## 2.5 Properties of the composite material

The uniaxial behavior of the composite material is described next with regard to the material axes, namely the directions parallel and normal to the bed joints.

### 2.5.1 Uniaxial compressive behavior of masonry

The compressive strength of masonry in the direction normal to the bed joints has been traditionally regarded as the sole relevant structural material property, at least until the recent introduction of numerical methods for masonry structures. A test frequently used to obtain this uniaxial compressive strength is the stacked bond prism, see Figure 2.10a, but it is still somewhat unclear what are the consequences in the masonry strength of using this type of specimens, Mann and Betzler (1994). It is commonly accepted that the real uniaxial compressive strength of masonry in the direction normal to the bed

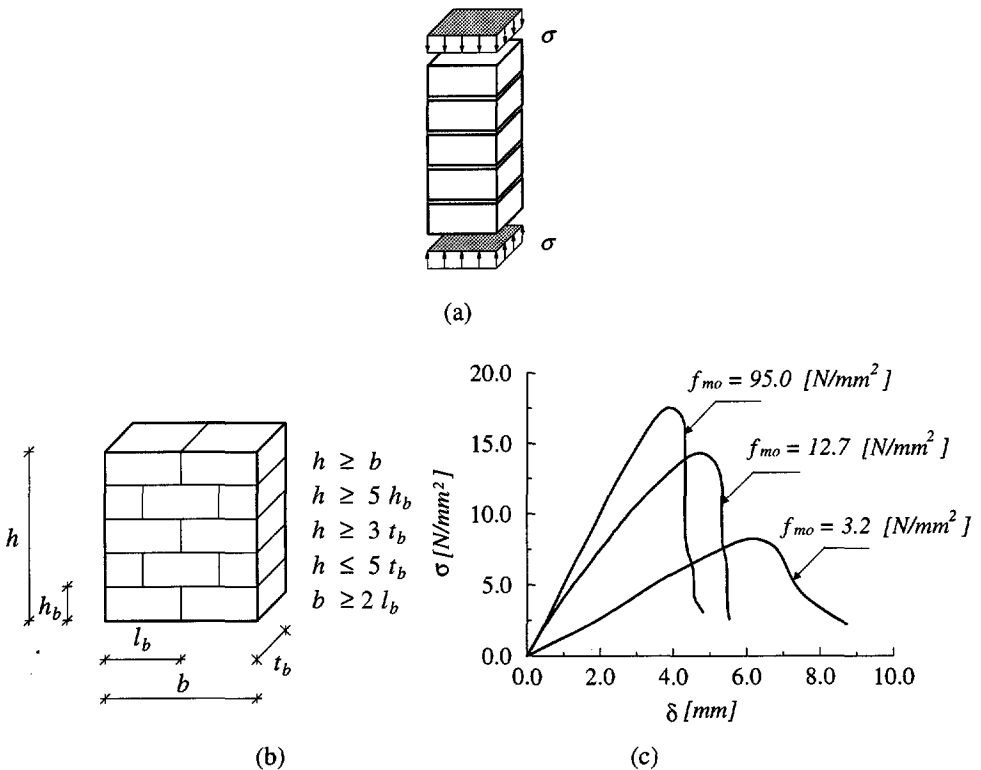


Figure 2.10 Uniaxial behavior of masonry upon loading normal to the bed joints: (a) stacked bond prism; (b) schematic representation of RILEM test specimen; (c) typical experimental stress-displacement diagrams for  $500 \times 250 \times 600$  [mm<sup>3</sup>] prisms of solid soft mud brick, Binda *et al.* (1988). Here,  $f_{mo}$  is the mortar compressive strength.

joints can be obtained from the so-called RILEM test, see Wesche and Ilanzis (1980), shown in Figure 2.10b. The RILEM specimen is however relatively large and costly to execute, especially when compared to the standard cube or cylinder tests for concrete. Since the pioneering work of Hilsdorf (1969) it has been accepted by the masonry community that the difference in elastic properties of the unit and mortar is the precursor of failure. Uniaxial compression of masonry leads to a state of triaxial compression in the mortar and of compression/biaxial tension in the unit. Mann and Betzler (1994) observed that, initially, vertical cracks appear in the units along the middle line of the specimen, i.e. continuing a vertical joint. Upon increasing deformation additional cracks appear, normally vertical cracks at the small side of the specimen, that lead to failure by splitting of the prism. Examples of load-displacement diagrams obtained in  $500 \times 250 \times 600$  [mm<sup>3</sup>] prisms of solid soft mud bricks are shown in Figure 2.10c. Increasing strength leads to a more brittle behavior. The quite high value of the compressive fracture energy  $G_c$ , which equals  $\sim 45$  [Nmm/mm<sup>2</sup>], can be explained by the continuum fracture energy and the 600 [mm] height of the specimen, see Vonk (1992). Atkinson and Yan (1990) collected information about the compressive stress-strain relation for masonry, but these results are not energy based.

Uniaxial compression tests in the direction parallel to the bed joints have received substantially less attention from the masonry community. However, masonry is an anisotropic material and, particularly in the case of low longitudinal compressive strength of the units due to high or unfavorable perforation, the resistance to compressive loads parallel to the bed joints can have a decisive effect on the load bearing capacity. According to Hoffmann and Schubert (1994), the ratio between the uniaxial compressive strength parallel and normal to the bed joints ranges from 0.2 to 0.8. These ratios were obtained for masonry samples of solid and perforated clay units, calcium-silicate units, lightweight concrete units and aerated concrete units.

### 2.5.2 Uniaxial tensile behavior of masonry

For tensile loading perpendicular to the bed joints, failure is generally caused by failure of the relatively low tensile bond strength between the bed joint and the unit. As a rough approximation, the masonry tensile strength can be equated to the tensile bond strength between the joint and the unit, see Section 2.4.1.

In masonry with low strength units and greater tensile bond strength between the bed joint and the unit, e.g. high-strength mortar and units with numerous small perforations, which produce a dowel effect, failure may occur as a result of stresses exceeding the unit tensile strength. As a rough approximation, the masonry tensile strength in this case can be equated to the tensile strength of the unit, see Section 2.3.

For tensile loading parallel to the bed joints a complete test program was set-up by Backes (1985). The specimen consists of four courses, initially laid down in the usual manner, see Figure 2.11a. A special device attached to the specimen turns it 90° in the

intended direction of testing shortly before the test time, see Figure 2.11b. The load is applied via steel plates attached to the top and bottom of the specimen by a special glue. The entire load-displacement diagram is traced upon displacement control.

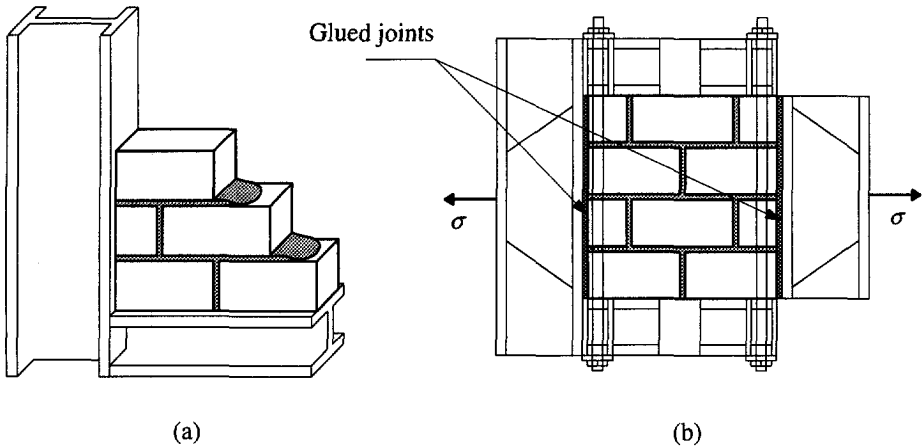


Figure 2.11 Test set-up for tensile strength of masonry parallel to the bed joints, Backes (1985): (a) building of the test specimen; (b) test specimen before 90° rotation and testing.

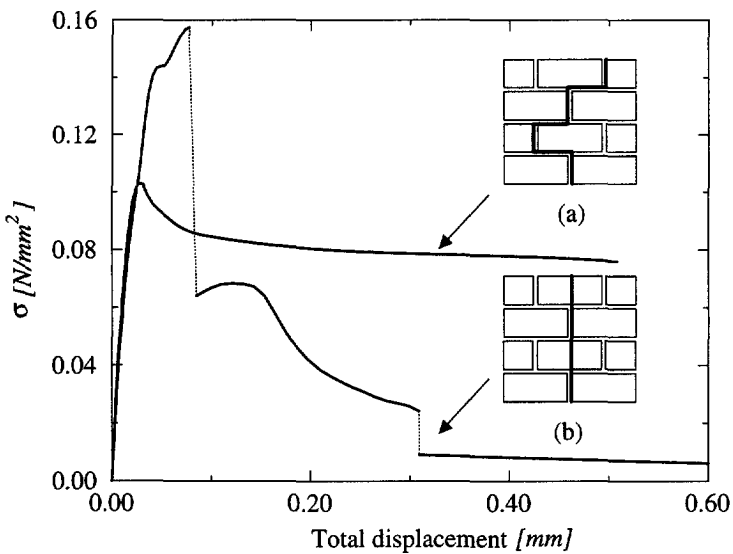


Figure 2.12 Typical experimental stress-displacement diagrams for tension in the direction parallel to the bed joints, Backes (1985): (a) failure occurs with a stepped crack through head and bed joints; (b) failure occurs vertically through head joints and units.

Two different types of failure are possible, depending on the relative strength of joints and units, see Figure 2.12. In the first type of failure cracks zigzag through head and bed joints. A typical stress-displacement diagram shows some residual plateau upon increasing deformation. The post-peak response of the specimen is governed by the fracture energy of the head joints and the post-peak mode II behavior of bed joints. In the second type of failure cracks run almost vertically through the units and head joints. A typical stress-displacement diagram shows progressive softening until zero. The post-peak response is governed by the fracture energy of the units and head joints.

### 2.5.3 Biaxial behavior

The constitutive behavior of masonry under biaxial states of stress cannot be completely described from the constitutive behavior under uniaxial loading conditions. The influence of the biaxial stress state has been investigated up to peak stress to provide a biaxial strength envelope, which cannot be described solely in terms of principal stresses because masonry is an anisotropic material. Therefore, the biaxial strength envelope of masonry must be either described in terms of the full stress vector in a fixed set of material axes or, in terms of principal stresses and the rotation angle  $\theta$  between the principal stresses and the material axes. The most complete set of experimental data of masonry subjected to proportional biaxial loading is shown in Figure 2.13, Page (1981, 1983). The tests were carried out with half scale solid clay units. Both the orientation of the principal stresses with regard to the material axes and the principal stress ratio considerably influence the failure mode and strength. The different modes of failure are illustrated in Figure 2.14.

For uniaxial tension, failure occurred by cracking and sliding of the head and bed joints. The influence of the lateral tensile stress in the tensile strength is not known because no experimental results are available. A lateral compressive stress decreases the tensile strength, which can be explained by the damage induced in the composite material, by microslip of the joints and microcracking of the units. In the tension-compression loading cases failure occurred either by cracking and sliding of the joints alone or in a combined mechanism involving both units and joints. Similar types of failure occurred for uniaxial compression but a smooth transition is found to other type of failure mode in biaxial compression. In biaxial compression failure typically occurred by splitting of the specimen at mid-thickness, in a plane parallel to its free surface, regardless of the orientation of the principal stresses. For principal stress ratios  $\ll 1$  and  $\gg 1$ , the orientation played a significant role and failure occurred in a combined mechanism involving both joint failure and lateral splitting. The increase of compressive strength under biaxial compression can be explained by friction in the joints and internal friction in the units and mortar.

For concrete, the failure envelope seems to be largely independent of the loading path, Nelissen (1972), which confirms the presence of a single failure mode, i.e. continuous crack growth at the microlevel. Presently, it is not known if the masonry failure

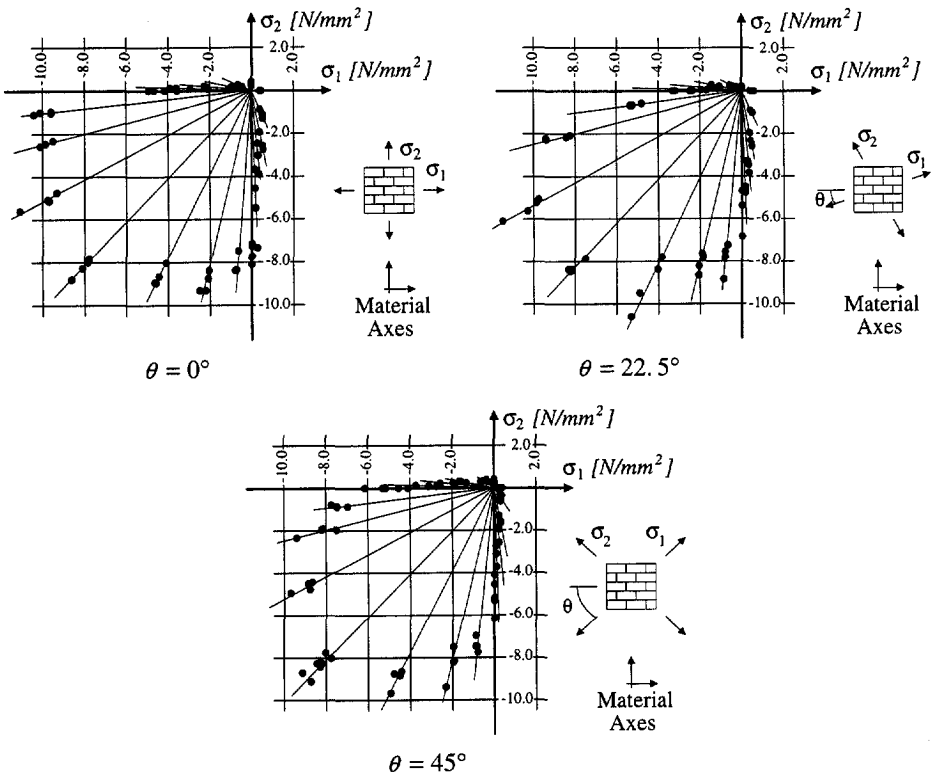


Figure 2.13 Biaxial strength of solid clay units masonry, Page (1981, 1983).

envelope obtained by Page (1981, 1983) is valid for nonproportional loading, particularly because different failure modes can be triggered. Another point is that experimental data about the softening of masonry under biaxial loading are scarce even if the softening of masonry is certainly influenced by the biaxial stress state.

It is further noted that the strength envelope shown in Figure 2.13 is of limited applicability for other types of masonry. Different strength envelopes and different failure modes are likely to be found for different materials, unit shapes and geometry. A comprehensive program to characterize the biaxial strength of different masonry types has been carried out in Switzerland using full scale specimens, see Ganz and Thürlimann (1982) for hollow clay units masonry, Guggisberg and Thürlimann (1987) for clay and calcium-silicate units masonry and Lurati *et al.* (1990) for concrete units masonry.

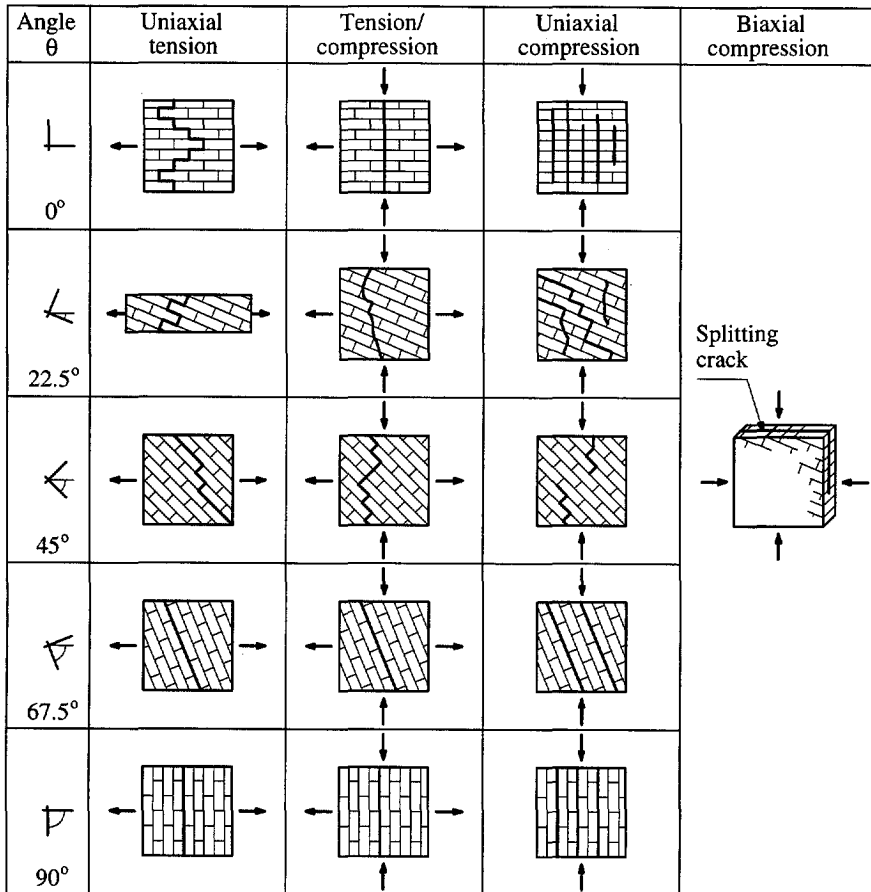


Figure 2.14 Modes of failure of solid clay units masonry under biaxial loading, Dhanasekar *et al.* (1985).

### 2.6 Summary

Masonry is a composite material that consists of units and mortar. The failure mechanism of the components loaded in tension and compression is essentially the same, viz. crack growth at the microlevel of the material. In this process inelastic strains result from a dissipative process in which fracture energy is released during the process of internal fracture. The composite material shows, however, another type of failure, sliding or mode II, which results in a dry friction process between the components once softening is completed. If a micro-modeling strategy is used all these phenomena can be incorporated in the model because joints and units are represented separately. In a macro-modeling strategy joints are smeared out in an anisotropic homogeneous

continuum and the interaction between the components cannot be incorporated in the model. Instead, a relation between average stresses and strains is established.

Independently of the type of strategy adopted, accurate masonry models can only be used if a complete material description is available. This is not generally the case because experimental data suitable for numerical purpose are scarce, especially in the softening regime. An overview of relevant testing apparatus and results has been given in this Chapter. The objective is not only to give insight in the material behavior, but also to demonstrate that it is possible to fully characterize the material behavior in the form necessary to accurate nonlinear finite element analyses. It requires only close cooperation between the numerical and experimental scientific community.

### 3. FINITE ELEMENTS AND PLASTICITY

In this study the finite element method is adopted to simulate the structural behavior. A mathematical description of the material behavior, which yields the relation between the stress and strain tensor in a material point of the body, is necessary for this purpose. This mathematical description is commonly named a constitutive model. Constitutive models will be developed here in a plasticity framework according to a phenomenological approach in which the observed mechanisms are represented in such a fashion that simulations are in reasonable agreement with experiments. It is not realistic to try to formulate constitutive models which fully incorporate all the interacting mechanisms of a specific material because any constitutive model or theory is a simplified representation of reality. It is believed that more insight can be gained by tracing the entire response of a structure than by modeling it with a highly sophisticated material model or theory which does not result in a converged solution close to the failure load. An important objective in the present study is thus to obtain robust numerical tools, capable of predicting the behavior of the structure from the linear elastic stage, through cracking and degradation until complete loss of strength. Only then, it is possible to control the serviceability limit state, to fully understand the failure mechanism and assess the safety of the structure. To achieve this objective it is necessary that robust constitutive algorithms are complemented with advanced solution procedures of the system of equations that results from the finite element discretization. The theory of plasticity is well established and sound numerical algorithms have been implemented, e.g. Simo *et al.* (1988b). It is a natural constitutive description for metals, Hill (1950), but it can also be used for quasi-brittle cementitious materials loaded in triaxial compression and shear-compression problems where inelastic non-recoverable strains are observed, Pijaudier-Cabot *et al.* (1994). The incapability of the theory to reproduce the elastic stiffness degradation of quasi-brittle materials subjected mainly to tension cannot be accepted for cyclic loading, in which case the damage theory, e.g. Pijaudier-Cabot *et al.* (1994), plastic-fracturing models, e.g. Chen and Han (1988), or discrete/smeared cracking models are more appropriate. However, for monotonic loading conditions, good results have been found, e.g. Feenstra (1993) and De Borst *et al.* (1994).

This Chapter contains a brief introduction to nonlinear finite elements and solution procedures. For a complete formulation of the finite element method the reader is referred to text books, see Zienkiewicz and Taylor (1989, 1991) and Bathe (1982). Further, the algorithmic aspects of the theory of single and multisurface rate independent plasticity are reviewed in modern concepts. A comprehensive description of the plasticity theory can be found elsewhere, e.g. Hill (1950) and Chen and Han (1988).

### 3.1 Nonlinear finite elements

In finite element computations based on the displacement method the structure is subdivided into elements, each with its own material properties and for which relations between the nodal forces and displacements can be derived. The assembly of the elements with the consideration of external loads and boundary conditions results in a system of equations describing the equilibrium of the structure, which has to be solved to obtain the nodal displacements of the structure. From these displacements it is possible to obtain strains and stresses in the integration points, as it is assumed that the element stiffness matrix is numerically integrated.

Figure 3.1 illustrates two element types widely used in this study, a plane stress continuum element and a zero-thickness line interface element. For continuum elements the constitutive model yields the relation between the stress and strain tensors, defined by the stress vector  $\boldsymbol{\sigma}$  and the strain vector  $\boldsymbol{\varepsilon}$ , respectively, as

$$\begin{aligned}\boldsymbol{\sigma} &= \{ \sigma_x \quad \sigma_y \quad \tau_{xy} \}^T \\ \boldsymbol{\varepsilon} &= \{ \varepsilon_x \quad \varepsilon_y \quad \gamma_{xy} \}^T\end{aligned}\quad (3.1)$$

Continuum elements are normally integrated with a Gauss scheme. Interface elements allow discontinuities in the displacement field and establish a direct relation between the tractions  $\mathbf{t}$  and the relative displacements along the interface  $\Delta\mathbf{u}$ , which are given by

$$\begin{aligned}\mathbf{t} &= \{ \boldsymbol{\sigma} \quad \boldsymbol{\tau} \}^T \\ \Delta\mathbf{u} &= \{ \Delta u_n \quad \Delta u_s \}^T\end{aligned}\quad (3.2)$$

Here, these quantities are conveniently defined as generalized stress vector  $\boldsymbol{\sigma}$  and generalized strain vector  $\boldsymbol{\varepsilon}$ , so that the same notation is adopted for continuum and discontinuous elements. This conceptually attractive notation is further confirmed by the fact that zero-thickness interface elements can be obtained by degeneration of continuum elements, Hohberg (1992). The formulation of interface elements is fairly standard, see Hohberg (1992) for an exhaustive discussion, even if it is usually not covered by finite

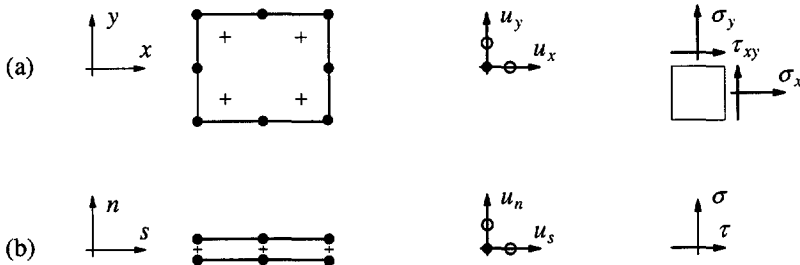


Figure 3.1 Examples of finite elements utilized in this study: (a) eight-noded plane stress element with Gauss integration; (b) six-noded line interface element with Lobatto integration.

elements text books. One of the most important issues is the selection of an appropriate integration scheme as Gauss integration was reported to lead to erroneous oscillations of stresses when based on the penalty approach, see also Rots (1988) and Schellekens (1992). In this study the interface elements are integrated with a Lobatto scheme, which overcomes the above deficiency.

### 3.1.1 Iterative techniques for the solution of nonlinear problems

The type of nonlinearity introduced in this study arises naturally in materials exhibiting inelastic constitutive laws in which the stress  $\sigma$  depends in some complex fashion on the strain  $\epsilon$  and its history. The case of material nonlinearity can be simply handled without rewriting the basic variational principles of linear problems, Zienkiewicz and Taylor (1989, 1991). The solution of the nonlinear problem can be obtained by some trial and error (iterative) application of the linear procedures until, at the final stage, a solution is achieved and the material constants are adjusted in such a way that equilibrium and the appropriate constitutive law are fulfilled.

The solution of a nonlinear problem does not necessarily exist and, when it exists, it is not necessarily unique. For this reason, a (converged) physically realistic solution is, usually, obtained with an incremental approach in which the total load is applied in small steps. Such steps are particularly necessary if the relation between stresses and strains is path dependent.

The problem is formulated in terms of a discretization set  $\mathbf{a}$ , which is the vector that collects all the nodal displacements. At the stage  $n + 1$  the system of equations to be solved reads, see Zienkiewicz and Taylor (1991),

$$\Psi_{n+1} = \Psi(\mathbf{a}_{n+1}) = \mathbf{p}(\mathbf{a}_{n+1}) - \mathbf{f}_{n+1} = \mathbf{0} \quad (3.3)$$

where  $\Psi$  is the vector of residuals (or unbalanced forces),  $\mathbf{p}$  is the vector of internal forces and  $\mathbf{f}$  is the vector of external forces. The (near) equilibrium solution from the previous load stage  $n$

$$\mathbf{a} = \mathbf{a}_n \quad \Psi_n = \mathbf{0} \quad \mathbf{f} = \mathbf{f}_n \quad (3.4)$$

is altered when the next load increment is applied

$$\mathbf{f}_{n+1} = \mathbf{f}_n + \Delta\mathbf{f}_{n+1} \quad (3.5)$$

The determination of the change of the nodal displacements vector  $\Delta\mathbf{a}_{n+1}$  such that

$$\mathbf{a}_{n+1} = \mathbf{a}_n + \Delta\mathbf{a}_{n+1} \quad (3.6)$$

will be the objective and, generally, the load increment  $\Delta\mathbf{f}_{n+1}$  will be kept reasonably small so that path dependence can be followed. Such procedure is further useful in

avoiding an excessive number of iterations, falling outside the radius of convergence of the iterative procedure and, indeed, in following the physically correct path. Different proposals for self-adaptive loading methods have been put forward, see Clarke and Hancock (1990) for an overview, but these methods will not be resorted to here. It is believed that further insight into the structural behavior can be obtained by manual adjustment of the load increments and continuous monitoring of the structure's behavior, as required by convergence constraints and reasoning.

The nonlinear problem is solved with a locally quadratic convergent Newton-Raphson method, which is derived by finding the root of an approximation of eq. (3.3) at the current state as

$$\Psi(\mathbf{a}_{n+1}^{i+1}) \approx \Psi(\mathbf{a}_{n+1}^i) + \left( \frac{\partial \Psi}{\partial \mathbf{a}} \right)_{n+1}^i \delta \mathbf{a}_{n+1}^{i+1} = \mathbf{0} \quad (3.7)$$

Here  $i$  is the iteration counter starting with  $\mathbf{a}_{n+1}^0 = \mathbf{a}_n$  and

$$\left( \frac{\partial \Psi}{\partial \mathbf{a}} \right)_{n+1}^i = \left( \frac{\partial \mathbf{p}}{\partial \mathbf{a}} \right)_{n+1}^i = (\mathbf{K}_t)_{n+1}^i \quad (3.8)$$

where  $\mathbf{K}_t$  is the assembled tangential stiffness matrix. Eq. (3.7) gives immediately the iterative correction of the nodal displacements increment as

$$\delta \mathbf{a}_{n+1}^{i+1} = -(\mathbf{K}_t^{-1})_{n+1}^i \Psi_{n+1}^i \quad (3.9)$$

A series of successive approximations gives

$$\mathbf{a}_{n+1}^{i+1} = \mathbf{a}_n + \Delta \mathbf{a}_{n+1}^{i+1} = \mathbf{a}_{n+1}^i + \delta \mathbf{a}_{n+1}^{i+1} \quad (3.10)$$

with

$$\Delta \mathbf{a}_{n+1}^{i+1} = \sum_{k=1}^{i+1} \delta \mathbf{a}_{n+1}^k \quad (3.11)$$

until convergence within a prescribed tolerance is obtained<sup>†</sup>.

A severe limitation of the Newton-Raphson method is the fact that it is not globally convergent, i.e. convergent to *some* solution of a system of nonlinear equations *from almost any starting point*. In structural problems, the most used strategy for proceeding from a solution estimate outside the radius of convergence of the Newton-Raphson method is the technique of line searches. The search direction is the most critical part of

† It is essential to utilize the total increment  $\Delta \mathbf{a}_{n+1}^{i+1}$  in place of the iterative increment  $\delta \mathbf{a}_{n+1}^{i+1}$  if the constitutive law is path dependent, which is the case of the plasticity theory. Otherwise, spurious unloading can be found during the current load step, see also Nyssen (1981) and Marques (1984).

the technique, see Dennis and Schnabel (1983) for an overview. The approach normally used for structural problems is to write

$$\mathbf{a}_{n+1}^{i+1, j} = \mathbf{a}_{n+1}^i + \mu_{ij} \delta \mathbf{a}_{n+1}^{i+1} \quad (3.12)$$

where  $j$  is the counter of line searches and the line search factor  $\mu$  scales the incremental displacement field. The line search factor is determined such that the projection of the residuals in the search direction  $\delta \mathbf{a}_{n+1}^{i+1}$  is made zero, reading

$$(\delta \mathbf{a}_{n+1}^{i+1})^T \Psi(\mathbf{a}_{n+1}^i + \mu_{ij} \delta \mathbf{a}_{n+1}^{i+1}) = 0 \quad (3.13)$$

which is solved using the regula-falsi (or secant) method. If the line search algorithm is applied, generally the additional cost is negligible compared with the calculation of the internal force vector. The initial energy for  $\mu = 0$  is available from the previous iteration and the energy for  $\mu = 1$  is also readily available because the internal force vector is always calculated once. The condition given in eq. (3.13) is not satisfied exactly because the use of a weak acceptance criterion normally performs better, Dennis and Schnabel (1983). While no step-acceptance rule will always be optimal, it is common practice to require that

$$|(\delta \mathbf{a}_{n+1}^{i+1})^T \Psi(\mathbf{a}_{n+1}^i + \mu_{ij} \delta \mathbf{a}_{n+1}^{i+1})| \leq \eta |(\delta \mathbf{a}_{n+1}^{i+1})^T \Psi(\mathbf{a}_{n+1}^i)| \quad (3.14)$$

with  $\eta$  a tolerance factor which is usually chosen equal to 0.8 for the Newton-Raphson method. If the load increment is sufficiently small and the system of non-linear equations is not singular or ill-posed, this criterion is usually fulfilled without need of further line searches. A cut-off criterion is used if an extrapolation is calculated, Schweizerhof and Wriggers (1986). In the present study this technique will be used throughout the analyses with the continuum masonry model developed in Chapter 6. In the past most line search techniques have been applied together with modified or quasi Newton-Raphson methods to accelerate convergence, see e.g. Crisfield (1982). This is not the objective pursued here because the full Newton-Raphson method used is probably the most rapidly convergent process to solve a well-posed system of nonlinear equations. It is stressed again that, as in Feenstra (1993), the aim is a globally convergent algorithm.

### 3.1.2 Softening behavior: constrained Newton-Raphson method

The most natural way of controlling the loading process of nonlinear finite element analyses is to prescribe positive increments of the external load vector  $\mathbf{f}$  in eq. (3.3). In structural problems this is usually a set of loads that can be assumed proportional to a normalized load vector  $\mathbf{f}_0$ , so that one can write

$$\Delta \mathbf{f}_{n+1} = \Delta \lambda_{n+1} \mathbf{f}_0 \quad (3.15)$$

where  $\Delta\lambda$  is the load factor. The standard load control in which the initial load factor is kept constant during equilibrium fails at limit points, when negative increments of the external load must follow. As a remedy, one may use direct displacement control and increment certain continuously increasing degrees-of-freedom, i.e. components of the nodal displacement vector  $\mathbf{a}$ . The prescribed components are transferred to the right-hand side of eq. (3.9), while the other components and the load factor are solved from the reduced set which is generally well-conditioned. The approach is unable to handle strong localizations and suffers from lack of generality since only a limited number of engineering problems can be modeled in such a way. The arc-length method, introduced by Riks (1970) and Wempner (1971), overcomes these deficiencies by adding a constraint equation to the system of nonlinear equations so that the original problem, cf. eq. (3.3), is rewritten as

$$\begin{cases} \Psi_{n+1} = \mathbf{p}(\mathbf{a}_n + \Delta\mathbf{a}_{n+1}) - (\lambda_n + \Delta\lambda_{n+1}) \mathbf{f}_0 = \mathbf{0} \\ f(\Delta\lambda_{n+1}, \Delta\mathbf{a}_{n+1}) = 0 \end{cases} \quad (3.16)$$

in which  $\Delta\lambda_{n+1}$  is an additional variable. However, in order to prevent the banded nature and possible symmetry of the system from being destroyed, an alternative procedure has been proposed, Crisfield (1981) and Ramm (1981). For a given iteration the nodal displacement update can be written as

$$\begin{aligned} \delta\mathbf{a}_{n+1}^{i+1} &= -(\mathbf{K}_t^{-1})_{n+1}^i \Psi_{n+1}^i \\ &= -(\mathbf{K}_t^{-1})_{n+1}^i (\mathbf{p}_{n+1}^i - \mathbf{f}_n - \Delta\lambda_{n+1}^{i+1} \mathbf{f}_0) \\ &= \{(\mathbf{K}_t^{-1})_{n+1}^i (\mathbf{f}_n - \mathbf{p}_{n+1}^i)\} + \Delta\lambda_{n+1}^{i+1} \{(\mathbf{K}_t^{-1})_{n+1}^i \mathbf{f}_0\} \\ &= \delta^I \mathbf{a}_{n+1}^{i+1} + \Delta\lambda_{n+1}^{i+1} \delta^II \mathbf{a}_{n+1}^{i+1} \end{aligned} \quad (3.17)$$

where the first part  $\delta^I \mathbf{a}_{n+1}^{i+1}$  results from the difference between the external forces at the beginning of the load step and the internal forces after iteration  $i$ , and the second part  $\delta^II \mathbf{a}_{n+1}^{i+1}$  reflects the external load component that is being applied within the current loading step. Subsequently,  $\Delta\lambda_{n+1}^{i+1}$  is obtained by substituting  $\delta^I \mathbf{a}_{n+1}^{i+1}$  and  $\delta^II \mathbf{a}_{n+1}^{i+1}$  in the constraint equation. In this study the method based on the orthogonality between the tangent vector and update vector is adopted, see Ramm (1981). Update of the normal plane after each iteration gives

$$(\Delta\mathbf{a}_{n+1}^i)^T \delta\mathbf{a}_{n+1}^{i+1} = 0 \quad (3.18)$$

Substitution of eq. (3.17)<sub>4</sub> (here the subscript indicates a specific line in the equation) in eq. (3.18) yields the load factor as

$$\Delta\lambda_{n+1}^{i+1} = - \frac{(\Delta\mathbf{a}_{n+1}^i)^T \delta^I \mathbf{a}_{n+1}^{i+1}}{(\Delta\mathbf{a}_{n+1}^i)^T \delta^II \mathbf{a}_{n+1}^{i+1}} \quad (3.19)$$

De Borst (1986) reported this solution to fail in case of strong localizations and proposed to confine the number of degrees-of-freedom in the constraint equation. This indirect displacement control method has been reported as highly successful in concrete crack propagation, see De Borst (1986) and Rots (1988), and discrete cracking of composite laminates, see Schellekens (1992). For problems of cracking or sliding an adequate selection is provided by two displacements at either side of an active crack or slip line. Subtracting these components leads to some mode I or mode II Crack Opening Displacement (COD) as a scalar parameter. Eq. (3.19) then becomes

$$\Delta\lambda_{n+1}^{i+1} = - \frac{\delta^I COD_{n+1}^{i+1}}{\delta^{II} COD_{n+1}^{i+1}} \quad (3.20)$$

This technique will be used here in most analyses with the interface micro-model developed in Chapter 4. Another interesting variation of the general arc-length formulation is the indirect displacement control with a single degree-of-freedom which is actually the displacement control method used by Batoz and Dhett (1979) and Ramm (1981). The displacement vector in the constraint equation is now given by

$$\Delta\mathbf{a} = \{ 0, 0, 0, \dots, \Delta\bar{a}_p, \dots, 0, 0, 0 \}^T \quad (3.21)$$

with  $\Delta\bar{a}_p$  the prescribed displacement increment of the active degree-of-freedom. The choice of this degree-of-freedom should be made with engineering judgment and should fulfil the requirement that it is a continuously increasing degree-of-freedom. The incremental load vector is now given by

$$\Delta\lambda_{n+1}^{i+1} = - \frac{\delta^I a_{p, n+1}^{i+1}}{\delta^{II} a_{p, n+1}^{i+1}} \quad (3.22)$$

which follows directly from the prescribed displacement which should be constant during the iterations, i.e.  $\delta a_{p, n+1}^{i+1} = 0$ . In the present study this variation of the arc-length technique will be used extensively for the analyses in Chapter 5 and Chapter 6.

### 3.2 Numerical implementation of plasticity theory

A fundamental notion in the plasticity theory is the existence of a yield function that bounds the elastic domain. Yielding can only occur if the stresses  $\sigma$  satisfy the general yield criterion

$$f(\sigma, \bar{\sigma}(\kappa)) = 0 \quad (3.23)$$

where the yield stress value  $\bar{\sigma}$  is a function, commonly named hardening law, of the scalar  $\kappa$ , which is introduced as a measure for the amount of hardening or softening. In general, however, it is extremely complex to describe the material behavior with a single

yield surface in an appropriate manner and one must resort to the theory of multisurface plasticity. In this case the elastic domain is defined by a number of functions  $f_i < 0$  which define a composite yield surface. Loading/unloading can be conveniently established in standard Kuhn-Tucker form by means of the conditions

$$\dot{\lambda}_i \geq 0 \quad f_i \leq 0 \quad \dot{\lambda}_i f_i = 0 \quad (3.24)$$

where  $\dot{\lambda}_i$  is the plastic multiplier rate. Plastic behavior is characterized by a non-unique stress-strain relationship with the presence of irreversible strains on load removal. This is obtained by the usual decomposition of the strain rate vector  $\dot{\epsilon}$  in an elastic, reversible part,  $\dot{\epsilon}^e$  and a plastic, irreversible part,  $\dot{\epsilon}^p$

$$\dot{\epsilon} = \dot{\epsilon}^e + \dot{\epsilon}^p \quad (3.25)$$

where the elastic strain rate is related to the stress rate by the elastic (constitutive) stiffness matrix  $\mathbf{D}$  as

$$\dot{\sigma} = \mathbf{D} \dot{\epsilon}^e \quad (3.26)$$

and, for single surface plasticity, the assumption of a non-associated flow rule yields

$$\dot{\epsilon}^p = \dot{\lambda} \frac{\partial g}{\partial \sigma} \quad (3.27)$$

where  $g$  is the plastic potential. Usually, simplified algorithms are obtained if the plastic potential  $g$  has separate variables, i.e. it can be written as

$$g(\sigma, \kappa) = \Phi(\sigma) + \Omega(\kappa) \quad (3.28)$$

where  $\Phi$  and  $\Omega$  represent generic functions. In the case of strain hardening (or softening) the scalar  $\dot{\kappa}$  reads

$$\dot{\kappa} = \dot{\epsilon}^{eps} \quad (3.29)$$

where the equivalent plastic strain rate  $\dot{\epsilon}^{eps}$  must always be positive and increasing. The simplest combination of this kind which is dimensionally correct is<sup>†</sup>

$$\dot{\kappa} = \dot{\epsilon}^{eps} = \sqrt{(\dot{\epsilon}^p)^T \dot{\epsilon}^p} \quad (3.30)$$

Another possibility is to define the equivalent plastic strain rate from the plastic work

---

† It is noted that stresses and strains are in fact tensorial quantities and the tensor shear strains are half of the engineering shear strains. For standard three dimensional continuum eq. (3.30) should be understood as  $\dot{\kappa} = \dot{\epsilon}^{eps} = \sqrt{(\dot{\epsilon}^p)^T \mathbf{Q} \dot{\epsilon}^p}$ , with  $\mathbf{Q} = \text{diag} \{ 1, 1, 1, 1/2, 1/2, 1/2 \}$

per unit of volume in the form

$$\dot{W}^P = \boldsymbol{\sigma}^T \dot{\boldsymbol{\varepsilon}}^P \stackrel{def}{=} \bar{\sigma} \dot{\varepsilon}^{eps} \quad (3.31)$$

which gives

$$\dot{\kappa} = \dot{\varepsilon}^{eps} = \frac{1}{\bar{\sigma}} \boldsymbol{\sigma}^T \dot{\boldsymbol{\varepsilon}}^P \quad (3.32)$$

In the case of work hardening (or softening), the scalar  $\dot{\kappa}$  should be a work measure and simply read

$$\dot{\kappa} = \dot{W}^P = \boldsymbol{\sigma}^T \dot{\boldsymbol{\varepsilon}}^P \quad (3.33)$$

For practical applications, it seems that, in general, the choice of a hardening formulation for the parameter  $\kappa$  is not critical because the available experimental data are scarce. In this study the choice of a hardening formulation will be dictated by simplicity and robustness of the numerical algorithm.

For multisurface plasticity the intersection of the different yield surfaces defines corners. Without lack of generality it is assumed that the composite yield surface is defined by two yield surfaces. According to Koiter's generalization, Koiter (1953), the plastic strain rate  $\dot{\boldsymbol{\varepsilon}}^P$  in the corner is obtained from a linear combination of the plastic strain rates of the two yield surfaces, reading

$$\dot{\boldsymbol{\varepsilon}}^P = \dot{\boldsymbol{\varepsilon}}_1^P + \dot{\boldsymbol{\varepsilon}}_2^P = \dot{\lambda}_1 \frac{\partial g_1}{\partial \boldsymbol{\sigma}} + \dot{\lambda}_2 \frac{\partial g_2}{\partial \boldsymbol{\sigma}} \quad (3.34)$$

The yield surfaces can also be explicitly coupled by introducing composite hardening scalar rates  $\dot{\kappa}_1^c$  and  $\dot{\kappa}_2^c$

$$\dot{\kappa}_1^c = \dot{\kappa}_1^c(\dot{\kappa}_1, \dot{\kappa}_2) \quad \dot{\kappa}_2^c = \dot{\kappa}_2^c(\dot{\kappa}_1, \dot{\kappa}_2) \quad (3.35)$$

where  $\dot{\kappa}_1 = \dot{\kappa}_1(\dot{\boldsymbol{\varepsilon}}_1^P)$  and  $\dot{\kappa}_2 = \dot{\kappa}_2(\dot{\boldsymbol{\varepsilon}}_2^P)$  are defined according to one of eqs. (3.29,3.33). The superscript *c* refers to composite. Alternatively, for the corner, implicit coupling can be formulated upon direct substitution of eq. (3.34) in eqs. (3.29,3.33). Implicit coupling will not be used here because it is more complex to handle in the frame of a local Newton-Raphson iterative procedure, it cannot be controlled directly and it is present even when physically not acceptable.

### 3.2.1 Integration of the elastoplastic equations

The integration of the rate equations is a problem of evolution that can be regarded as follows. At a stage  $n$  the total strain field and the plastic strain field as well as the hardening parameter(s) are known:

$$\{\boldsymbol{\varepsilon}_n, \boldsymbol{\varepsilon}_n^p, \kappa_{i,n}\} \quad (3.36)$$

The elastic strain and stress fields are regarded as dependent variables which can always be obtained from the basic variables through the relations

$$\boldsymbol{\varepsilon}_n^e = \boldsymbol{\varepsilon}_n - \boldsymbol{\varepsilon}_n^p \quad \boldsymbol{\sigma}_n = \mathbf{D} \boldsymbol{\varepsilon}_n^e \quad (3.37)$$

Therefore, the stress field at a stage  $n+1$  is computed once the strain field is known (in the following the subscript  $n+1$  will be generally dropped for convenience in the derivatives). The problem is strain driven in the sense that the total strain  $\boldsymbol{\varepsilon}$  is trivially updated according to the exact formula

$$\boldsymbol{\varepsilon}_{n+1} = \boldsymbol{\varepsilon}_n + \Delta \boldsymbol{\varepsilon}_{n+1} \quad (3.38)$$

It remains to update the plastic strains and the hardening parameter(s). These quantities are determined by integration of the flow rule(s) and hardening law(s) over the step  $n \rightarrow n+1$ . In the frame of an implicit Euler backward algorithm this problem is transformed into a constrained optimization problem governed by discrete Kuhn-Tucker conditions as shown by Simo *et al.* (1988b). It has been shown in different studies, e.g. Ortiz and Popov (1985) and Simo and Taylor (1986), that the implicit Euler backward algorithm is unconditionally stable and accurate for  $J_2$ -plasticity. But even when the yield surface is highly distorted the Euler backward algorithm is unconditionally stable, Ortiz and Popov (1985), and accurate, De Borst and Feenstra (1990) and Schellekens and De Borst (1991). For single surface plasticity, in the general case of  $g = g(\boldsymbol{\sigma}, \kappa)$ , this algorithm results in the following set of nonlinear equations in the presence of yielding:

$$\begin{cases} \mathbf{D}^{-1}(\boldsymbol{\sigma}_{n+1} - \boldsymbol{\sigma}^{trial}) + \Delta \boldsymbol{\varepsilon}_{n+1}^p = \mathbf{0} \\ \Delta \kappa_{n+1} = \Delta \kappa_{n+1}(\boldsymbol{\sigma}_{n+1}, \Delta \boldsymbol{\varepsilon}_{n+1}^p) \\ f_{n+1}(\boldsymbol{\sigma}_{n+1}, \kappa_{n+1}) = 0 \end{cases} \quad (3.39)$$

in which  $\Delta \boldsymbol{\varepsilon}_{n+1}^p$  reads

$$\Delta \boldsymbol{\varepsilon}_{n+1}^p = \Delta \lambda_{n+1} \left. \frac{\partial g}{\partial \boldsymbol{\sigma}} \right|_{n+1} \quad (3.40)$$

$\Delta\kappa_{n+1}$  results from the integration of one of the rate equations, eqs. (3.29,3.33), and the elastic predictor step returns the value of the elastic trial stress  $\sigma^{trial}$

$$\sigma^{trial} = \sigma_n + \mathbf{D} \Delta\epsilon_{n+1} \quad (3.41)$$

The unknowns of the system of nonlinear equations are the components of the stress vector  $\sigma_{n+1}$  plus the state variables  $\Delta\kappa_{n+1}$  and  $\Delta\lambda_{n+1}$ . The system is solved with a regular Newton-Raphson method where the starting point is given by the elastic predictor:  $\sigma_{n+1} = \sigma^{trial}$ ,  $\Delta\kappa_{n+1} = 0$  and  $\Delta\lambda_{n+1} = 0$ . Yielding occurs because the elastic trial stress  $\sigma^{trial}$  lies outside the current (at step  $n$ ) elastic domain. The plastic corrector, given by eqs. (3.39), "brings back" the stress update to the yield surface and is thus termed return mapping.

If the plastic potential has separate variables, in most cases, and for the yield functions used later in Chapters 4 and 5, eq. (3.39)<sub>1</sub> can be solved in order to obtain explicitly the updated stress value as a function of the updated plastic multiplier,

$$\sigma_{n+1} = \sigma_{n+1}(\Delta\lambda_{n+1}) \quad (3.42)$$

Furthermore, inserting eq. (3.40) in eq. (3.39)<sub>2</sub> yields

$$\Delta\kappa_{n+1} = \Delta\kappa_{n+1}(\sigma_{n+1}, \Delta\lambda_{n+1}) \quad (3.43)$$

Substitution of these two equations in the yield function, cf. eq. (3.39)<sub>3</sub>, leads to a nonlinear equation in one variable, namely  $\Delta\lambda_{n+1}$ :  $f_{n+1}(\Delta\lambda_{n+1}) = 0$ . This constitutive equation is solved again with a local Newton-Raphson method. The derivative of  $f_{n+1}(\Delta\lambda_{n+1})$  with respect to  $\Delta\lambda_{n+1}$ , which is needed in this procedure, reads, after some manipulation,

$$\left. \frac{\partial f}{\partial \Delta\lambda} \right|_{n+1} = \gamma^T \frac{\partial \sigma}{\partial \Delta\lambda} - h \quad (3.44)$$

where the modified yield surface gradient  $\gamma$  and the hardening modulus  $h$  are given by

$$\gamma = \left. \frac{\partial f}{\partial \sigma} + \frac{\partial f}{\partial \kappa} \frac{\partial \kappa}{\partial \sigma} \right|_{n+1} \quad h = - \left. \frac{\partial f}{\partial \kappa} \frac{\partial \kappa}{\partial \Delta\lambda} \right|_{n+1} \quad (3.45)$$

For multisurface surface plasticity, in the general case of  $g = g(\sigma, \kappa)$ , the Euler backward algorithm results in the following set of nonlinear equations in the presence of yielding:

$$\left\{ \begin{array}{l} \mathbf{D}^{-1}(\boldsymbol{\sigma}_{n+1} - \boldsymbol{\sigma}^{trial}) + \Delta \boldsymbol{\varepsilon}_{1,n+1}^p + \Delta \boldsymbol{\varepsilon}_{2,n+1}^p = \mathbf{0} \\ \Delta \kappa_{1,n+1}^c = \Delta \kappa_{1,n+1}^c(\boldsymbol{\sigma}_{n+1}, \Delta \boldsymbol{\varepsilon}_{1,n+1}^p, \Delta \boldsymbol{\varepsilon}_{2,n+1}^p) \\ \Delta \kappa_{2,n+1}^c = \Delta \kappa_{2,n+1}^c(\boldsymbol{\sigma}_{n+1}, \Delta \boldsymbol{\varepsilon}_{1,n+1}^p, \Delta \boldsymbol{\varepsilon}_{2,n+1}^p) \\ f_{1,n+1}(\boldsymbol{\sigma}_{n+1}, \kappa_{1,n+1}^c) = 0 \\ f_{2,n+1}(\boldsymbol{\sigma}_{n+1}, \kappa_{2,n+1}^c) = 0 \end{array} \right. \quad (3.46)$$

in which  $\Delta \boldsymbol{\varepsilon}_{1,n+1}^p$  and  $\Delta \boldsymbol{\varepsilon}_{2,n+1}^p$  read

$$\Delta \boldsymbol{\varepsilon}_{1,n+1}^p = \Delta \lambda_{1,n+1} \left. \frac{\partial g_1}{\partial \boldsymbol{\sigma}} \right|_{n+1} \quad \Delta \boldsymbol{\varepsilon}_{2,n+1}^p = \Delta \lambda_{2,n+1} \left. \frac{\partial g_2}{\partial \boldsymbol{\sigma}} \right|_{n+1} \quad (3.47)$$

and  $\Delta \kappa_{1,n+1}$ ,  $\Delta \kappa_{2,n+1}$  result from the integration of one of the rate equations, eqs. (3.29,3.33). The unknowns of the system of nonlinear equations are the components of the stress vector  $\boldsymbol{\sigma}_{n+1}$  plus the state variables  $\Delta \kappa_{1,n+1}$ ,  $\Delta \kappa_{2,n+1}$ ,  $\Delta \lambda_{1,n+1}$  and  $\Delta \lambda_{2,n+1}$ . The system is solved with a regular Newton-Raphson method where the starting point is given by the elastic predictor:  $\boldsymbol{\sigma}_{n+1} = \boldsymbol{\sigma}^{trial}$ ,  $\Delta \kappa_{1,n+1} = 0$ ,  $\Delta \kappa_{2,n+1} = 0$ ,  $\Delta \lambda_{1,n+1} = 0$  and  $\Delta \lambda_{2,n+1} = 0$ . It is equally assumed that the plastic potentials have separate variables and eq. (3.46)<sub>1</sub> can be solved to obtain explicitly the updated stress value as a function of the updated plastic multipliers,

$$\boldsymbol{\sigma}_{n+1} = \boldsymbol{\sigma}_{n+1}(\Delta \lambda_{1,n+1}, \Delta \lambda_{2,n+1}) \quad (3.48)$$

As for single surface plasticity, eqs. (3.46)<sub>2,3</sub> yield then

$$\left\{ \begin{array}{l} \Delta \kappa_{1,n+1}^c = \Delta \kappa_{1,n+1}^c(\boldsymbol{\sigma}_{n+1}, \Delta \lambda_{1,n+1}, \Delta \lambda_{2,n+1}) \\ \Delta \kappa_{2,n+1}^c = \Delta \kappa_{2,n+1}^c(\boldsymbol{\sigma}_{n+1}, \Delta \lambda_{1,n+1}, \Delta \lambda_{2,n+1}) \end{array} \right. \quad (3.49)$$

Substitution of eqs. (3.48,3.49) in the active yield functions, cf. eqs. (3.46)<sub>4,5</sub>, leads to a system of nonlinear equations with a set of scalar unknowns, namely  $\Delta \lambda_{1,n+1}$  and  $\Delta \lambda_{2,n+1}$ :

$$\left\{ \begin{array}{l} f_{1,n+1}(\Delta \lambda_{1,n+1}, \Delta \lambda_{2,n+1}) = 0 \\ f_{2,n+1}(\Delta \lambda_{1,n+1}, \Delta \lambda_{2,n+1}) = 0 \end{array} \right. \quad (3.50)$$

This nonlinear system of equations is solved by a Newton-Raphson iterative method. The Jacobian necessary for this procedure reads

$$\mathbf{J}_{n+1} = \begin{bmatrix} \gamma_1^T \frac{\partial \sigma}{\partial \Delta \lambda_1} - h_1 & | & \gamma_1^T \frac{\partial \sigma}{\partial \Delta \lambda_2} + \frac{\partial f_1}{\partial \kappa_1^c} \frac{\partial \kappa_1^c}{\partial \Delta \lambda_2} \\ \hline \gamma_2^T \frac{\partial \sigma}{\partial \Delta \lambda_1} + \frac{\partial f_2}{\partial \kappa_2^c} \frac{\partial \kappa_2^c}{\partial \Delta \lambda_1} & | & \gamma_2^T \frac{\partial \sigma}{\partial \Delta \lambda_2} - h_2 \end{bmatrix} \quad (3.51)$$

where

$$\gamma_i = \frac{\partial f_i}{\partial \sigma} + \frac{\partial f_i}{\partial \kappa_i^c} \frac{\partial \kappa_i^c}{\partial \sigma} \Bigg|_{n+1} \quad h_i = - \frac{\partial f_i}{\partial \kappa_i^c} \frac{\partial \kappa_i^c}{\partial \Delta \lambda_i} \Bigg|_{n+1} \quad (3.52)$$

The problem that remains is how to determine whether only one or both yield surfaces are active. The location of the corner, i.e. the intersection between the two yield surfaces, is unknown at the beginning of the load step and the trial stress cannot provide a sufficient criterion to determine which yield surface(s) is active at the end of the load step. Simo *et al.* (1988b) proposed an algorithm in which the assumption is made that the number of active yield surfaces in the final state is less or equal than the number of yield surfaces active in the trial state. Already Pramono and Willam (1989) questioned this procedure advocating that the trial value of the yield functions cannot provide a sufficient criterion for determining which surface is active near a singular region. Feenstra (1993) suggests a quite elegant and efficient computational implementation, best suitable when the number of yield functions is small. The system of non-linear equations, eqs. (3.50), is substituted by

$$\begin{cases} c_1 f_{1, n+1}(\Delta \lambda_{1, n+1}, \Delta \lambda_{2, n+1}) = 0 \\ c_2 f_{2, n+1}(\Delta \lambda_{1, n+1}, \Delta \lambda_{2, n+1}) = 0 \end{cases} \quad (3.53)$$

where  $c_i$  represents a set of unitary constants that are set to zero if in iteration  $j$  the correspondent  $(\Delta \lambda_{n+1}^i)_j$  is negative. The update of the Jacobian is made with the Broyden's method, see Dennis and Schnabel (1983). This procedure is particularly interesting as there is no need to change the Jacobian according to the number of current active yield surfaces. One problem that remains is the calculation of the initial Jacobian, approximated by this author from the linearization of both yield surfaces in the trial state, assuming implicitly that all the yield functions are active. Unfortunately this procedure does not guarantee that the updated Jacobian will converge to the exact Jacobian with the inherent risks of divergence and poor rate of convergence. None of those problems were reported by Feenstra (1993). However, in Lourenço (1994) it is shown that the Broyden's method can fail to converge in case of large steps and strong non-linearities.

In the present study, following Pramono and Willam (1989), a trial and error procedure to solve the return mapping is used. It will be assumed that the set of initial active yield functions is the one defined by Simo *et al.* (1988b) ( $f_i^{trial} \geq 0$ ). If, after the return mapping is completed, any  $\Delta\lambda_{i, n+1} < 0$  or  $f_{i, n+1} > 0$  is found, the number of active yield surfaces is adjusted accordingly and the return mapping is restarted. During this process, for the composite models developed in this study, one restart may be required or, rarely and only for larger increments, more restarts may be required before the correct number of active yield surfaces is obtained.

### 3.2.2 Evaluation of the tangent operator

The solution of the nonlinear equations following from the finite element discretization will be solved using the Newton-Raphson method as has been discussed in Section 3.1. The nonlinear problem is then linearized in a sequence of iterations until the problem is converged. The linearization of the equations results in the tangent stiffness matrix which plays a crucial role in the performance and robustness of the Newton-Raphson method. It has been emphasized in the classical paper about consistent tangent operators for mathematical plasticity, Simo and Taylor (1985), that the tangent stiffness matrix must be obtained by consistent linearization of the stress update resulting from the return mapping algorithm at the end of iteration  $n + 1$ . It is shown in eqs. (3.39,3.46) that the return mapping algorithm contains as unknowns the components of the stress vector  $\sigma_{n+1}$  and some other state variables, namely  $\Delta\kappa_{i, n+1}$  and  $\Delta\lambda_{i, n+1}$ , which are now conveniently collected in a vector of state variables  $\mathbf{q}_{n+1}$ . The number of components of  $\mathbf{q}_{n+1}$ ,  $n_q$ , is two for single surface plasticity and four for the corner of a composite yield surface, cf. eqs. (3.39,3.46). Then linearization of eqs. (3.39) or eqs. (3.46) yields

$$\mathbf{J} \begin{Bmatrix} d\sigma_{n+1} \\ \text{---} \\ d\mathbf{q}_{n+1} \end{Bmatrix} = \begin{bmatrix} \mathbf{J}_{n_\sigma \times n_\sigma} & | & \mathbf{J}_{n_\sigma \times n_q} \\ \text{---} & + & \text{---} \\ \mathbf{J}_{n_q \times n_\sigma} & | & \mathbf{J}_{n_q \times n_q} \end{bmatrix} \begin{Bmatrix} d\sigma_{n+1} \\ \text{---} \\ d\mathbf{q}_{n+1} \end{Bmatrix} = \begin{Bmatrix} d\boldsymbol{\varepsilon}_{n+1} \\ \text{---} \\ \mathbf{0} \end{Bmatrix} \quad (3.54)$$

where  $\mathbf{J}$  is the Jacobian calculated previously to solve the return mapping and  $n_\sigma$  is the number of components of the stress vector  $\sigma$ . Then, the consistent tangent stiffness matrix  $\mathbf{D}^{ep}$  can simply be obtained as

$$\mathbf{D}^{ep} = \left. \frac{d\sigma_{n+1}}{d\boldsymbol{\varepsilon}_{n+1}} \right|_{n+1} = (\mathbf{J}^{-1})_{n_\sigma \times n_\sigma} \quad (3.55)$$

where  $(\mathbf{J}^{-1})_{n_\sigma \times n_\sigma}$  is the *top-left*  $n_\sigma \times n_\sigma$  submatrix of the inverse of the Jacobian  $\mathbf{J}$ . It is also possible to condense the system of equations in eqs. (3.54) by removing the  $d\mathbf{q}_{n+1}$  components, which yields yet another expression for the consistent tangent stiffness matrix  $\mathbf{D}^{ep}$  as

$$\mathbf{D}^{ep} = \left. \frac{d\boldsymbol{\sigma}_{n+1}}{d\boldsymbol{\varepsilon}_{n+1}} \right|_{n+1} = [\mathbf{J}_{n_\sigma \times n_\sigma} - \mathbf{J}_{n_\sigma \times n_q} \mathbf{J}_{n_q \times n_q}^{-1} \mathbf{J}_{n_q \times n_\sigma}]^{-1} \quad (3.56)$$

It is noted that this last expression is only defined if the submatrix  $\mathbf{J}_{n_q \times n_q}$  is not singular. The novel expressions for the consistent tangent stiffness matrix given above are of general application and clearly show the interest of using a local Newton-Raphson method to solve the return mapping because the Jacobian calculated is directly utilized. For single surface plasticity, under the assumption that the plastic potential has separate variables, eq. (3.56) and the Sherman-Morrison formula yield a more standard expression as, see also Lourenço *et al.* (1994),

$$\mathbf{D}^{ep} = \left. \frac{d\boldsymbol{\sigma}}{d\boldsymbol{\varepsilon}} \right|_{n+1} = \mathbf{H} - \frac{\mathbf{H} \frac{\partial g}{\partial \boldsymbol{\sigma}} \boldsymbol{\gamma}^T \mathbf{H}}{h + \boldsymbol{\gamma}^T \mathbf{H} \frac{\partial g}{\partial \boldsymbol{\sigma}}} \quad (3.57)$$

where the modified stiffness matrix  $\mathbf{H}$  reads

$$\mathbf{H} = \left[ \mathbf{D}^{-1} + \Delta\lambda_{n+1} \frac{\partial^2 g}{\partial \boldsymbol{\sigma}^2} \right]^{-1} \quad (3.58)$$

and the modified yield surface gradient  $\boldsymbol{\gamma}$  and the hardening modulus  $h$  have been defined in eq. (3.45). This expression for  $\mathbf{D}^{ep}$  is particularly interesting as it demonstrates that a non-symmetric tangent stiffness matrix will be obtained even in the case of associated plasticity if the hardening parameter update is not a linear function of the plastic multiplier update, i.e if  $\Delta\kappa_{n+1} \neq c \Delta\lambda_{n+1}$ , where  $c$  is a constant.

Similarly, applying the Riggs and Powel (1990) formulation, for multisurface plasticity eq. (3.54) can be manipulated to obtain an expression equivalent to eq. (3.57) as, see also Lourenço *et al.* (1994),

$$\mathbf{D}^{ep} = \left. \frac{d\boldsymbol{\sigma}}{d\boldsymbol{\varepsilon}} \right|_{n+1} = \mathbf{H} - \mathbf{H} \mathbf{U} \left( \mathbf{E} + \mathbf{V}^T \mathbf{H} \mathbf{U} \right)^{-1} \mathbf{V}^T \mathbf{H} \quad (3.59)$$

where the modified stiffness matrix  $\mathbf{H}$  reads

$$\mathbf{H} = \left[ \mathbf{D}^{-1} + \Delta\lambda_{1, n+1} \frac{\partial^2 g_1}{\partial \boldsymbol{\sigma}^2} + \Delta\lambda_{2, n+1} \frac{\partial^2 g_2}{\partial \boldsymbol{\sigma}^2} \right]^{-1} \quad (3.60)$$

the gradient matrices  $\mathbf{U}$  and  $\mathbf{V}$  read

$$\mathbf{U} = \begin{bmatrix} \frac{\partial g_1}{\partial \sigma} & \frac{\partial g_2}{\partial \sigma} \end{bmatrix} \quad \mathbf{V} = \begin{bmatrix} \gamma_1 & \gamma_2 \end{bmatrix} \quad (3.61)$$

and the hardening matrix  $\mathbf{E}$  reads

$$\mathbf{E} = \begin{bmatrix} -h_1 & | & \frac{\partial f_1}{\partial \kappa_1^c} & \frac{\partial \kappa_1^c}{\partial \Delta \lambda_2} \\ \hline \frac{\partial f_2}{\partial \kappa_2^c} & \frac{\partial \kappa_2^c}{\partial \Delta \lambda_1} & | & -h_2 \end{bmatrix} \quad (3.62)$$

It is noted that the modified yield surface gradient  $\gamma_i$  and the hardening modulus  $h_i$  were defined in eq. (3.52).

### 3.3 Summary

The system of nonlinear equations that results from the finite element discretization is solved by means of an incremental-iterative Newton-Raphson method. To overcome limit points and strong localizations, the Newton-Raphson method will be constrained with the updated-normal-plane method. The robustness of the iteration method will be enhanced with a line search algorithm, with a maximum of line searches set to five and a convergence tolerance  $\eta = 0.8$ . A load increment is assumed to be converged if the variation of internal strain energy is less or equal to  $10^{-4}$  times the variation of internal strain energy calculated at the beginning of the load step.

The relation between the stress and strain tensor in a point of the body is necessary to define the material behavior. The theory of multisurface plasticity will be used for this purpose. A general formulation is given in modern concepts for all the modes of a composite yield surface. The implicit Euler backward return mapping is solved using a local Newton-Raphson method. The tangent stiffness matrix is calculated consistently with the update equations so that the quadratic convergence of the global equilibrium system of equations is retained.

In the applications which will be presented in this study, no attempt will be made to compare different solution techniques. The analyses show that, with the proposed solution techniques, convergent solutions could be obtained, both at structural and local level, which indicates that the proposed combination of techniques results in a stable solution procedure.

## 4. MICRO-MODELING: A COMPOSITE INTERFACE MODEL FOR MASONRY

Micro-models are, probably, the best tool available to understand the behavior of masonry. The benefit of using such an approach is that all the different failure mechanisms can be considered. In this Chapter, attention is given to a simplified modeling strategy, in which interface elements are used as potential crack, slip or crushing planes. A composite interface model, which includes a tension cut-off for mode I failure, a Coulomb friction envelope for mode II failure and a cap mode for compressive failure, is developed in modern plasticity concepts. In addition, interface elements are considered to model potential cracks in the units. The assumption that all the inelastic phenomena occur in the interface elements leads to a robust type of modeling, capable of following the complete load path of a structure until total degradation of stiffness. The performance of the numerical implementation has been assessed elsewhere, see Lourenço (1994), and will not be reviewed here.

The fact that little importance has been given to numerical modeling of masonry is confirmed by the absence of any well established micro-model. A few attempts to use interfaces for the modeling of masonry were carried out in the last decade with reasonably simple models, see Anthoine (1992) for a comprehensive review. In particular, gradual softening behavior after crack or slip and all failure mechanisms have not been fully included. To the knowledge of the author, previous numerical micro-analyses are also limited to the structural pre-peak regime.

### 4.1 Adopted modeling strategy

An accurate micro-model must include all the basic types of failure mechanisms that characterize masonry, viz. (a) cracking of the joints, (b) sliding along the bed or head joints at low values of normal stress, (c) cracking of the units in direct tension, (d) diagonal tensile cracking of the units at values of normal stress sufficient to develop friction in the joints and (e) "masonry crushing", commonly identified with splitting of units in tension as a result of mortar dilatancy at high values of normal stress, as illustrated in Figure 4.1. It is clear from the described phenomena that (a,b) are joint mechanisms, (c) is a unit mechanism and (d,e) are combined mechanisms involving units and joints. The question remains of how to consider all phenomena in the model. The approach followed here is to concentrate all the damage in the relatively weak joints and, if necessary, in potential pure tensile cracks in the units placed vertically in the middle of each unit, see Figure 4.2. These potential cracks in the units are able to reproduce a jump from one head joint to the other (immediately below or above), which is a typical masonry characteristic. The joint interface yield criterion has then to include all the mechanisms referred above except uniaxial tensile cracking of the unit. Inclusion of the

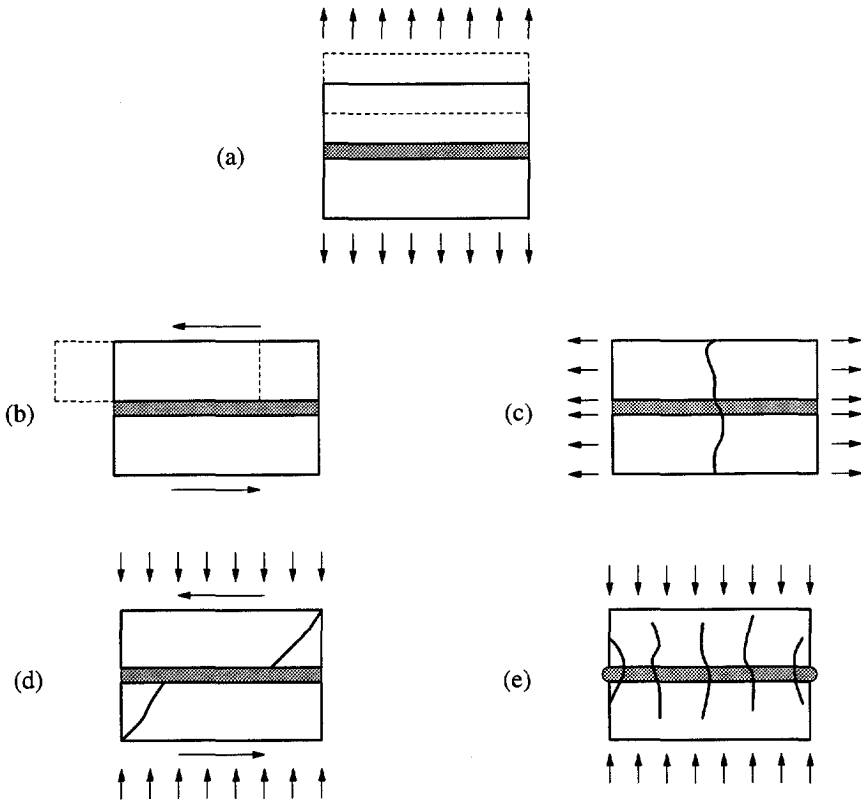


*Figure 4.1* Masonry failure mechanisms: (a) joint tensile cracking; (b) joint slipping; (c) unit direct tensile cracking; (d) unit diagonal tensile cracking; (e) masonry crushing.

first two mechanisms (tensile and shear failure of the joint) has been pursued before, e.g. Page (1978) and Rots *et al.* (1994), but the compressive cap here set forth is novel. By limiting the compressive/shear stress combinations, diagonal tensile cracking of the units and masonry crushing, failure mechanisms (d,e) in Figure 4.1, can be incorporated in the model. It is noted that the composite interface model developed next is used at a micro-level. Remarkably, experiments carried out in shear walls, see Mann and Müller (1982), and panels subjected to a uniform state of stress, see Dialer (1990), resulted in similar macro-level failure envelopes.

Interface elements, which were introduced in Chapter 3, permit discontinuities in the displacement field and their behavior is described in terms of a relation between the tractions  $\mathbf{t}$  and relative displacements  $\Delta \mathbf{u}$  across the interface. The linear elastic relation between these generalized stresses and strains can be written in the standard form as

$$\boldsymbol{\sigma} = \mathbf{D} \boldsymbol{\varepsilon} \quad (4.1)$$

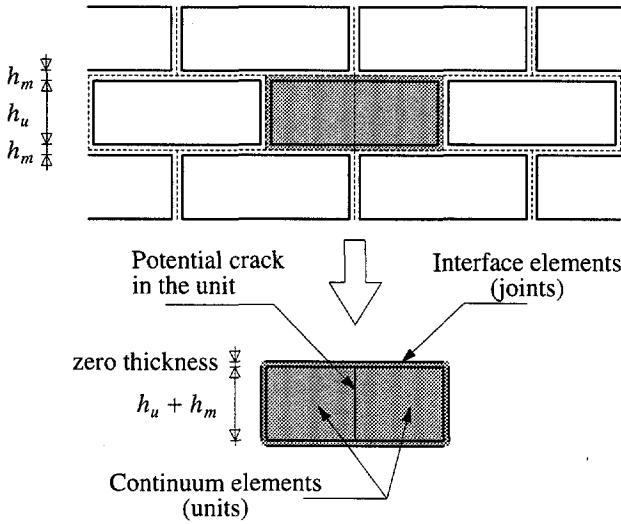


**Figure 4.2** Suggested modeling strategy. Units ( $u$ ), which are expanded in both directions by the mortar thickness, are modeled with continuum elements. Mortar joints ( $m$ ) and potential cracks in the units are modeled with zero-thickness interface elements.

where, for a 2D configuration,  $\sigma = \{\sigma, \tau\}^T$ ,  $\mathbf{D} = \text{diag}\{k_n, k_s\}$  and  $\varepsilon = \{\Delta u_n, \Delta u_s\}^T$ , with  $n$  and  $s$  denoting the normal and shear components, respectively. The elastic stiffness matrix  $\mathbf{D}$  can be obtained from the properties of the two masonry components (units and mortar) and the thickness of the joint. Figure 4.2 shows that, due to the zero thickness inherent to the interface element formulation, the size of the units has to be expanded by the mortar thickness  $h_m$  in both directions. It follows that the elastic properties of the “expanded unit” and the “interface joint” must be adjusted to yield correct results. One possibility is to reduce the stiffness of the unit and use interface elements with high dummy stiffness to avoid interpenetration of the continuum. This approach will not be followed here. Due to the relative dimensions of mortar and unit, it is assumed that the elastic properties of the unit remain unchanged. Then, under the assumption of stack bond, i.e. a serial chain connection of the components, and uniform stress distributions both in the unit and mortar, the components of the elastic stiffness matrix  $\mathbf{D}$  read, CUR (1994),

$$k_n = \frac{E_u E_m}{h_m(E_u - E_m)} \quad k_s = \frac{G_u G_m}{h_m(G_u - G_m)} \quad (4.2)$$

where  $E_u$  and  $E_m$  are the Young’s moduli,  $G_u$  and  $G_m$  are the shear moduli, respectively, for unit and mortar and  $h_m$  is the actual thickness of the joint. The stiffness values obtained from these formulae do not correspond to a penalty approach, which means that overlap of neighboring units subjected to compression will become visible. This

feature is, however, intrinsic to the interface elements formulation and is independent of the values of normal stiffness, even if it is clear that the amount of penetration will be higher with decreasing interface stiffness. The interface model includes a compressive cap where the complete inelastic behavior of masonry in compression is lumped. This is a phenomenological representation of masonry crushing because the failure process in compression is, in reality, explained by the microstructure of units and mortar and the interaction between them. In the model the failure mechanism is represented in such a way that the global stress-displacement diagram is captured and corresponds to one unit literally imploding over the other. As can be gathered from some confusing statements in the literature, it takes some time to get used to this zero or “negative” volume (in compressed state) of interface elements.

The following generic example demonstrates the accuracy of the formulae given by eq. (4.2). A wall made of 18 courses of  $210 \times 52 \times 100$  [mm<sup>3</sup>] clay bricks and a 10 [mm] thick mortar joint is assumed for this purpose. Two different models are considered: the “continuum model”, in which units as well as mortar are modeled with 8-noded continuum elements, and the “interface model”, in which “expanded units” are modeled with 8-noded continuum elements and joints are modeled with 6-noded interface elements. The integration schemes used are  $2 \times 2$  points Gauss integration for the continuum elements and 3 points Lobatto integration for the interface elements. The material properties used are given in Table 4.1, where  $\nu$  is the Poisson’s ratio.

Table 4.1 Material properties.

Continuum model		Interface model	
Unit	$E = 20000$ [N/mm <sup>2</sup> ] $\nu = 0.15$	“Unit”	$E = 20000$ [N/mm <sup>2</sup> ] $\nu = 0.15$
Mortar	$E = 2000$ [N/mm <sup>2</sup> ] $\nu = 0.125$	Joint	$k_n = 222$ [N/mm <sup>3</sup> ] $k_s = 99$ [N/mm <sup>3</sup> ]

Four different load cases are considered: two uniform loads along one edge and two point loads distributed over the right top unit, see Figure 4.3. These loads are introduced by a force  $F$  equal to 1.0 [MN] and the control parameter is the displacement  $d$  along the direction of the resultant force  $F$ . In a Silicon Graphics Indigo R4400, on average, the continuum model used 333.5 [s] of CPU time and the interface model 26.6 [s] (8 %). Table 4.2 gives the results for the displacement  $d$  obtained in a linear elastic calculation. The comparison results in a difference smaller than 2.5 % between the two models and thus the global behavior of the simplified modeling shows excellent agreement with the global behavior of the detailed modeling. Figures 4.4 to 4.6 further demonstrate that the deformational behavior and the stress distribution for both modelings are similar. It is noted that Figure 4.5 does not include the state of stress in the vertical joints and the stresses are shown at the integration point level of the interface model. Locally, however, some differences can be found because the local stress

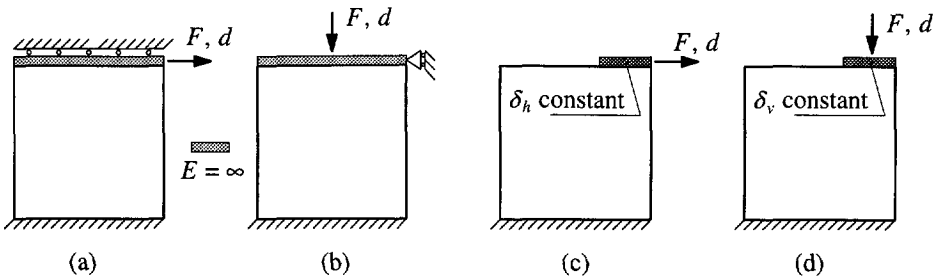


Figure 4.3 Loads applied in a masonry wall to assess the micro-modeling strategy: (a) load 1, uniformly distributed horizontal load; (b) load 2, uniformly distributed vertical load; (c) load 3, horizontal load in a single brick; (d) load 4, vertical load in a single brick.

Table 4.2 Continuum vs. interface modeling. Linear elastic results of the displacement  $d$  for all loading cases.

	Continuum model				Interface model			
	Load 1	Load 2	Load 3	Load 4	Load 1	Load 2	Load 3	Load 4
$d$ [mm]	5.39	1.35	12.41	3.82	5.39	1.33	12.28	3.74

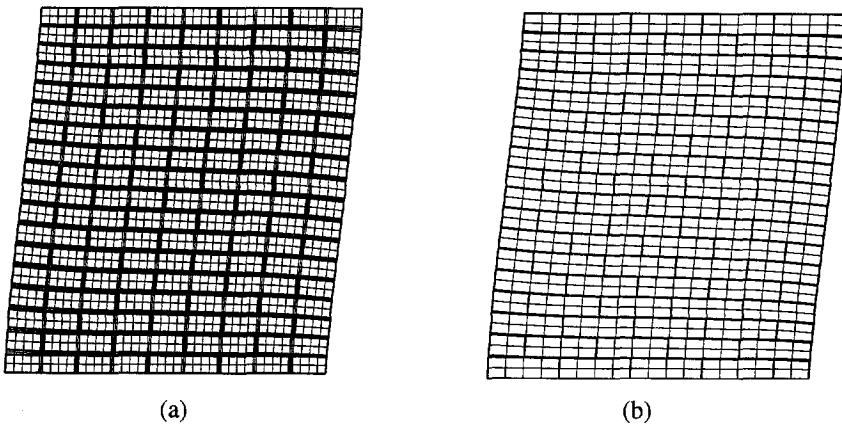


Figure 4.4 Deformed mesh for load 1: (a) continuum model; (b) interface model.

gradients due to the different Young's moduli of bricks and mortar can be averaged by the simplified model. This is illustrated by the detail shown in Figure 4.6, in which the results for the continuum model are obtained with a mesh refined by a factor four. The local stress gradients are, of course, strongly mesh dependent. It is believed that the local gradients are irrelevant for the global structural behavior because they are quickly smoothed in the presence of nonlinear constitutive laws, which is the case of the present study.

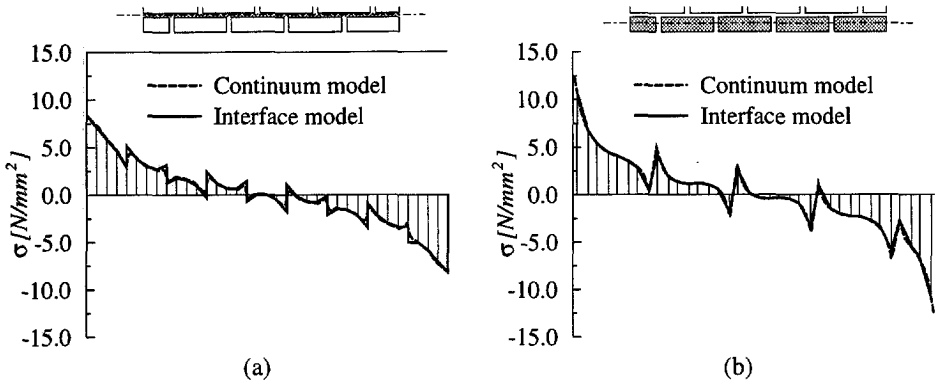


Figure 4.5 Vertical stresses for the complete wall at the base, load 1: (a) mortar; (b) brick.

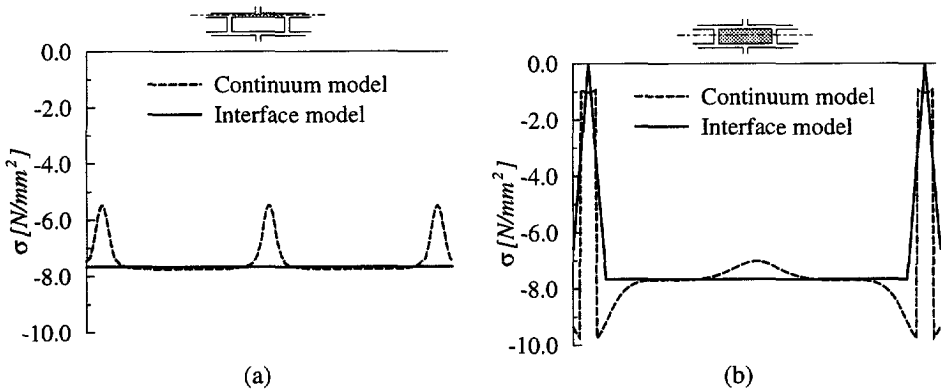


Figure 4.6 Vertical stresses over a brick length at the center of the wall, load 2: (a) mortar; (b) brick.

This example illustrates also the benefit of using a simplified over a detailed micro-modeling strategy. For a linear elastic analysis, with a small reduction in accuracy, the simplified model is 12.5 times faster than the detailed model. For a complete nonlinear analysis, the interface unit-mortar must also be included in the detailed model and the calculation time ratio will be even larger.

## 4.2 Formulation of the composite interface model

Cap models originated in the field of soil mechanics. The introduction of a spherical cap for the Drucker-Prager model was firstly made by Drucker *et al.* (1957) for the purpose of describing plastic compaction and to enhance the behavior in hydrostatic compression. Since then, the name “cap model” has been adopted for a broad set of models

which include a compressive cap, e.g. the well-known Cam-clay model of Roscoe and Burland (1968) and the material model for granular soils proposed by DiMaggio and Sandler (1971). Recently the numerical algorithm has been revised by Simo *et al.* (1988a) and Hofstetter *et al.* (1993) with the use of unconditionally stable closest point projection return mappings, tangent operators consistent with the integration algorithm and proper handling of the corners. Cap models have been, in general, limited to associated plasticity and hardening of the cap while the other yield surfaces remained in ideal plasticity.

For the application envisaged here the behavior found experimentally leads to a more complex model. Masonry joints have extremely low dilatancy and the model must be formulated in the context of non-associated plasticity. Also softening behavior should be included for all modes of the composite yield surface. The model presented in this study is of general application but the formulation is shown in the characteristic interface  $(\sigma, \tau)$ -space. The reader can assume the usual  $(I_1, \sqrt{J_2})$ -space formulation for regular continuum elements.

The rate independent interface model is defined by a convex composite yield criterion which consists of a tension cut-off  $f_1(\sigma, \kappa_1)$ , the Coulomb friction model  $f_2(\sigma, \kappa_2)$  and an elliptical cap  $f_3(\sigma, \kappa_3)$ , see Figure 4.7.

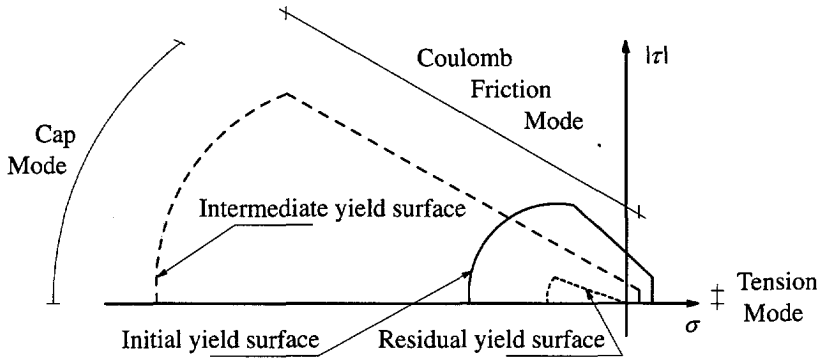


Figure 4.7 Proposed model for interfaces. An "interface cap model".

#### 4.2.1 The tension cut-off criterion

For the tension mode, exponential softening on the tensile strength is assumed according to the mode I experiments, see Figure 4.8. The yield function reads

$$f_1(\sigma, \kappa_1) = \sigma - \bar{\sigma}_1(\kappa_1) \quad (4.3)$$

where the yield value  $\bar{\sigma}_1$  reads

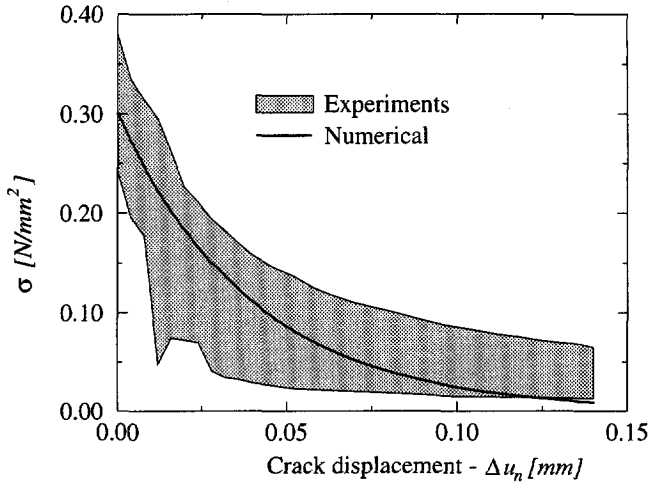


Figure 4.8 Tensile behavior of present model vs. experimental results from Van der Pluijm (1992), with  $f_t = 0.30 [N/mm^2]$  and  $G_f^I = 0.012 [Nmm/mm^2]$ .

$$\bar{\sigma}_1 = f_t \exp\left(-\frac{f_t}{G_f^I} \kappa_1\right) \quad (4.4)$$

In the above  $f_t$  is the tensile strength of the joint or, more precisely, of the unit-mortar interface, which is, generally, the weakest link, and  $G_f^I$  is the mode I fracture energy. An associated flow rule and a strain softening hypothesis are considered. Assuming that only the normal plastic relative displacement controls the softening behavior, eq. (3.29) yields

$$\dot{\kappa}_1 = |\Delta \dot{u}_n^p| = \dot{\lambda}_1 \quad (4.5)$$

The stress update equations, cf. eq. (3.39)<sub>1</sub>, can be manipulated to obtain

$$\begin{cases} \sigma_{n+1} = \sigma^{trial} - \Delta \lambda_{1, n+1} k_n \\ \tau_{n+1} = \tau^{trial} \end{cases} \quad (4.6)$$

and the derivative necessary for the iterative local Newton-Raphson method, cf. eq. (3.44), reads

$$\left. \frac{\partial f_1}{\partial \Delta \lambda_1} \right|_{n+1} = -k_n - h_1 \quad (4.7)$$

where

$$h_1 = \frac{\partial \bar{\sigma}_1}{\partial \kappa_1} \quad (4.8)$$

and the consistent tangent stiffness matrix, cf. eq. (3.57), reads

$$\mathbf{D}_1^{ep} = \left. \frac{\partial \boldsymbol{\sigma}}{\partial \boldsymbol{\varepsilon}} \right|_{n+1} = \begin{bmatrix} \frac{h_1 k_n}{h_1 + k_n} & 0 \\ 0 & k_s \end{bmatrix} \quad (4.9)$$

#### 4.2.2 The Coulomb friction criterion

For the Coulomb friction mode, the yield function reads

$$f_2(\boldsymbol{\sigma}, \kappa_2) = |\tau| + \sigma \tan \phi(\kappa_2) - \bar{\sigma}_2(\kappa_2) \quad (4.10)$$

where the yield value  $\bar{\sigma}_2$  reads

$$\bar{\sigma}_2 = c \exp\left(-\frac{c}{G_f^II} \kappa_2\right) \quad (4.11)$$

and the friction angle is coupled with cohesion softening via the expression

$$\tan \phi = \tan \phi_0 + (\tan \phi_r - \tan \phi_0) \frac{c - \bar{\sigma}_2}{c} \quad (4.12)$$

In the above  $c$  is the cohesion of the unit-mortar interface,  $\phi_0$  is the initial friction angle,  $\phi_r$  is the residual friction angle and  $G_f^II$  is the mode II fracture energy. Exponential softening is assumed for the cohesion, and, for simplicity, the softening of the friction angle is taken proportional to the softening of the cohesion. This last assumption leads to a non-constant mode II fracture energy under increasing confining pressure. For an initial friction angle larger than the residual friction angle, i.e.  $\tan \phi_0 > \tan \phi_r$ , the mode II fracture energy increases under increasing confining pressure which is confirmed by the experimental results of Van der Pluijm (1993).

A non-associated plastic potential  $g_2$ ,

$$g_2 = |\tau| + \sigma \tan \psi - c \quad (4.13)$$

with a dilatancy angle  $\psi$  and a strain softening hypothesis are considered. In the computational implementation of the model, the dilatancy angle is considered as a function of the plastic relative shear displacement and the normal confining pressure. Under increasing values of these two quantities, the dilatancy angle tends to zero. This is physically realistic, given the microstructure of the unit-mortar interface, and is confirmed by the experiments, see Chapter 2. Similar behavior has been reported for jointed rock

masses, see e.g. Gens *et al.* (1989). The implementation of a variable dilatancy angle can be easily carried out according to the general procedure reviewed in Chapter 3. This implementation will not be given here because quite lengthy expressions are obtained. Assuming that the softening behavior is controlled by the shear plastic relative displacement, eq. (3.29) yields

$$\dot{\kappa}_2 = |\Delta \dot{u}_s^p| = \dot{\lambda}_2 \quad (4.14)$$

With the assumptions given above reasonable agreement with experimental results could be obtained, see Figure 4.9. The formulation was kept as easy as possible, trying to limit the number of parameters necessary to define the Coulomb friction model to the minimum. To obtain the results shown in Figure 4.9, only 4 material parameters are necessary whereas the general model found in Gens *et al.* (1989) needs 10 material parameters.

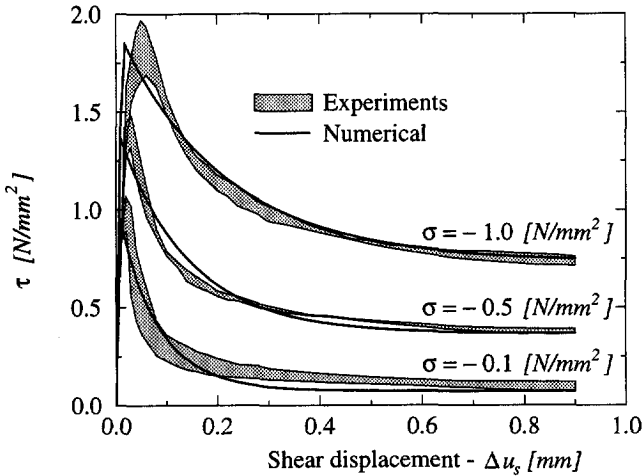


Figure 4.9 Shear behavior of present model vs. experimental results by Van der Pluijm (1993) for different confinement levels, with  $c = 0.87$  [N/mm<sup>2</sup>];  $\tan \phi_0 = 1.01$ ;  $\tan \phi_r = 0.73$ ;  $G_f^H = 0.058 - 0.13\sigma$  [Nmm/mm<sup>2</sup>].

The stress update equations, cf. eq. (3.39)<sub>1</sub>, can be manipulated to obtain

$$\begin{cases} \sigma_{n+1} = \sigma^{trial} - \Delta\lambda_{2, n+1} k_n \tan \psi \\ \tau_{n+1} = \tau^{trial} - \Delta\lambda_{2, n+1} k_s \frac{\tau^{trial}}{|\tau^{trial}|} \end{cases} \quad (4.15)$$

Note that the sign of  $\tau_{n+1}$  must be the same as the sign of  $\tau^{trial}$ . The derivative necessary

for the iterative local Newton-Raphson method, cf. eq. (3.44), reads

$$\left. \frac{\partial f_2}{\partial \Delta \lambda_2} \right|_{n+1} = -k_n \tan \phi \tan \psi - k_s - h_2 \quad (4.16)$$

where

$$h_2 = \left[ \sigma_{n+1} \left( \frac{\tan \phi_r - \tan \phi_0}{c} \right) + 1 \right] \frac{\partial \bar{\sigma}_2}{\partial \kappa_2} \quad (4.17)$$

and the consistent tangent stiffness matrix, cf. eq. (3.57), reads

$$\mathbf{D}_2^{ep} = \left. \frac{\partial \sigma}{\partial \varepsilon} \right|_{n+1} = \frac{1}{h_2 + k_n \tan \phi \tan \psi + k_s} \cdot \left[ \begin{array}{cc|cc} k_n (h_2 + k_s) & & -k_n k_s \tan \psi \frac{\tau_{n+1}}{|\tau_{n+1}|} & \\ \hline -k_n k_s \tan \phi \frac{\tau_{n+1}}{|\tau_{n+1}|} & & (h_2 + k_n \tan \phi \tan \psi) k_s & \end{array} \right] \quad (4.18)$$

### 4.2.3 The compressive cap criterion

For the cap mode, the ellipsoid interface model firstly introduced by Schellekens (1992) for orthotropic plasticity in a 3D configuration is used. The yield function, for a 2D configuration, is now given by

$$f_3(\sigma, \kappa_3) = C_{nn} \sigma^2 + C_{ss} \tau^2 + C_n \sigma - (\bar{\sigma}_3(\kappa_3))^2 \quad (4.19)$$

with  $C_{nn}$ ,  $C_{ss}$  and  $C_n$  a set of material parameters and  $\bar{\sigma}_3$  the yield value. The parameters  $C_{nn}$  and  $C_n$  control the center of the cap and its intersection with the tensile part of the normal stress axis whereas the parameter  $C_{ss}$  controls the contribution of the shear stress to failure, see Figure 4.10. In this study a centered cap with  $C_{nn} = 1$  and  $C_n = 0$  is adopted because a tension cut-off will be included in the composite yield surface. Then, the ultimate shear strength  $\tau_u$  equals  $f_m / \sqrt{C_{ss}}$ .

For the hardening/softening behavior the law shown in Figure 4.11 is adopted, where the subscripts  $i$ ,  $m$ ,  $p$  and  $r$  of the yield value  $\bar{\sigma}$  denote respectively, the initial, medium, peak and residual values. The peak value  $\bar{\sigma}_p$  equals the masonry compressive strength  $f_m$ . The proposed hardening/softening law leads to a  $C^1$  continuous  $\sigma - \varepsilon$  relationship as shown in Figure 4.12. The approach used in Figure 4.11, in which several  $\kappa$  and  $\bar{\sigma}$  values are adjusted to fit the stress-displacement curve obtained experimentally, can be used for interface elements because a direct relation between stresses and

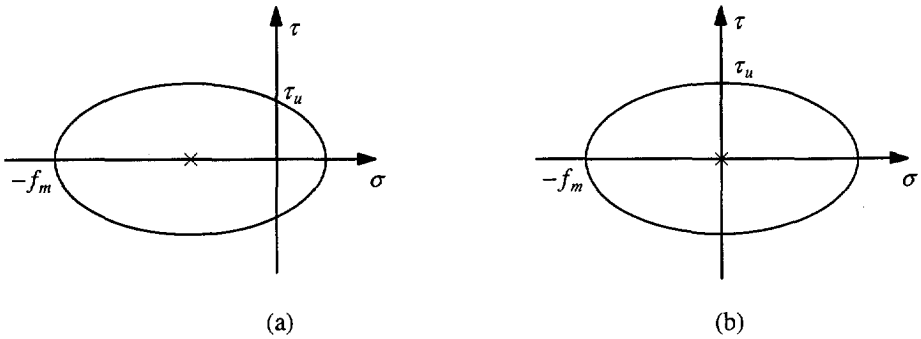


Figure 4.10 Elliptical yield surface adopted for the compressive cap: (a) Non-centered cap with different tensile and compressive strengths; (b) centered cap with  $C_m = 1$  and  $C_n = 0$  (adopted in this study).

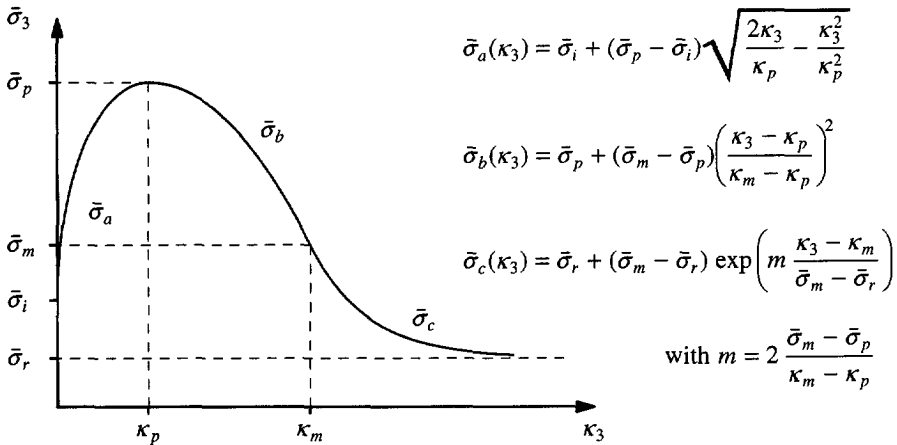


Figure 4.11 Hardening/softening law for cap mode.

displacements is established. The energy under the curve cannot be directly related to the compressive fracture energy  $G_c$  introduced in Chapter 2 because an energy-based approach requires that the energy under the  $\bar{\sigma}_3 - \kappa_3$  diagram is finite, i.e the residual compressive strength is zero. However, allowing the compressive cap to shrink until the origin leads to considerable additional difficulties to the model, as an extra corner must be defined by a possible intersection of the cap with the tension cut-off. Also, in case the cap falls completely inside the shear/tension regime, additional procedures would make the computational code extremely cumbersome. It is recognized that once compressive softening is completed, no further material strength should be available for shear and tension. But, for monotonical quasi-static loading, large stress redistributions are no longer expected at this final stage and the residual value is not expected to affect the results significantly. To ensure that the intersection between the cap and shear modes

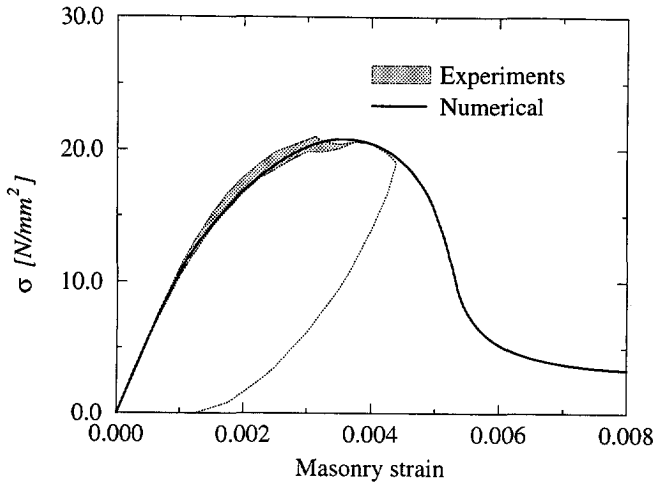


Figure 4.12 Model vs. experimental compressive behavior, Van der Pluijm and Vermeltoort (1991), with  $f_m = 20.8 [N/mm^2]$  and inelastic parameters from Atkinson and Yan (1990).

always occurs before the intersection between the cap and the tensile modes, the residual  $\bar{\sigma}_r$  value is determined by

$$\bar{\sigma}_r > \sqrt{C_{nn}f_t^2 + C_{ss}(c - f_t \tan \phi_0)^2 + C_n f_t} \quad (4.20)$$

Using matrix notation, eq. (4.19) can be rewritten in a form more amenable to computational implementation, as

$$f_3(\boldsymbol{\sigma}, \kappa_3) = 1/2 \boldsymbol{\sigma}^T \mathbf{P} \boldsymbol{\sigma} + \mathbf{p}^T \boldsymbol{\sigma} - (\bar{\sigma}_3(\kappa_3))^2 \quad (4.21)$$

where the projection matrix  $\mathbf{P}$  equals  $\text{diag}\{2 C_{nn}, 2 C_{ss}\}$  and the projection vector  $\mathbf{p}$  equals  $\{C_n, 0\}^T$ . An associated flow rule and a strain hardening/softening hypothesis are considered. This yields, upon substitution in eq. (3.30),

$$\dot{\kappa}_3 = \dot{\lambda}_3 \sqrt{(\mathbf{P} \boldsymbol{\sigma} + \mathbf{p})^T (\mathbf{P} \boldsymbol{\sigma} + \mathbf{p})} \quad (4.22)$$

The stress update equations, cf. eq. (3.39)<sub>1</sub>, can be manipulated to obtain

$$\boldsymbol{\sigma}_{n+1} = (\mathbf{D}^{-1} + \Delta\lambda_{3, n+1} \mathbf{P})^{-1} (\boldsymbol{\varepsilon}_{trial}^e - \Delta\lambda_{3, n+1} \mathbf{p}) \quad (4.23)$$

with  $\boldsymbol{\varepsilon}_{trial}^e = \mathbf{D}^{-1} \boldsymbol{\sigma}^{trial}$ . The derivative necessary for the iterative local Newton-Raphson method reads

$$\left. \frac{\partial f_3}{\partial \Delta\lambda_3} \right|_{n+1} = \left( \frac{\partial f_3}{\partial \boldsymbol{\sigma}} + \frac{\partial f_3}{\partial \kappa_3} \frac{\partial \kappa_3}{\partial \boldsymbol{\sigma}} \right)^T \frac{\partial \boldsymbol{\sigma}}{\partial \Delta\lambda_3} - h_3 \quad (4.24)$$

where

$$\begin{aligned}
 \frac{\partial f_3}{\partial \boldsymbol{\sigma}} &= \mathbf{P}\boldsymbol{\sigma}_{n+1} + \mathbf{p} & \frac{\partial \kappa_3}{\partial \boldsymbol{\sigma}} &= \Delta\lambda_{3, n+1} \frac{\mathbf{P}(\mathbf{P}\boldsymbol{\sigma}_{n+1} + \mathbf{p})}{\sqrt{(\mathbf{P}\boldsymbol{\sigma}_{n+1} + \mathbf{p})^T (\mathbf{P}\boldsymbol{\sigma}_{n+1} + \mathbf{p})}} \\
 \frac{\partial f_3}{\partial \kappa_3} &= -2\bar{\sigma}_{3, n+1} \frac{\partial \bar{\sigma}_3}{\partial \kappa_3} & \frac{\partial \boldsymbol{\sigma}}{\partial \Delta\lambda_3} &= -(\mathbf{D}^{-1} + \Delta\lambda_{3, n+1} \mathbf{P})^{-1} (\mathbf{P}\boldsymbol{\sigma}_{n+1} + \mathbf{p}) \quad (4.25) \\
 h_3 & & h_3 &= -\frac{\partial f_3}{\partial \kappa_3} \sqrt{(\mathbf{P}\boldsymbol{\sigma}_{n+1} + \mathbf{p})^T (\mathbf{P}\boldsymbol{\sigma}_{n+1} + \mathbf{p})}
 \end{aligned}$$

The consistent tangent stiffness matrix cannot be written in a simple form and is evaluated according to eq. (3.57). All the necessary terms are given in eq. (4.25) except the modified stiffness matrix  $\mathbf{H}$  which reads

$$\mathbf{H} = \left[ \mathbf{D}^{-1} + \Delta\lambda_{3, n+1} \mathbf{P} \right]^{-1} \quad (4.26)$$

#### 4.2.4 A composite yield criterion

One important feature of the composite yield surface is the coupling of tension and shear softening because both phenomena are related to the bond or adhesion between unit and mortar. Here, isotropic<sup>†</sup> softening is assumed, which means that the percentages of the cohesion and tensile strength softening are equal throughout the entire degradation process. Experimental results for mixed (shear-tension) stress paths are not available because, as reported by Van der Pluijm (1993), even for low (compressive) confining stresses brittle results were found with potential instability of the test set-up. The assumption of isotropic softening comes only by physical reasoning because any amount of coupling between tension and shear can be introduced in the model. However, it seems natural to assume equal degradation of strength because both phenomena are due to the breakage of the same bridges that exist at micro-level between unit and mortar.

For the purpose of defining isotropic softening for the tension/shear corner, the starting point can be to assume that only the tension mode is active, meaning that  $\Delta\lambda_{1, n+1} > 0$  and  $\Delta\lambda_{2, n+1} = 0$ . Then, the yield value  $\bar{\sigma}_{1, n+1}$  at the end of the local iterative procedure reads

† The term *isotropic* softening will be used in this study according to the plasticity standard definition, see e.g. Chen and Han (1988), which means that the *yield surface* shrinks in the stress space but keeps the origin. This definition should not be confounded with the notion of isotropic softening in most damage models, where all the *stress components* are simultaneously reduced towards the origin. The effect of the plasticity isotropic softening is reflected in the yield values and, not necessarily, in all the stress components.

$$\bar{\sigma}_{1, n+1} = f_t \exp\left(-\frac{f_t}{G_f^I} \kappa_{1, n+1}^c\right) = \bar{\sigma}_{1, n} \exp\left(-\frac{f_t}{G_f^I} \Delta\kappa_{1, n+1}^c\right) \quad (4.27)$$

where  $\Delta\kappa_{1, n+1}^c = \Delta\lambda_{1, n+1}$ . If decohesion is coupled with tensile softening also the yield value  $\bar{\sigma}_{2, n+1}$  at the end of the iterative procedure must be updated and reads

$$\bar{\sigma}_{2, n+1} = c \exp\left(-\frac{c}{G_f^H} \kappa_{2, n+1}^c\right) = \bar{\sigma}_{2, n} \exp\left(-\frac{c}{G_f^H} \Delta\kappa_{2, n+1}^c\right) \quad (4.28)$$

where  $\Delta\kappa_{2, n+1}^c$  must be calculated under the assumption of isotropic softening. From the equality  $\bar{\sigma}_{1, n+1} / \bar{\sigma}_{1, n} = \bar{\sigma}_{2, n+1} / \bar{\sigma}_{2, n}$ , it immediately follows

$$\Delta\kappa_{2, n+1}^c = \frac{G_f^H}{G_f^I} \frac{f_t}{c} \Delta\lambda_{1, n+1} \quad (4.29)$$

Similarly, the update of the softening scalar of the tension mode  $\kappa_1^c$ , when only the Coulomb mode is active, reads

$$\Delta\kappa_{1, n+1}^c = \frac{G_f^I}{G_f^H} \frac{c}{f_t} \Delta\lambda_{2, n+1} \quad (4.30)$$

Thus, it would seem natural to define the rates of the softening scalars for the composite yield surface, cf. eqs. (3.35, 4.5, 4.14), as

$$\dot{\kappa}_1^c = \dot{\lambda}_1 + \frac{G_f^I}{G_f^H} \frac{c}{f_t} \dot{\lambda}_2 \quad \dot{\kappa}_2^c = \frac{G_f^H}{G_f^I} \frac{f_t}{c} \dot{\lambda}_1 + \dot{\lambda}_2 \quad (4.31)$$

These equations will not be used because they represent a penalization of the corner regime in comparison with adjacent single surface regimes. Figure 4.13 shows three different possible trial stress states close to the corner and the respective return mapping. It is further assumed that the yield surface at stage  $n+1$  is the same for the three cases (this is clearly wrong but yields a more legible picture), the stiffness matrix is equal to the identity matrix and the dilatancy angle equals zero. Then, either for the shear or tension modes, the amount of softening is measured by the distance  $\Delta\lambda_{i, n+1} = |\sigma^{trial} - \sigma_{n+1}|$  (note that the subscript  $n+1$  is dropped in the figure for convenience). In the corner, according to eqs. (4.31), the two values would be added representing a penalty of the singular point without any physical ground. For this reason a quadratic combination is used to replace eq. (4.31), reading

$$\dot{\kappa}_1^c = \sqrt{(\dot{\lambda}_1)^2 + \left(\frac{G_f^I}{G_f^H} \frac{c}{f_t} \dot{\lambda}_2\right)^2} \quad \dot{\kappa}_2^c = \sqrt{\left(\frac{G_f^H}{G_f^I} \frac{f_t}{c} \dot{\lambda}_1\right)^2 + (\dot{\lambda}_2)^2} \quad (4.32)$$

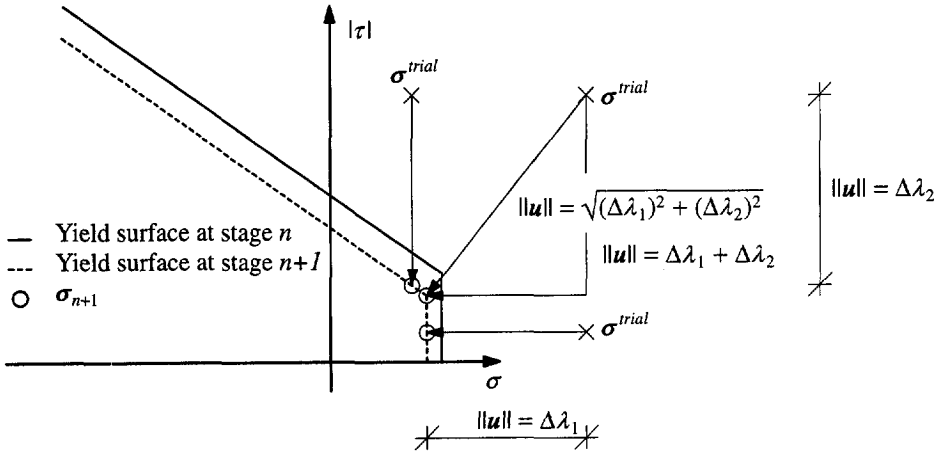


Figure 4.13 Definition of the amount of softening for the tension/shear corner. The norm of vector  $u$  controls the amount of softening.

The corners of the composite yield surface are singular points that have to be handled according to the procedures reviewed in Chapter 3. For the tension/shear corner, the stress update equations, cf. eq. (3.46)<sub>1</sub>, can be manipulated to obtain

$$\begin{cases} \sigma_{n+1} = \sigma^{trial} - \Delta\lambda_{1, n+1} k_n - \Delta\lambda_{2, n+1} k_n \tan \psi \\ \tau_{n+1} = \tau^{trial} - \Delta\lambda_{2, n+1} k_s \frac{\tau^{trial}}{|\tau^{trial}|} \end{cases} \quad (4.33)$$

and the components  $j$  of the Jacobian necessary for the iterative local Newton-Raphson method, cf. eq. (3.51), read

$$\begin{aligned} j_{11} &= -k_n - \frac{\partial \bar{\sigma}_1}{\partial \kappa_1^c} \frac{\Delta\lambda_{1, n+1}}{\Delta\kappa_1^c} \\ j_{12} &= -k_n \tan \psi - \frac{\partial \bar{\sigma}_1}{\partial \kappa_1^c} \left( \frac{G_f^I}{G_f^{II}} \frac{c}{f_t} \right)^2 \frac{\Delta\lambda_{2, n+1}}{\Delta\kappa_1^c} \\ j_{21} &= -k_n \tan \phi - \left[ \sigma_{n+1} \left( \frac{\tan \phi_r - \tan \phi_0}{c} \right) + 1 \right] \frac{\partial \bar{\sigma}_2}{\partial \kappa_2^c} \left( \frac{G_f^{II}}{G_f^I} \frac{f_t}{c} \right)^2 \frac{\Delta\lambda_{1, n+1}}{\Delta\kappa_2^c} \\ j_{22} &= -k_n \tan \phi \tan \psi - k_s - \left[ \sigma_{n+1} \left( \frac{\tan \phi_r - \tan \phi_0}{c} \right) + 1 \right] \frac{\partial \bar{\sigma}_2}{\partial \kappa_2^c} \frac{\Delta\lambda_{2, n+1}}{\Delta\kappa_2^c} \end{aligned} \quad (4.34)$$

The consistent tangent stiffness matrix is evaluated according to eq. (3.59).

The cap and shear modes are assumed to be uncoupled, which means that the definition of the scalar that controls the amount of hardening/softening of the cap mode remains unchanged, cf. eq. (4.22). Again, the physical reasoning behind this assumption is clear. The shear mode represents a unit-mortar interface phenomenon whereas the cap mode represents, basically, masonry crushing. For the compression/shear corner, the stress update equations, cf. eq. (3.46)<sub>1</sub>, can be manipulated to obtain

$$\begin{cases} \sigma_{n+1} = \frac{\sigma^{trial} - \Delta\lambda_{2, n+1} k_n \tan \psi - \Delta\lambda_{3, n+1} k_n C_n}{1 + 2 \Delta\lambda_{3, n+1} k_n C_{nn}} \\ \tau_{n+1} = \frac{\tau^{trial} - \Delta\lambda_{2, n+1} k_s \frac{\tau^{trial}}{|\tau^{trial}|}}{1 + 2 \Delta\lambda_{3, n+1} k_s C_{ss}} \end{cases} \quad (4.35)$$

and the components  $j$  of the Jacobian necessary for the iterative local Newton-Raphson method, cf. eq. (3.51), read

$$\begin{aligned} j_{11} &= \frac{\partial \sigma}{\partial \Delta\lambda_2} \tan \phi + \frac{\partial \tau}{\partial \Delta\lambda_2} \frac{\tau^{trial}}{|\tau^{trial}|} - h_2 \\ j_{12} &= \frac{\partial \sigma}{\partial \Delta\lambda_3} \tan \phi + \frac{\partial \tau}{\partial \Delta\lambda_3} \frac{\tau^{trial}}{|\tau^{trial}|} \\ j_{21} &= \left( \frac{\partial f_3}{\partial \sigma} + \frac{\partial f_3}{\partial k_3} \frac{\partial k_3}{\partial \sigma} \right)^T \frac{\partial \sigma}{\partial \Delta\lambda_2} \\ j_{22} &= \left( \frac{\partial f_3}{\partial \sigma} + \frac{\partial f_3}{\partial k_3} \frac{\partial k_3}{\partial \sigma} \right)^T \frac{\partial \sigma}{\partial \Delta\lambda_3} - h_3 \end{aligned} \quad (4.36)$$

where

$$\begin{aligned} \frac{\partial \sigma}{\partial \Delta\lambda_2} &= - \frac{k_n \tan \psi}{1 + 2 \Delta\lambda_{3, n+1} k_n C_{nn}} & \frac{\partial \sigma}{\partial \Delta\lambda_3} &= - \frac{k_n C_n + 2 k_n C_{nn} \sigma_{n+1}}{1 + 2 \Delta\lambda_{3, n+1} k_n C_{nn}} \\ \frac{\partial \tau}{\partial \Delta\lambda_2} &= - \frac{k_s \frac{\tau^{trial}}{|\tau^{trial}|}}{1 + 2 \Delta\lambda_{3, n+1} k_s C_{ss}} & \frac{\partial \tau}{\partial \Delta\lambda_3} &= - \frac{2 k_s C_{ss} \tau_{n+1}}{1 + 2 \Delta\lambda_{3, n+1} k_s C_{ss}} \end{aligned} \quad (4.37)$$

The consistent tangent stiffness matrix is evaluated according to eq. (3.59).

### 4.3 Validation

The micro-modeling strategy is validated next by a comparison with experimental results available in the literature. Traditionally, experiments on shear walls have been adopted by the masonry community as the most common in-plane large test. Yet, little

understanding still exists about the behavior of this type of structures. In this study, special attention is devoted to the shear wall tests carried out in the Netherlands, see Raijmakers and Vermeltoort (1992), Vermeltoort and Raijmakers (1993) and CUR (1994), because most of the parameters necessary to characterize the material model are available from micro-experiments. It is noted however, that masonry experimental results show typically a wide scatter, not only in large structures but also in small tests. The main concern of this work is, thus, to demonstrate the ability of the model to capture the behavior observed in the experiments and not a close quantitative reproduction of the experimental results. The large number and variability of the material parameters necessary to characterize the developed model permits to adopt a set of parameters suitable to closely fit the experimental load-displacement diagrams. This objective will not be pursued here.

For the numerical analyses, units are represented by plane stress continuum elements (8-noded) while line interface elements (6-noded) are adopted for the joints and for the potential vertical cracks in the middle of the unit. Each unit is modeled with  $4 \times 2$  elements. For the joints, the composite interface model described in this study is adopted and, for the potential cracks in the units, a simple mode I cracking model with exponential tensile softening and immediate drop to zero of the shear stress after initiation of the crack is assumed (a reason for this choice will become clear later in the text).

The friction angle, measured by  $\tan \phi$ , is assumed constant, i.e.  $\phi = \phi_0 = \phi_r$ , and equal to 0.75. This is the (residual) value obtained by Van der Pluijm (1993), which seems to be almost independent of the unit and mortar type as discussed in Chapter 2. Given the fact that shear micro-tests, with samples obtained from the shear walls analyzed in this study, were not carried out, the adopted value is likely to be the most adequate. The dilatancy angle, measured by  $\tan \psi$ , is assumed to equal zero. It is discussed in Chapter 2 that the dilatancy angle decreases to zero with increasing plastic shear slip and confining normal pressure (an extrapolation of the results from Van der Pluijm (1993) indicates that a normal confining pressure ranging from 1.0 to 2.0  $[N/mm^2]$  is enough to yield a dilatancy angle of zero!). The combination of these two factors in the confined structures analyzed next leads to an extremely fast degradation of the dilatancy angle and the assumption of a constant zero dilatancy angle should affect the results only marginally. The parameter  $C_{ss}$  which controls the contribution of the shear stress to compressive failure is taken equal to 9.0. A reason for this choice is given in Section 4.4.2. Unless otherwise stated, the analyses are carried out with indirect displacement control, whereas the snap-backs and snap-throughs are traced with COD control over the most active interface.

### 4.3.1 TU Eindhoven shear walls

Tests on masonry shear walls were carried out within the scope of the CUR project, CUR (1994), by Raijmakers and Vermeltoort (1992) and Vermeltoort and Raijmakers (1993). Two types of walls were considered, either with or without a central opening.

The shear walls have a width/height ratio of one with dimensions  $990 \times 1000$  [mm<sup>2</sup>], built up with 18 courses, from which 16 courses are active and 2 courses are clamped in steel beams, see Figure 4.14. In this figure, the arrow with a circle indicates a displacement. The walls are made of wire-cut solid clay bricks with dimensions  $210 \times 52 \times 100$  [mm<sup>3</sup>] and 10 [mm] thick mortar, prepared with a volumetric cement:lime:sand ratio of 1:2:9. Different vertical precompression uniformly distributed forces  $p$  are applied to the walls, before a horizontal load is monotonically increased under top displacement control  $d$  in a confined way, i.e. keeping the bottom and top boundaries horizontal and precluding any vertical movement, see Figure 4.14. The material data are obtained from existent results on tension, compression and shear tests as reported in Chapter 2, as well as from samples collected for each wall.

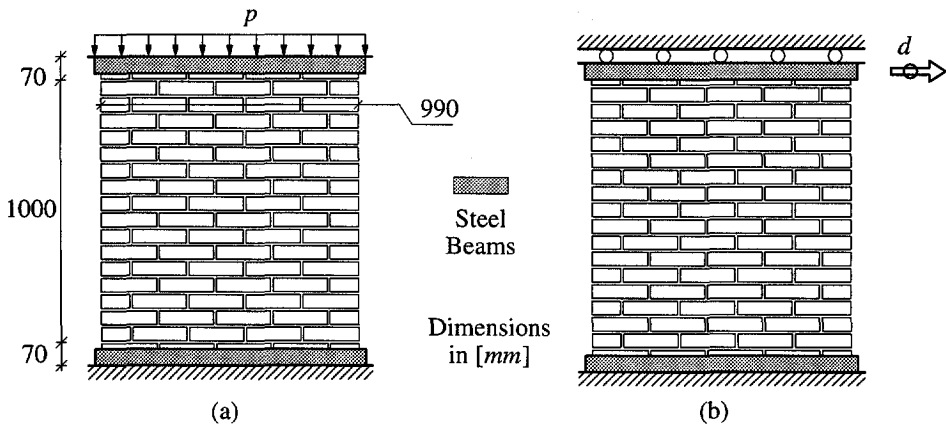


Figure 4.14 Loads for TU Eindhoven shear walls: (a) phase 1 - vertical loading; (b) phase 2 - horizontal loading under displacement control.

#### Walls JD. Shear walls without opening

The first walls to be presented, here denoted JD, are solid without any opening. Different initial vertical loads  $p$  were applied: for walls J4D and J5D the load  $p$  equals  $0.30$  [N/mm<sup>2</sup>]  $\equiv$   $30$  [kN], for wall J6D the load  $p$  equals  $1.21$  [N/mm<sup>2</sup>]  $\equiv$   $120$  [kN] and for wall J7D the load  $p$  equals  $2.12$  [N/mm<sup>2</sup>]  $\equiv$   $210$  [kN]. The experimental crack patterns for the different walls tested are shown in Figure 4.15. The behavior of the walls is similar. For the lower initial vertical load (walls J4D and J5D), horizontal tensile cracks develop at the bottom and top of the wall at an early loading stage but, for all the walls, a diagonal stepped crack leads to collapse, simultaneously with cracks in the bricks and crushing of the compressed toes.

The micro-properties for the different materials are obtained from Raijmakers and Vermeltfoort (1992), Vermeltfoort and Raijmakers (1993) and CUR (1994), see Table 4.3 to Table 4.5. Note that an elastic dummy stiffness is considered for the potential cracks in the bricks. When more than one value is given in the same column, it means

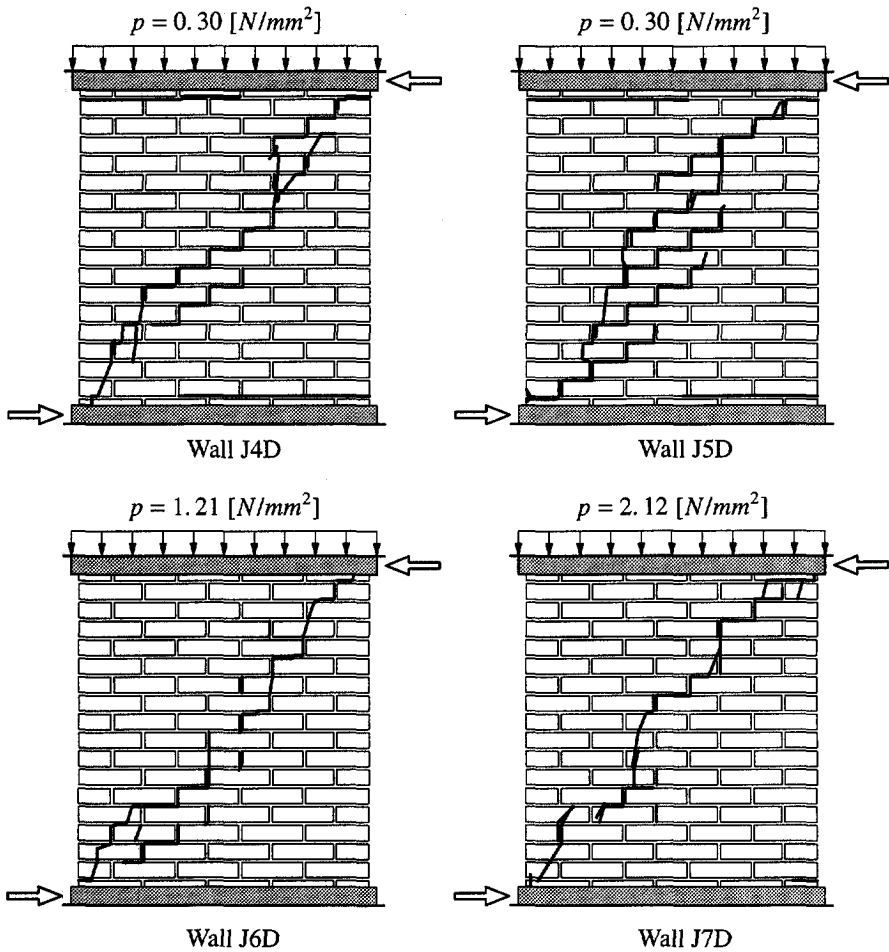


Figure 4.15 Walls JD. Experimental crack patterns for different tests.

that different parameters are used for the walls with an initial vertical load of, respectively, 0.30, 1.21 and 2.12  $[N/mm^2]$ . These parameters were obtained from samples of each test. The only exception is the elastic properties of the mortar, which have been adjusted to reproduce the stiffness of the wall observed in the experiments. The hardening/softening law for the cap mode is defined by the set  $\{\bar{\sigma}_3, \kappa_3\}_i = \{(f_m / 3, 0.0) ; (f_m, 0.09) ; (f_m / 2, 0.49) ; (f_m / 7, +\infty)\}$ .

Table 4.3 Walls JD. Properties for the potential brick cracks.

$k_n$	$k_s$	$f_t$	$G_f^I$
$1.0 \times 10^6$	$1.0 \times 10^6$	2.0	0.08
$[N/mm^3]$	$[N/mm^3]$	$[N/mm^2]$	$[Nmm/mm^2]$

Table 4.4 Walls JD. Elastic properties for the bricks and joints.

Brick		Joint	
E	$\nu$	$k_n$	$k_s$
16700	0.15	82;110;82	36;50;36
[N/mm <sup>2</sup> ]		[N/mm <sup>3</sup> ]	[N/mm <sup>3</sup> ]

Table 4.5 Walls JD. Inelastic properties for the joints.

Tension		Shear				Cap	
$f_t$	$G'_f$	$c$	$\tan \phi$	$\tan \psi$	$G''_f$	$f_m$	$C_{ss}$
0.25;0.16;0.16	0.018;0.012;0.012	$1.4f_t$	0.75	0.0	0.125;0.050;0.050	10.5;11.5;11.5	9.0
[N/mm <sup>2</sup> ]	[Nmm/mm <sup>2</sup> ]	[N/mm <sup>2</sup> ]			[Nmm/mm <sup>2</sup> ]	[N/mm <sup>2</sup> ]	

The comparison between numerical and experimental load-displacement diagrams is shown in Figure 4.16. The experimental behavior is satisfactorily reproduced and the collapse load can be estimated within a 15 % range of the experimental values. The sudden load drops are due to cracking in a single integration point of the potential cracks in a brick and opening of each complete crack across one brick. All the walls behave in a rather ductile manner, which seems to confirm the idea that confined masonry can withstand substantial post-peak deformation with reduced loss of strength. The behavior normally experienced by shear walls, see e.g. the analyses of reinforced concrete shear walls in Feenstra (1993) and the analyses of masonry shear walls in Chapter 6, is that higher initial vertical loads lead to increasing strength but also increasing brittleness. Such type of behavior might be considered odd because one might expect that higher confinement lead to increasing ductility. This is not the case in shear walls where

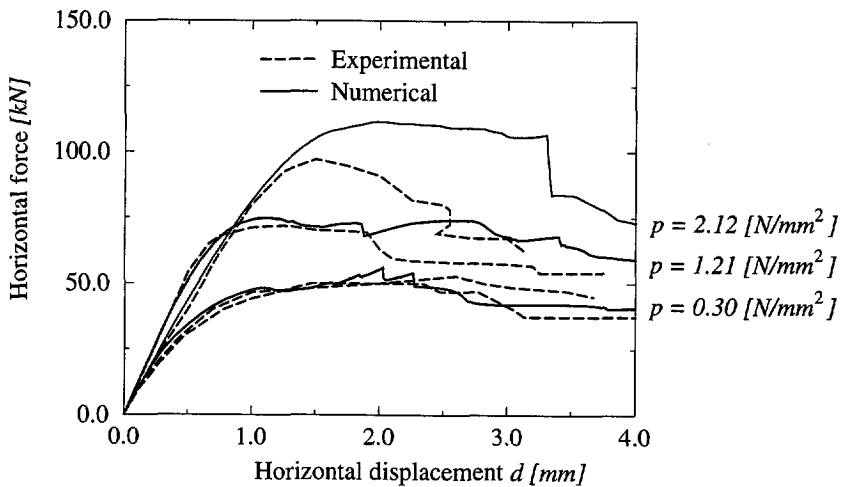


Figure 4.16 Walls JD. Load - displacement diagrams.

the softening regime is, generally, governed by failure of the compressed toes of wall, which is free to occur because the material can always fail in the out-of-plane direction. Higher failure loads correspond to higher normal stresses in the supports, which means that redistributions of stresses upon crushing of the compressed toes become more and more difficult. The results obtained both experimentally and numerically show indeed that higher initial vertical loads lead to increasing strength of the shear walls, but it is striking that higher failure loads do not correspond to increasing brittleness. This can be explained by the internal force distribution at failure, which is shown later in this text.

Walls J4D and J5D, with an initial vertical load of  $0.30 [N/mm^2]$ , were chosen for further discussion because two tests were successfully carried out. The behavior of the wall is well captured by the model as illustrated in Figure 4.17 and Figure 4.18. In these

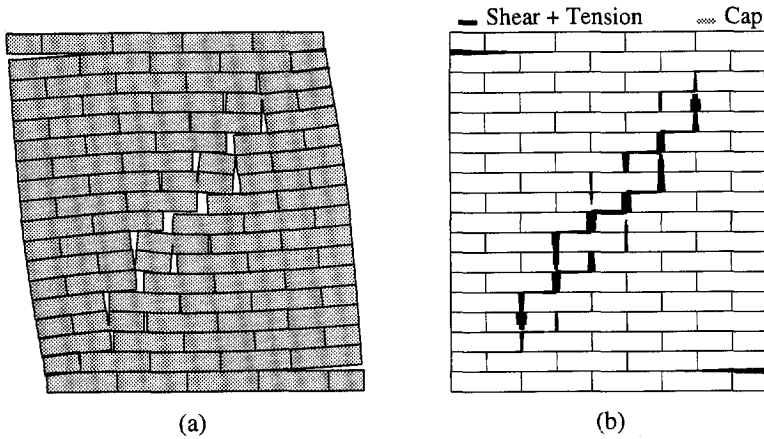


Figure 4.17 Walls J4D and J5D. Results of the analysis at a displacement of  $2.0 [mm]$ : (a) deformed mesh; (b) damage.

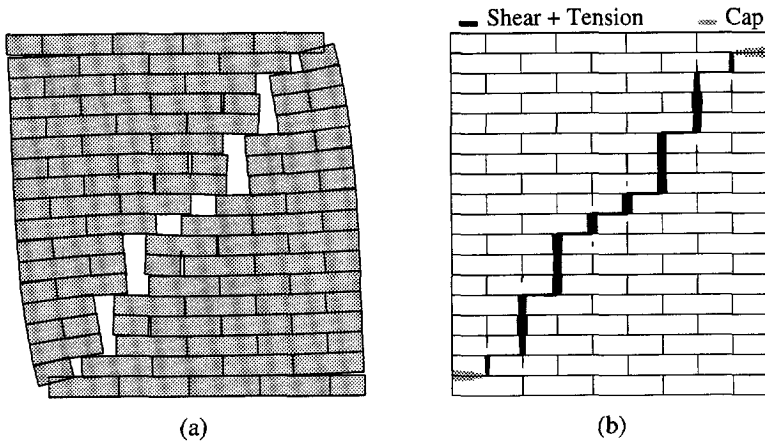


Figure 4.18 Walls J4D and J5D. Results of the analysis at a displacement of  $4.0 [mm]$ : (a) deformed mesh; (b) damage.

figures, the word “damage” is used for the equivalent plastic strain from each mode of the composite interface model. Note that the “damage” of the compressive cap is only shown in the softening regime, not during hardening. Initially, two horizontal tensile cracks develop at the bottom and top of the wall. A stepped diagonal crack through head and bed joints immediately follows. This crack starts in the middle of the wall and is accompanied by initiation of cracks in the bricks, see Figure 4.17. Under increasing deformation, the crack progresses in the direction of the supports and, finally, a collapse mechanism is formed with crushing of the compressed toes and a complete diagonal crack through joints and bricks, see Figure 4.18.

In the experiments also the vertical reaction was measured. This permits additional comparisons and further assessment of the model performance. Figure 4.19a demonstrates that the dilatant behavior is reproduced well. The redistribution of vertical stresses in the supports is also closely followed as illustrated in Figure 4.19b by the eccentricity of the vertical reaction with respect to the middle line of the wall. This reaction moves initially from the middle line of the wall in the direction of the compressed toes. Due to plastification/crushing of the compressed zone and cracking of the joints/bricks close to the compressed toes the vertical reaction drifts back in the direction of the middle line of the wall at a later stage, see also Figure 4.20.

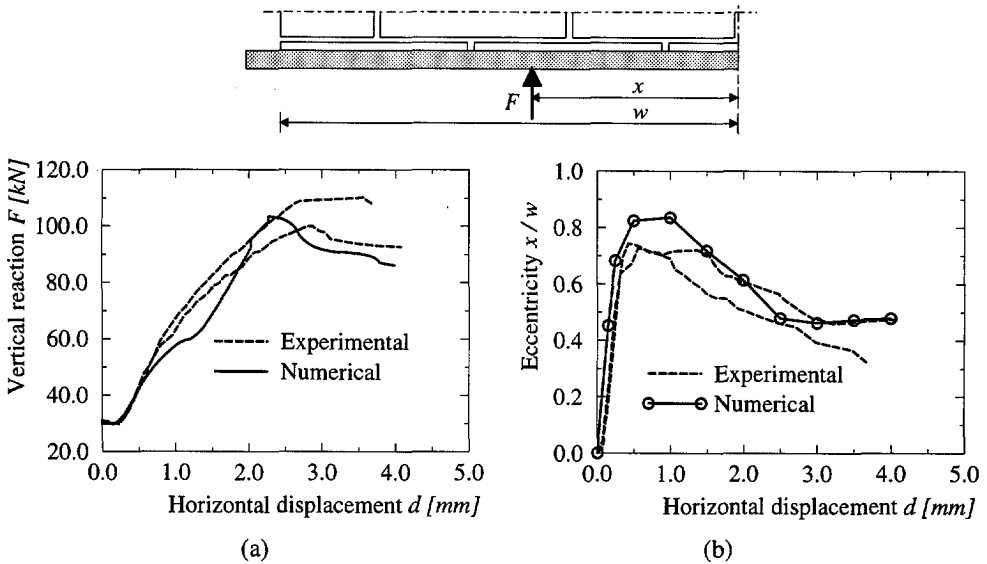


Figure 4.19 Walls J4D and J5D. Vertical reaction: (a) norm; (b) position.

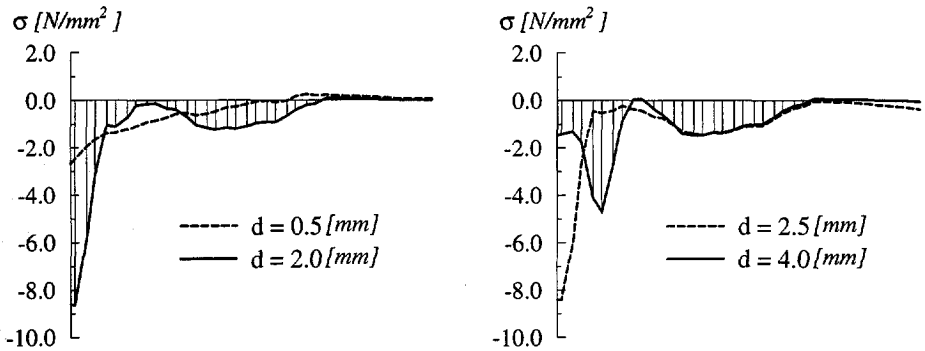


Figure 4.20 Walls J4D and J5D. Diagram of vertical stresses close to the bottom support, for different values of the horizontal displacement  $d$ .

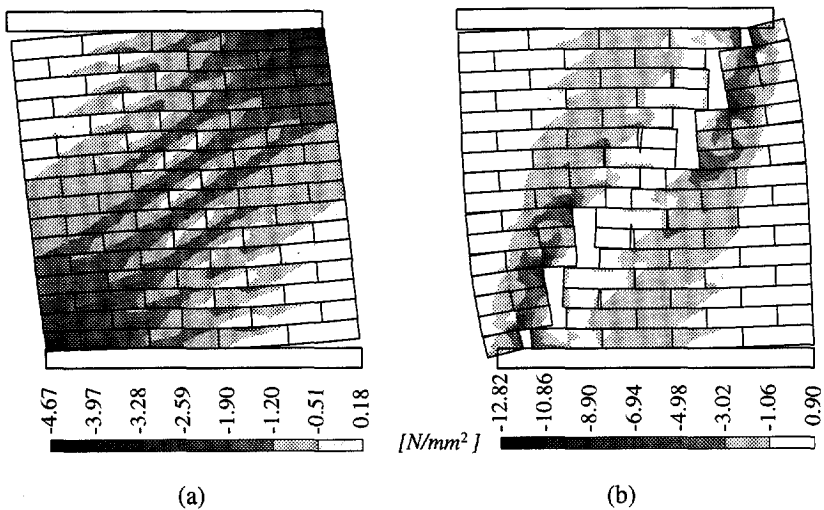


Figure 4.21 Walls JD4 and JD5. Minimum principal stresses at a displacement of (a) 1.0 [mm] and (b) 4.0 [mm].

The phenomena just described can be easily understood from the stress distribution shown in Figure 4.21. Initially, the stress profiles are essentially “continuous”. At this early stage, due to the different stiffnesses of joints and bricks, small struts are oriented parallel to the diagonal line defined by the center of the bricks, see Figure 4.21a. This means that the direction of the principal stresses is mainly determined by the geometry of the bricks. After initiation of the diagonal crack the orientation of the compressive stresses gradually rotates. The diagonal crack prevents the formation of compressive struts parallel to the diagonal line defined by the center of the bricks and, therefore, the internal force flow between the two sides of the diagonal crack must be transmitted by shearing of the bed joints. Finally, when the diagonal crack is fully open, two distinct

struts are formed, one at each side of the diagonal crack, see Figure 4.21b. The fact that the stress distribution at the supports is of “discontinuous” nature leads to an early collapse of the wall due to compressive crushing. In Section 4.4.3, it will be shown that a continuous stress distribution, in the case of an initial vertical load of  $0.30 [N/mm^2]$ , can lead to a collapse load 2.5 times larger than the observed value.

The ductile behavior of all the tests is now evident. Upon increasing initial vertical load the shear transfer across the bed joints in the diagonal crack zone is augmented, which means that the opening of the diagonal crack is reduced. Therefore, a more continuous stress distribution is found with larger compression zones at the supports, which lead to reasonable ductility with delayed compressive failure at the toes.

The aspects related to the adoption of a simple mode I crack model for the potential cracks in the units are addressed now. All the calculated load-displacement diagrams, shown in Figure 4.16, present sudden load drops which are due to cracking in a single integration point of potential cracks in a brick or opening of each complete crack across one brick (when a potential vertical crack is almost complete across one brick, relatively high shear stresses are set to zero in a single step). In the former case a mesh refinement would smooth the curve but, in the latter, a snap-through or snap-back will, as in case of the walls analyzed next, most certainly be found. The analyses were carried out with direct displacement control and these points were sporadically “jumped over” by the use of a secant stiffness instead of a tangent stiffness, only for the discrete cracking criterion in the bricks. For the composite interface model derived in this study the consistent tangent operator was used throughout the analysis. It was also tried to obtain a gradual release of the shear stress after initiation of the crack in the units, both with a “rotating-type” crack model and with the composite interface model (shear and tension regimes). It turned out that, at a certain load increment, convergence could not be achieved due to bifurcations, with the incapability of the structure to select, at a certain location around the diagonal crack, whether to propagate the crack in the unit or the crack/slip in the head and bed joints around the unit.

The decision to set the shear stress in the unit to zero upon initiation of the crack was thus adopted by numerical reasons. This decision should affect the results only marginally and, indeed, solves the bifurcations problems. Of course the procedure lacks of some numerical robustness as a large amount of energy can be released in a single load step. However, if sufficiently fine meshes are adopted, the solution obtained is, in principle, mesh insensitive and independent of the size of the load increments. For the purpose of assessing the robustness of the composite interface model developed in the present study, cracks in the units will then not be included in the examples shown in the rest of this Section.

#### *Walls JG. Shear walls with opening*

The next analysis concerns two tests successfully carried out for walls with a central opening, here denoted J2G and J3G. The walls are subjected to the same initial vertical load  $p$ , which equals  $0.30 [N/mm^2] \equiv 30 [kN]$ , and the material properties are the same



remain active and the wall behaves similarly to four rigid blocks connected by the hinges shown. The experimental crack patterns of the two walls successfully tested are illustrated in Figure 4.23.

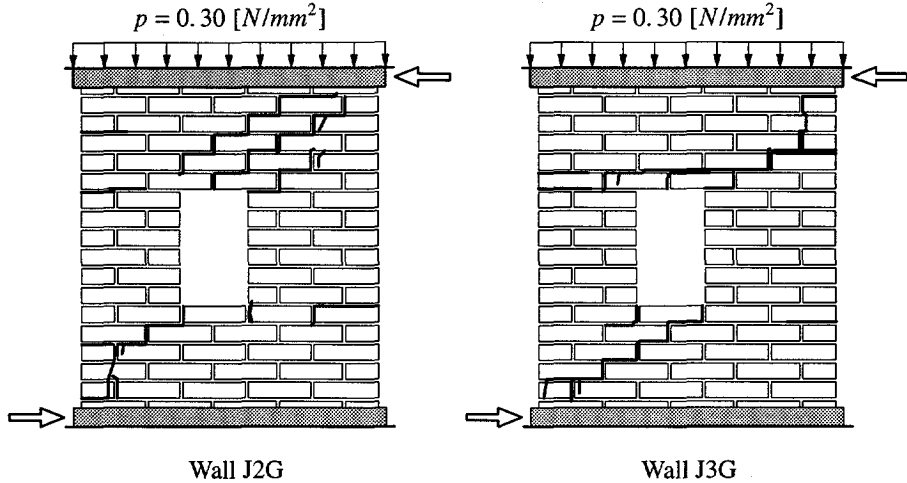


Figure 4.23 Walls JG. Experimental crack patterns for different tests.

The comparison between the calculated and experimental load-displacement diagrams is shown in Figure 4.24. The results agree reasonably well. The calculated failure load is equal to the failure load of the wall J2G whereas the wall J3G features a collapse load 20 % lower than the calculated value. A good impression about the behavior of the model is also obtained because the calculated softening stiffness of the structure agrees reasonably well with the softening stiffness of the wall J2G. This indicates that the

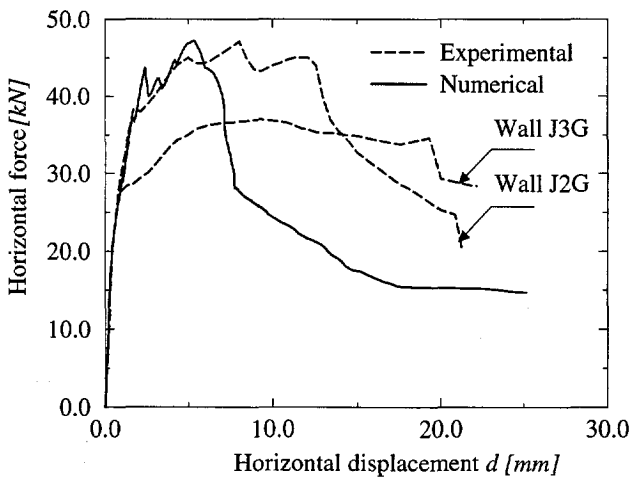


Figure 4.24 Walls JG. Load - displacement diagrams.

correct failure mechanism is predicted. It is however recognized that the behavior obtained numerically is more brittle than the experimental observations.

Globally, the analysis captures well the experimental behavior of the walls, as illustrated in Figures 4.25 to 4.27. Initially, two diagonal cracks arise from the corners of the opening. These cracks are accompanied by less evident horizontal cracks in the top and bottom of the small piers as well as one horizontal crack in the bottom of the wall, see Figure 4.25. Under increasing deformation, the diagonal cracks that arose initially cannot progress to the compressed toes and two additional diagonal cracks start to open, see Figure 4.26. These become gradually predominant and, when the compressed toes at the

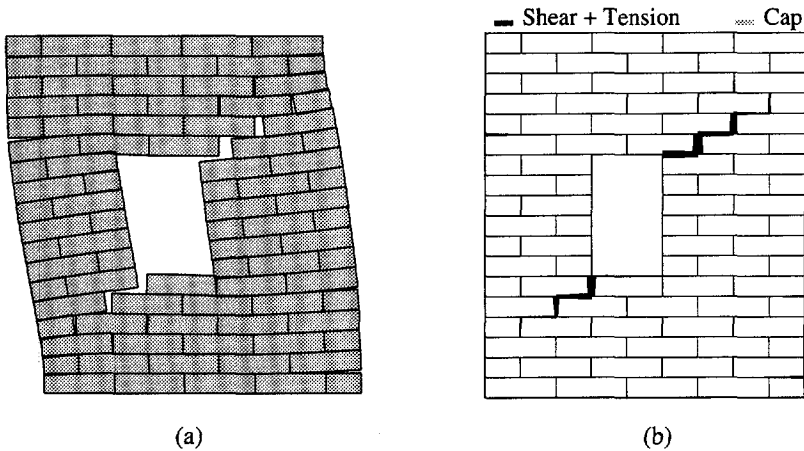


Figure 4.25 Walls JG. Results of the analysis at a displacement of 1.0 [mm]: (a) deformed mesh; (b) damage.

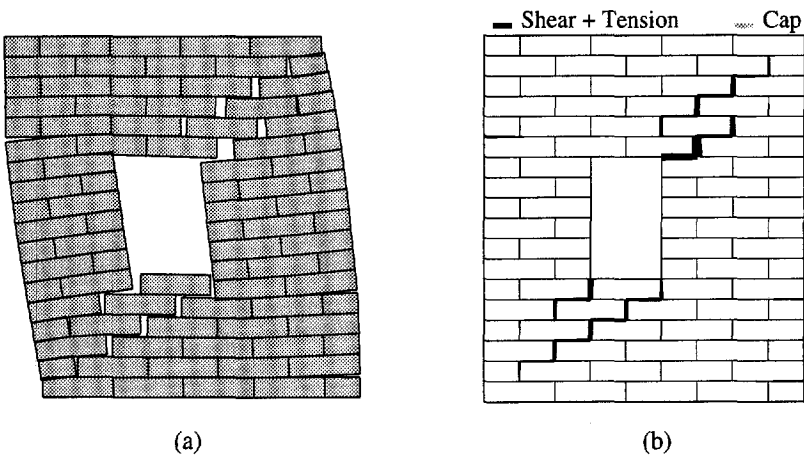


Figure 4.26 Walls JG. Results of the analysis at a displacement of 2.0 [mm]: (a) deformed mesh; (b) damage.

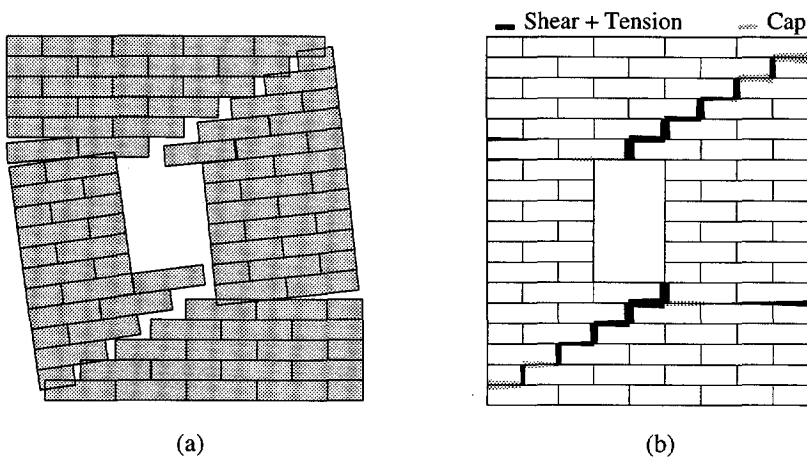


Figure 4.27 Walls JG. Results of the analysis at a displacement of 25.0 [mm]: (a) deformed mesh; (b) damage.

bottom and top of the wall begin to crush, the previous diagonal cracks become inactive. Finally, a complete collapse mechanism is formed with the failure of the small piers in bending, i.e. crushing of the compressed toes and extended horizontal tensile cracks, see Figure 4.27. The failure mode shows good agreement with the four hinge model of Figure 4.22d.

Figure 4.28 shows the distribution of minimum principal stresses for two other loading stages, of which one at peak load. These figures confirm that failure is governed by all modes of the composite interface model. Initially, two large compressive struts are formed, see Figure 4.28a. For higher loads, the diagonal cracks through the middle of

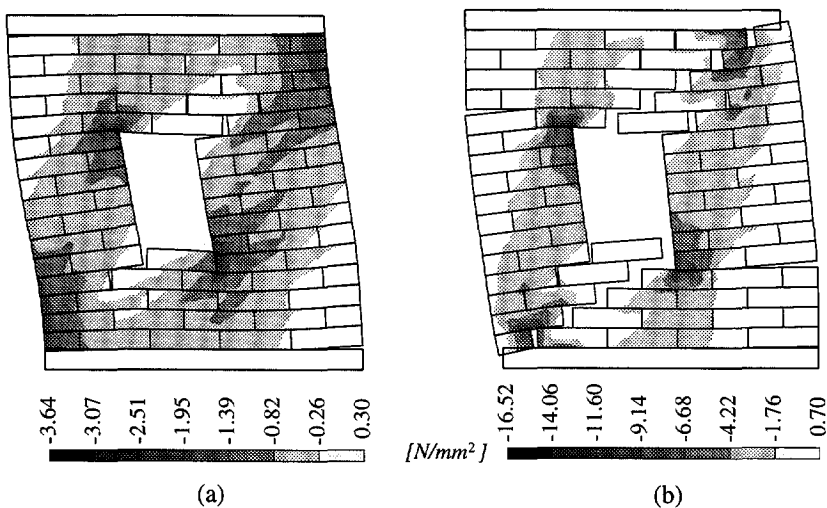


Figure 4.28 Walls JG. Minimum principal stresses at a displacement (a) 0.5 [mm] and (b) 5.4 [mm] (peak).

the wall progress towards the supports and the two compressive struts become narrower, Figure 4.28b. At peak, compressive softening of the toes in the bottom and top of the wall is already noticeable, which forces the vertical reaction on the supports to move from the external side of the wall back to the middle of the wall.

During the entire pre- and post-peak regime, full convergence with an energy norm of  $10^{-4}$  was obtained in less than 5 iterations. As a rule 2 to 3 iterations were needed. A good impression about the robustness of the model is obtained because it is possible to trace the complete path of the test without numerical difficulties. In particular, the snap-throughs found in the numerical analysis, which occur due to the opening of new diagonal cracks and closing of previous diagonal cracks, are also converged states.

It is noted that, under the same loading conditions, the responses of the two walls, J2G and J3G, in terms of load-displacement diagrams, are different, see Figure 4.24, and correspond to different crack patterns, see Figure 4.23. It is believed that this is due to the combination of the scatter in the material properties and the small number of units that constitute the wall. It seems that different crack locations can be triggered for reasonably close failure loads, i.e. within the observed 20 % range. The lower collapse load and more ductile behavior observed for the wall J3G correspond to an early sliding failure mode, involving the part of the wall above the opening, see Figure 4.23b. This is in opposition with the bending failure mode (with opening of the top-right corner) of the same part of the wall featured by the wall J2G, see Figure 4.23a. A possible approach to reproduce an observed failure mode is to penalize or strengthen a certain number of joints in order to obtain exactly the crack pattern observed in a specific test. As an example of inverse fitting, new analyses have been carried out in an iterative way to obtain a better agreement with the wall J2G. Figure 4.29 shows that the experimental load-displacement diagram can be closely reproduced if the shear properties are reduced 30 %, the compressive strength 20 % and the compressive fracture energy is multiplied by three.

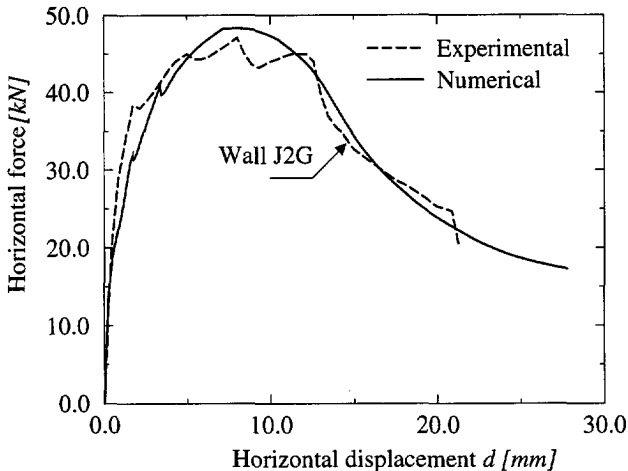


Figure 4.29 Wall J2G. Load-displacement diagram for new analysis.

### 4.3.2 Deep beam

Page (1978) tested the masonry deep beam illustrated in Figure 4.30, with dimensions  $757 \times 457$  [mm<sup>2</sup>] and supported at each side over a 188 [mm] length. The top load  $P$  is applied via a stiff steel beam of 381 [mm] length. The deep beam was made of pressed solid clay bricks and 5 [mm] thick mortar with a volumetric cement:lime:sand ratio of 1:1:6. Four half scale bricks were sawn from each full scale brick. The dimensions of each half scale brick were typically  $122 \times 37 \times 54$  [mm<sup>3</sup>]. The author reported that “cracks only became apparent at or near failure”, indicating a brittle collapse as well as a very likely quasi linear pre-peak response and high stress gradients in the zones of the structure close to the application of loads.

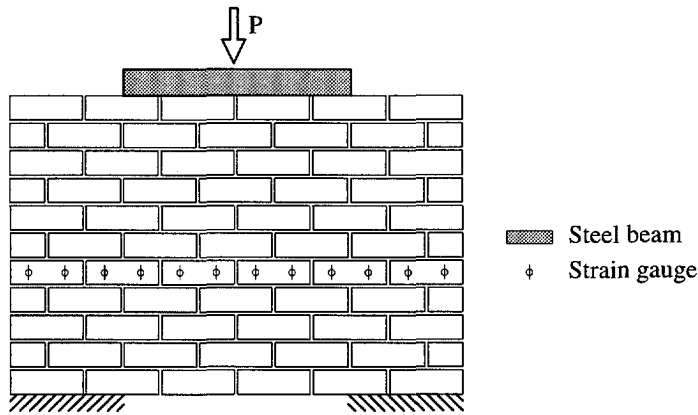


Figure 4.30 Deep beam test, Page (1978).

Very little experimental observations were reported by Page (1978) and, in particular, experimental crack patterns are not available. This example is, however, of interest because it serves as an additional verification object for studying the performance of the composite interface model, especially under localized compressive failure.

For the numerical simulation no relative displacements were allowed at the supports and only half of the structure is discretized due to symmetry. Considerations about symmetric and non-symmetric solutions of the problem, bifurcations and the post-peak energy consumed in the symmetric mode do not fall in the scope of this study. The objective of this example is only qualitative. The material properties, according to Page (1978), are given in Table 4.6 and Table 4.7 (note that the bricks feature orthotropic elastic behavior). Here  $E_x$  is the Young's modulus in the direction parallel to the bed joints,  $E_y$  is the Young's modulus in the direction normal to bed joints and  $G_{xy}$  is the shear modulus. The values for the cohesion and friction angle measured by the author are debatable because  $f_i > c / \tan \phi$ . Therefore, the average values for these parameters given in Chapter 2 are adopted. The hardening/softening law for the cap mode is defined by the set  $\{\bar{\sigma}_3, \kappa_3\}_i = \{ (f_m / 3, 0.0) ; (f_m, 0.07) ; (f_m / 2, 0.34) ; (f_m / 7, +\infty) \}$ .

Table 4.6 Deep beam. Elastic properties.

Brick				Joint	
$E_x$	$E_y$	$\nu_{xy}$	$G_{xy}$	$k_n$	$k_s$
5920	7550	0.167	2890	180.0	80.0
[N/mm <sup>2</sup> ]	[N/mm <sup>2</sup> ]		[N/mm <sup>2</sup> ]	[N/mm <sup>3</sup> ]	[N/mm <sup>3</sup> ]

Table 4.7 Deep beam. Inelastic properties.

Tension		Shear				Cap	
$f_t$	$G_f^I$	$c$	$\tan \phi$	$\tan \psi$	$G_f^{II}$	$f_m$	$C_{ss}$
0.29	0.018	$1.4 f_t$	0.75	0.0	0.050	8.6	9.0
[N/mm <sup>2</sup> ]	[Nmm/mm <sup>2</sup> ]	[N/mm <sup>2</sup> ]			[Nmm/mm <sup>2</sup> ]	[N/mm <sup>2</sup> ]	

The experimental load-displacement diagram was not reported by Page (1978) but the collapse load and the stress distributions until  $\approx 75\%$  of the collapse load are available, at the locations shown in Figure 4.30. The explosive behavior found in the experiment is, however, well reproduced in the numerical simulation by the pronounced snap-back shown in Figure 4.31. Here, the vertical displacement refers to the nodes at the top of the wall located on the symmetry axis. Note that no post-peak strength of the specimen is recorded in the structure except the residual plateau given at constitutive level. The analysis was performed with indirect displacement control up to peak load. The post-peak response was traced with arc-length control over the nodes in the masonry crushing zone. The calculated collapse load found (149.4 [kN]) is 37 % higher than the experimental value (109.2 [kN]). However, this can be explained by the sensitivity of the analysis to the parameters assumed for the cap mode. For the sake of completeness, another numerical analysis was carried out assuming another shape for the cap

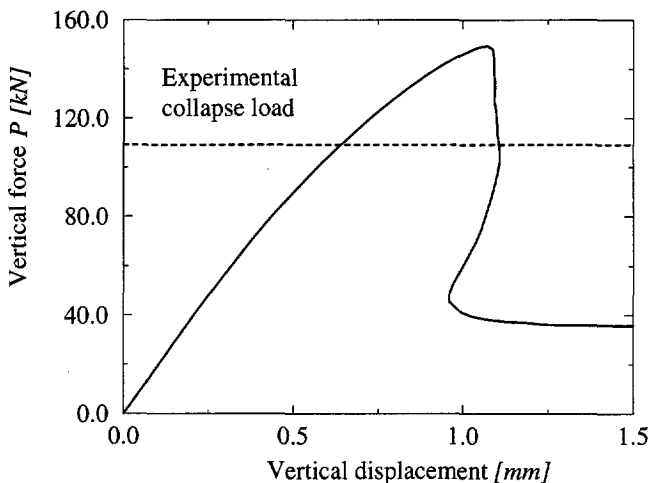


Figure 4.31 Deep beam. Calculated load - displacement diagram.

( $C_{ss} = 16.0$ ) and a more brittle material (half of the compressive fracture energy considered above). This analysis resulted in a collapse load of 115.0 [kN], only 5 % higher than the value obtained in the test.

Again, a good impression about the robustness of the model is obtained because it is possible to trace the complete path of the test without numerical difficulties. The complete response could be obtained in circa 100 load increments and during the entire pre- and post-peak regime, convergence with an energy norm of  $10^{-4}$  was obtained in less than 5 iterations. As a rule 2 to 3 iterations were needed.

The experimental and calculated profiles of vertical stresses are compared in Figure 4.32. Note that, in the absence of additional information about the location of the strain gauges, the stress values obtained numerically are given at the mid-height of the bricks. Similar two-peaked stress profiles are obtained both numerically and experimentally. Practically no stress redistributions occurred for the loading stages measured by the author which confirm the calculated quasi-linear pre-peak response.

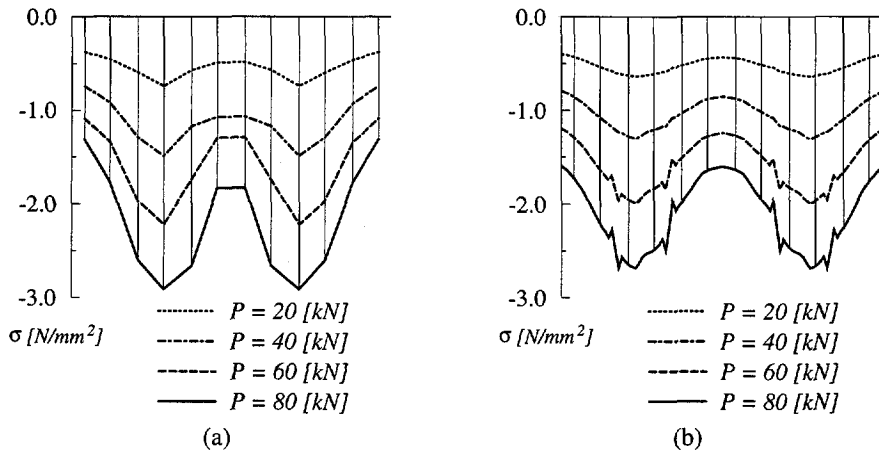
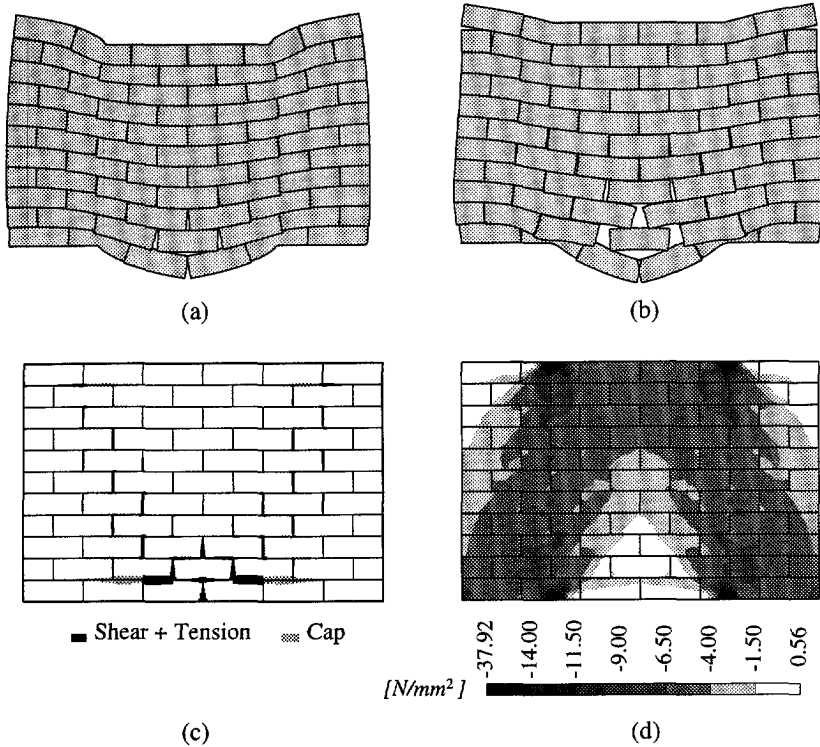
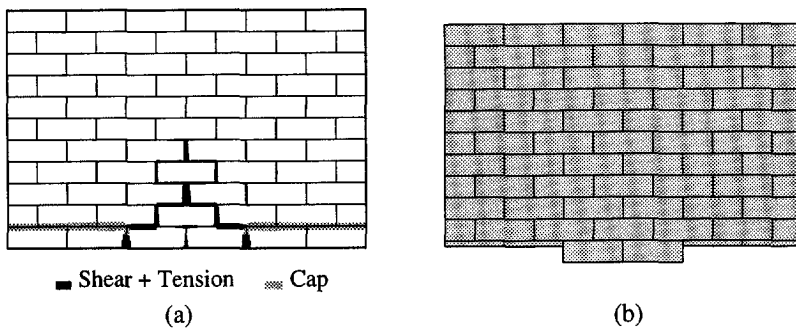


Figure 4.32 Deep beam. Profiles of vertical stresses for different vertical forces  $P$ : (a) experimental values; (b) calculated values.

Figure 4.33 illustrates the results of the analysis at peak by means of the deformed meshes, stress distribution and damage. Two large compression struts are formed from the top steel beam to the supports with large stress concentrations at the ends of the steel beam and the inner part of the supports. The damage of the structure at peak is concentrated near the supports with initiation of compressive softening and shearing of the bed joints immediately above the supports. The lower masonry courses, in the small span between the supports, show essentially tensile failure. Additionally, shearing of most of the head joints in the compressive struts are visible. Before peak, severe compressive damage already occurred in approximately one-fourth of the supports length, see Figure 4.33c. The peak represents thus a critical stage after which uncontrolled compressive damage grows. The post-failure response is exclusively governed by crushing of



**Figure 4.33** Deep beam. Results of the analysis at peak: (a) total deformed mesh; (b) incremental deformed mesh; (c) damage; (d) minimum principal stresses.



**Figure 4.34** Deep beam. Results of the analysis at ultimate stage: (a) damage; (b) incremental deformed mesh.

masonry in the supports, see Figure 4.34. All inelastic behavior concentrates in the bed joints above the supports whereas the rest of the structure moves in a rigid block. This is a phenomenological representation of compressive failure as discussed in Section 4.1.

It is obvious from the results that units will crack. In fact, tensile stresses as high as  $14.0 [N/mm^2]$  have been recorded for the units during the analysis. However, it is stressed again that, with this example, we put a premium in the behavior and robustness of the composite interface model.

#### 4.4 Reflections on the modeling strategy

The composite interface model developed in this study has five strength parameters ( $f_t$ ,  $c$ ,  $\tan \phi$ ,  $f_m$  and  $C_{ss}$ ) and four inelastic parameters ( $G_f^I$ ,  $G_f^H$ ,  $\tan \psi$  and  $G_{fc}$ ), if it is assumed that the inelastic behavior in compression is, basically, one material parameter. A complete sensitivity analysis of the structures analyzed in the previous Section, with respect to all material parameters, would be unwieldy. In Lourenço and Rots (1993) and CUR (1994) some parameter studies have, however, been reported. From the author's experience, in general, most material parameters do not strongly affect the results of the analyses and, in the present study, attention is driven only to the more relevant material parameters and aspects of the modeling strategy.

##### 4.4.1 Modeling cracking of the units

In Section 4.1, it was discussed that a complete masonry micro-model must include transverse cracking of the units. The question of how to model such cracking is a more delicate subject. Fracture is generally identified as a localized, true, geometrical discontinuity. The so-called smeared cracking models are most valuable for distributed fracture, as in large-scale reinforced concrete structures. Such cases provide a true physical basis for smeared concepts, at least if the scale of the representative continuum is large compared to the crack spacing. But this is not the case of the localized fracture in the units. Additionally, in the presence of softening, the classical continuum loses ellipticity and the problem becomes ill-posed. Results show typically mesh dependency with respect to mesh size and mesh orientation. Several techniques can be used to enhance standard continuum, see e.g. De Borst *et al.* (1993). These techniques are of difficult application for the analysis of the large structures considered here due to their inherent complexity and the need of using fine meshes in the fracture zone.

In fact, the all idea of using a discrete model for the joints and a smeared model for the units is not natural and a discrete cracking model should be preferably used. In the present study, potential vertical cracks are placed in the middle of each unit. These potential cracks are able to capture a jump from head joint to head joint which should cover practically all cases of tensile failure in units, if not exactly (when the crack does not occur completely vertical or really at the middle of the unit) at least with reasonable approximation. For the case of the JD shear walls (without opening) the cracks in the units were indeed considered to assess the micro-modeling strategy. It was also evident from the experimental results that generalized cracking of the units occurred. Of course,

in real practice, it is hardly possible to determine in advance whether this failure mechanism is likely to occur.

The behavior of the JD shear walls (without opening) according to the two types of modeling, whether cracking of the units is included or not, is illustrated in Figure 4.35. If the cracks in the units are not modeled, principal tensile stresses as high as four times the tensile strength of the units can be found. Thus, an overstiff response is obtained and a collapse load considerably higher than the experimental collapse load is found. Note that the first plateau found in both types of modeling is the same and corresponds to the initiation of stepped diagonal cracks through head and bed joints. Afterwards the behavior is different for the two cases. If cracking of the units is allowed, the units begin to crack, cf. Figure 4.17, and a complete diagonal crack across units and joints is found accompanied by crushing of the compressed toes. This behavior is confirmed by the experiments. If cracking of the units is precluded, three long diagonal cracks through

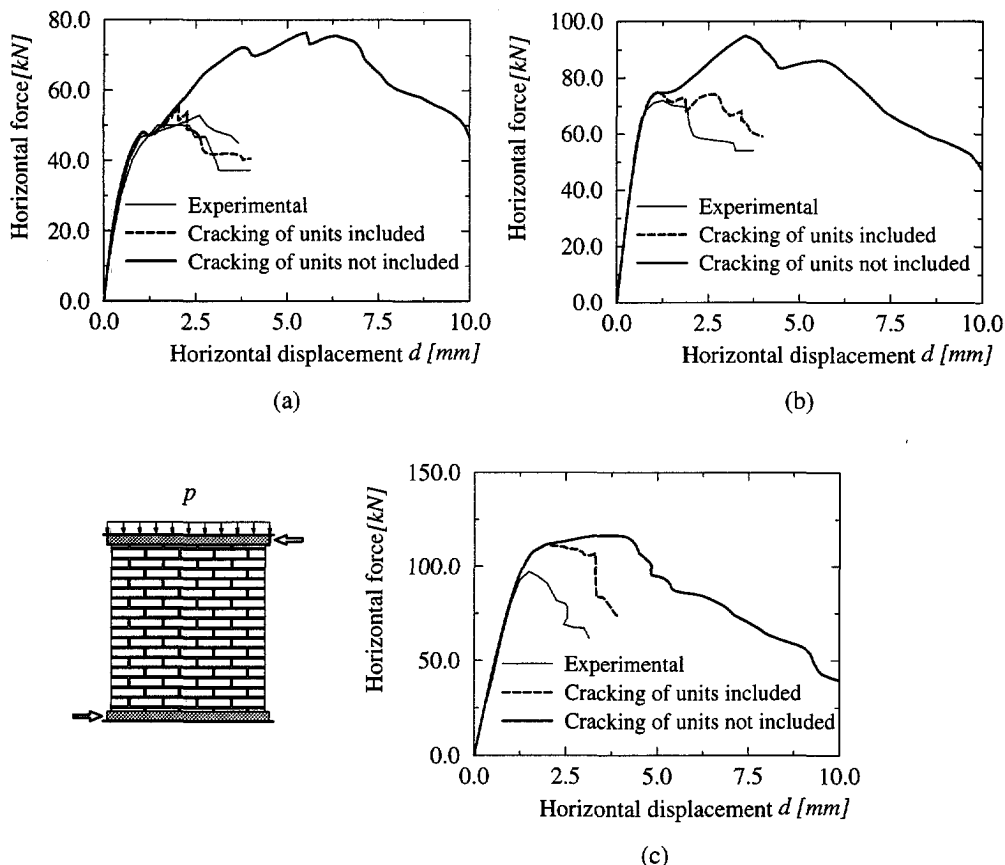


Figure 4.35 Walls JD. Influence of modeling the cracks in the units for different initial vertical loads  $p$ : (a)  $0.30 \text{ [N/mm}^2\text{]}$ ; (b)  $1.21 \text{ [N/mm}^2\text{]}$ ; (c)  $2.12 \text{ [N/mm}^2\text{]}$ .

head and bed joints are active throughout the analyses, as some shear locking in the bed joints is present due to bending of the units. This leads to a more "continuous" vertical stress distribution at the supports which delays compressive failure. Finally, when the compressed toes crush, a collapse mechanism is formed and a descending branch is obtained in the load-displacement diagram.

It was observed in the analyses that the cracks start indeed to open in pure mode I but, when the cracks progress across the units, also the misalignment between the potential cracks and the direction of principal stresses increases. A practical solution for this problem is not simple and, presently, is not envisaged but a better modeling should affect only marginally the results shown in this study. A novel solution which might be applicable to this type of problems is the consideration of finite elements capable of including strong discontinuities via jump functions, see e.g. Simo *et al.* (1993) and Oliver (1995).

The above results indicate that, in real practice, potential cracks in the units must always be included in a micro-modeling strategy to ensure that the correct behavior of masonry structures is predicted.

#### 4.4.2 Modeling compressive failure

In this study compressive failure of masonry is modeled via the interface elements. In preceding analyses, see Lourenço and Rots (1993), the compressive failure was modeled via Von Mises plasticity for the continuum elements. The idea of modeling compressive failure of masonry in the interface arose as a process to model diagonal cracking in the units by limiting the shear stresses in the interface. Experimental results in rock joints subjected to high confining stresses show some deviation from the usual linear Coulomb friction model to a parabolic Mohr failure envelope, see e.g. Hoek (1983). The proposed elliptical cap can easily include all these phenomena. It is also conceptually attractive and numerically more robust to lump all damage in the interface elements.

For the walls J4D and J5D (without opening) analyzed previously, a comparison between modeling the compressive failure in the brick, with the Von Mises yield criterion, and in the interface, via the elliptical cap, is given in Figure 4.36 for different cap fittings. Both models are of the type hardening/ideal plasticity because softening would lead to localization of deformation and debatable results. Potential cracks in the bricks are not included.

Figure 4.36b shows the caps used in comparison with the ultimate Mohr-circle in compression, which should be applicable if masonry was a homogeneous material. Here  $C_{ss}$  controls the shape of the cap, cf. eq. (4.19). If the cap is fitted to approximate the ultimate Mohr-circle in compression, i.e.  $C_{ss} = 4$ , similar results are obtained for both types of modeling. The above value of  $C_{ss}$  leads to a fictitious shear strength  $\tau_u$  of the cap mode, i.e. the intersection of the cap with the shear stress axis, equal to half of the masonry strength  $f_m$ . In the present study, a higher value  $C_{ss} = 9$ , i.e.  $\tau_u$  equals one-third of the  $f_m$ , was adopted to further limit the shear strength, because the cap aims at

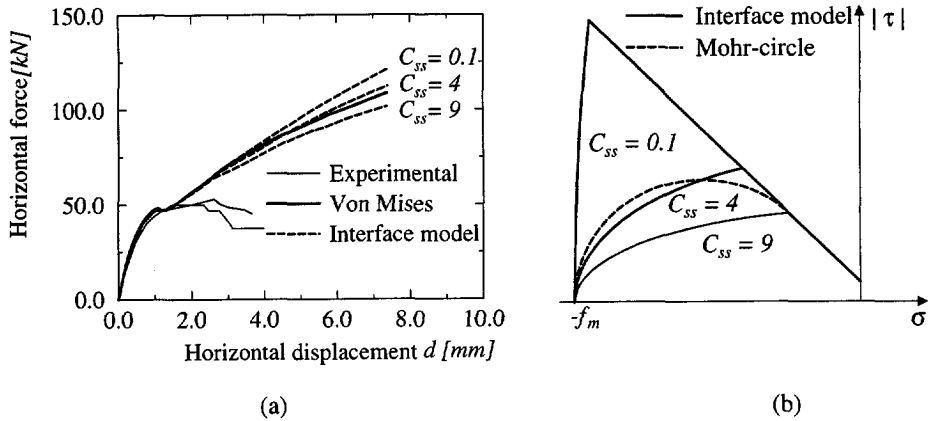


Figure 4.36 Walls J4D and J5D (without opening). Comparison between Von Mises for the continuum and compressive cap for the interface (softening in compression not included): (a) load - displacement diagram; (b) compression part of the composite interface model.

describing also some transverse cracking in the unit.

Another interesting result from Figure 4.36a is the demonstration of the importance of compressive softening to reproduce the shear walls behavior. In the absence of (compressive) softening, the strength of the wall builds-up after opening of the diagonal cracks (small unloading in Figure 4.36a at a horizontal displacement  $d \approx 1.0$  [mm]) with an enormous overprediction of the collapse load.

#### 4.4.3 Influence of dilatancy

The dilatancy angle  $\psi$  measures the uplift upon shearing. It was shown in Chapter 2 that the dilatancy angle tends to zero with increasing plastic shear slipping or increasing normal confining pressure. These phenomena occur often combined, particularly in confined masonry, because shear slip with dilatancy necessarily induces normal compressive stresses. It was discussed earlier that it is expected that the combined action of these two factors will produce a fast degradation of the dilatancy. For this reason and to avoid the introduction of at least, two additional material parameters in the material model, viz. the initial dilatancy angle and some form of dependency on the normal stress level, the dilatancy angle  $\psi$  has been taken equal to zero in the analyses carried out in this Chapter. This means that one unit can slide over the other without producing any vertical displacement and should affect only marginally the results. The comparison with experimental results seems to confirm this assumption and further discussion about this issue is given in Section 5.3.

The crucial role of the dilatancy angle for the analysis of masonry structures was recently pointed out by Lourenço and Rots (1993) and Rots in CUR (1994). Here, the results of two additional analyses for the shear walls are presented. The dilatancy angle,

measured by  $\tan \psi = 0.4$ , is changed to  $22^\circ$  while the other material parameters are kept constant. Figure 4.37 shows the comparison between the load-displacement diagrams of the new and previous analyses with  $\tan \psi = 0.0$ . The influence of the dilatancy is extremely large. In the case of  $\tan \psi = 0.4$ , the failure load is 1.5 times larger for the shear walls with an opening and 2.5 times larger for the shear walls without an opening. These large increases in strength are easily explained by the confinement of the walls. The boundaries are kept horizontal in such a way that any vertical displacement is prevented. This generates high normal stresses and high shear stresses upon shearing of the units which lead to almost complete locking of the units between the joints and a very

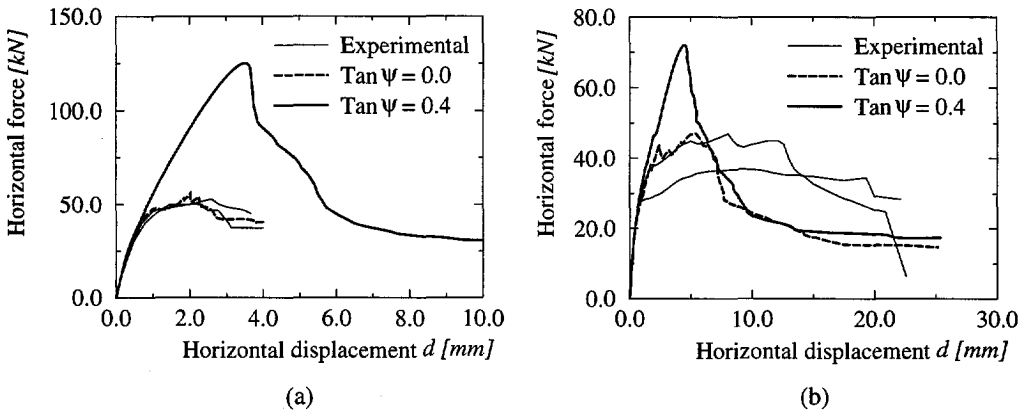


Figure 4.37 Influence of the dilatancy angle in the structural response: (a) J4D and J5D walls (without opening); (b) JG walls (with opening).

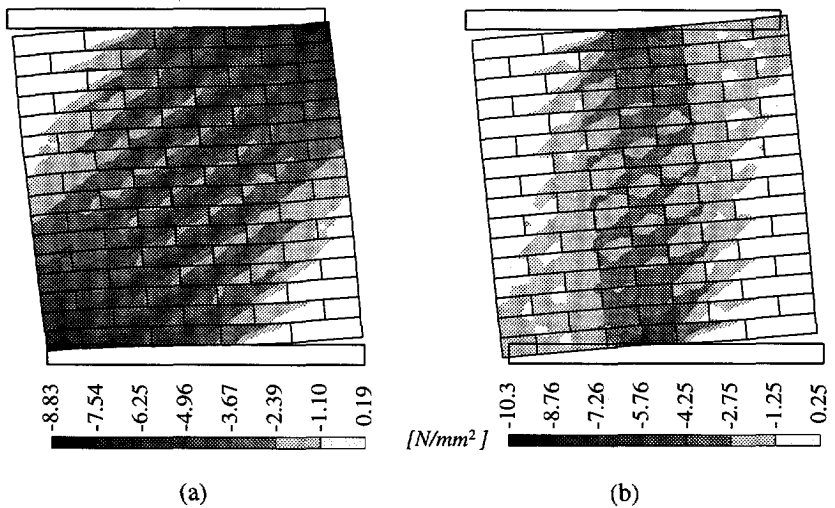


Figure 4.38 Results with  $\tan \psi = 0.4$  for walls J4D and J5D. Minimum principal stresses at a displacement of (a) 3.5 [mm] (peak) and (b) 6.0 [mm].

stiff response. The results for the walls without opening are most interesting because the possibilities of the material to “escape” from confinement are minimal and locking is so severe that diagonal cracking is not predicted at all, see Figure 4.38 and compare with Figure 4.21. Only compressive softening governs failure and, given that the stress distribution is, in essence, continuous, an impressive increase of 150 % in strength is found. For the JG walls, the presence of the opening leads to weaker constraints of the top and bottom boundaries. The failure mechanism is similar to the mechanism found in the case of  $\tan \psi = 0$ , see Figure 4.27, with four rigid blocks connected by hinges. Failure, which is governed by compressive softening, occurs at a much later stage due to shear locking of the diagonal cracks in the joints and an increase of 50 % in strength is found. After an horizontal displacement  $d = 7.5$  [mm] the solutions with  $\tan \psi = 0$  and  $\tan \psi = 0.4$  are similar because the residual compressive strength controls the response.

These results demonstrate the importance of the dilatancy angle to predict the behavior of masonry structures with a micro-model. For practical purposes, it is recommended to adopt a value of  $\tan \psi$  equal to zero.

#### 4.4.4 Mesh sensitivity of the composite interface model

In the analyses given in Section 4.3 each unit was modeled with  $4 \times 2$  quadratic plane stress elements. The units were bonded together by the necessary number of quadratic line interface elements. The mesh sensitivity of the composite interface model is evaluated next with additional numerical analyses, in which each unit is modeled with  $8 \times 4$  elements. This leads to 4 times as many continuum elements and 2 times as many interface elements.

The examples of the JG shear wall (with opening) and the deep beam described in the previous Section are considered. As shown in Figure 4.39 no significant differences are found upon mesh refinement, both in the collapse load and in the load-

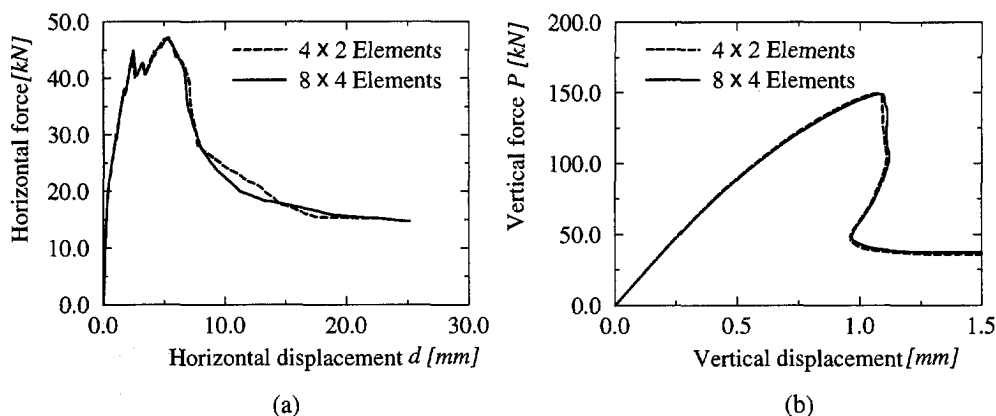


Figure 4.39 Mesh (in)sensitivity for two discretizations. Load-displacement diagrams for: (a) JG wall (with opening); (b) deep beam.

displacement diagram used to characterize the behavior of the structure. It is striking that snap-backs and snap-throughs almost coincide in both analyses, which only confirms the physical nature of these unloads. The composite interface model can be considered mesh insensitive.

#### 4.5 Summary

A micro-modeling strategy for masonry has been presented, in which the units are discretized with continuum elements and the joints are discretized with interface elements. A composite interface model that includes softening for tension, shear and compression has been developed. The model is implemented in an accurate and robust algorithm. The fully implicit Euler backward return mapping is solved with a Newton-Raphson technique for all modes of the cap model, including the corners. Tangent operators, consistent with the integration algorithm are derived for all the modes of the cap model. Isotropic coupling is assumed between tensile softening and decohesion.

Validation of the model against experiments carried out in shear walls and a deep beam was successful and provided additional knowledge about the behavior of masonry structures. The model is able to reproduce the complete path of the structures up to and beyond peak until total degradation of strength without numerical difficulties.

The crucial roles of the dilatancy angle, compressive softening and cracking of the units in the analysis of masonry structures are demonstrated. It is also shown that the proposed composite interface model is mesh insensitive.



## 5. FROM MICRO TO MACRO: HOMOGENIZATION TECHNIQUES

Composite materials consist of two or more different constituent materials that form regions large enough to be regarded as continua and which are usually bonded together by an interface. Many natural and artificial materials are immediately recognized to be of this nature, e.g. laminated composites (as used in the aerospace and tire industry), alloys, porous media, cracked media (as jointed rock masses), masonry, laminated wood and many other. However, several composite materials are normally assumed to be homogeneous. This is the case of concrete, even if at a meso-level aggregates and matrix are already recognizable, or metals, which are in fact polycrystalline aggregates.

The existence of randomly distributed constituents was one of the first problems to be discussed by researchers, see Paul (1960), Hashin and Shtrikman (1962) and Hill (1963). The Hashin-Shtrikman bounds for the elastic characteristics of composites were derived from a variational principle and enjoy some popularity up to present. The bounds are, however, only valid for arbitrary statistically isotropic phase geometries, see Figure 5.1. An additional condition for the practical use of these bounds is that the constituents stiffness ratios are “close” to the unitary value, see Hashin and Shtrikman (1962) and Watt and O’Connell (1980). They cannot obviously provide good estimates for extreme constituent stiffness ratios, such as one rigid phase or an empty phase (porous or cracked media), which precludes inelastic behavior.

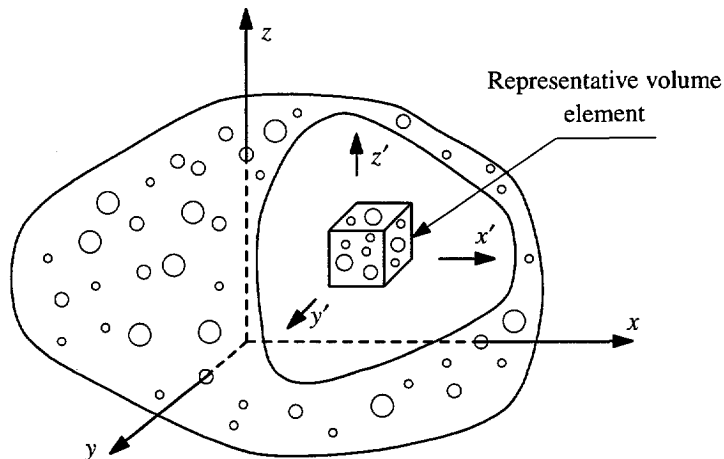


Figure 5.1 Representative volume element in a composite body.

The basis underlying the above approach is however important. It is only natural to regard any composite as a homogeneous material, provided that the structural size is substantially larger than the size of the inhomogeneities. Masonry is a composite

material made of units and mortar, normally arranged in a periodic way. In Chapter 4 it was shown that, by using the material properties and actual geometry of both components, it is possible to numerically reproduce the behavior of masonry structures. The limitation is that, even a simplified micro-modeling strategy as the one presented becomes impractical in case of real masonry structures comprising a large number of units. The alternative is to describe the composite behavior in terms of macro or average stresses and strains so that masonry can be assumed to be a homogeneous material. This problem can be approached, basically, from two directions. A possible direction is to gather, collate and interpret extensive experimental data and, ultimately, manipulate it in the form of master curves in terms of nondimensionable variables. One step further can be, eventually, carried out and seek empirical analytical expressions that seem to fit the experimental data. This approach is certainly necessary because the knowledge about the composite behavior of masonry is extremely scarce. The results are however limited to the conditions under which the data are obtained. New materials and/or application of a well known material in different loading conditions might compel a different set of costly experimental programs. Here, a more fundamental approach is sought, one that grants us a predictive capability. In Section 5.1, the use of approximate homogenization techniques is discussed. It is shown how to obtain an anisotropic macro-constitutive law from the micro-constitutive laws and geometry of the composite, in such a way that the macro-constitutive law is not actually implemented, or even known at all. The response of the composite can only be obtained a posteriori for given load paths. In Section 5.2 the methodology described in Section 5.1 is used to determine the elastic characteristics of masonry and, in Section 5.3, the micro-model developed in Chapter 4 is used to predict the uniaxial tensile behavior of masonry. The objective of these two Sections is to obtain material data to feed macro-models as the one developed in Chapter 6. This is akin to the act of carrying out experiments in the composite material subjected to uniform loading conditions. The difference between the objectives of Section 5.1 and Sections 5.2/5.3 is significant. In the former case the objective is the macro-model, which uses as input data the micro-parameters and the non-discretized geometry, whereas in the latter the objective is to obtain macro-parameters as input data of an independent macro-model.

## **5.1 The elastoplastic homogenization of layered materials**

The techniques of homogenization are currently becoming increasingly popular among the masonry community. A method that would permit to establish constitutive relations in terms of averaged stresses and strains from the constitutive relations of the individual components would represent a major step forward in masonry modeling. This would mean that, a change in the geometry of the components would not imply different material models or costly experiments, which is relevant because different unit dimensions and mortar thicknesses are normally used. The reverse side is that quite often the properties of the constituents are unknown, or the properties of the constituents in the

composite differ from their bulk properties, and have to be determined from the properties of the composite by inverse fitting.

In Anthoine (1995) and Urbanski *et al.* (1995) the homogenization theory for periodic media is rigorously applied to the analysis of the *basic cell*, i.e. a periodic pattern associated to some frame of reference, see Figure 5.2. The objective of these authors seems to be, however, the determination of the macro-parameters and not, actually, the use of the theory in large scale structures. In fact, the rigorous application of homogenization theory for the nonlinear behavior of the complex masonry basic cell implies solving the problem for all possible macroscopic loading histories, since the superposition principle does not apply anymore. Thus, the complete determination of the homogenized constitutive law requires an infinite number of computations. Keeping in mind the objective of large scale analyses most authors, see e.g. Pande *et al.* (1989), Papa (1990) and Pietruszczak and Niu (1992), have used these techniques in an approximate manner. The homogenization has generally been performed in two steps, head and bed joints being introduced successively. In this case masonry can be assumed to be a layered material, which simplifies the problem significantly. In the present study a novel matrix formulation capable of representing the elastic and inelastic behavior of such a solid is aimed at. Here, only a standard continuum is considered, while the extension to a micro-polar (Cosserat) continuum is given in Lourenço (1995a). The benefits of a matrix formulation comprise not only a much clearer implementation of linear elastic homogenization algorithms but also a relatively simple extension to nonlinear behavior. This represents a new perspective of the work developed by other authors. In Pande *et al.* (1989) only the case of linear elastic behavior is considered and in Pietruszczak and Niu (1992) the process of homogenization itself is approximated.

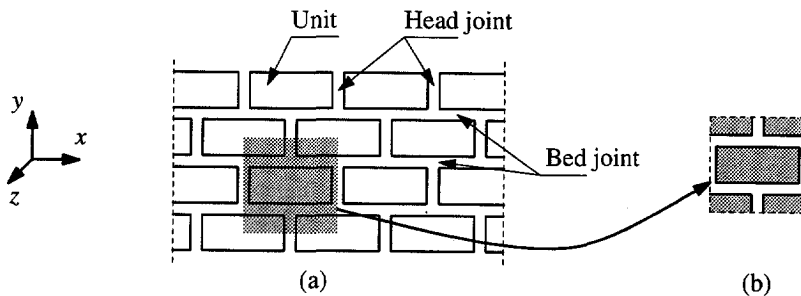
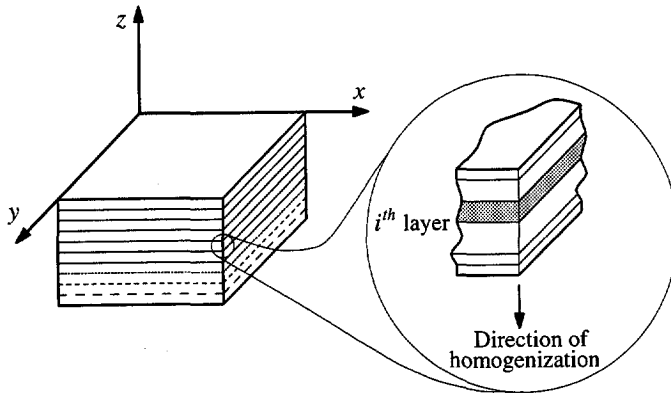


Figure 5.2 The definition of the masonry *basic cell*: (a) masonry sample with running bond; (b) basic cell.

Attention is thus given to the special case of layered composites, the only restriction being imposed on the periodicity of the material along the structure, see Figure 5.3, which is usually fulfilled in numerous engineering applications. Examples include aerospace industries, laminated wood, stratified or sedimentary soils, stratified rock masses, etc.



*Figure 5.3* The periodic layered composite material and the structure of the basic cell.

### 5.1.1 Elastic formulation

Several mathematical techniques of different complexity are available to solve problems of homogenization, see e.g. Sanchez-Palencia (1980, 1987), but for periodic structures the method of *asymptotic analysis* has gained some popularity, see also Bakhvalov and Panasenko (1989). The extension of this method to inelastic behavior is however not simple. Knowledge of the actual macro or homogenized constitutive law requires knowledge of an infinite number of internal variables, namely the whole set of inelastic micro-strains, Suquet (1985). Therefore, a simplified model with piecewise constant inelastic strains will be proposed in this study. The asymptotic expansion of the displacement and stress fields is used for example in Paipetis *et al.* (1993) and Papa (1990) to obtain the elastic stiffness matrix of the homogenized continuum. The solution is however presented in an explicit form for each coefficient of the stiffness matrix. Other authors, e.g. Salamon (1968) and Gerrard (1982), used an engineering approach based on the solution of a complete boundary value problem for the basic cell. Again, explicit formulae were obtained, in which the elastic characteristics, viz. Young's moduli and Poisson's ratios, of the homogenized continuum are written as a function of the elastic characteristics of the individual components. These solutions are not practical for computational implementation and almost preclude the use of homogenization techniques in the presence of inelastic behavior. For this reason, the approach proposed by Salamon (1968), which originated in the field of rock mechanics, will be revisited and recast in a matrix form. This novel formulation makes it possible to handle inelastic material behavior with little effort.

The layered material shown in Figure 5.3 is built from a periodic system of parallel layers, each of which is assumed to be an isotropic elastic material. This assumption is by no means necessary, see Lourenço (1995a), but it will be adopted here for simplicity.

The layers are aligned perpendicular to a given direction, e.g. the  $z$  axis. The basic cell, in the form of a representative prism, is shown in Figure 5.4. In the homogenization direction  $z$ , the dimension of the prism is defined by the periodicity of the structure and, in the other two directions, a unitary length can be assumed.

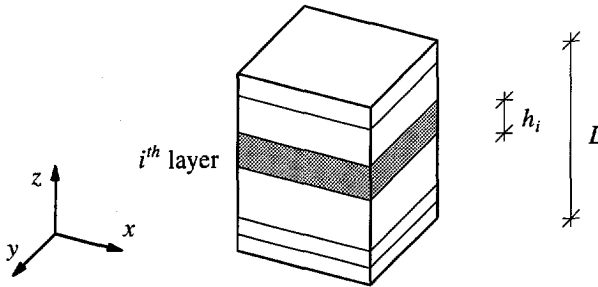


Figure 5.4 Basic cell. Representative volume prism for system of parallel layers.

It is assumed that the system of layers remains continuous after deformation and that no relative displacement takes place in the interfaces between layers. The latter assumption simplifies the problem to a great extent but, at least mathematically, discontinuities in the displacements field can be incorporated under the assumption of linear elastic materials, Bakhvalov and Panasenko (1989). The prism representative of the composite material is further assumed to be subjected to homogeneous distributions of stresses and strains, meaning that the volume of the prism must be sufficiently small to make negligible, in the equivalent medium, the variation of stresses and strains across it<sup>†</sup>. The objective is to obtain a macro or homogenized constitutive relation between homogenized stresses  $\sigma$  and homogenized strains  $\epsilon$ ,

$$\sigma = \mathbf{D}^h \epsilon \quad (5.1)$$

where

$$\begin{aligned} \sigma &= \{ \sigma_x \quad \sigma_y \quad \sigma_z \quad \tau_{xy} \quad \tau_{yz} \quad \tau_{xz} \}^T \\ \epsilon &= \{ \epsilon_x \quad \epsilon_y \quad \epsilon_z \quad \gamma_{xy} \quad \gamma_{yz} \quad \gamma_{xz} \}^T \end{aligned} \quad (5.2)$$

Here,  $\mathbf{D}^h$  is the homogenized stiffness matrix, which will be obtained from the micro-constitutive relations. In order to establish the macro-constitutive stress-strain relation, the components of the stress and strain tensors, respectively  $\sigma_j$  and  $\epsilon_j$ , are defined by the integral over the representative volume as

<sup>†</sup> Homogenization also applies in the case of a “not so small” basic cell if the macroscopic stresses induced by the structural loads vary slowly within the structure or if the characteristics of the basic cell change slowly within the structure, i.e. if adjacent cells are almost identical.

$$\begin{aligned}\sigma_j &= \frac{1}{V} \int_V (\sigma_j)_i dV = \frac{1}{V} \sum_i \int_{V_i} (\sigma_j)_i dV \\ \varepsilon_j &= \frac{1}{V} \int_V (\varepsilon_j)_i dV = \frac{1}{V} \sum_i \int_{V_i} (\varepsilon_j)_i dV\end{aligned}\quad (5.3)$$

where  $i$  is the layer number. Auxiliary stresses ( $t_x$ ,  $t_y$  and  $t_{xy}$ ) and auxiliary strains ( $e_z$ ,  $e_{yz}$  and  $e_{xz}$ ) are introduced as a deviation measure of the  $i^{\text{th}}$  layer stress/strain state from the averaged values. Under the given assumptions, the stress components for the  $i^{\text{th}}$  layer read

$$\begin{aligned}\sigma_{xi} &= \sigma_x + t_{xi} & \sigma_{yi} &= \sigma_y + t_{yi} & \sigma_{zi} &= \sigma_z \\ \sigma_{xyi} &= \sigma_{xy} + t_{xyi} & \sigma_{yzi} &= \sigma_{yz} & \sigma_{xzi} &= \sigma_{xz}\end{aligned}\quad (5.4)$$

and the strain components for the  $i^{\text{th}}$  layer read

$$\begin{aligned}\varepsilon_{xi} &= \varepsilon_x & \varepsilon_{yi} &= \varepsilon_y & \varepsilon_{zi} &= \varepsilon_z + e_{zi} \\ \varepsilon_{xyi} &= \varepsilon_{xy} & \varepsilon_{yzi} &= \varepsilon_{yz} + e_{yzi} & \varepsilon_{xzi} &= \varepsilon_{xz} + e_{xzi}\end{aligned}\quad (5.5)$$

Now let the thickness of the  $i^{\text{th}}$  layer be  $h_i$  and the normalized thickness  $p_i$  be defined as

$$p_i = \frac{h_i}{L} \quad (5.6)$$

where  $L$  is the length of the representative prism in the  $z$  direction. Substitution of eqs. (5.4) in eqs. (5.3)<sub>1</sub> yields the following conditions for the auxiliary stress components:

$$\sum p_i t_{xi} = 0 \quad \sum p_i t_{yi} = 0 \quad \sum p_i t_{xyi} = 0 \quad (5.7)$$

Similarly, from eqs. (5.5) and eqs. (5.3)<sub>2</sub>, the auxiliary strain components are constrained by

$$\sum p_i e_{zi} = 0 \quad \sum p_i e_{yzi} = 0 \quad \sum p_i e_{xzi} = 0 \quad (5.8)$$

Note that, if the conditions given in the above equations are fulfilled, then the strain energy stored in the representative prism and the equivalent prism are the same, i.e.,

$$\frac{1}{2} \sum_i \int_{V_i} \sigma_i^T \varepsilon_i dV = \frac{1}{2} \sigma^T \varepsilon V \quad (5.9)$$

To obtain a matrix formulation of the homogenization theory, the vector of auxiliary stresses  $\mathbf{t}_i$  and the vector of auxiliary strains  $\mathbf{e}_i$  are defined as

$$\begin{aligned}\mathbf{t}_i &= \{ t_{xi} \quad t_{yi} \quad t_{zi} \quad t_{xyi} \quad t_{yzi} \quad t_{xzi} \}^T \\ \mathbf{e}_i &= \{ e_{xi} \quad e_{yi} \quad e_{zi} \quad e_{xyi} \quad e_{yzi} \quad e_{xzi} \}^T\end{aligned}\quad (5.10)$$

It is noted that half of the components of the auxiliary stress and strain vectors are zero, see eqs. (5.4,5.5). The non-zero components are assembled in a vector of unknowns  $\mathbf{x}_i$ , defined as

$$\mathbf{x}_i = \mathbf{P}_t \mathbf{t}_i + \mathbf{P}_e \mathbf{e}_i \quad (5.11)$$

where the projection matrix into the stress space  $\mathbf{P}_t$ , and the projection matrix into the strain space  $\mathbf{P}_e$  read

$$\begin{aligned} \mathbf{P}_t &= \text{diag}\{ 1 \ 1 \ 0 \ 1 \ 0 \ 0 \} \\ \mathbf{P}_e &= \text{diag}\{ 0 \ 0 \ 1 \ 0 \ 1 \ 1 \} \end{aligned} \quad (5.12)$$

for homogenization along the  $z$  axis. In a similar fashion, these matrices read

$$\begin{aligned} \mathbf{P}_t &= \text{diag}\{ 0 \ 1 \ 1 \ 0 \ 1 \ 0 \} \\ \mathbf{P}_e &= \text{diag}\{ 1 \ 0 \ 0 \ 1 \ 0 \ 1 \} \end{aligned} \quad (5.13)$$

for homogenization along the  $x$  axis and

$$\begin{aligned} \mathbf{P}_t &= \text{diag}\{ 1 \ 0 \ 1 \ 0 \ 0 \ 1 \} \\ \mathbf{P}_e &= \text{diag}\{ 0 \ 1 \ 0 \ 1 \ 1 \ 0 \} \end{aligned} \quad (5.14)$$

for homogenization along the  $y$  axis. Now, the auxiliary stresses and strains can be redefined as

$$\mathbf{t}_i = \mathbf{P}_t \mathbf{x}_i \quad \mathbf{e}_i = \mathbf{P}_e \mathbf{x}_i \quad (5.15)$$

The stresses  $\sigma_i$  and strains  $\varepsilon_i$  in the  $i^{\text{th}}$  layer read, cf. eqs. (5.4,5.5),

$$\sigma_i = \sigma + \mathbf{t}_i \quad \varepsilon_i = \varepsilon + \mathbf{e}_i \quad (5.16)$$

and the linear elastic stress-strain relation, for the  $i^{\text{th}}$  layer, reads

$$\sigma_i = \mathbf{D}_i \varepsilon_i \quad (5.17)$$

where the elastic stiffness matrix  $\mathbf{D}_i$ , under the assumption of isotropic behavior, reads

$$\mathbf{D}_i = \frac{E_i}{(1 + \nu_i)(1 - 2\nu_i)} \begin{bmatrix} 1 - \nu_i & \nu_i & \nu_i & 0 & 0 & 0 \\ \nu_i & 1 - \nu_i & \nu_i & 0 & 0 & 0 \\ \nu_i & \nu_i & 1 - \nu_i & 0 & 0 & 0 \\ 0 & 0 & 0 & 1/2(1 - 2\nu_i) & 0 & 0 \\ 0 & 0 & 0 & 0 & 1/2(1 - 2\nu_i) & 0 \\ 0 & 0 & 0 & 0 & 0 & 1/2(1 - 2\nu_i) \end{bmatrix} \quad (5.18)$$

Inserting eqs. (5.15,5.16) in eq. (5.17), algebraic manipulation yields

$$\mathbf{x}_i = (\mathbf{P}_i - \mathbf{D}_i \mathbf{P}_e)^{-1} (\mathbf{D}_i \boldsymbol{\varepsilon} - \boldsymbol{\sigma}) \quad (5.19)$$

which, using eqs. (5.7,5.8), can be recast as

$$\mathbf{0} = \sum_i p_i \mathbf{x}_i = \sum_i \left[ p_i (\mathbf{P}_i - \mathbf{D}_i \mathbf{P}_e)^{-1} (\mathbf{D}_i \boldsymbol{\varepsilon} - \boldsymbol{\sigma}) \right] \quad (5.20)$$

This equation yields, finally, the relation between averaged stresses and strains and the homogenized linear elastic stiffness matrix  $\mathbf{D}^h$  as

$$\mathbf{D}^h = \left[ \sum_i p_i (\mathbf{P}_i - \mathbf{D}_i \mathbf{P}_e)^{-1} \right]^{-1} \sum_i p_i (\mathbf{P}_i - \mathbf{D}_i \mathbf{P}_e)^{-1} \mathbf{D}_i \quad (5.21)$$

Once the averaged stresses and strains are known, also the stresses and strains in the  $i^{\text{th}}$  layer can be calculated. Using eq. (5.19), the vector of unknowns  $\mathbf{x}_i$  can be calculated. Algebraic manipulation of eqs. (5.15,5.16) yields

$$\begin{aligned} \boldsymbol{\sigma}_i &= \mathbf{T}_{ii} \boldsymbol{\sigma} & \text{with } \mathbf{T}_{ii} &= \mathbf{I} + \mathbf{P}_i (\mathbf{P}_i - \mathbf{D}_i \mathbf{P}_e)^{-1} (\mathbf{D}_i (\mathbf{D}^h)^{-1} - \mathbf{I}) \\ \boldsymbol{\varepsilon}_i &= \mathbf{T}_{ei} \boldsymbol{\varepsilon} & \text{with } \mathbf{T}_{ei} &= \mathbf{I} + \mathbf{P}_e (\mathbf{P}_i - \mathbf{D}_i \mathbf{P}_e)^{-1} (\mathbf{D}_i - \mathbf{D}^h) \end{aligned} \quad (5.22)$$

where  $\mathbf{I}$  is the identity matrix.

### 5.1.2 Elastoplastic formulation

In the present study, only application to  $J_2$ -plasticity is considered, while an extension of the method for other yield criteria is discussed in Lourenço (1995a). For  $J_2$ -plasticity the yield function reads

$$f = (3/2 \boldsymbol{\sigma}^T \mathbf{P} \boldsymbol{\sigma})^{1/2} - \bar{\sigma}(\kappa) \quad (5.23)$$

where the projection matrix  $\mathbf{P}$  reads

$$\mathbf{P} = \begin{bmatrix} 2/3 & -1/3 & -1/3 & 0 & 0 & 0 \\ -1/3 & 2/3 & -1/3 & 0 & 0 & 0 \\ -1/3 & -1/3 & 2/3 & 0 & 0 & 0 \\ 0 & 0 & 0 & 2 & 0 & 0 \\ 0 & 0 & 0 & 0 & 2 & 0 \\ 0 & 0 & 0 & 0 & 0 & 2 \end{bmatrix} \quad (5.24)$$

The (associated) flow rule is written in a standard fashion as

$$\dot{\boldsymbol{\varepsilon}}^p = \dot{\lambda} \frac{\partial f}{\partial \boldsymbol{\sigma}} = \frac{3/2 \dot{\lambda} \mathbf{P} \boldsymbol{\sigma}}{\sqrt{3/2} \boldsymbol{\sigma}^T \mathbf{P} \boldsymbol{\sigma}} \quad (5.25)$$

and, under the assumption of strain hardening, eq. (3.30) yields

$$\dot{\kappa} = \dot{\lambda} \quad (5.26)$$

The integration of the standard plasticity constitutive equations is detailed in Chapter 3. The stress field at a stage  $n + 1$  is computed once the strain field is known. The problem is *strain driven* in the sense that the total strain  $\boldsymbol{\varepsilon}$  is trivially updated according to the exact formula

$$\boldsymbol{\varepsilon}_{n+1} = \boldsymbol{\varepsilon}_n + \Delta \boldsymbol{\varepsilon}_{n+1} \quad (5.27)$$

It remains to update the plastic strains and the hardening parameter. These quantities are determined by integration of the flow rule and hardening law over the step  $n \rightarrow n + 1$ . For standard plasticity, it is straightforward to obtain the update of the stress vector  $\boldsymbol{\sigma}_{n+1}$ , cf. eq. (3.39)<sub>1</sub>, as

$$\boldsymbol{\sigma}_{n+1} = \mathbf{A} \boldsymbol{\sigma}^{trial} \quad (5.28)$$

where the mapping matrix  $\mathbf{A}$  reads

$$\mathbf{A} = \left[ \mathbf{I} + \frac{3/2 \Delta \lambda_{n+1}}{\bar{\sigma}_{n+1}} \mathbf{D} \mathbf{P} \right]^{-1} \quad (5.29)$$

Application of the standard algorithm to the homogenized continuum results in increasing difficulties. The homogenized material consists of several layers with individual elastic and inelastic properties. As given in eqs. (5.4,5.5), different stresses and strains are obtained for each layer, which are again different from the average stresses and strains. Due to this feature and the fact that inelastic behavior is considered for the layers, it is not possible to calculate immediately the strain increments for each layer from a given average strain increment. This precludes the use of a standard plasticity algorithm due to the fact that the algorithm is strain driven. An *equivalent return mapping*

must be carried out, in which all the layers are considered simultaneously i.e., a return mapping in terms of average strains and average stresses. If the individual layers are considered, eq. (5.28) for the  $i^{\text{th}}$  layer must be rewritten as

$$\sigma_{n+1,i} = \mathbf{A}_i \sigma_i^{\text{trial}} \quad (5.30)$$

with

$$\sigma_i^{\text{trial}} = \sigma_{n,i} + \mathbf{D}_i \Delta \varepsilon_{n+1,i} \quad (5.31)$$

where the mapping matrix,  $\mathbf{A}_i$ , is a function of  $\Delta \lambda_{n+1,i}$ . If all the layers are now considered simultaneously, the question arises whether one particular layer is elastic or plastic, but this is considered trivial in the proposed algorithm. In fact, in case of an elastic layer, eq. (5.30) remains valid if the mapping matrix is equal to the identity matrix (i.e.  $\Delta \lambda_{n+1,i} = 0$ ),

$$\mathbf{A}_i = \mathbf{I} \quad (\text{if layer is elastic}) \quad (5.32)$$

Inserting eqs. (5.16) in eq. (5.30), the latter can be rewritten in terms of average stresses and strains ( $\sigma$  and  $\varepsilon$ ) and auxiliary stresses and strains of the  $i^{\text{th}}$  layer ( $\mathbf{t}_i$  and  $\mathbf{e}_i$ ) at stage  $n + 1$  as

$$\sigma_{n+1} + \mathbf{t}_{n+1,i} = \mathbf{A}_i (\bar{\sigma}_i^{\text{trial}} + \mathbf{D}_i \Delta \varepsilon_{n+1,i}) \quad (5.33)$$

where the modified trial stress  $\bar{\sigma}_i^{\text{trial}}$  for the  $i^{\text{th}}$  layer is defined as

$$\bar{\sigma}_i^{\text{trial}} = \sigma_{n,i} + \mathbf{D}_i \Delta \varepsilon_{n+1,i} \quad (5.34)$$

(note that the average strain is included in the expression instead of the strain of the  $i^{\text{th}}$  layer). Inserting eqs. (5.15) we obtain

$$\mathbf{x}_{n+1,i} = (\mathbf{P}_t - \mathbf{A}_i \mathbf{D}_i \mathbf{P}_e)^{-1} (-\sigma_{n+1} + \mathbf{A}_i \bar{\sigma}_i^{\text{trial}}) \quad (5.35)$$

which can be recast as

$$\mathbf{0} = \sum_i p_i \mathbf{x}_{n+1,i} = \sum_i p_i \left[ (\mathbf{P}_t - \mathbf{A}_i \mathbf{D}_i \mathbf{P}_e)^{-1} (-\sigma_{n+1} + \mathbf{A}_i \bar{\sigma}_i^{\text{trial}}) \right] \quad (5.36)$$

where the vector of unknowns  $\mathbf{x}_{n+1,i}$  includes now the total values of the auxiliary stresses and the incremental values of the auxiliary strains. This equation yields, finally, the update of the average stress as

$$\sigma_{n+1} = \left[ \sum_i p_i (\mathbf{P}_t - \mathbf{A}_i \mathbf{D}_i \mathbf{P}_e)^{-1} \right]^{-1} \sum_i p_i (\mathbf{P}_t - \mathbf{A}_i \mathbf{D}_i \mathbf{P}_e)^{-1} \mathbf{A}_i \bar{\sigma}_i^{\text{trial}} \quad (5.37)$$

Note that the summation is extended to *all* the layers (elastic and plastic). The return mapping procedure is now established in a standard fashion. From the average stresses it is possible to calculate the stresses in the  $i^{\text{th}}$  layer. This results from the vector of unknowns  $\mathbf{x}_{n+1}$ , as defined in eq. (5.35), and eqs. (5.15,5.16). At this point it is clear that a system of nonlinear equations in  $\Delta\lambda_{n+1}$ 's can be built:  $f_i(\Delta\lambda_{n+1,1}, \dots, \Delta\lambda_{n+1,j}) = 0, i = 1, \dots, j$ . This system has as many unknowns (and equations) as the number of plastic layers. Finally, when convergence is reached the state variables ( $\boldsymbol{\varepsilon}$ ,  $\boldsymbol{\varepsilon}^p$  and  $\kappa$ ) can be updated.

The calculation of the tangent stiffness matrix consistent with the integration algorithm results trivial. For the  $i^{\text{th}}$  layer it is possible to write, cf. eq. (3.57),

$$d\boldsymbol{\sigma}_{n+1,i} = \mathbf{D}_i^{ep} d\boldsymbol{\varepsilon}_{n+1,i} \quad (5.38)$$

The elastic stiffness matrix can, of course, be considered a special case of the tangent stiffness matrix, where  $\mathbf{D}_i^{ep}$  equals  $\mathbf{D}_i$ . The consistent tangent stiffness matrix for the homogenized material,  $(\mathbf{D}^{ep})^h$  can be obtained similarly to eq. (5.23), if the vector of unknowns  $\mathbf{x}$ , includes now the infinitesimal auxiliary stresses and strains, and reads

$$(\mathbf{D}^{ep})^h = \left[ \sum_i p_i (\mathbf{P}_t - \mathbf{D}_i^{ep} \mathbf{P}_e)^{-1} \right]^{-1} \sum_i p_i (\mathbf{P}_t - \mathbf{D}_i^{ep} \mathbf{P}_e)^{-1} \mathbf{D}_i^{ep} \quad (5.39)$$

The complete algorithm for layered homogenized continua is shown in Box 5.1. The algorithm presents some similitude with the algorithms of multisurface plasticity described in Chapter 3. The problem of solving a system of nonlinear equations with plastic multipliers as unknowns arises in both cases. The most severe consequence is that is not possible to any  $\Delta\lambda$  to become negative during the return mapping procedure. If this happens the constraint associated with that  $\Delta\lambda$  vanishes (in the present case the layer becomes elastic). The reverse problem occurs when any yield criterion is violated during the return mapping procedure. In this case an additional constraint appears (in the present case the layer becomes plastic). In the present implementation, a new constraint is removed or added, at each iteration, if a layer becomes, respectively, elastic or plastic. The nonlinear system of equations is solved with a regular Newton-Raphson method and the necessary Jacobian is calculated numerically. Note that is not particularly difficult to calculate an exact expression to the Jacobian but the result will be lengthy and cumbersome. A numerical calculation gives a much clearer code.

### 5.1.3 Validation

In the following, a few examples will be presented to assess the performance of the proposed methodology. Additional numerical examples in plane stress, plane strain and three-dimensional loading conditions can be found in Lourenço (1995a). For all the

**Box 5.1** Elastoplastic algorithm for layered homogenized continua.

- Compute elastic trial stresses. Check for plastic behavior

$$\boldsymbol{\sigma}_{n+1}^{trial} = \boldsymbol{\sigma}_n + \mathbf{D}^h \Delta \boldsymbol{\varepsilon}_{n+1}$$

For all the layers:

$$\boldsymbol{\sigma}_{n+1,i}^{trial} = \mathbf{T}_{ii} \boldsymbol{\sigma}_{n+1}^{trial}$$

$$\text{with } \mathbf{T}_{ii} = \mathbf{I} + \mathbf{P}_i (\mathbf{P}_t - \mathbf{D}_i \mathbf{P}_e)^{-1} (\mathbf{D}_i (\mathbf{D}^h)^{-1} - \mathbf{I})$$

If  $f(\boldsymbol{\sigma}_{n+1,i}, \kappa_{n,i}) > 0 \rightarrow$  Layer is plastic

If  $f(\boldsymbol{\sigma}_{n+1,i}, \kappa_{n,i}) \leq 0 \rightarrow$  Layer is elastic

If all layer are elastic, update stresses and strains  $\rightarrow$  Exit

- Calculate modified trial stresses

For all the layers:

$$\bar{\boldsymbol{\sigma}}_{n+1,i}^{trial} = \boldsymbol{\sigma}_{n,i} + \mathbf{D}_i \Delta \boldsymbol{\varepsilon}_{n+1}$$

- Consistency at stage  $n + 1$ : Solve system of nonlinear equations

$$f_i(\boldsymbol{\sigma}_{n+1,i}, \kappa_{n+1,i}) = f_i(\Delta \lambda_{n+1}' s) = 0 \text{ for all plastic layers}$$

$$\boldsymbol{\sigma}_{n+1}(\Delta \lambda_{n+1}' s) = \left[ \sum_i p_i (\mathbf{P}_t - \mathbf{A}_i \mathbf{D}_i \mathbf{P}_e)^{-1} \right]^{-1} \sum_i p_i (\mathbf{P}_t - \mathbf{A}_i \mathbf{D}_i \mathbf{P}_e)^{-1} \mathbf{A}_i \bar{\boldsymbol{\sigma}}_i^{trial}$$

For all the layers:

$$\boldsymbol{\sigma}_{n+1,i}(\Delta \lambda_{n+1}' s) = \boldsymbol{\sigma}_{n+1} + \mathbf{P}_i (\mathbf{P}_t - \mathbf{A}_i \mathbf{D}_i \mathbf{P}_e)^{-1} (-\boldsymbol{\sigma}_{n+1} + \mathbf{A}_i \bar{\boldsymbol{\sigma}}_i^{trial})$$

Update hardening parameter:  $\kappa_{n+1,i}$  (plastic layers)

Calculate  $f_i(\boldsymbol{\sigma}_{n+1,i}, \kappa_{n+1,i})$ . If a converged state is found  $\rightarrow$  Exit

If layer is plastic  $\rightarrow$  Update  $\Delta \lambda_{n+1,i}$  and calculate  $\mathbf{A}_i$

If layer is elastic  $\rightarrow \mathbf{A}_i = \mathbf{I}$

- Compute consistent elastoplastic tangent operator

$$(\mathbf{D}^{ep})^h = \left[ \sum_i p_i (\mathbf{P}_t - \mathbf{D}_i^{ep} \mathbf{P}_e)^{-1} \right]^{-1} \sum_i p_i (\mathbf{P}_t - \mathbf{D}_i^{ep} \mathbf{P}_e)^{-1} \mathbf{D}_i^{ep}$$

- **Note:** The summation  $\sum$  is extended to *all* layers

examples, a composite material built from two layers, viz. a “weak” and a “strong” layer with different elastic and inelastic behavior, is assumed, see Table 5.1 and Figure 5.5. For standard continuum, only hardening behavior is considered, whereas softening behavior will be introduced in a Cosserat continuum. The calculations have been carried out with two-dimensional homogenized plane stress quadratic elements (8-noded quads) with  $2 \times 2$  Gauss integration and three-dimensional quadratic elements (20-noded bricks) with  $3 \times 3$  Gauss integration.

Table 5.1 Elastic properties.

Material	E [ $N/mm^2$ ]	$\nu$	Volume p [%]
1	4000	0.15	25
2	20000	0.15	75

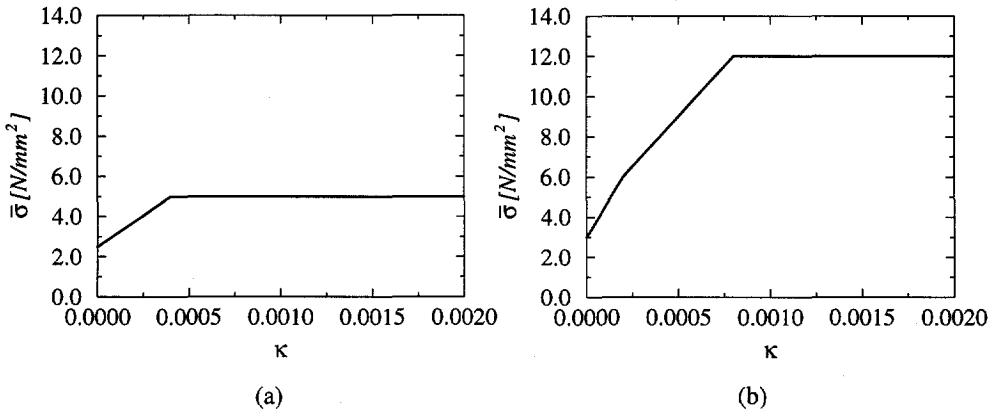


Figure 5.5 Hardening law for the two layers of the homogenized continuum: (a) material 1 - weak layer; (b) material 2 - strong layer.

#### Example 1: Cube with normal loading

The first example consists of a  $1000 \times 1000 \times 1000$  [ $mm^3$ ] cube with an applied uniform loading along the  $z$  axis, see Figure 5.6. All the faces of the cube are constrained to have the same displacement in the direction normal to the face, but in such a way that the resultant force in the  $x$  and  $y$  directions are null. This load and boundary conditions yield a uniform state of stress in both materials.

The cube can be modeled with 3D standard continuum elements but also with a single 2D (and even 1D) homogenized continuum element because the average stresses in the  $x$  and  $y$  directions are zero. Here, the 2D homogenized continuum element mentioned above was used for the calculation. Under the particular loading conditions, the assumptions made before are exact and no comparison is given between the

homogenized and 3D results (they are exactly the same). The response of the equivalent material is given in Figure 5.7 for a cycle of loading-unloading-reloading.

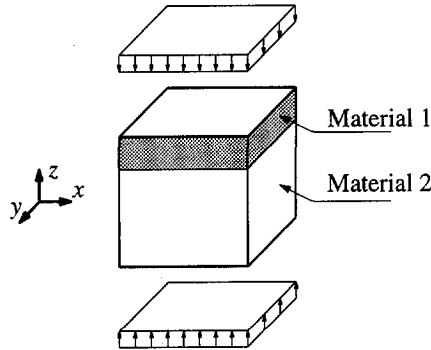


Figure 5.6 Representative volume for two-layered material. Loading along the  $z$  axis.

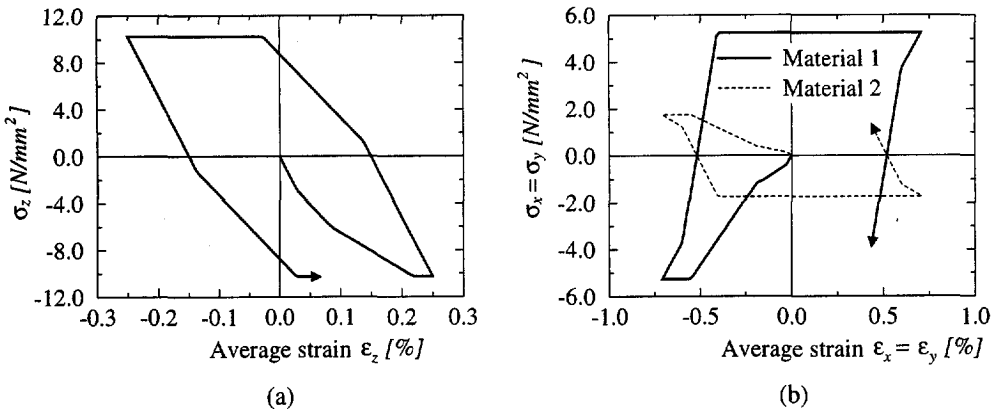


Figure 5.7 Stress - strain diagrams for homogenized material: (a) along the  $z$  axis; (b) along the  $x$  and  $y$  axes.

The most important characteristic of the response is that, even if the average state of stress is two-dimensional, the 3D effect is always present in the algorithm. It is shown that uniaxial compression in the equivalent material induces a triaxial compressive state of stress in the weak layer (Material 1) and “out-of-axis” tensile stresses in the strong layer (Material 2). The physical meaning of this behavior is evident. Such a phenomenon can be observed for example in masonry structures in uniaxial compression, in which failure occurs by splitting of the units (“the strong layer”) whereas the mortar (“the weak layer”) is subjected to a triaxial compressive state of stress. The ultimate load of the composite is, in general, substantially larger than the uniaxial compressive strength of the mortar. Another important feature of the results is the resemblance (and

difference) between Figure 5.7 and the fraction model proposed by Besseling (1958). It seems that the homogenized model is also capable of modeling the Bauschinger effect as well as anisotropic hardening, commonly observed in metals. The fraction model leads to a much easier numerical implementation under the assumption that the total strain is equal for all fractions (parallel chain) whereas the homogenized continuum comprehends simultaneously “sequential chains” (along the homogenization direction) and “parallel chains” (in the direction normal to the homogenization axis), see Figure 5.8. Another difference is that the layered homogenized continuum has a physical correspondence whereas, as stated by Besseling (1958), in the case of the fraction model “the stress-strain relations for inelastic deformation (...) are based on a mathematical rather than a physical model of deformation process of an actual material”.

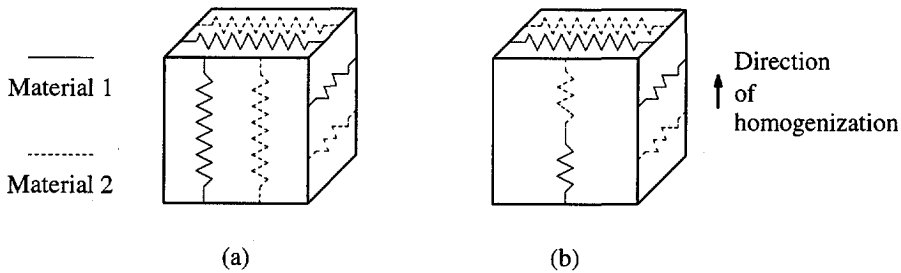


Figure 5.8 Schematic representation of fraction and homogenized models: (a) fraction model; (b) homogenized model.

Interesting applications of homogenization techniques are, thus, possible in the field of micro-mechanics. Appealing models can be considered with layered materials, for example, in the case of metals, a parallel chain of “strings” or, in the case of concrete, an assembly of brittle spheres or lattice models. For metals, as in the fraction model of Besseling (1958), such an approach is able to predict difficult phenomena as the Bauschinger effect or anisotropic hardening. It is also a well known fact that only two mechanisms of deformation (i.e. two layers), namely one elastic and the other with secondary creep, are enough to explain primary creep. For concrete, modeling the heterogeneity of the material in combination with stochastic methods might be able to predict the well-known size effect observed in experiments and a normal or asymptotic stochastic distribution of strength also found in the experiments. In particular, studies are being carried out with the aim of defining damaged media as continua with microdefects distributed in a quasi-periodic manner, see Suquet (1985).

#### Example 2: Cantilever beam with uniform vertical load

The example analyzed next is the  $2000 \times 800 \times 100$  [mm<sup>3</sup>] cantilever beam shown in Figure 5.9. The beam is subjected to a uniform load on the top and supported along the left end. Note that, with the exception of one edge, free displacements are allowed in the “out-of-plane” direction so that an average zero normal stress state is found in the

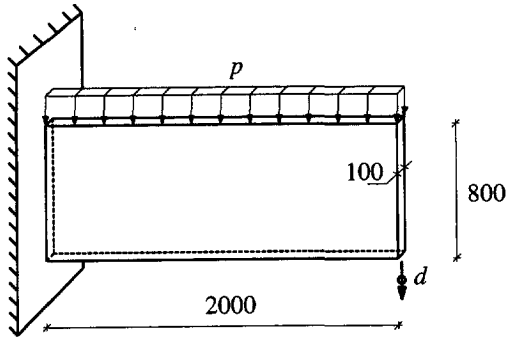


Figure 5.9 Cantilever beam with uniform vertical loading.

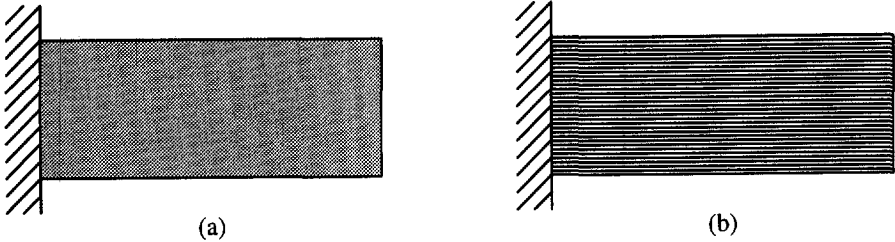


Figure 5.10 Cantilever beam. Different types of modeling: (a) 2D homogenized model; (b) 3D layered model.

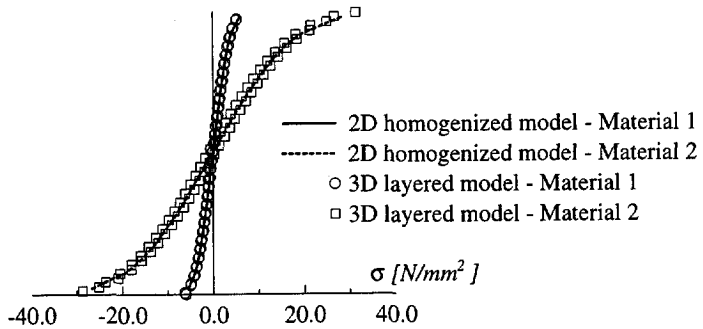


Figure 5.11 Cantilever beam. Horizontal stresses at the support for a linear elastic analysis.

out-of-plane direction. The 2D homogenized model is capable of predicting such behavior exactly. However only a 3D layered model (or a generalized plane strain model) can be used in this case due to the non-zero normal out-of-plane stress for both components.

This example is meant to assess the performance of the homogenization technique in a situation mostly constrained by the material behavior. Failure is localized near the clamped section due to an obvious distribution of stresses.

A comparison is given between the 2D homogenized continuum and a 3D layered model with 32 “basic cells”, see Figure 5.10. In the latter case, each basic cell consists of two 3D elements (one weak and one strong) in the vertical direction and sixteen elements in the horizontal direction. The vertical displacement  $d$  at the free end of the beam, obtained in a linear elastic analysis for a vertical uniform distributed load  $p$  with a value of  $1.0 \text{ [N/mm}^2\text{]}$ , reads  $3.654 \text{ [mm]}$  for the 2D homogenized model and  $3.655 \text{ [mm]}$  for the 3D layered model. Figure 5.11 shows the comparison between the horizontal stresses next to the support for the 2D homogenized model and the 3D layered model. The stresses are given at the integration point level of the 2D homogenized model.

The results obtained in a nonlinear analysis for the different discretizations are illustrated in Figure 5.12. Indirect displacement control of the uppermost right corner of the beam is applied in 30 equally spaced steps of  $0.5 \text{ [mm]}$ . Figure 5.13 shows the deformed meshes and the plastic zones for the two models. Good agreement is found.

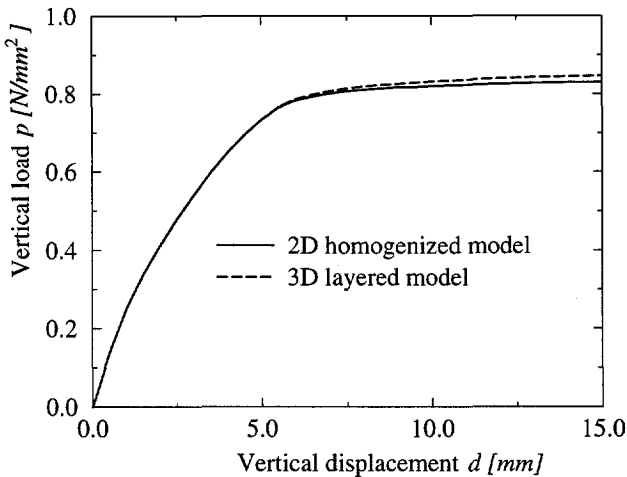
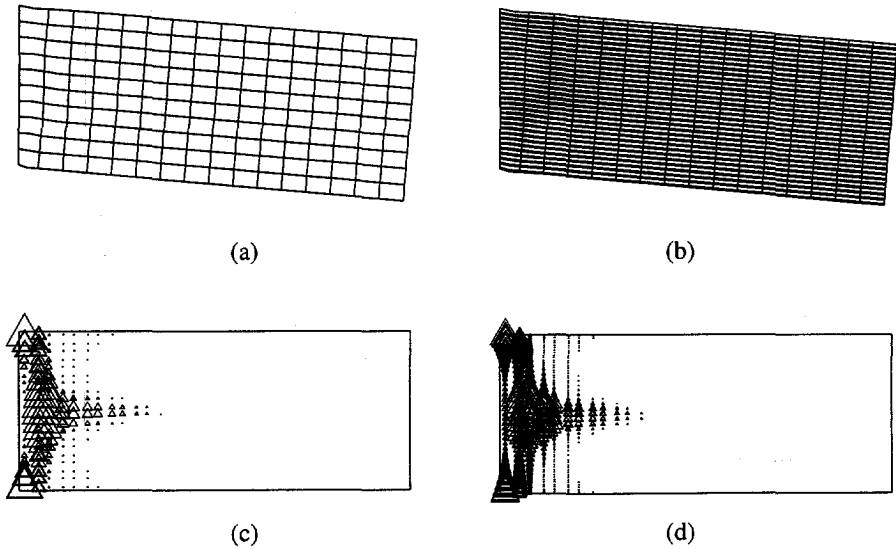


Figure 5.12 Cantilever beam. Force - displacement diagrams.

### Example 3: Embedded indentation test

The next example to be presented is an embedded indentation test. A rough  $200 \times 475 \times 20 \text{ [mm}^3\text{]}$  rod is pushed into a wall, see Figure 5.14a. Again, average plane stress conditions are assumed. Only half of the mesh is considered due to symmetry conditions. This example is meant to assess the performance of the homogenization technique in situations which are not only constrained by the material behavior, as was the case in



**Figure 5.13** Cantilever beam. Numerical results at failure: deformed mesh for (a) 2D homogenized model and (b) 3D layered model; equivalent plastic strain ( $> 0.5 \times 10^{-4}$ ) for (a) 2D homogenized model and (b) 3D layered model.

the previous example, but also by geometric constraints: a localized failure is obtained around the rod area. A comparison is given between the 2D homogenized and a 3D layered discretization with 32 “basic cells”, see Figure 5.14b,c. Again, each basic cell consists of two 3D elements (one weak and one strong) in the vertical direction.

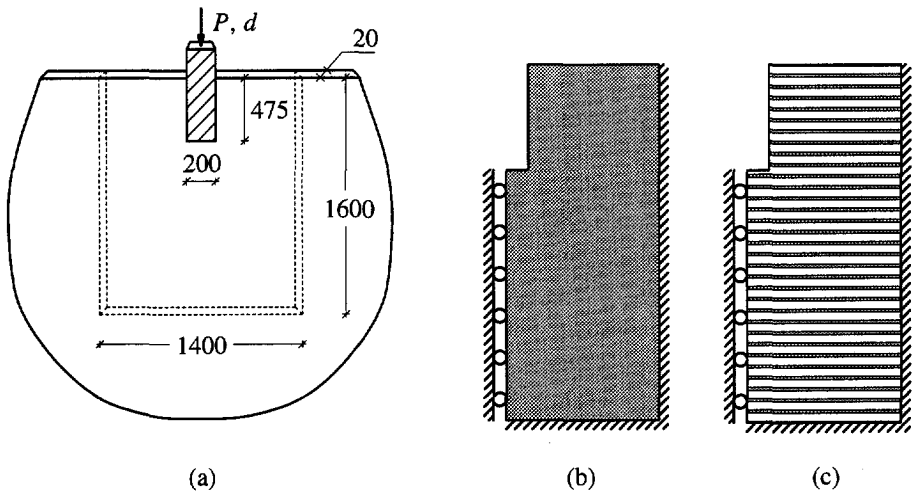


**Figure 5.14** Embedded indentation test: (a) geometry and loading; (b) 2D homogenized model; (c) 3D layered model.

The indentation force  $P$  obtained in a linear analysis for a vertical displacement  $d$  with a value of 1.0 [mm] reads: 143.1 [kN] for the 2D homogenized model and 144.4 [kN] for the 3D layered model. The results obtained in a nonlinear analysis are illustrated in Figure 5.15. Note that all the nodes correspondent to the contact between the wall and the rod are tied to have equal displacements. Direct displacement control of the rod is applied in 20 equally spaced steps of 0.1 [mm]. Figure 5.16 gives the deformed meshes and the plastic points at failure for the discretizations. Some differences are found. In the 2D homogenized model, failure is concentrated in the head and around the rod with pronounced shearing along the interface whereas, for the 3D layered model, failure

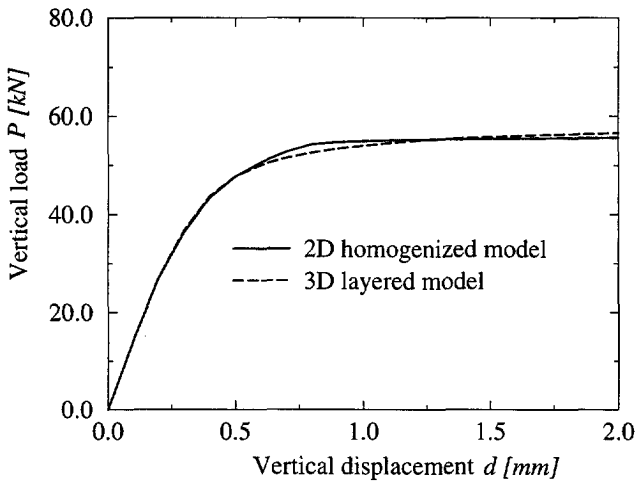


Figure 5.15 Embedded indentation test. Force - displacement diagrams.

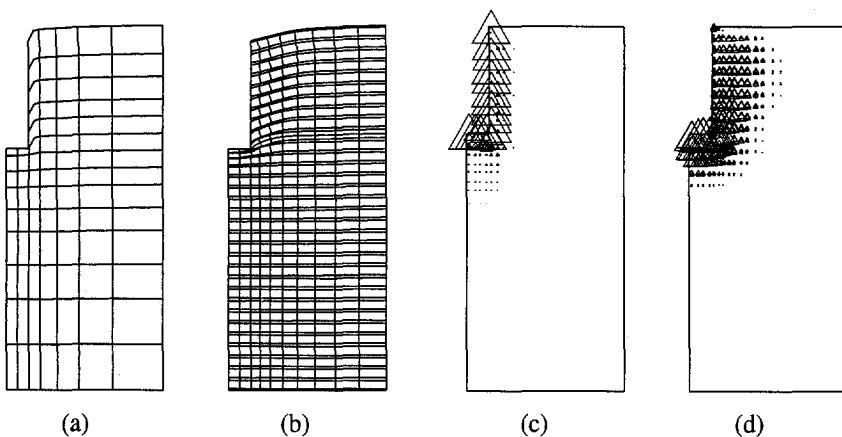


Figure 5.16 Embedded indentation test. Numerical results at failure: deformed mesh for (a) 2D homogenized model and (b) 3D layered model; equivalent plastic strain ( $> 0.5 \times 10^{-4}$ ) for (c) 2D homogenized model and (d) 3D layered model.

around the rod is not evident. This agrees well with the force-displacement diagrams shown in Figure 5.15. The 2D homogenized model yields a visible plateau, completely horizontal, whereas the 3D layered model exhibits still a (very) slight hardening behavior. Even if the calculation of the 3D model is carried out further, a better agreement in terms of deformation patterns is not found, Lourenço (1995a), because the deformation around the rod is due almost exclusively to the collapse of the weak layers. This is also observed in the homogenized model in terms of plastic strains but cannot be reproduced by the deformation patterns because the real geometry is not discretized.

*Example 4: Shear layer (softening behavior)*

For the last example, the Cosserat continuum will be utilized because now softening is included in the model. Figure 5.17 shows the infinitely long shear layer introduced by De Borst (1993). It is assumed that the shear layer is infinitely long, both in the negative and positive  $y$  direction. Basically the problem is one-dimensional and the use of three-dimensional elements, as done originally by Groen *et al.* (1994), requires the addition of linear constraint equations. The complete boundary conditions adopted in this study as well as the material properties can be found in Lourenço (1995a). In contrast to a standard continuum, a homogeneous strain state is not obtained under pure shear loading for a Cosserat continuum, at least not with the essential boundary conditions adopted, De Borst (1993). Therefore, localization arises naturally in the shear layer without the need to introduce any imperfections.

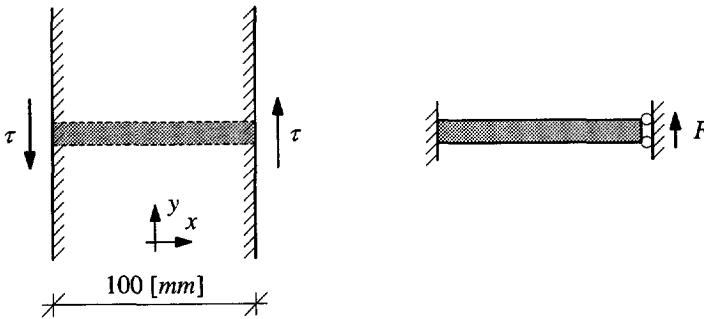


Figure 5.17 Infinitely long shear layer. Applied loading.

To compare the performance of the homogenization technique with the layered discretizations in a Cosserat continuum, two different discretizations are considered, corresponding to 16 and 32 “basic cells”. Direct displacement control of one end of the shear layer is applied in 30 equally spaced steps of 0.2 [mm]. To assess the influence of the discretization in a strain-softening Cosserat continuum, different levels of mesh refinement are considered until convergence is found to a unique force-displacement diagram upon mesh refinement. Figure 5.18 shows the deformed meshes at the termination of

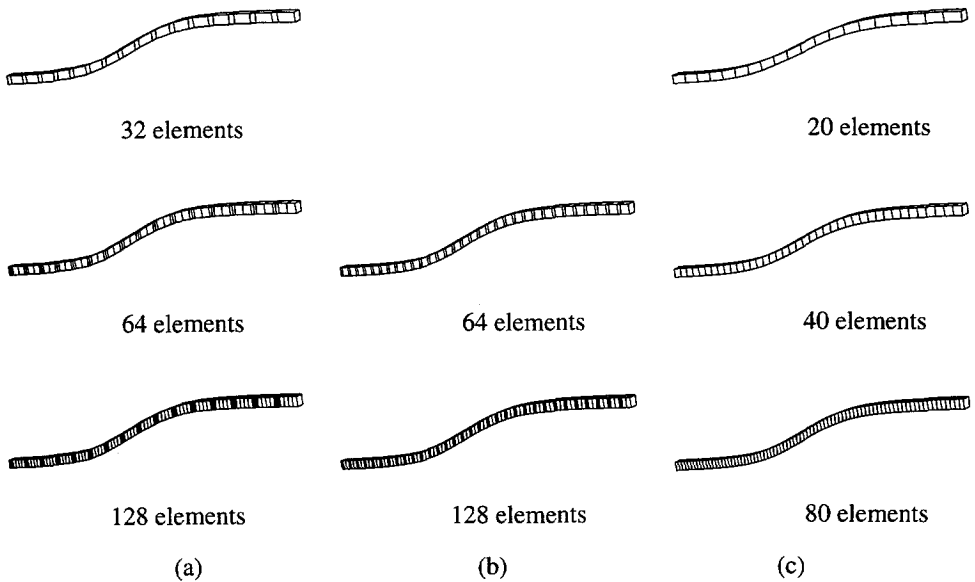


Figure 5.18 Shear layer. Deformed meshes for different discretizations: (a) 16 basic cells; (b) 32 basic cells; (c) homogenized model.

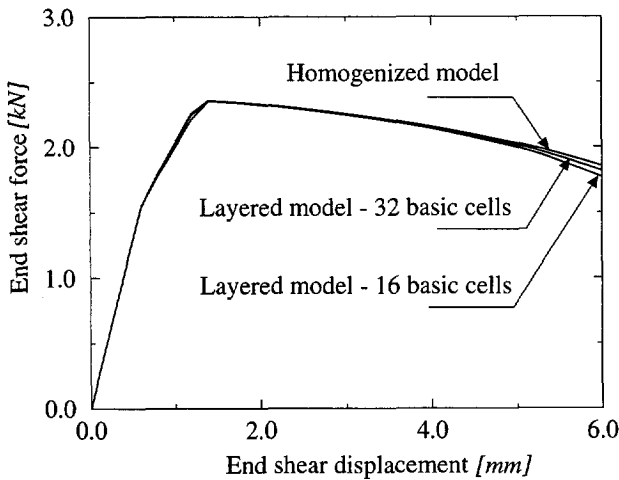


Figure 5.19 Shear layer. Force - displacement diagrams.

loading, respectively for the layered and homogenized models. It is shown that the localization develops smoothly and gradually in the middle of the shear layer. The width of the numerically predicted localization zone becomes constant and the obtained load-displacement responses converge, with an increasing number of elements, to a unique and physically realistic solution. Localization extends well outside the basic cell which allows an accurate homogenization procedure. If localization occurs inside the basic

cell, see Lourenço (1995a), non-smooth displacement fields are obtained. This type of failure cannot ever be predicted by a homogenized model because it requires the discretization of the basic cell. The comparison between the homogenized and layered models is illustrated in Figure 5.19. Only the results with the finer meshes are shown, not only to increase the legibility of the graph but also, because the converged response upon mesh refinement is the only meaningful one. Good agreement is found. An increasing number of layers corresponds to a response closer to the homogenized solution.

## 5.2 Derivation of the elastic characteristics of masonry

The basic cell of masonry has clearly a non-layered structure but different authors have suggested an approximate approach based in a two-step homogenization procedure, under the assumption of layered materials, see Figure 5.20.

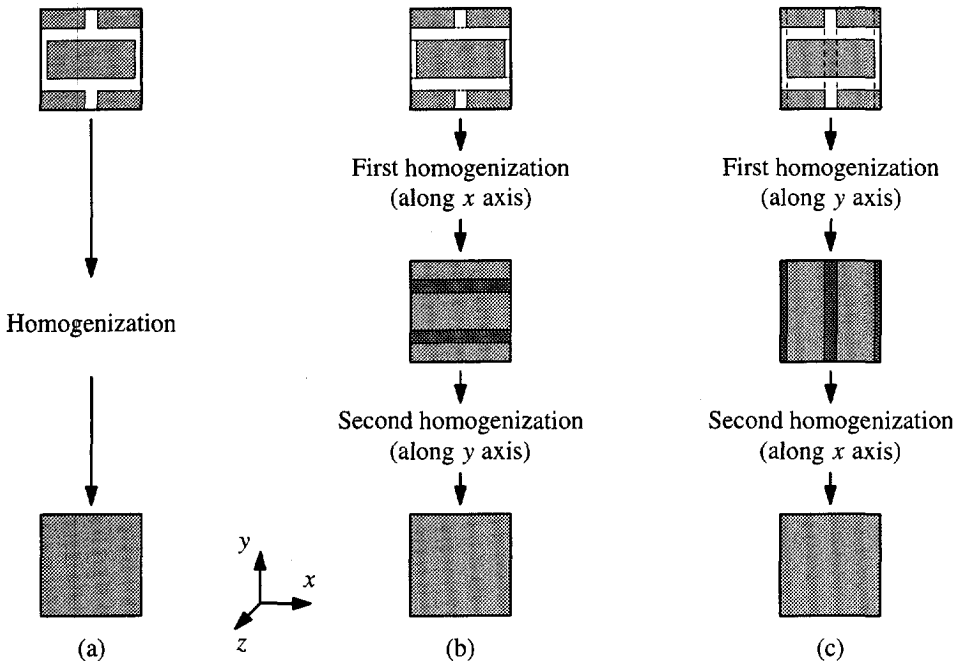


Figure 5.20 Two-step homogenization procedure usually adopted for masonry structures: (a) objective of homogenization; (b) homogenization  $xy$ ; (c) homogenization  $yx$ .

The process used by Pande *et al.* (1989) consists of a first step, in which a horizontal homogenization is performed, including the units and the vertical joints. In a second step, the vertical homogenization is performed, including the material homogenized

before and the horizontal joints, see Figure 5.20b. The opposite approach is used by Papa (1990). Now, in a first step, a vertical homogenization is performed, including the units and the vertical joints as well as the units and the bed joints. In a second step, the horizontal homogenization is performed, with the materials previously obtained, see Figure 5.20c. Here, the former technique is denoted by “Homogenization  $xy$ ” and the latter by “Homogenization  $yx$ ”. It is noted that different results will be obtained according to the process used, which means that the procedure is not objective, even in a linear elastic analysis. It is only natural to expect the differences to grow in presence of nonlinear behavior.

The adequacy of the two-step homogenization technique to calculate the elastic characteristics of masonry is investigated next. It is stressed again that the hypothesis of uniform strains in the out-of-plane direction yields three-dimensional stress states for the unit and the mortar. Of course, this precludes the use of plane stress conditions during the homogenization procedures, even if a plane stress state can effectively be used for the equivalent material.

### 5.2.1 Accuracy of the methodology for different stiffness ratios

A comparison is made between the behavior of the real masonry cell and the two-step homogenization, for different stiffness ratios of the masonry components. The entire basic cell is considered here to obtain more legible figures, even though the symmetry of the cell with respect to the three cartesian axes. Modeling of the cell is carried out with 10-noded tetrahedrons and 4 points Gauss integration over the volume. The mesh used is depicted in Figure 5.21. The unit dimensions are  $210 \times 52 \times 100$  [ $mm^3$ ] and the mortar thickness equals 10 [ $mm$ ]. The material properties of the unit are kept constant, whereas the properties of the mortar are varied. For the unit, the Young's modulus  $E_u$  is equal to 20000 [ $N/mm^2$ ] and the Poisson's ratio  $\nu_u$  is equal to 0.15. For the mortar, different Young's moduli  $E_m$  are considered, yielding a ratio  $E_u/E_m$  ranging from 1 to 1000. The Poisson's ratio  $\nu_m$  is kept constant and equal to 0.15. The ratios  $E_u/E_m$  considered (up to 1000) are, of course, extremely large if one considers linear elastic properties. However, in the case that inelastic behavior is included in the model, these

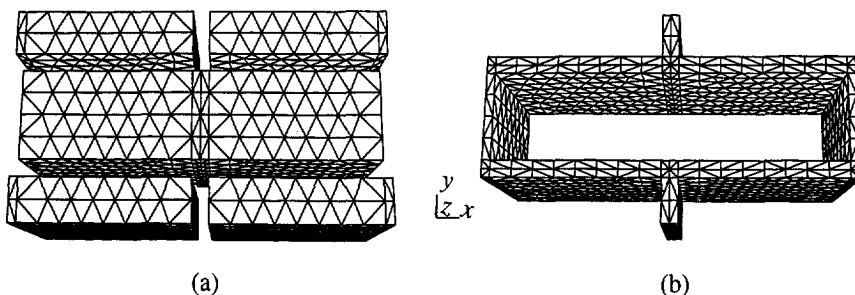


Figure 5.21 Basic cell. Finite element mesh: (a) unit; (b) mortar.

high values are indeed encountered. Note that this ratio tends to infinity when softening of the mortar is completed and the unit remains active.

In order to calculate the Young's modulus of the equivalent material in a given direction, e.g.  $x$  axis, the masonry cell is subjected to uniform loading along this direction and admissible displacement fields are imposed in the transverse directions by the proper constraints on the surface nodes, see Figure 5.22. The uniform displacement fields force the macro-deformation of the basic cell and the equivalent material to be the same, meaning that both systems contain the same strain energy. A similar procedure holds for the other two material axes,  $y$  and  $z$ . A comparison between the real values and the values obtained with the two-step homogenization is given in Figure 5.23. Some relevant remarks for the particular geometrical arrangement are as follows:

- For the off-plane direction ( $z$  axis) and  $E_z$  no differences are found between the "real" and homogenized values. This is due to the uniform stress distribution along the  $z$  axis;
- For the in-plane directions, the error increases with larger  $E_u/E_m$  ratios, i.e. stronger deviation from a homogeneous material;
- Homogenization  $xy$  performs better than homogenization  $yx$ , which is due to the different thickness ratios in both directions. The unit is four times larger in the  $x$  direction;
- Noticeable errors are found in the  $x$  direction for both homogenization techniques and large ( $>10$ )  $E_u/E_m$  ratios (in the case of homogenization  $yx$  the values found are clearly non-acceptable). This is explained by two reasons. First, the vertical joints are discontinuous and, second, the thickness ratio in the  $x$  direction is quite large (20%). The combination of these two factors leads to an extremely non-uniform stress field as the stresses must "go around" the vertical joints, see Figure 5.24. The fact that the vertical joints are discontinuous, by itself, is not quite relevant as confirmed by the results in the  $y$  direction. For the  $E_y$  and homogenization  $xy$ , the maximum error found is only 2%. This is, of course, due to the low thickness ratio in this direction (5%).

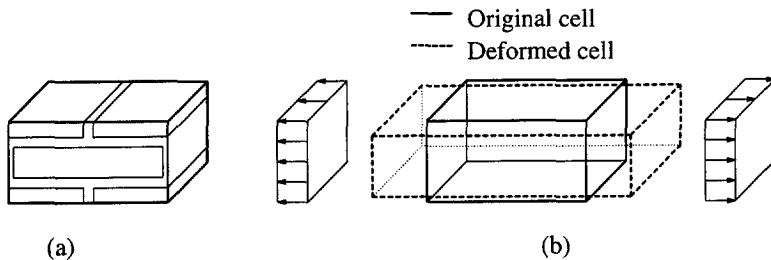


Figure 5.22 Loading case: (a) basic cell; (b) typical loading (along  $x$  axis).

In fact, the stress distributions can deviate immensely from a quasi-uniform state of stress. This is shown in Figure 5.25 where different ratios  $E_u/E_m$  have been chosen for the vertical joints ( $E_u/E_m = 1000$ ) and bed joints ( $E_u/E_m = 10$ ). Unfortunately this is not

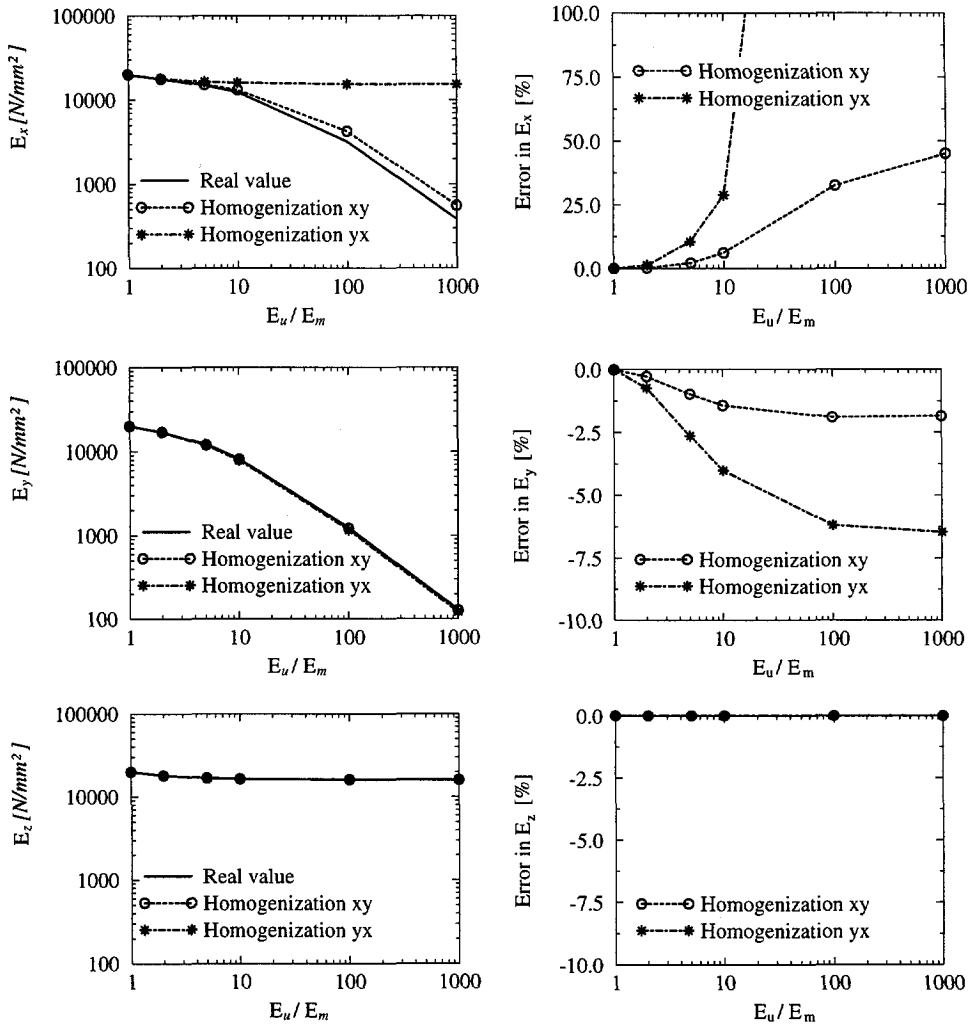


Figure 5.23 Comparison between real masonry cell and two-step homogenization.

an academic discussion but represents a quite real loading of masonry structures. This would be the case of compression normal to the bed joints and tension parallel to the bed joints. For such a loading combination, the stiffness of the vertical joints will degrade and tend to zero. Table 5.2 demonstrates that unacceptable predictions are obtained, even for the more accurate homogenization  $xy$ .

From the above results, it is possible to conclude that the two-step homogenization can be used for the calculation of the linear characteristics of masonry. However, in the presence of nonlinear behavior the technique is likely to yield large errors, at least locally, and, in the present form, it is not recommended. Similar conclusions are reported in Anthoine (1995) for different material properties and geometry. Attention

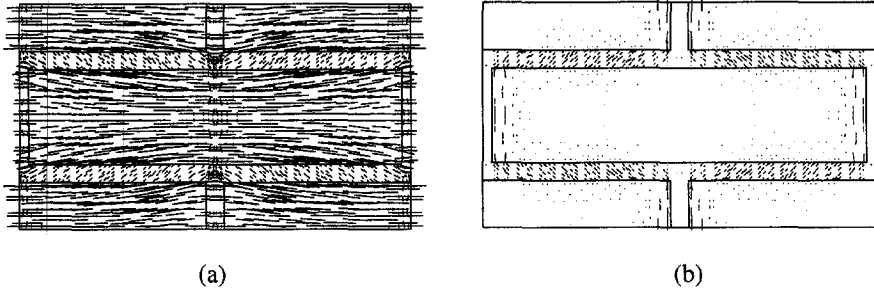


Figure 5.24 Surface principal stresses in the  $x, y$ -plane for  $E_u/E_m = 1000$ : (a) tensile stresses; (b) compressive stresses.

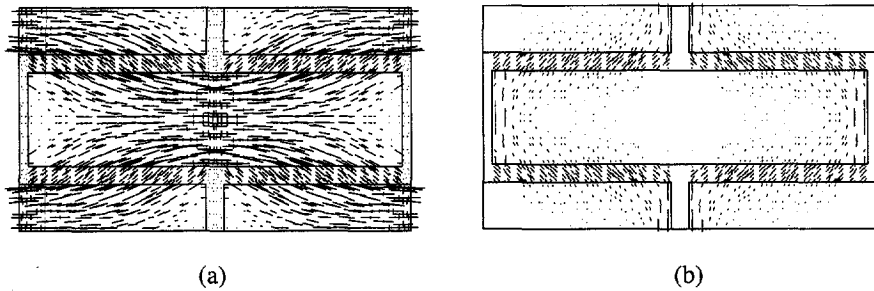


Figure 5.25 Surface principal stresses in the  $x, y$ -plane for new analysis: (a) tensile stresses; (b) compressive stresses. Bed joints -  $E_u/E_m = 10$ . Head joints -  $E_u/E_m = 1000$ .

Table 5.2 Comparison between real masonry cell and homogenization  $xy$  for new analysis. Bed joints -  $E_u/E_m = 10$ . Head joints -  $E_u/E_m = 1000$  (Values in  $[N/mm^2]$ ).

	Real value	Homogenization $xy$	Error
$E_x$	6355	711	830%
$E_y$	7705	8190	6%
$E_z$	16305	16335	0%

is also driven to the fact that cracking or slipping in the interface was not included in the model. In Chapter 4, it is, however, shown that these phenomena are mostly responsible for the inelastic response. Therefore, due to the inaccuracies expected in a complete nonlinear analysis, the implementation of the complete algorithm developed in Section 5.1 is not pursued any further. In Chapter 6, another approach to model the composite behavior of masonry structures in the presence of nonlinear material behavior, will be presented, which is more worthwhile to invest effort.

### 5.2.2 Results of a masonry shear wall

With the analysis of the masonry basic cell just described, it was concluded that the two-step homogenization can be successfully used in the presence of linear elastic material behavior. The performance of the method in the analysis of large structures can be further evaluated with a generic calculation. The shear wall introduced in Chapter 4, built with 18 courses of  $210 \times 52 \times 100$  [mm<sup>3</sup>] bricks and 10 [mm] thick mortar joints, is considered for this purpose. For an assessment of the two-step homogenization technique, two models are considered: the “continuum model”, in which units and mortar are modeled with 8-noded continuum elements and, the “homogenized model”, in which the homogenized material is modeled with 8-noded continuum elements. A  $2 \times 2$  Gauss integration scheme is used and the material properties are given in Table 5.3. Note that the two different types of homogenization, viz. homogenization  $xy$  and homogenization  $yx$ , given in the previous caption are considered.

Table 5.3 Material properties.

	$E$ [N/mm <sup>2</sup> ]	$\nu$
Unit	20000	0.15
Mortar	2000	0.125

Four different load cases are considered: two uniform loads along one edge and two point loads distributed over the right top unit. These loads, which are introduced by a force  $F$  equal to 1.0 [MN], and the parameter adopted to control the performance of the two models, which is the displacement  $d$  along the direction of the resultant force  $F$ , are shown in Figure 5.26.

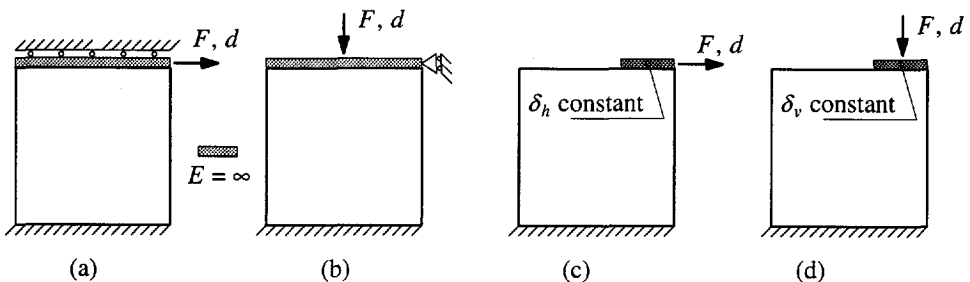


Figure 5.26 Loads applied in masonry wall to assess the two-step homogenization technique: (a) load 1, uniformly distributed horizontal load; (b) load 2, uniformly distributed vertical load; (c) load 3, horizontal load in a single brick; (d) load 4, vertical load in a single brick.

In a Silicon Graphics Indigo R4400, on average, the continuum model used 333.5 [s] of CPU time and the homogenized model 5.7 [s] (2%). Table 5.4 gives the results obtained in a linear elastic calculation. The comparison results in a difference, between the two

**Table 5.4** Continuum vs. homogenized modeling. Linear elastic results of the displacement  $d$  for all loading cases.

	Continuum model			
	Load 1	Load 2	Load 3	Load 4
$d$ [mm]	5.39	1.35	12.41	3.82

	Homogenized $xy$ model				Homogenized $yx$ model			
	Load 1	Load 2	Load 3	Load 4	Load 1	Load 2	Load 3	Load 4
$d$ [mm]	5.79	1.36	12.80	3.78	5.86	1.42	12.82	3.92

models, smaller than 7% (for the  $xy$  homogenization) and 8% (for the  $yx$  homogenization). It is noted that the basic cell is far from being small when compared to the size of the structure analyzed. In practice even smaller errors are expected to occur. This example illustrates also the benefit of using a macro-modeling strategy, to be detailed in Chapter 6, over a micro-modeling strategy, as given in Chapter 4. The calculation with the homogenized model is five times faster than the calculation with the simplified micro-model, see Section 4.1. In reality, this ratio is even higher because coarser meshes would be considered for the (macro-)analysis with homogenized elastic characteristics. The global behavior of the homogenized model shows excellent agreement with the behavior of the detailed modeling. Locally, however, some differences can be found and a detailed comparison will be given for the uniform loads and a homogenization  $xy$ . Figures 5.27 to 5.29 demonstrate that the deformational behavior and the stress distribution for both modelings are similar. It is discussed before, see Section 4.1, that a simplified modeling cannot reproduce local stress gradients, e.g. Figure 5.29, but the gradients are strongly mesh dependent and irrelevant for the global structural behavior.

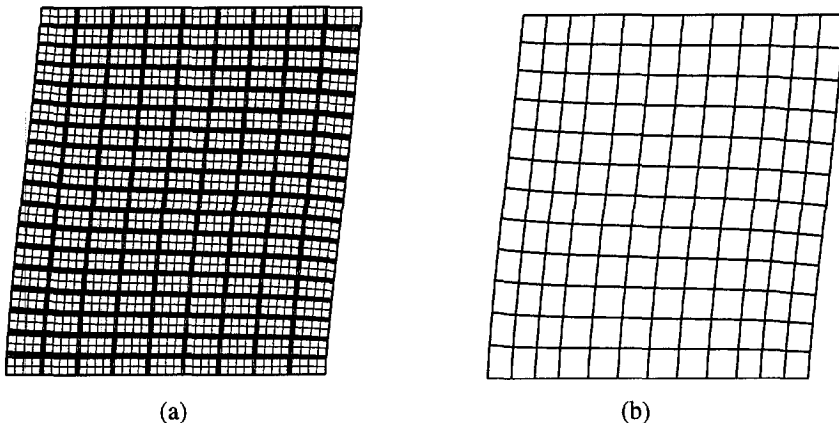


**Figure 5.27** Deformed mesh for load 1: (a) continuum model; (b) homogenized  $xy$  model.

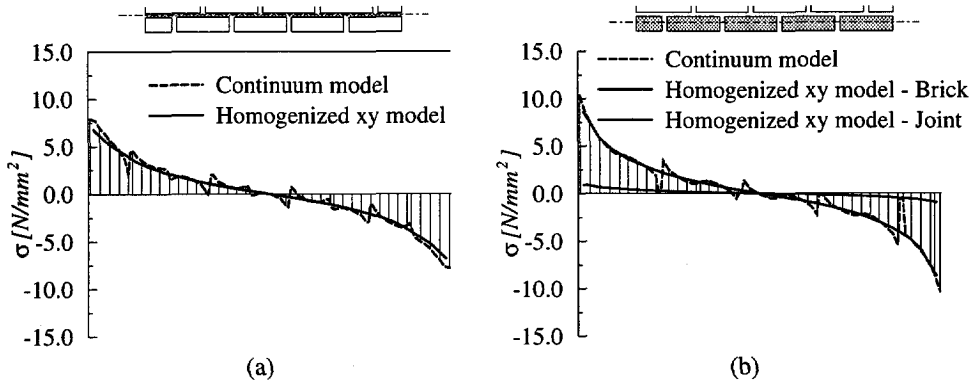


Figure 5.28 Vertical stresses for the complete wall at the base, load 1: (a) horizontal joint; (b) brick and vertical joint.

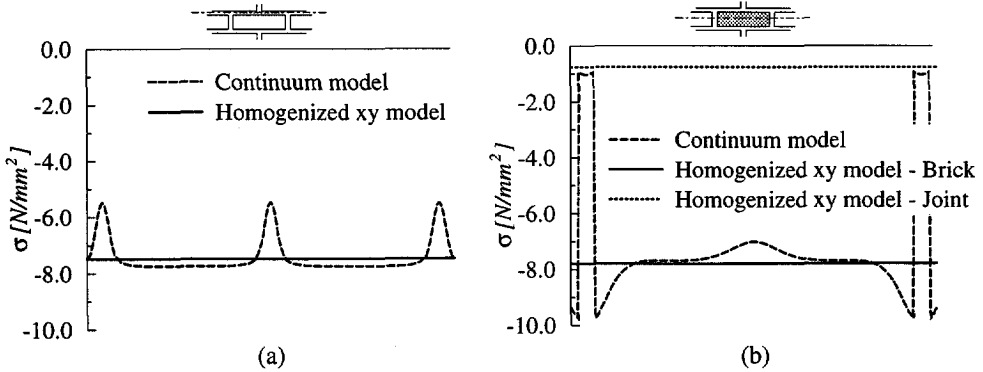


Figure 5.29 Vertical stresses over a brick length at the center of the wall, load 2: (a) horizontal joint; (b) brick and vertical joint.

### 5.3 Tensile behavior parallel to the bed joints

Homogenization techniques that include some approximation as discussed earlier in this Chapter are one possibility to describe the composite material behavior of masonry. Another possibility is to use a micro-model to predict the complete macro-behavior through elastic and inelastic regimes. Here, the micro-model proposed in Chapter 4 will be adopted to describe the macro-behavior of masonry under tension parallel to the bed joint, which is required when studying crack formation in walls under e.g. restrained shrinkage, see also Chapter 7. This example illustrates how the inelastic properties of the composite can be obtained from the micro-properties of the components (unit, mortar and interface) and the geometrical arrangement.

Figure 5.30 shows a masonry detail extracted from an infinitely large masonry wall under tension as introduced by Rots, see CUR (1994) and Rots *et al.* (1994), with

$900 \times 600 \times 100$  [mm] calcium-silicate units and thin glued joints. These dimensions include the thickness of the thin joints, which amount to 2 [mm] for the bed joints and 3 [mm] for the head joints. The mesh used in the numerical analyses is also depicted in Figure 5.30. In the vertical direction, only two half units are modeled due to symmetry conditions, whereas, in the horizontal direction, two and a half units are modeled. In the middle of the specimen a potential crack/slip line through head and bed joints is included. With this modeling it seems to be implicitly assumed that the crack distance is 2250 [mm] (or two and a half units) even if it is known that deformation, in an infinitely long masonry wall under tension, must localize in a single crack. However, the adopted length of the specimen (two and a half units) is, according to the Saint-Venant principle, enough to obviate any influence of the left and right boundaries in the stress distribution around the crack zone. It is noted that the masonry basic cell with a single unit length, see Figure 5.2 or Figure 5.20, *cannot* be used because the results would be influenced by the boundaries.

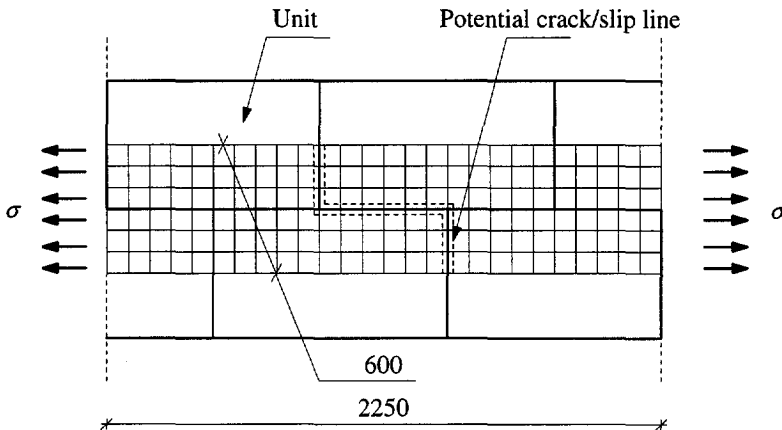


Figure 5.30 Masonry detail of an infinitely long wall under tensile loading parallel to the bed joints.

Units are modeled with continuum elements and joints are modeled with interface elements, according to the strategy proposed in Chapter 4. All the interface elements remain elastic except the elements along the potential crack/slip line. For these elements, the composite interface model developed in Chapter 4, where only the tension and Coulomb friction modes are active, is adopted (the compressive stresses remain small and do not trigger the cap mode). The material parameters adopted in CUR (1994) are used, see Table 5.5 and Table 5.6. The initial stiffness of the interfaces is obtained from the elastic properties of mortar and interface according to  $k_n = E_m/h_m$  and  $k_s = E_m/2(1 + \nu_m)/h_m$ , where  $E_m = 1000$  [N/mm<sup>2</sup>],  $\nu_m = 0.2$  and  $h_m$  is the thickness of the joint. The analyses are performed with indirect displacement control where possible. Local snap-backs must be traced with COD control over the most active interface.

The numerical stress-displacement diagrams are given in Figure 5.31. Figure 5.31a shows the relation between the masonry tensile stress parallel to the bed joints and the relative displacement of the left and right boundaries, i.e. considering the total specimen length. This result (the displacements and not the stresses) depends on the specimen length and is, therefore, of little importance for practical purposes. The relation between tensile stress and “crack” displacement, which can be obtained by subtracting the elastic unloading of the undamaged part of the specimen from the relative displacement of the boundaries, is much more interesting because it is independent of the specimen length, see Figure 5.31b. In particular, the area under the stress-crack-displacement diagram measures the composite fracture energy of masonry.

Table 5.5 Masonry strip. Elastic properties, CUR(1994).

Unit		Bed joint		Head joint	
E	$\nu$	$k_n$	$k_s$	$k_n$	$k_s$
5000	0.2	500	209	333	139
$[N/mm^2]$		$[N/mm^3]$	$[N/mm^3]$	$[N/mm^3]$	$[N/mm^3]$

Table 5.6 Masonry strip. Inelastic properties, CUR(1994).

Tension		Shear				Unit
$f_t$	$G_f^I$	$c$	$\tan \phi$	$\tan \psi$	$G_f^{II}$	$f_t$
0.5	0.01	0.75	0.75	0.2	0.05	1.3
$[N/mm^2]$	$[Nmm/mm^2]$	$[N/mm^2]$			$[Nmm/mm^2]$	$[N/mm^2]$

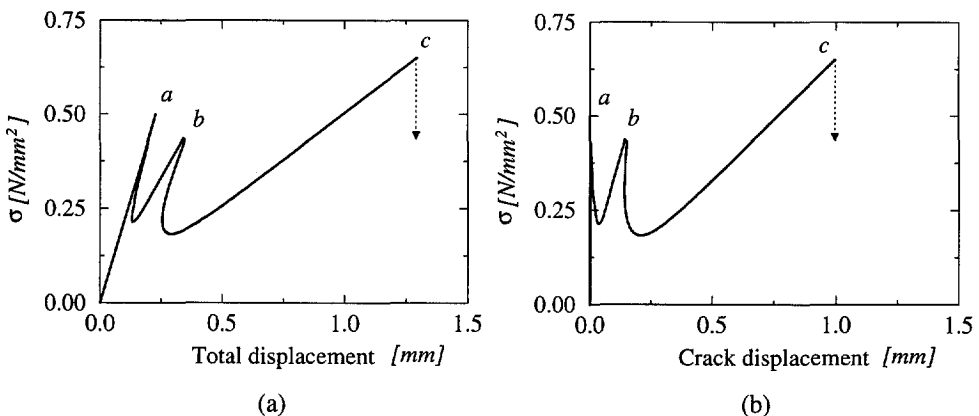
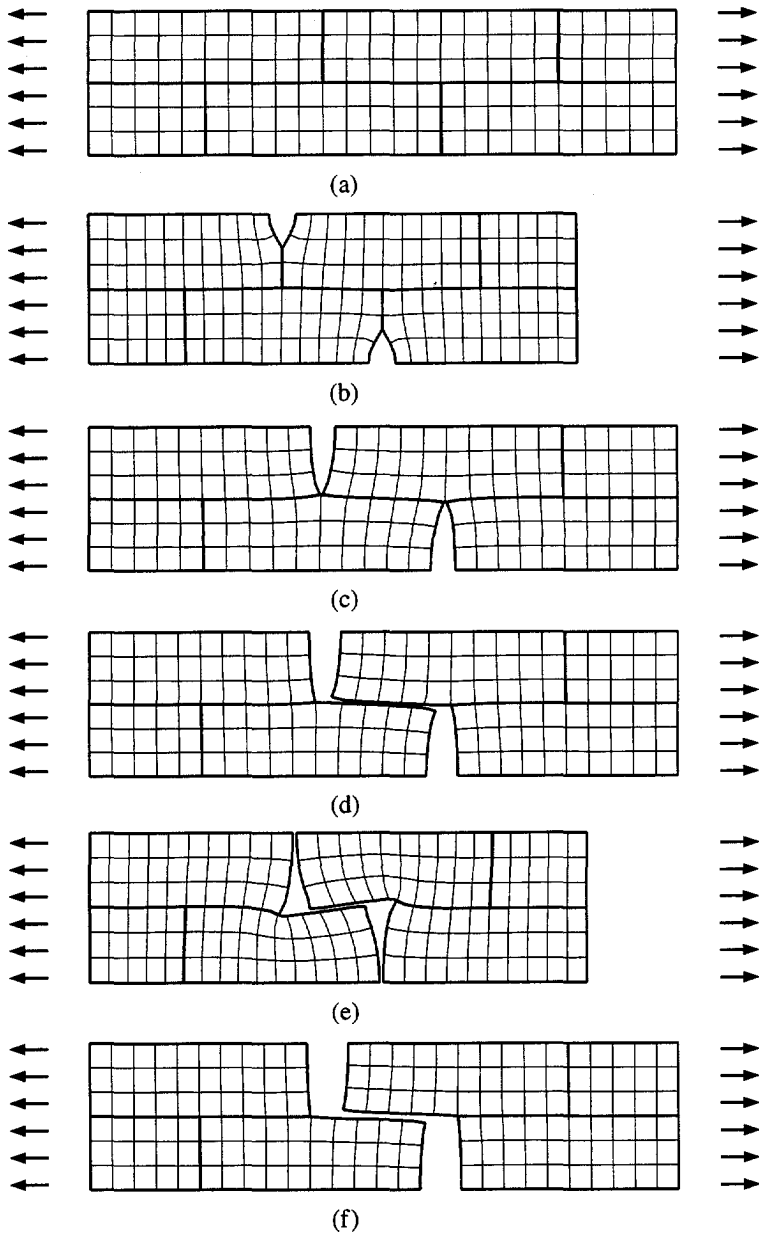
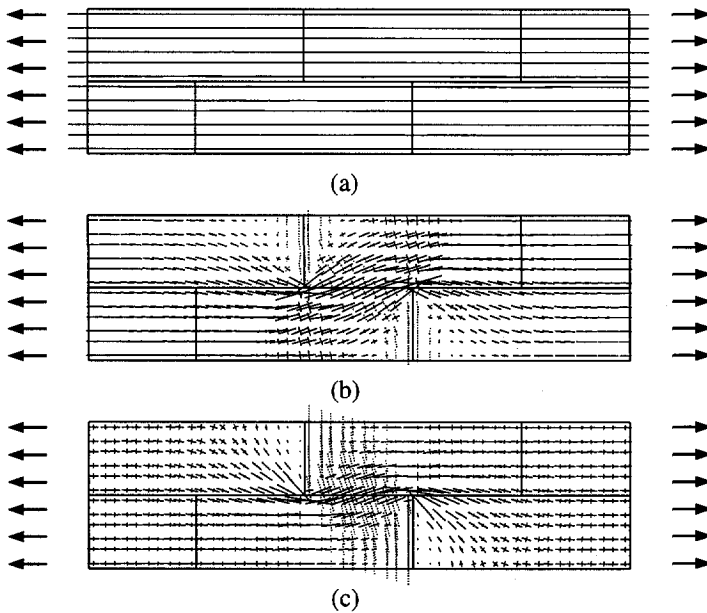


Figure 5.31 Tension parallel to the bed joints. Stress - displacement diagrams for (a) total specimen length and (b) “crack” displacement.



*Figure 5.32* Tension parallel to the bed joints. Deformation process: (a) initial state, head and bed joints still uncracked; (b) head joints partially cracked (incremental displacements, shortly before peak *a* in Figure 5.31); (c) head joints totally cracked (shortly after peak *a*); (d) bed joint partially cracked (shortly before peak *b*); (e) bed joint totally cracked (incremental displacements, shortly after peak *b*); (f) residual mechanism controlled by dilatancy of the bed joint (shortly before peak *c*).

Figure 5.31 shows three peaks with multiple snap-back behavior, which is not necessarily the case of all masonry types, see also Backes (1985). This result is, probably, typical of calcium-silicate masonry because the interface shows an extremely low fracture energy due to the smoothness of the units, Van der Pluijm (1992). Peak *a* corresponds to the onset of cracking in the head joints, which is a pure mode I phenomenon. Peak *b* corresponds to the onset of slipping in the bed joint, which is a pure mode II phenomenon. The last peak *c* corresponds to tensile failure along the middle of the units. This type of failure is not predicted by the modeling because a potential crack in the units was not included. The value shown, half of the unit tensile strength, assumes a uniform distribution of horizontal stresses, which is not true, see also Figure 5.33c, but can be used as an approximation. In the following, it will be demonstrated that potential cracks in the units do not need to be modeled for these particular material parameters and geometry. The mechanisms involved in the failure process are depicted in Figure 5.32 and Figure 5.33 where the deformed meshes and principal stresses are given at different loading stages. Clearly, a mode I process controls the opening of the head joints, Figure 5.32b,c and Figure 5.33a. Once softening of the head joints is completed, the internal forces must flow across the bed joint, Figure 5.33b. The principal tensile stresses make a relatively small angle with the bed joint, which is then subjected to high shear stresses. The resultant mode II crack is shown in Figure 5.32d,f.



*Figure 5.33* Tension parallel to the bed joints. Principal stresses: (a) initial state, head and bed joints still uncracked; (b) once softening of head joints is completed; (c) residual state, locking of the units with normal compressive stresses due to dilatancy of the bed joints.

The present results illustrate well the possible behavior of masonry under tension parallel to the bed joints. However, the third peak of the analysis must be questioned. In fact, it is physically clear and experimentally confirmed, Backes (1985), that cracking of the units does not occur after pronounced slipping of the bed joints. The behavior obtained in the analysis can be explained by the significant role of the dilatancy angle  $\psi$ .

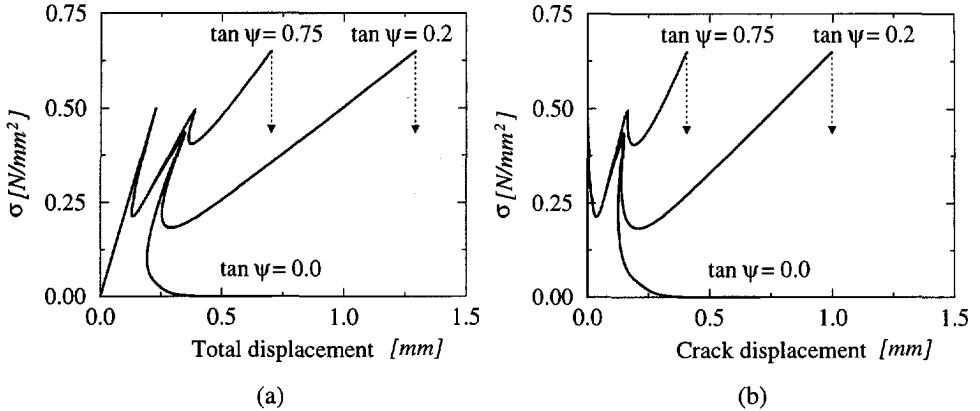


Figure 5.34 Tension parallel to the bed joints. Influence of dilatancy angle  $\psi$ . Stress - displacements diagrams for (a) total specimen length and (b) "crack" displacement.

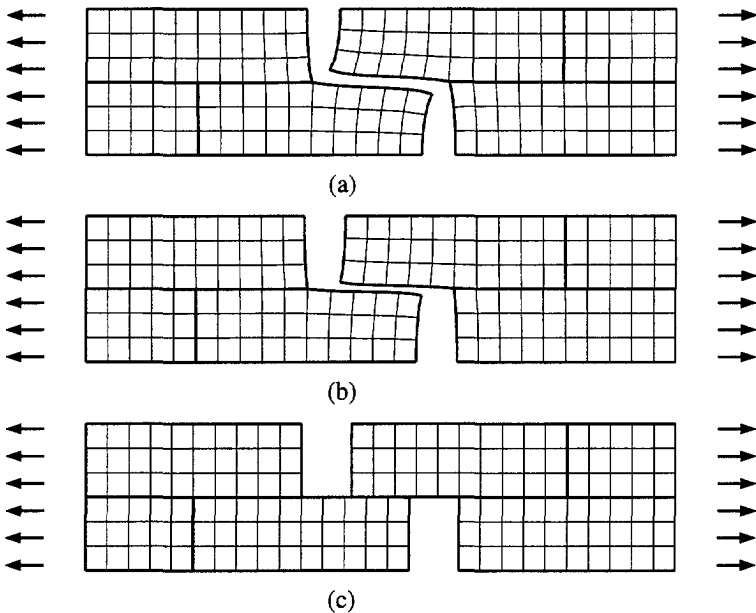


Figure 5.35 Tension parallel to the bed joints. Influence of dilatancy angle  $\psi$ . Deformed meshes at ultimate stage: (a)  $\tan \psi = 0.75$ ; (b)  $\tan \psi = 0.2$ ; (c)  $\tan \psi = 0$ .

Figure 5.34 shows the results obtained if different dilatancy angles, taken as  $\tan \psi = 0$  and  $\tan \psi = 0.75$  respectively, are considered. With zero dilatancy no force is built up upon shearing of the bed joints, whereas an associated flow rule, i.e.  $\tan \psi = \tan \phi = 0.75$ , leads to higher strength and a much stiffer response. Locking of the units is due to an increasing uplift, upon shearing with higher dilatancy angles, see Figure 5.35, which is restrained by the confined nature of the boundary conditions (top and bottom are forced to remain straight and horizontal).

This strong dependency of the results on the dilatancy angle complies with previous numerical analyses, e.g. Chapter 4 and CUR (1994). In fact, using a constant dilatancy angle is unrealistic. This calls for an extension towards dilatancy softening, as measured experimentally by Van der Pluijm (1993), into the interface model described in Chapter 4. Such an extension is presented now.

The introduction of dilatancy softening is novel in the modeling of masonry structures but its crucial role is demonstrated next. It was shown in Chapter 2 that the dilatancy angle tends to zero with increasing plastic slip. For simplicity, the softening of the dilatancy angle is taken proportional to the softening of the cohesion, which is similar to the assumed friction softening, cf. eq. (4.12), and reads

$$\tan \psi = \tan \psi_i \frac{\bar{\sigma}_2}{c} \quad (5.40)$$

where  $\tan \psi_i$  is the initial dilatancy angle. The results of the new analyses with a variable dilatancy angle are illustrated in Figure 5.36. In this figure, the extreme values found in Van der Pluijm (1993) for the initial dilatancy angle are adopted,  $\tan \psi_i = 0.6$  and  $\tan \psi_i = 0.3$  respectively. It is observed that, ultimately, an ideally plastic behavior is obtained with a residual non-zero strength. This is due to the normal stress built up during shearing of the interface. Once softening of the dilatancy angle is completed, ideally

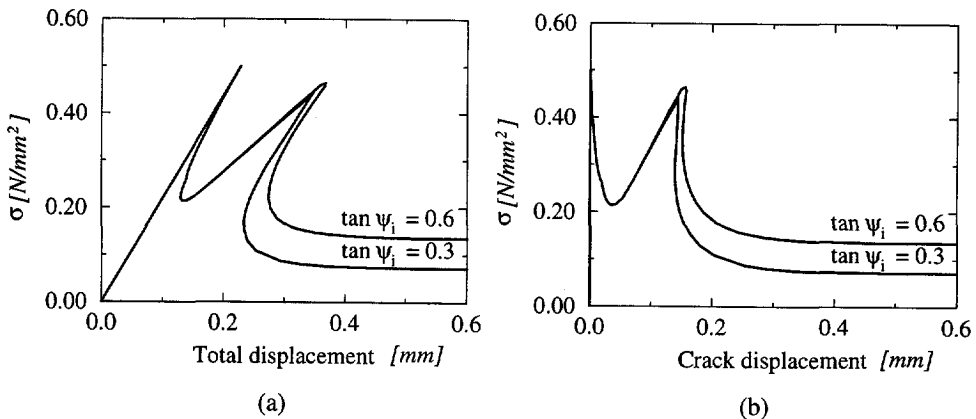


Figure 5.36 Tension parallel to the bed joints. New analysis with variable dilatancy angle (ultimate  $\tan \psi$  equals zero). Stress - displacements diagrams for (a) total specimen length and (b) "crack" displacement.

plastic behavior is retrieved. It is now observed that the response depends only moderately on the value of the initial dilatancy angle  $\psi_i$ . In particular, the variation in the residual plateau value seems proportional to the variation in the tangent of the initial dilatancy angle.

This type of behavior for calcium-silicate units is realistic and confirmed experimentally, Backes (1985). A quantitative comparison between the model predictions and the available experimental results of Backes (1985) is hindered by the fact that the complete set of micro-parameters, for the materials used by this author, are not known.

Figure 5.37 shows typical stress-displacement responses obtained by Backes (1985) for the two different possible types of masonry failures under tension parallel to the bed joints. Either a zigzag crack through head and bed joints or a straight crack through head joints and middle of the units occurs. In the first case, softening is governed by the mode II fracture energy and dilatant behavior of the bed joints. A residual strength value is found after the peak strength. In the second case, softening is governed by the unit fracture energy and the masonry tensile strength tends to zero. It is noted that these experimental peak values are extremely small when compared to the values found by Van der Pluijm (1992) for mode I failure of joints. This is partly due to the fact that the head joints are only partially filled but also due to different material properties. This confirms the heterogeneity of masonry. In particular, the two-peaked diagram obtained in Figure 5.36 can be considered representative only for very large calcium-silicate units with thin glued joints. The smoother responses of Figure 5.37 are due to the geometry of

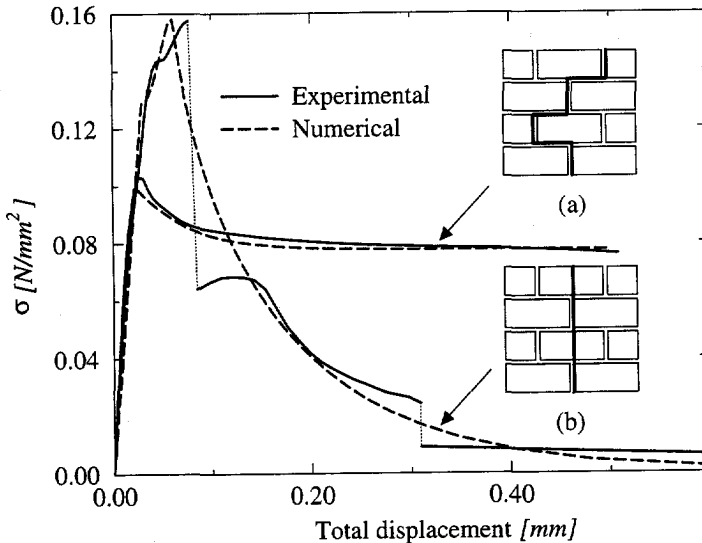


Figure 5.37 Tension parallel to bed joints: (a) failure occurs with a stepped crack through head and bed joints; (b) failure occurs vertically through head joints and units. Experimental stress - displacement diagrams, Backes (1985), vs. stress - displacement diagrams calculated with inverse fitting.

the units and normal strength mortar. For example, the small experimental and numerical pre-peak reduction of stiffness in Figure 5.37b is due to opening of the head joints. Unloading is not found because the bed joints take over the strength degradation of the head joints. More research is needed before definitive conclusions can be made and it is likely that the simple softening laws adopted for the different parameters of the Coulomb friction mode must be refined. However, the experimental results appear to be satisfactorily reproduced by the model. The available material strength properties in Backes (1985) were used but (non-available) reasonable post-peak material properties had to be assigned by inverse fitting.

## 5.4 Summary

The adequacy of using homogenization techniques for the analysis of masonry structures has been discussed. The idea is to use both the geometrical arrangement and the material properties of the units and mortar to predict the homogenized behavior of the composite.

Different aspects are investigated. Initially, attention is given to the two step-homogenization proposed by several authors, based in the successive application of the theory of layered materials, for two orthogonal directions. For this purpose, in Section 5.1, a novel matrix formulation for the elastoplastic analysis of layered materials is introduced. The comparison between the results obtained with layered and homogenized models shows excellent agreement both in the elastic and inelastic regimes. In Section 5.2, it is shown that the two-step homogenization can be successfully used for the derivation of the elastic characteristics of masonry. However, some precaution is recommended, if nonlinear behavior is incorporated in the model, especially in the case of softening materials. In such case, large errors will be encountered in the analysis due to the combined action of the non-layered structure of masonry and the large difference in stiffness between units and mortar.

Finally, in Section 5.3, the behavior of masonry under tension parallel to the bed joints is dissected as an example of the application of exact nonlinear homogenization techniques to the real masonry cell. It is shown that the experimental macro-behavior can be satisfactorily reproduced by the micro-model developed in Chapter 4. An important improvement has been included in the model: dilatancy softening. It is shown that, in the absence of dilatancy softening, unrealistic results can be obtained.

The main advantage of using homogenization techniques is that, once the properties of the constituents are fully known, the composite behavior of the material can be predicted without costly and, for masonry, necessarily large tests. This would mean that changes of geometry, e.g. dimensions of units and thickness of the joints, or geometrical arrangements could be handled exclusively numerically. However, at the present stage, it seems clear that experimental research must be carried out to confirm the numerical results. It is believed that the basis for the reliable use of nonlinear homogenization techniques, in which micro-models are used to predict some of the macro-properties of

masonry, is the existence of deformation controlled test results at micro- and macro-level. Only a thorough comparison between predicted and observed results can provide the necessary level of confidence for future use of homogenization techniques.

## 6. MACRO-MODELING: AN ANISOTROPIC CONTINUUM MODEL FOR MASONRY

The analysis of masonry structures built from a large number of units and joints can only be carried out with macro-models, in which a relation between average stresses and strains in the composite material is established. The effective constitutive behavior of masonry features anisotropy arising from the geometrical arrangement of units and mortar, even if the properties of these constituents are isotropic. It might be expected that, to model masonry as a composite, sound numerical implementations of anisotropic plasticity models, which are generalizations of existing isotropic realizations, will be required.

The modern plasticity framework detailed in Chapter 3 is general enough to apply equally well to both isotropic and anisotropic plasticity models. However, it appears that while many anisotropic plasticity models have been proposed from purely theoretical and experimental standpoints, e.g. Hill (1948), Hoffman (1967) and Tsai and Wu (1971), only a few numerical implementations and calculations have actually been carried out. Examples include the work of De Borst and Feenstra (1990) and Schellekens and De Borst (1990) which fully treated the implementation of, respectively, an elastic-perfectly-plastic Hill yield criterion and an elastic-perfectly-plastic Hoffman yield criterion. In principle, hardening behavior could be simulated with the fraction model of Besseling (1958) but not much effort has been done in this direction. More recent attempts are given in Swan and Cakmak (1994), which included linear tensorial hardening in the Hill yield criterion, and Li *et al.* (1994), which included linear hardening in a modified (pressure dependent) Von Mises to fit either the uniaxial tensile or compressive behavior, but not both.

That few anisotropic models have been successfully implemented and tested is not surprising, especially in the light of the difficulties that remain associated with many of the isotropic plasticity models. One particular difficulty is the existence of singular points on the yield surface, e.g. apex of Drucker-Prager yield criterion or corners of Mohr-Coulomb yield criterion. While this problem can be acute for isotropic plasticity models, it can become even more pronounced for anisotropic models where algebraic simplifications are hardly possible. The present Chapter represents a step further in the formulation of anisotropic plasticity models. A composite yield criterion suitable for the modeling of anisotropic materials under plane stress conditions is presented. Individual yield criteria are considered for tension and compression, according to different failure mechanisms. The former is associated with a localized fracture process, denoted by cracking of the material, and, the latter, is associated with a more distributed fracture process which is usually termed as crushing of the material.

### 6.1 Formulation of the anisotropic continuum model

An accurate analysis of masonry structures in a macro-modeling (or composite) perspective requires a material description for all stress states. Difficulties arise especially due to the fact that almost no comprehensive experimental results are available (either for pre- and post-peak behavior), but also due to the intrinsic complexity of formulating anisotropic inelastic behavior. Only a few authors tried to develop specific macro-models for the analysis of masonry structures, in which anisotropic elasticity is combined with anisotropic inelastic behavior. To the knowledge of the author, only Dhanasekar *et al.* (1985,1986) and Seim (1994) - based on the work of Ganz (1985) - dealt with the implementation of a specific numerical model for masonry. The cited authors proposed rather complex yield surfaces which almost preclude the use of modern plasticity concepts and an accurate representation of inelastic behavior (hardening and softening). The yield surface to be developed in the present study combines the

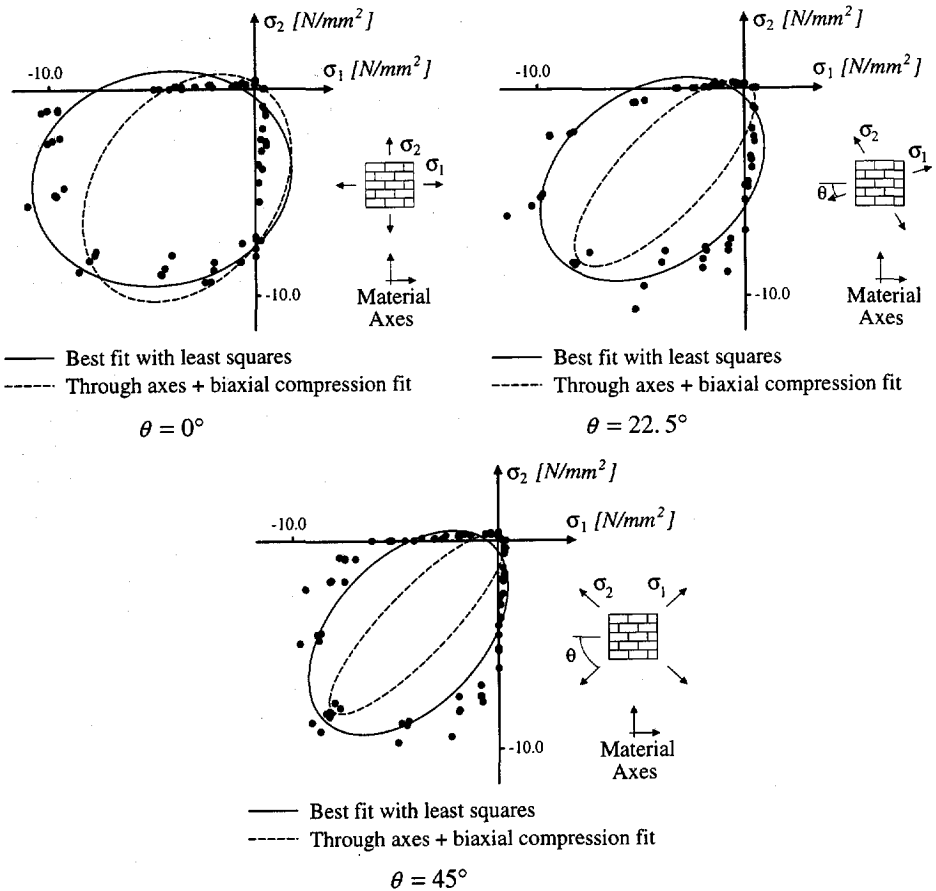


Figure 6.1 Comparison between a Hoffman type yield surface and experimental results from Page (1981,1983).

advantages of modern plasticity concepts with a powerful representation of anisotropic material behavior, which includes different hardening/softening behavior along each material axis.

It is noted that a representation of an orthotropic yield surface in terms of principal stresses or stress invariants only is not possible. For plane stress situations, which is the case of the present study, a graphical representation in terms of the full stress vector ( $\sigma_x$ ,  $\sigma_y$  and  $\tau_{xy}$ ) is necessary. The material axes are assumed to be defined by the bed joints direction ( $x$  direction) and the head joints direction ( $y$  direction). Another possible representation can be obtained in terms of principal stresses and an angle  $\theta$ . The angle  $\theta$  measures the rotation between the principal stress axes and the material axes. Clearly, different principal stress diagrams are found according to different values of  $\theta$ .

Basically, two different approaches for the macro-modeling of masonry can be used. The first approach is to describe the material behavior with a single yield criterion. The Hoffman yield criterion is quite flexible and attractive to use, see Schellekens and De Borst (1990) and Scarpas and Blaauwendraad (1993), but yields a non-acceptable fit of the masonry experimental values as shown in Figure 6.1. A least squares fit of the experimental results from Page (1981,1983) with a Hoffman type<sup>†</sup> yield criterion turns out to show no tensile strength in uniaxial behavior. A manual fit through the different uniaxial strengths and the compressive failure obtained upon loading with  $\sigma_1 = \sigma_2$  and  $\theta = 0^\circ$  gives a very poor representation of the diagrams for the other  $\theta$  values and a critical overestimation of strength in the tension-compression regime. A single surface fit of the experimental values would lead to an extremely complex yield surface with a mixed hardening/softening rule in order to describe properly the inelastic behavior. It is believed that this approach is practically non-feasible. Thus, a second approach, which consists of an extension of conventional formulations for isotropic quasi-brittle materials to describe orthotropic behavior, will be adopted. Formulations of isotropic quasi-brittle materials behavior consider, generally, different inelastic criteria for tension and compression. In the present study, an extension of the work of Feenstra and De Borst (1996), who utilized this approach for concrete with a Rankine and a Drucker-Prager criterion, will be presented. In order to model orthotropic material behavior, a Hill type<sup>‡</sup> yield criterion for compression and a Rankine type<sup>‡</sup> yield criterion for tension, see Figure 6.2, will be proposed.

The performance of the numerical implementation has been assessed elsewhere, see

- 
- (†) The word *type* is used here because the original authors, see Hill (1948) and Hoffman (1967), assumed a three-dimensional formulation. The influence of the out-of-plane direction is generally unknown and will not be considered in this study. The yield surfaces adopted should, in fact, be considered as a particular case of the complete quadratic formulation from Tsai and Wu (1971).
- (‡) The word *type* is used here because the Rankine yield criterion represents the material strength along the maximum principal stress. For an anisotropic material such definition is clearly not possible. The proposed yield surface for tension will be derived from the original Rankine yield criterion but represents solely a fit of experimental results.

Lourenço (1995b), and will not be reviewed here. The formulation will be presented in typical plane stress conditions, with three stress components. For the purpose of standardization of the DIANA code and for a simpler future extension of the model to a three-dimensional stress-state, the implementation has been actually carried out in plane strain conditions, with four stress components, according to the expansion/compression mechanism introduced by De Borst (1991). The implementation with four stress components is described in Lourenço (1995b).

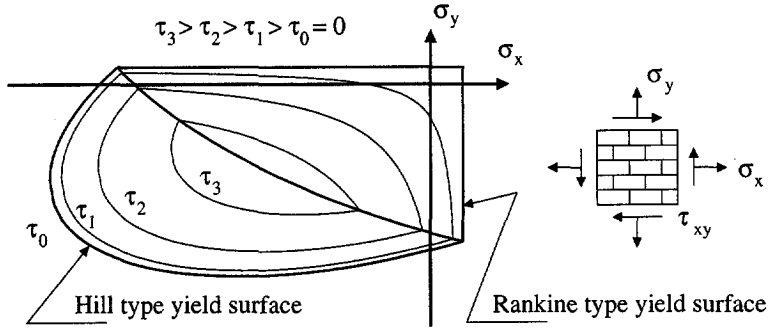


Figure 6.2 Proposed composite yield surface with iso-shear stress lines. Different strength values for tension and compression along each material axis.

### 6.1.1 Discretization aspects

The softening behavior of masonry is modeled with a smeared approach in which the damaged material is still considered as a continuum. With this assumption, the localized damage can be represented by the scalar  $\kappa$ , which is related by an equivalent length to the released energy per unit cracked area,  $G_f$ . In a finite element calculation this equivalent length should correspond to a representative dimension of the mesh size so that the results obtained are objective with regard to mesh refinement, see Bažant and Oh (1983). The equivalent length, denoted by  $h$ , depends in general on the chosen element type, element size, element shape, integration scheme and even on the particular problem considered. In this study it is assumed that the equivalent length is related to the area of an element by, see Feenstra (1993),

$$h = \alpha_h \sqrt{A_e} = \alpha_h \left( \sum_{\xi=1}^{n_\xi} \sum_{\eta=1}^{n_\eta} \det(\mathbf{J}) w_\xi w_\eta \right)^{1/2} \quad (6.1)$$

in which  $w_\xi$  and  $w_\eta$  are the weight factors of the Gaussian integration rule as it is tacitly assumed that the elements are always integrated numerically. The local, isoparametric coordinates of the integration points are given by  $\xi$  and  $\eta$ . The factor  $\alpha_h$  is a modification factor which is equal to one for quadratic elements and equal to  $\sqrt{2}$  for linear elements, see Rots (1988).

The inelastic work  $g_f$  is defined by the integral

$$g_f = \int \boldsymbol{\sigma}^T d\boldsymbol{\varepsilon} = \int \boldsymbol{\sigma}^T d\boldsymbol{\varepsilon}^p \quad (6.2)$$

which corresponds to the area under the stress-strain diagram for uniaxial loading. Assuming that the inelastic work  $g_f$  is uniformly distributed over the equivalent length, the relation between the fracture energy  $G_f$  and the work  $g_f$  is given by

$$g_f = \frac{G_f}{h} \quad (6.3)$$

This results in a material model related to the energy which has to be dissipated due to the irreversible damage in the material. The concept of an equivalent length has been used extensively in the analysis of concrete structures. In this study, this concept will be used to model the tensile and compressive softening behavior of masonry, although it is recognized that the latter mechanism is physically more a volume-driven process than a surface-driven process.

### 6.1.2 A Rankine type criterion

The difficulties of formulating the Rankine yield criterion in the principal stress space are addressed, for example, in Feenstra (1993). A more adequate formulation of the Rankine yield criterion is given by a single function, which is governed by the first principal stress and one equivalent stress  $\bar{\sigma}_t$ , which describes the softening behavior of the material, as, see Feenstra and De Borst (1995),

$$f_1 = \frac{\sigma_x + \sigma_y}{2} + \sqrt{\left(\frac{\sigma_x - \sigma_y}{2}\right)^2 + \tau_{xy}^2} - \bar{\sigma}_t(\kappa_t) \quad (6.4)$$

where the scalar  $\kappa_t$  controls the amount of softening. The assumption of isotropic softening is not completely valid for a material such as concrete or masonry which can be loaded up to the tensile strength even if in the perpendicular direction damage has already occurred. This problem is partially solved in Feenstra and De Borst (1995) by using kinematic softening such that the yield surface is shifted in the direction of the first principal stress. It is noted that the above formulation of kinematic softening is also not quite realistic. If the material, initially, is loaded along a certain direction until softening is completed and, then, is loaded in a direction orthogonal to the crack previously open, ideally plastic behavior is found. This is due to the fact that all the fracture energy has been consumed during the opening of the first crack. An elegant solution seemed to be the use of two independent softening parameters to control the shifting of the yield surface. Such a formulation of the Rankine yield criterion, which reproduces exactly the material feature in tension just described, is given in Lourenço *et al.* (1995). Then,

the response of the model seems to lie between the fixed and rotating crack models. Therefore, it comprises the benefit of a model with memory and a flexible shear response. Unfortunately, for certain values of the trial stress the return mapping becomes ill-posed and an almost singular Jacobian is found close to the solution. This precludes the use of the formulation of Lourenço *et al.* (1995) in large scale computations due to the lack of robustness and the need to consider extremely small steps, together with advanced solution procedures at the local level.

Here, a single scalar is used to control an orthotropic Rankine type yield surface. The scalar measures the amount of softening simultaneously in the two material axes, but the model still incorporates two different fracture energies. This approach is less attractive from a physical point of view but leads to a robust algorithm and should be preferred in practice. The expression for the Rankine yield criterion, cf. eq. (6.4), can be rewritten as

$$f_1 = \frac{(\sigma_x - \bar{\sigma}_t(\kappa_t)) + (\sigma_y - \bar{\sigma}_t(\kappa_t))}{2} + \sqrt{\left(\frac{(\sigma_x - \bar{\sigma}_t(\kappa_t)) - (\sigma_y - \bar{\sigma}_t(\kappa_t))}{2}\right)^2 + \tau_{xy}^2} \quad (6.5)$$

where coupling exists between the stress components and the yield value. Setting forth a Rankine type yield surface for an orthotropic material, with different tensile strengths along the  $x, y$  directions, see Figure 6.3, is now straightforward if eq. (6.5) is modified to

$$f_1 = \frac{(\sigma_x - \bar{\sigma}_{t1}(\kappa_t)) + (\sigma_y - \bar{\sigma}_{t2}(\kappa_t))}{2} + \sqrt{\left(\frac{(\sigma_x - \bar{\sigma}_{t1}(\kappa_t)) - (\sigma_y - \bar{\sigma}_{t2}(\kappa_t))}{2}\right)^2 + \alpha \tau_{xy}^2} \quad (6.6)$$

where the parameter  $\alpha$ , which controls the shear stress contribution to failure, reads

$$\alpha = \frac{f_{tx} f_{ty}}{\tau_u^2} \quad (6.7)$$

Here,  $f_{tx}$ ,  $f_{ty}$  and  $\tau_u$  are, respectively, the uniaxial tensile strengths in the  $x, y$  directions and the pure shear strength. Note that the material axes are now fixed with respect to a specific frame of reference and it shall be assumed that all stresses and strains for the elastoplastic algorithm are given in the material reference axes, see also Section 6.1.5. Eq. (6.6) can be recast in a matrix form as

$$f_1 = (1/2 \xi^T \mathbf{P}_t \xi)^{1/2} + 1/2 \pi^T \xi \quad (6.8)$$

where the projection matrix  $\mathbf{P}_t$  reads

$$\mathbf{P}_t = \begin{bmatrix} 1/2 & -1/2 & 0 \\ -1/2 & 1/2 & 0 \\ 0 & 0 & 2\alpha \end{bmatrix} \quad (6.9)$$

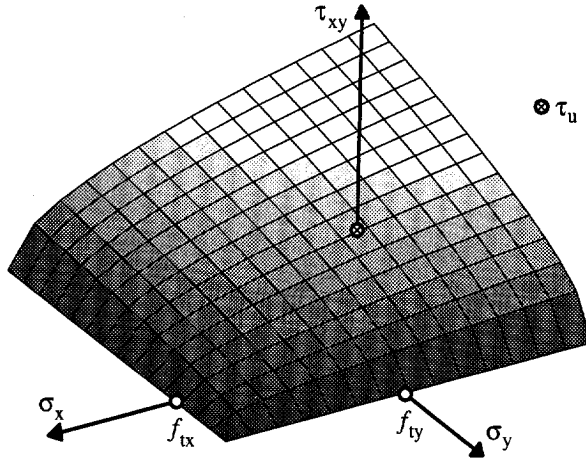


Figure 6.3 Orthotropic Rankine type yield surface (shown for  $\tau_{xy} \geq 0$ ).

the projection vector  $\pi$  reads

$$\pi = \{ 1 \ 1 \ 0 \}^T \quad (6.10)$$

the reduced stress vector  $\xi$  reads

$$\xi = \sigma - \eta \quad (6.11)$$

the stress vector  $\sigma$  and the back stress vector  $\eta$  read

$$\sigma = \{ \sigma_x \quad \sigma_y \quad \tau_{xy} \}^T \quad (6.12)$$

$$\eta = \{ \bar{\sigma}_{t1}(\kappa_t) \quad \bar{\sigma}_{t2}(\kappa_t) \quad 0 \}^T$$

Exponential tensile softening is considered for both equivalent stress-equivalent strain diagrams, with different fracture energies ( $G_{fx}$  and  $G_{fy}$ ) for each yield value, which reads

$$\bar{\sigma}_{t1} = f_{tx} \exp\left(-\frac{h f_{tx}}{G_{fx}} \kappa_t\right) \quad \bar{\sigma}_{t2} = f_{ty} \exp\left(-\frac{h f_{ty}}{G_{fy}} \kappa_t\right) \quad (6.13)$$

It is noted that the equivalent length  $h$ , cf. eq. (6.1), can lead to a snap-back at constitutive level if the element size is large. Then, the concept of fracture energy which has been assumed is no longer satisfied. In such a case, the strength limit has to be reduced in order to obtain an objective fracture energy by a sudden stress drop, resulting at a

certain stage in brittle failure, see Rots (1988). The condition of maximum equivalent length is given by

$$h \leq \frac{G_{fi} E_i}{f_{ii}^2} \quad (6.14)$$

where  $E_i$  is the Young's modulus and the subscript  $i$  refers to the material axis. If this condition is violated, for any of the material axes, the tensile strength  $f_{ii}$  is reduced according to

$$f_{ii} = \left( \frac{G_{fi} E_i}{h} \right)^{1/2} \quad (6.15)$$

It is noted that eq. (6.15) yields a reduction on the material strength without any physical ground, where the idea is solely to obtain an energy release independent of the mesh size. It is believed that this objective should be accomplished by means of a mesh refinement and not with a strength reduction.

Finally, for an orthotropic material with different yield values along the material axes, it would seem only natural to assume two different equivalent lengths along the material axes (this is of course irrelevant in the special case of a mesh with square elements). However, the equivalent length depends on so many factors that more complex assumptions are disregarded.

A non-associated plastic potential  $g_1$

$$g_1 = (1/2 \xi^T \mathbf{P}_g \xi)^{1/2} + 1/2 \pi^T \xi \quad (6.16)$$

is considered, where the projection matrix  $\mathbf{P}_g$  represents the Rankine plastic flow and reads

$$\mathbf{P}_g = \begin{bmatrix} 1/2 & -1/2 & 0 \\ -1/2 & 1/2 & 0 \\ 0 & 0 & 2 \end{bmatrix} \quad (6.17)$$

The inelastic behavior is described by a strain softening hypothesis, cf. eq. (3.29), given by the maximum principal plastic strain  $\dot{\epsilon}_1^p$  as

$$\dot{\kappa}_t = \dot{\epsilon}_1^p = \frac{\dot{\epsilon}_x^p + \dot{\epsilon}_y^p}{2} + 1/2 \sqrt{(\dot{\epsilon}_x^p - \dot{\epsilon}_y^p)^2 + (\dot{\gamma}_{xy}^p)^2} \quad (6.18)$$

This expression can be recast in a matrix form as

$$\dot{\kappa}_t = \dot{\epsilon}_1^p = \left( 1/2 (\dot{\epsilon}^p)^T \mathbf{Q} \dot{\epsilon}^p \right)^{1/2} + 1/2 \pi^T \dot{\epsilon}^p \quad (6.19)$$

where

$$\mathbf{Q} = \begin{bmatrix} 1/2 & -1/2 & 0 \\ -1/2 & 1/2 & 0 \\ 0 & 0 & 1/2 \end{bmatrix} \quad (6.20)$$

which reduces to the particularly simple expression

$$\dot{\kappa}_t = \dot{\lambda}_t \quad (6.21)$$

The return mapping algorithm, cf. eq. (3.39), reduces to the following set of four equations containing four unknowns (the  $\sigma_{n+1}$  components and  $\Delta\kappa_{t, n+1} = \Delta\lambda_{t, n+1}$ )

$$\begin{cases} \mathbf{D}^{-1} (\sigma_{n+1} - \sigma^{trial}) + \Delta\lambda_{t, n+1} \frac{\partial g_1}{\partial \sigma} \Big|_{n+1} = \mathbf{0} \\ f_{1, n+1} = (1/2 \xi_{n+1}^T \mathbf{P}_t \xi_{n+1})^{1/2} + 1/2 \pi^T \xi_{n+1} = 0 \end{cases} \quad (6.22)$$

where  $\mathbf{D}$  represents the symmetric orthotropic elasticity tensor. Due to the coupling of the  $\sigma_{n+1}$  and  $\kappa_{t, n+1}$  values it is not possible to obtain an explicit one variable nonlinear equation. The Jacobian necessary for the iterative local Newton-Raphson method reads

$$\mathbf{J}_{n+1} = \begin{bmatrix} \mathbf{D}^{-1} + \Delta\lambda_{t, n+1} \frac{\partial^2 g_1}{\partial \sigma^2} & | & \frac{\partial g_1}{\partial \sigma} + \Delta\lambda_{t, n+1} \frac{\partial^2 g_1}{\partial \sigma \partial \kappa_t} \\ \hline \left( \frac{\partial f_1}{\partial \sigma} \right)^T & | & \frac{\partial f_1}{\partial \kappa_t} \end{bmatrix} \quad (6.23)$$

where

$$\begin{aligned} \frac{\partial f_1}{\partial \sigma} &= \frac{\mathbf{P}_t \xi_{n+1}}{2(1/2 \xi_{n+1}^T \mathbf{P}_t \xi_{n+1})^{1/2}} + 1/2 \pi & \frac{\partial g_1}{\partial \sigma} &= \frac{\mathbf{P}_g \xi_{n+1}}{2(1/2 \xi_{n+1}^T \mathbf{P}_g \xi_{n+1})^{1/2}} + 1/2 \pi \\ \frac{\partial f_1}{\partial \kappa_t} &= - \left( \frac{\partial f_1}{\partial \sigma} \right)^T \frac{\partial \eta}{\partial \kappa_t} & \frac{\partial^2 g_1}{\partial \sigma \partial \kappa_t} &= - \frac{\partial^2 g_1}{\partial \sigma^2} \frac{\partial \eta}{\partial \kappa_t} \\ \frac{\partial \eta}{\partial \kappa_t} &= \left\{ \frac{\partial \bar{\sigma}_{t1}}{\partial \kappa_t}, \frac{\partial \bar{\sigma}_{t2}}{\partial \kappa_t}, 0 \right\}^T & & \\ \frac{\partial^2 g_1}{\partial \sigma^2} &= \frac{\mathbf{P}_g}{2(1/2 \xi_{n+1}^T \mathbf{P}_g \xi_{n+1})^{1/2}} - \frac{\mathbf{P}_g \xi_{n+1} \xi_{n+1}^T \mathbf{P}_g}{4(1/2 \xi_{n+1}^T \mathbf{P}_g \xi_{n+1})^{3/2}} & & \end{aligned} \quad (6.24)$$

However, this numerical algorithm is not stable for the entire stress domain. In the apex of the yield surface the gradient of the plastic potential, cf. eq. (6.24)<sub>1</sub>, is not

defined. It is further noted that even if the proposed plastic potential, cf. eq.(6.16), is rewritten in a quadratic form as

$$g_1 = 1/2 \xi^T \mathbf{P}_g \xi + 1/4 \xi^T \boldsymbol{\pi} |\xi^T \boldsymbol{\pi}| \quad (6.25)$$

the problem of a non-defined gradient in the apex is not solved. The new expression for the gradient reads

$$\frac{\partial g_1}{\partial \boldsymbol{\sigma}} = \mathbf{P}_g \xi + 1/2 \boldsymbol{\pi} |\xi^T \boldsymbol{\pi}| \quad (6.26)$$

which degenerates to a point in the apex ( $\frac{\partial g_1}{\partial \boldsymbol{\sigma}} = \mathbf{0}$ ) due to the singularity of yield surface. For the apex regime, however, a quite simple algorithm can be used because  $\tau_{xy} = 0$ . In this case, the stress update cf. eq. (6.22)<sub>1</sub>, is simply a return mapping to the apex, independently of the trial stress value, and reads

$$\boldsymbol{\sigma}_{n+1} = \boldsymbol{\eta}_{n+1} \quad (6.27)$$

The above stress update is sufficient to fulfil  $f_{1, n+1} = 0$ . It remains to update the softening scalar according to eq. (6.19). For this purpose a nonlinear equation in one variable can be written as

$$F(\Delta \kappa_{t, n+1}) = \Delta \kappa_{t, n+1} - \Delta \boldsymbol{\varepsilon}_{1, n+1}^p = \left( 1/2 (\Delta \boldsymbol{\varepsilon}_{n+1}^p)^T \mathbf{Q} \Delta \boldsymbol{\varepsilon}_{n+1}^p \right)^{1/2} + 1/2 \boldsymbol{\pi}^T \Delta \boldsymbol{\varepsilon}_{n+1}^p = 0 \quad (6.28)$$

where the increment of the plastic strain vector  $\Delta \boldsymbol{\varepsilon}_{n+1}^p$  can be calculated from

$$\Delta \boldsymbol{\varepsilon}_{n+1}^p = \mathbf{D}^{-1} (\boldsymbol{\sigma}^{trial} - \boldsymbol{\sigma}_{n+1}) \quad (6.29)$$

A secant method is used to solve this nonlinear equation instead of the regular Newton-Raphson method. This has proven robust and fast, see Lourenço (1994,1995b).

The consistent tangent stiffness matrix is directly obtained from eq. (3.55) for the standard regime. For the apex, differentiation of the update equations yields, after algebraic manipulation,

$$\mathbf{D}^{ep} = \frac{\partial \boldsymbol{\sigma}}{\partial \boldsymbol{\varepsilon}} \Big|_{n+1} = \left[ \mathbf{I} + \frac{\partial \boldsymbol{\eta}}{\partial \kappa_t} \left( \frac{\partial \Delta \kappa_t}{\partial \boldsymbol{\varepsilon}^p} \right)^T \mathbf{D}^{-1} \right]^{-1} \frac{\partial \boldsymbol{\eta}}{\partial \kappa_t} \left( \frac{\partial \Delta \kappa_t}{\partial \boldsymbol{\varepsilon}^p} \right)^T \quad (6.30)$$

with

$$\frac{\partial \Delta \kappa_t}{\partial \boldsymbol{\varepsilon}^p} = \frac{\mathbf{Q} \Delta \boldsymbol{\varepsilon}_{n+1}^p}{2 \left( 1/2 (\Delta \boldsymbol{\varepsilon}_{n+1}^p)^T \mathbf{Q} \Delta \boldsymbol{\varepsilon}_{n+1}^p \right)^{1/2}} + 1/2 \boldsymbol{\pi} \quad (6.31)$$

### 6.1.3 A Hill type criterion

The simplest yield surface that features different compressive strengths along the material axes is a rotated centered ellipsoid in the full plane stress space ( $\sigma_x$ ,  $\sigma_y$  and  $\tau_{xy}$ ), see Figure 6.4. The expression for such a quadric is

$$f_2 = A \sigma_x^2 + B \sigma_x \sigma_y + C \sigma_y^2 + D \tau_{xy}^2 - 1 = 0 \quad (6.32)$$

where A, B, C and D are four material parameters such that  $B^2 - 4AC < 0$ , in order to ensure convexity.

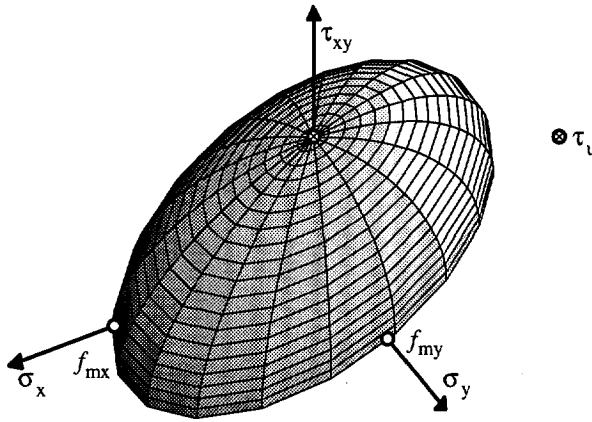


Figure 6.4 The Hill type yield surface (shown for  $\tau_{xy} \geq 0$ ).

For the numerical implementation the yield surface can be advantageously recast in a square root matrix form and the variables can be defined in a more amenable way. With the definition of  $A = 1 / (\bar{\sigma}_{c1}(\kappa_c))^2$ ,  $B = \beta / (\bar{\sigma}_{c1}(\kappa_c) \bar{\sigma}_{c2}(\kappa_c))$ ,  $C = 1 / (\bar{\sigma}_{c2}(\kappa_c))^2$  and  $D = \gamma / (\bar{\sigma}_{c1}(\kappa_c) \bar{\sigma}_{c2}(\kappa_c))$ , where  $\bar{\sigma}_{c1}(\kappa_c)$  and  $\bar{\sigma}_{c2}(\kappa_c)$  are, respectively, the yield values along the material axes  $x$  and  $y$ , the proposed yield surface can be rewritten as

$$f_2 = (1/2 \boldsymbol{\sigma}^T \mathbf{P}_c \boldsymbol{\sigma})^{1/2} - \bar{\sigma}_c(\kappa_c) \quad (6.33)$$

where the projection matrix  $\mathbf{P}_c$  reads

$$\mathbf{P}_c = \begin{bmatrix} 2 \frac{\bar{\sigma}_{c2}(\kappa_c)}{\bar{\sigma}_{c1}(\kappa_c)} & \beta & 0 \\ \beta & 2 \frac{\bar{\sigma}_{c1}(\kappa_c)}{\bar{\sigma}_{c2}(\kappa_c)} & 0 \\ 0 & 0 & 2\gamma \end{bmatrix} \quad (6.34)$$

the yield value  $\bar{\sigma}_c$  is given by

$$\bar{\sigma}_c = \sqrt{\bar{\sigma}_{c1} \bar{\sigma}_{c2}} \quad (6.35)$$

and the scalar  $\kappa_c$  controls the amount of hardening and softening. It is noted that the  $\beta$  and  $\gamma$  values introduced in eq. (6.34) are additional material parameters that determine the shape of the yield surface. The parameter  $\beta$  controls the coupling between the normal stress values, i.e. rotates the yield surface around the shear stress axis, and must be obtained from one additional experimental test, e.g. biaxial compression with a unit ratio between principal stresses. If this test is used to obtain the parameter  $\beta$ , the collapse load under biaxial compression ( $\sigma_x = \sigma_y = -f_{45^\circ}$  and  $\tau_{xy} = 0$ ) leads to

$$\beta = \left[ \frac{1}{f_{45^\circ}^2} - \frac{1}{f_{mx}^2} - \frac{1}{f_{my}^2} \right] f_{mx} f_{my} \quad (6.36)$$

The parameter  $\gamma$ , which controls the shear stress contribution to failure, can be obtained from

$$\gamma = \frac{f_{mx} f_{my}}{\tau_u^2} \quad (6.37)$$

where  $\tau_u$  is the material pure shear strength.

The inelastic law proposed in Chapter 4 for the elliptical cap is again adopted here. Parabolic hardening followed by parabolic/exponential softening is considered for both equivalent stress-equivalent strain diagrams, with different compressive fracture energies ( $G_{fcx}$  and  $G_{fcy}$ ) along the material axes. The problem of mesh objectivity of the analyses with strain softening materials is a well debated issue, at least for tensile behavior, and the stress-strain diagram must be adjusted according to a characteristic length  $h$  to provide an objective energy dissipation. The inelastic law shown in Figure 6.5 features hardening, softening and a residual plateau of ideally plastic behavior. A redefined compressive fracture energy  $G_{fci}$  (shaded area in Figure 6.5) corresponds only to the local contribution of the  $\bar{\sigma}_{ci}$ - $\kappa_c$  diagram, where the subscript  $i$  refers to the material axis. The basis for the present definition is only numerical, so that objective analyses with regard to mesh refinement are obtained, see also Section 6.3.3. However, some experimental evidence exists on a local and non-local component for the total compressive fracture energy, see Vonk (1992). The peak strength value is assumed to be reached simultaneously on both materials axes, i.e. isotropic hardening, followed by anisotropic softening as determined by the different fracture energies. A residual strength value is considered to avoid a cumbersome code (precluding the case when the compressive mode falls completely inside the tension mode) and to achieve a more robust code (precluding degeneration of the yield surface to a point). For practical reasons, it is

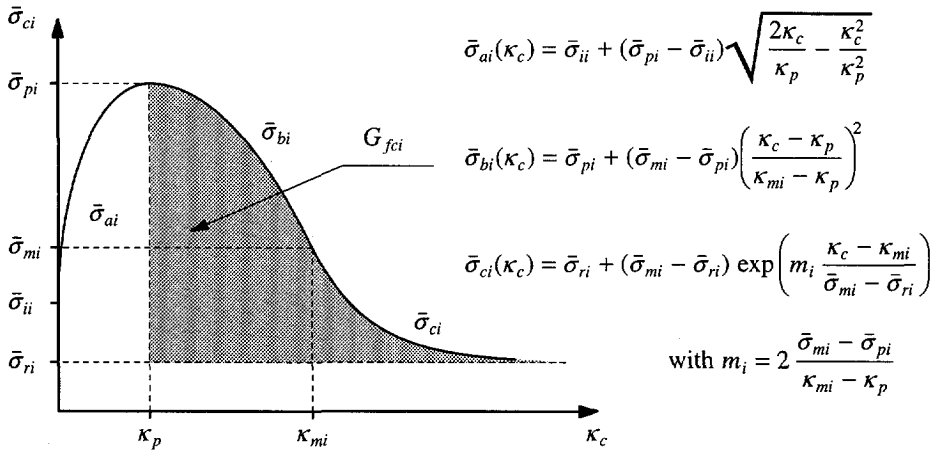


Figure 6.5 Hardening/softening law for compression.

assumed that all the stress values for the inelastic law are determined from the peak value  $\bar{\sigma}_{pi} = f_{mi}$  as follows:  $\bar{\sigma}_{ii} = 1/3 f_{mi}$ ,  $\bar{\sigma}_{mi} = 1/2 f_{mi}$  and  $\bar{\sigma}_{ri} = 1/10 f_{mi}$ . The equivalent plastic strain  $\kappa_p$ , corresponding to the peak compressive strength, is assumed to be an additional material parameter. In the case that no experimental results are available, this material parameter can be calculated assuming a total peak strain equal to  $2 \times 10^{-3}$ . In order to obtain a mesh independent energy dissipation the parameter  $\kappa_{mi}$  is given by

$$\kappa_{mi} = \frac{75}{67} \frac{G_{fci}}{h f_{mi}} + \kappa_p \quad (6.38)$$

To avoid a possible snap-back at constitutive level, the condition

$$\kappa_{mi} \geq \frac{f_{mi}}{E_i} + \kappa_p \quad (6.39)$$

is required. Otherwise, in order to obtain an objective fracture energy, the strength limit must be reduced to

$$f_{mi} = \left( \frac{75}{67} \frac{G_{fci} E_i}{h} \right)^{1/2} \quad (6.40)$$

An associated flow rule and a hardening/softening hypothesis according to eq. (3.32) are considered. This yields

$$\dot{\kappa}_c = \frac{1}{\bar{\sigma}_c} \boldsymbol{\sigma}^T \dot{\boldsymbol{\varepsilon}}^p = \dot{\lambda}_c \quad (6.41)$$

The return mapping algorithm, cf. eq. (3.39), reduces to the following set of four equations containing four unknowns (the  $\sigma_{n+1}$  components and  $\Delta\kappa_{c, n+1} = \Delta\lambda_{c, n+1}$ )

$$\begin{cases} \mathbf{D}^{-1} (\boldsymbol{\sigma}_{n+1} - \boldsymbol{\sigma}^{trial}) + \Delta\lambda_{c, n+1} \left. \frac{\partial f_2}{\partial \boldsymbol{\sigma}} \right|_{n+1} = \mathbf{0} \\ f_{2, n+1} = (1/2 \boldsymbol{\sigma}_{n+1}^T \mathbf{P}_{c, n+1} \boldsymbol{\sigma}_{n+1})^{1/2} - \bar{\sigma}_{c, n+1} = 0 \end{cases} \quad (6.42)$$

The set of equations can be reduced to one nonlinear equation, namely  $f_2(\Delta\lambda_{c, n+1}) = 0$ , see Lourenço (1995b). This approach will not be followed here in order to obtain a consistent framework for the several modes of the composite yield surface. Alternatively, the system of four nonlinear equations is solved with a regular Newton-Raphson method. The Jacobian necessary for this procedure reads

$$\mathbf{J}_{n+1} = \begin{bmatrix} \mathbf{D}^{-1} + \Delta\lambda_{c, n+1} \frac{\partial^2 f_2}{\partial \boldsymbol{\sigma}^2} & | & \frac{\partial f_2}{\partial \boldsymbol{\sigma}} + \Delta\lambda_{c, n+1} \frac{\partial^2 f_2}{\partial \boldsymbol{\sigma} \partial \kappa_c} \\ \hline \left( \frac{\partial f_2}{\partial \boldsymbol{\sigma}} \right)^T & | & \frac{\partial f_2}{\partial \kappa_c} \end{bmatrix} \quad (6.43)$$

where

$$\begin{aligned} \frac{\partial f_2}{\partial \boldsymbol{\sigma}} &= \frac{\mathbf{P}_c \boldsymbol{\sigma}_{n+1}}{2(1/2 \boldsymbol{\sigma}_{n+1}^T \mathbf{P}_c \boldsymbol{\sigma}_{n+1})^{1/2}} & \frac{\partial^2 f_2}{\partial \boldsymbol{\sigma}^2} &= \frac{\mathbf{P}_c}{2(1/2 \boldsymbol{\sigma}_{n+1}^T \mathbf{P}_c \boldsymbol{\sigma}_{n+1})^{1/2}} - \frac{\mathbf{P}_c \boldsymbol{\sigma}_{n+1} \boldsymbol{\sigma}_{n+1}^T \mathbf{P}_c}{4(1/2 \boldsymbol{\sigma}_{n+1}^T \mathbf{P}_c \boldsymbol{\sigma}_{n+1})^{3/2}} \\ \frac{\partial f_2}{\partial \kappa_c} &= \frac{\boldsymbol{\sigma}_{n+1}^T \frac{\partial \mathbf{P}_c}{\partial \kappa_c} \boldsymbol{\sigma}_{n+1}}{4(1/2 \boldsymbol{\sigma}_{n+1}^T \mathbf{P}_c \boldsymbol{\sigma}_{n+1})^{1/2}} - \frac{\frac{\partial \bar{\sigma}_{c1}}{\partial \kappa_c} \bar{\sigma}_{c2, n+1} + \frac{\partial \bar{\sigma}_{c2}}{\partial \kappa_c} \bar{\sigma}_{c1, n+1}}{2\bar{\sigma}_{c, n+1}} \\ \frac{\partial^2 f_2}{\partial \boldsymbol{\sigma} \partial \kappa_c} &= \frac{\frac{\partial \mathbf{P}_c}{\partial \kappa_c} \boldsymbol{\sigma}_{n+1}}{2(1/2 \boldsymbol{\sigma}_{n+1}^T \mathbf{P}_c \boldsymbol{\sigma}_{n+1})^{1/2}} - \frac{(\boldsymbol{\sigma}_{n+1}^T \frac{\partial \mathbf{P}_c}{\partial \kappa_c} \boldsymbol{\sigma}_{n+1}) \mathbf{P}_c \boldsymbol{\sigma}_{n+1}}{8(1/2 \boldsymbol{\sigma}_{n+1}^T \mathbf{P}_c \boldsymbol{\sigma}_{n+1})^{3/2}} \end{aligned} \quad (6.44)$$

$$\frac{\partial \mathbf{P}_c}{\partial \kappa_c} = \text{diag} \left\{ 2 \left[ \frac{\frac{\partial \bar{\sigma}_{c2}}{\partial \kappa_c} \bar{\sigma}_{c1, n+1} - \frac{\partial \bar{\sigma}_{c1}}{\partial \kappa_c} \bar{\sigma}_{c2, n+1}}{\bar{\sigma}_{c1, n+1}^2} \right], 2 \left[ \frac{\frac{\partial \bar{\sigma}_{c1}}{\partial \kappa_c} \bar{\sigma}_{c2, n+1} - \frac{\partial \bar{\sigma}_{c2}}{\partial \kappa_c} \bar{\sigma}_{c1, n+1}}{\bar{\sigma}_{c2, n+1}^2} \right], 0 \right\}$$

The consistent tangent stiffness matrix is directly obtained from eq. (3.55).

### 6.1.4 A composite yield criterion

The tension and compression yield criteria are combined next in a composite yield surface, according to the aspects of multisurface plasticity reviewed in Chapter 3.

Assuming that the tension and compression regimes are uncoupled, the return mapping algorithm for the corner regime, cf. eq. (3.46), reduces to the following set of five equations containing five unknowns (the  $\sigma_{n+1}$  components,  $\Delta\kappa_{t, n+1} = \Delta\lambda_{t, n+1}$  and  $\Delta\kappa_{c, n+1} = \Delta\lambda_{c, n+1}$ )

$$\left\{ \begin{array}{l} \mathbf{D}^{-1} (\sigma_{n+1} - \sigma^{trial}) + \Delta\lambda_{t, n+1} \left. \frac{\partial g_1}{\partial \sigma} \right|_{n+1} + \Delta\lambda_{c, n+1} \left. \frac{\partial f_2}{\partial \sigma} \right|_{n+1} = \mathbf{0} \\ f_{1, n+1} = (1/2 \xi_{n+1}^T \mathbf{P}_t \xi_{n+1})^{1/2} + 1/2 \pi^T \xi_{n+1} = 0 \\ f_{2, n+1} = (1/2 \sigma_{n+1}^T \mathbf{P}_{c, n+1} \sigma_{n+1})^{1/2} - \bar{\sigma}_{c, n+1} = 0 \end{array} \right. \quad (6.45)$$

Due to the coupling of the  $\sigma_{n+1}$ ,  $\kappa_{t, n+1}$  and  $\kappa_{c, n+1}$  values it is not possible to obtain a two variable system of nonlinear equations. The Jacobian necessary for the iterative local Newton-Raphson method reads

$$\mathbf{J} = \left[ \begin{array}{ccc|ccc} \mathbf{D}^{-1} + \Delta\lambda_{t, n+1} \frac{\partial^2 g_1}{\partial \sigma^2} & | & \frac{\partial g_1}{\partial \sigma} + \Delta\lambda_{t, n+1} \frac{\partial^2 g_1}{\partial \sigma \partial \kappa_t} & | & \frac{\partial f_2}{\partial \sigma} + \Delta\lambda_{c, n+1} \frac{\partial^2 f_2}{\partial \sigma \partial \kappa_c} \\ + \Delta\lambda_{c, n+1} \frac{\partial^2 f_2}{\partial \sigma^2} & + & \text{-----} & + & \text{-----} \\ \left( \frac{\partial f_1}{\partial \sigma} \right)^T & | & \frac{\partial f_1}{\partial \kappa_t} & | & 0 \\ \text{-----} & + & \text{-----} & + & \text{-----} \\ \left( \frac{\partial f_2}{\partial \sigma} \right)^T & | & 0 & | & \frac{\partial f_2}{\partial \kappa_c} \end{array} \right] \quad (6.46)$$

where all the terms have been defined in eq. (6.24) and eq. (6.44). The consistent tangent stiffness matrix is directly obtained from eq. (3.55).

### 6.1.5 The orientation of the material axes

For the sake of simplicity, the formulation of the plasticity model was presented based on the assumption that the principal axes of orthotropy coincided with the frame of reference (local or global) for stresses and strains in finite element computations. Since this is not necessarily the case, such non-alignment effects must be taken into account.

Two different approaches can be followed. In the first approach, with each call to the plasticity model, stresses, strains and, finally, consistent tangent stiffness matrices must be rotated into and out of the material frame of reference, respectively, as pre- and post-processing. In the second approach, before the analysis begins, the elastic stiffness matrix  $\mathbf{D}$ , the projection matrices  $\mathbf{P}_t$  and  $\mathbf{P}_c$ , and the projection vector  $\boldsymbol{\pi}$  must be rotated from the material frame of reference into the global frame of reference at each quadrature point, eliminating the need of all subsequent rotation operations. The drawback of the latter approach is that the matrices then lose their sparse nature. For this reason, the plasticity model is implemented employing the former option.

## 6.2 Definition of the model parameters from experimental results

This section provides insight into the required information to define the anisotropic composite yield criterion and into the role of the different material parameters. This point becomes relevant due to the reduced existing experience in using anisotropic models and the complexity of the proposed material model.

### 6.2.1 Required information to define the yield criterion

The proposed material model has seven strength parameters ( $f_{tx}$ ,  $f_{ty}$ ,  $f_{mx}$ ,  $f_{my}$ ,  $\alpha$ ,  $\beta$  and  $\gamma$ ) and five inelastic parameters ( $G_{fx}$ ,  $G_{fy}$ ,  $G_{fxc}$ ,  $G_{fyc}$  and  $\kappa_p$ ). The first group of four strength parameters are the uniaxial tensile and compressive strength along the material axes, which are natural due to the orthotropic behavior of masonry. This means that a complete characterization of the material model requires the tests shown in Figure 6.6. It suffices that these tests are performed under displacement control conditions to obtain also the inelastic parameters that define the model, viz. the four independent fracture energies (tension and compression) and the peak strain in compression.

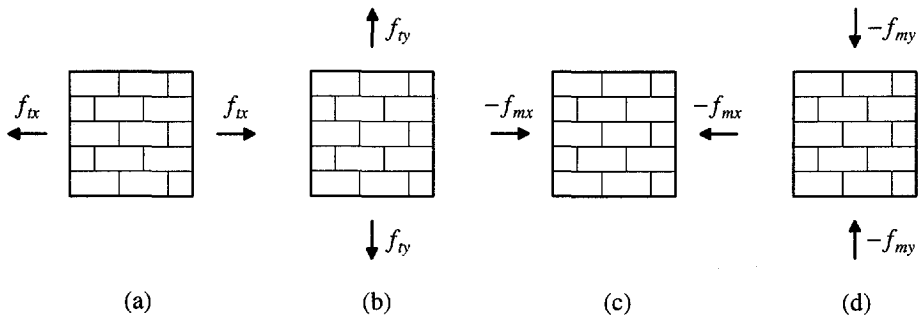


**Figure 6.6** Natural tests to calibrate the composite model: uniaxial tension (a) parallel to the bed joints and (b) normal to the bed joints; uniaxial compression (c) parallel to the bed joints and (d) normal to the bed joints.

Additional tests are necessary to fully calibrate the yield criterion. Figure 6.7 illustrates three possible tests to determine the parameter  $\alpha$ , which weights the shear stress contribution to tensile failure, parameter  $\beta$ , which controls the coupling between normal stress values in the case of compressive failure, and parameter  $\gamma$ , which weights the shear stress contribution to compressive failure.

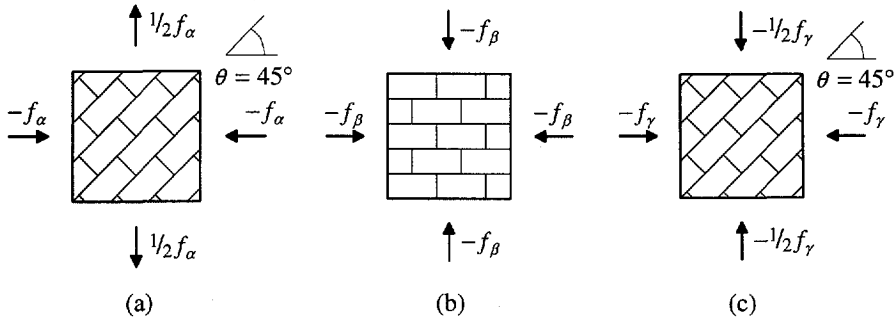


Figure 6.7 Possible non-standard tests to calibrate the composite model and calculate (a) parameter  $\alpha$ , (b) parameter  $\beta$  and (c) parameter  $\gamma$ .

With these tests, the model parameters  $\alpha$ ,  $\beta$  and  $\gamma$  read

$$\alpha = \frac{1}{9} \left( 1 + 4 \frac{f_{tx}}{f_\alpha} \right) \left( 1 + 4 \frac{f_{ty}}{f_\alpha} \right) \quad \beta = \left[ \frac{1}{f_\beta^2} - \frac{1}{f_{mx}^2} - \frac{1}{f_{my}^2} \right] f_{mx} f_{my} \quad (6.47)$$

$$\gamma = \left[ \frac{16}{f_\gamma^2} - 9 \left( \frac{1}{f_{mx}^2} + \frac{\beta}{f_{mx} f_{my}} + \frac{1}{f_{my}^2} \right) \right] f_{mx} f_{my}$$

Other loading paths can be adopted for the calculation of the parameters  $\alpha$ ,  $\beta$  and  $\gamma$  but a nice feature of the tests shown in Figure 6.7 is that they are equidistant from both material axes ( $\sigma_x = \sigma_y$ ). The most important characteristic of the proposed non-standard tests is, however, their ability to trigger the correct failure regime. Figure 6.8 shows the typical position of all tests with respect to the composite yield criterion. The picture demonstrates the importance of selecting adequate tests to calculate parameters  $\alpha$  and  $\gamma$ . The intersection of the tension and compression regimes is not known in advance and quite different shapes can be obtained for this intersection, see also Section 6.2.2. For this reason, the tests suggested to calculate parameters  $\alpha$  and  $\gamma$  include a lateral load capable of, in principle, leading to a failure mode distant from the corner regime. This has been checked for all the composite yield criteria presented in the next section.

It is stressed that, ideally, a large number of tests should be carried out for different loading paths so that the yield criterion can be determined resorting to the least squares method.

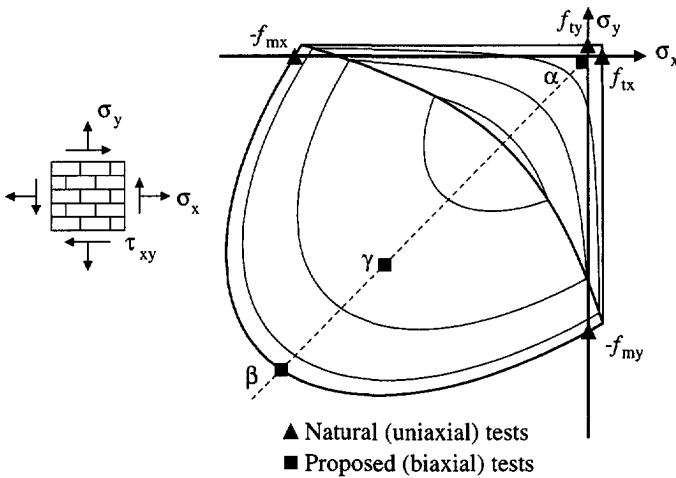


**Figure 6.8** Typical position of the natural tests and proposed non-standard tests with respect to the composite model.

## 6.2.2 Comparison with experimental data of masonry strength

The ability of the proposed model to reproduce the strength of different masonry types is assessed next. A comparison with different experimental data is carried out, in which the material parameters are calculated with the least squares method. For the tension regime, the tensile and shear strength values are adopted, where the data are available.

The most complete set of strength data of biaxially loaded masonry is given by Page (1981,1983) who tested 102 panels of half-scale solid clay brick masonry, with dimensions  $360 \times 360 \times 50$  [mm<sup>3</sup>]. The panels were loaded proportionally in the principal stress directions  $\sigma_1$  and  $\sigma_2$  along different orientations  $\theta$  with respect to the material axes. The comparison between the experimental values and the model is given in Figure 6.9. Globally, good agreement is found. The uniaxial compressive strength parallel to the bed joints seems to be overpredicted by the model, see Figure 6.9a, which is due to a debatable definition of failure in the experiments for these loading conditions (early splitting of the bed joints in tension), see Dhanasekar *et al.* (1985).

Figure 6.10 illustrates the shape of the composite yield criterion. The yield criterion features a low degree of anisotropy ( $f_{tx} / f_{ty} = 1.34$  and  $f_{mx} / f_{my} = 1.09$ ). The parameter  $\alpha$  equals 1.26 which is close to the unitary Rankine value and the parameter  $\beta$  is about -1.0, which will be shown to be typical of masonry structures. The parameter  $\gamma$  is, however, very large (9.59) and unexpected, if compared to a (isotropic) Von Mises model with a value of 3.0. This parameter seems to indicate a relatively small shear resistance for this particular type of masonry.

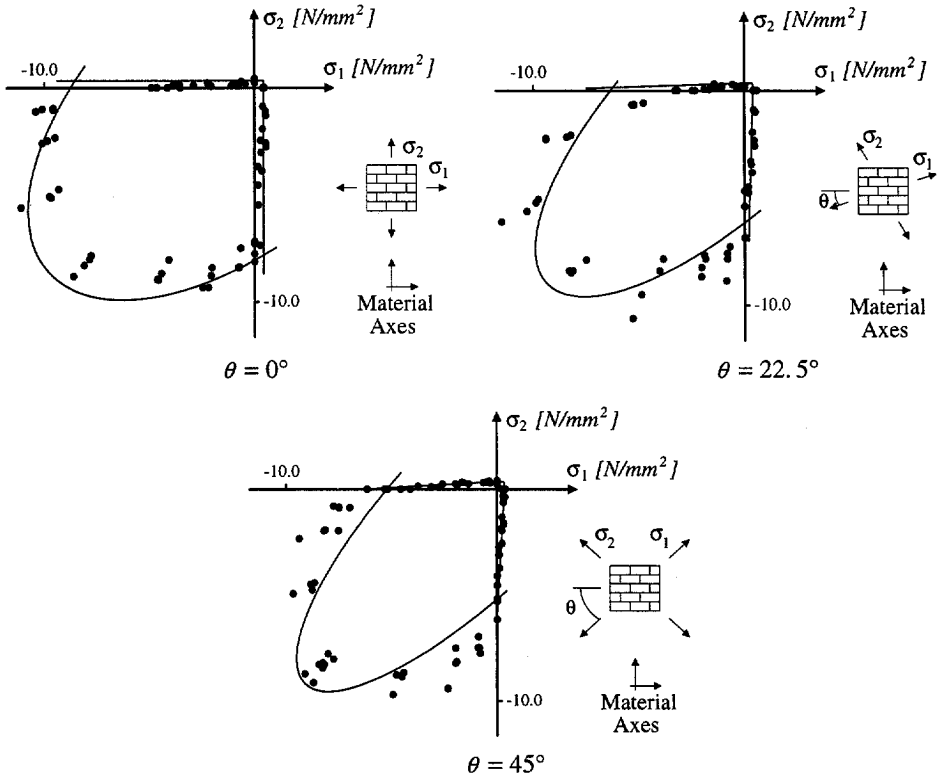


Figure 6.9 Comparison between the plasticity model and experimental results from Page (1981,1983). Material parameters:  $f_{tx} = 0.43 \text{ [N/mm}^2\text{]}$ ;  $f_{ty} = 0.32 \text{ [N/mm}^2\text{]}$ ;  $f_{mx} = 8.74 \text{ [N/mm}^2\text{]}$ ;  $f_{my} = 8.03 \text{ [N/mm}^2\text{]}$ ;  $\alpha = 1.26$ ;  $\beta = -1.17$ ;  $\gamma = 9.59$ .

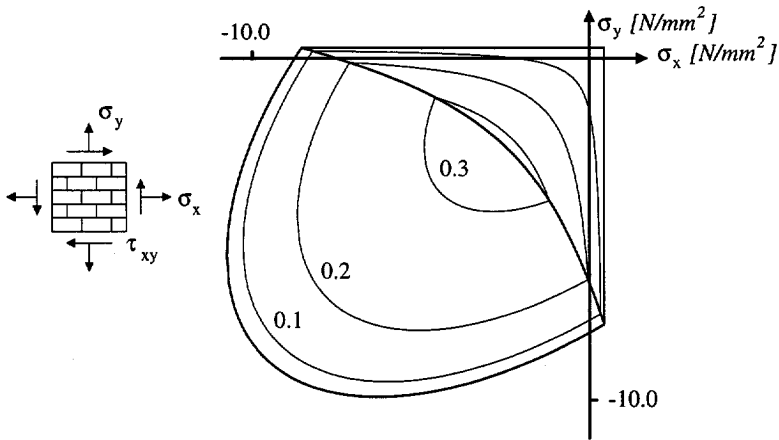


Figure 6.10 Calculated composite yield criterion for solid clay brick masonry of Page (1981,1983), with iso-shear stress lines. Contour spacing:  $0.1 f_{my}$ .

A smaller testing program of biaxially loaded masonry panels was carried out at ETH Zurich. The panels, with dimensions  $1200 \times 1200 \times 150$  [mm<sup>3</sup>], were loaded proportionally in the principal stress directions  $\sigma_1$  and  $\sigma_2$  along different orientations  $\theta$  with respect to the material axes as defined previously. Firstly, the twelve panels of hollow clay brick masonry, denoted by panels K1 to K12 and reported by Ganz and Thürlimann (1982), are considered. The test results, the proposed plasticity model results and the ratio between experimental and predicted failure are given in Table 6.1. Note that this ratio is obtained by calculating the intersection of the plasticity model with the given loading path. It is therefore a measure of the norm of the stress vector in the  $(\sigma_x, \sigma_y, \tau_{xy})$ -space which equals  $(\sigma_x^2 + \sigma_y^2 + \tau_{xy}^2)^{1/2}$ . Panels K5 and K9 are not included because the boundary conditions affected the failure mode of panel K5 and panel K9 includes reinforcement.

The plasticity model seems to be able to reproduce the strength behavior of this type of masonry with good accuracy. The large difference encountered for panel K8 is probably due to the critical loading path, with very low confining pressure in a practically no-tension material for the direction normal to the bed joints.

**Table 6.1** Comparison between plasticity model and experimental results from Ganz and Thürlimann (1982). Material parameters:  $f_{tx} = 0.28$  [N/mm<sup>2</sup>];  $f_{ty} = 0$  [N/mm<sup>2</sup>];  $f_{mx} = 1.87$  [N/mm<sup>2</sup>];  $f_{my} = 7.61$  [N/mm<sup>2</sup>];  $\alpha = 1.73$ ;  $\beta = -1.05$ ;  $\gamma = 1.20$ .

Panel	Regime	$\sigma_1/\sigma_2$	$\theta$ [°]	Experimental results			Plasticity model			Ratio
				$\sigma_x$ [N/mm <sup>2</sup> ]	$\sigma_y$ [N/mm <sup>2</sup> ]	$\tau_{xy}$ [N/mm <sup>2</sup> ]	$\sigma_x$ [N/mm <sup>2</sup> ]	$\sigma_y$ [N/mm <sup>2</sup> ]	$\tau_{xy}$ [N/mm <sup>2</sup> ]	
K1	Tens.	-0.088	22.5	-0.08	-0.92	0.42	-0.09	-1.00	0.46	0.92
K2	Tens.	-0.050	22.5	-0.17	-1.42	0.62	-0.16	-1.32	0.58	1.07
K3	Comp.	0.000	0.0	0.00	-7.63	0.00	0.00	-7.61	0.00	1.00
K4	Comp.	0.000	90.0	-1.83	0.00	0.00	-1.87	0.00	0.00	0.98
K6	Tens.	0.000	45.0	-0.32	-0.32	0.32	-0.38	-0.38	0.38	0.84
K7	Tens.	0.000	22.5	-0.39	-2.25	0.93	-0.38	-2.22	0.92	1.01
K8	Tens.	0.000	67.5	-0.22	-0.04	0.09	-0.38	-0.07	0.16	0.58
K10	Comp.	0.328	0.0	-2.11	-6.44	0.00	-2.12	-6.47	0.00	1.00
K11	Comp.	0.306	22.5	-2.04	-4.49	1.23	-2.05	-4.51	1.23	1.00
K12	Comp.	0.304	45.0	-2.03	-2.03	1.08	-1.98	-1.98	1.06	0.98

Figure 6.11 illustrates the shape of the yield criterion and the position of the tests. The yield criterion features an extreme degree of anisotropy with zero tensile strength in the direction normal to the bed joints and a ratio  $f_{mx} / f_{my}$  equal to 4.06. This high ratio is due to the high perforation of the clay bricks. The parameter  $\alpha$  equals 1.73 which is not quite close to the unitary Rankine value but the parameter  $\beta$  is still about -1.0. The

parameter  $\gamma$  is quite small (1.20) which is probably explained by the high degree of anisotropy, i.e. relatively high shear resistance due to the beneficial contribution of the strength  $f_{my}$ . It is noted that the peak yield value represents an "average" value equal to  $(f_{mx} f_{my})^{1/2}$ . In opposition with solid clay brick masonry, see Figure 6.10, it appears that the tension regime represents the majority of the composite yield surface domain.

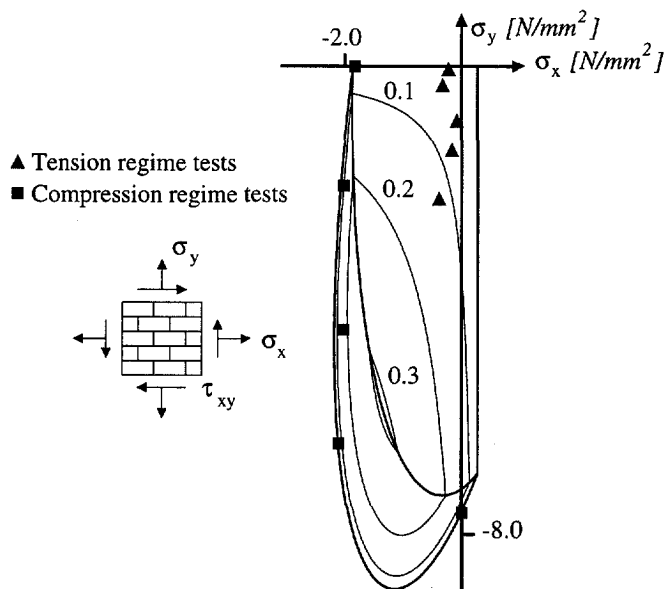


Figure 6.11 Calculated composite yield criterion for hollow clay brick masonry of Ganz and Thürliman (1982), with iso-shear stress lines. Contour spacing:  $0.1 f_{my}$ .

The nine panels of hollow concrete block masonry, denoted by panels ZSW1 to ZSW9 and tested by Lurati *et al.* (1990) as a part of the ETH Zurich program, are considered next. The test results, the proposed plasticity model results and the ratio between experimental and predicted values are given in Table 6.2. Panel ZSW3 is not considered because the head joints were not filled. Again, the model is able to capture the strength behavior of this type of masonry. For the tensile regime only three tests are available and, therefore, the plasticity model fit is exact. It is noted that a, basically, no-tension material is obtained and the parameter  $\alpha$  equals the unit value, i.e. (isotropic) Rankine is recovered. The yield criterion features a reasonable degree of anisotropy in compression with  $f_{mx} / f_{my} = 1.59$ . The parameter  $\beta$  is again about -1.0 and the parameter  $\gamma$ , which equals 3.36, is approximately equal to the Von Mises value. Figure 6.12 illustrates the shape of the composite yield criterion and the position of the tests.

The no-tension material was obtained from only three tests and is, of course, physically debatable. In particular, if a material does not possess any tensile strength, a

proportional loading path from the origin to calibrate the tension regime is a neutral path and, experimentally, cannot be stable.

**Table 6.2** Comparison between plasticity model and experimental results from Lurati *et al.* (1990). Material parameters:  $f_{tx} = 0.01 [N/mm^2]$ ;  $f_{ty} = 0.00 [N/mm^2]$ ;  $f_{mx} = 5.78 [N/mm^2]$ ;  $f_{my} = 9.21 [N/mm^2]$ ;  $\alpha = 1.00$ ;  $\beta = -0.97$ ;  $\gamma = 3.36$ .

Panel	Regime	$\sigma_1/\sigma_2$	$\theta$ [°]	Experimental results			Plasticity model			Ratio
				$\sigma_x$ [N/mm <sup>2</sup> ]	$\sigma_y$ [N/mm <sup>2</sup> ]	$\tau_{xy}$ [N/mm <sup>2</sup> ]	$\sigma_x$ [N/mm <sup>2</sup> ]	$\sigma_y$ [N/mm <sup>2</sup> ]	$\tau_{xy}$ [N/mm <sup>2</sup> ]	
ZSW1	Comp.	0.000	0.0	0.00	-9.12	0.00	0.00	-9.21	0.00	0.99
ZSW2	Comp.	0.136	0.0	-6.12	-0.83	0.00	-6.01	-0.82	0.00	1.02
ZSW4	Comp.	1.527	0.0	-5.98	-9.13	0.00	-5.81	-8.86	0.00	1.03
ZSW5	Tens.	0.000	45.0	-3.06	-3.06	3.06	-3.06	-3.06	3.06	1.00
ZSW6	Comp.	0.222	45.0	-4.60	-4.60	2.93	-4.51	-4.51	2.87	1.02
ZSW7	Comp.	1.000	45.0	-6.12	-6.12	0.00	-6.51	-6.51	0.00	0.94
ZSW8	Tens.	0.000	67.5	-2.34	-0.40	0.97	-2.34	-0.40	0.97	1.00
ZSW9	Tens.	0.000	22.5	-0.97	-5.66	2.35	-0.97	-5.66	2.35	1.00

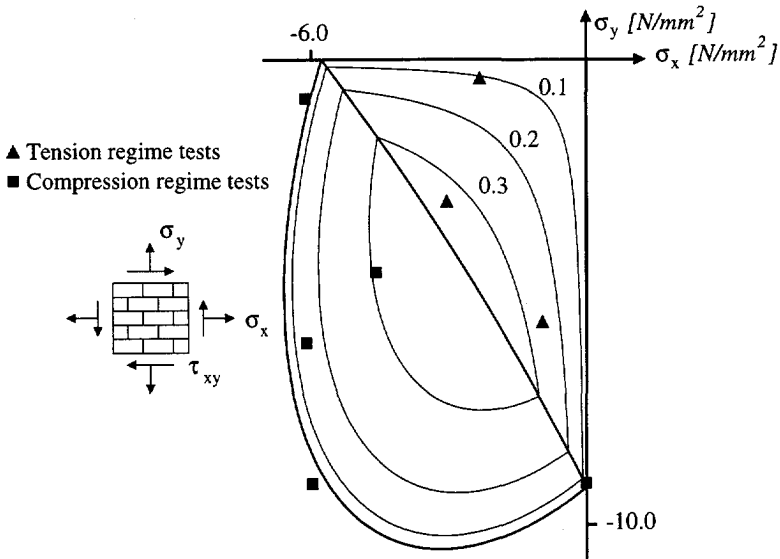


**Figure 6.12** Calculated composite yield criterion for hollow concrete block masonry of Lurati *et al.* (1990), with iso-shear stress lines. Contour spacing:  $0.1 f_{my}$ .

### 6.3 The inelastic behavior of the model. Elementary tests

This section provides insight into the inelastic behavior of the anisotropic composite yield criterion. Again, this is a relevant issue because the existing experience in using anisotropic models is scarce and the proposed material model possesses some inherent complexity.

#### 6.3.1 Orthotropic behavior in uniaxial tension

The ability of the proposed model to represent tensile orthotropic behavior is now discussed. For this purpose, we consider a single element test, with dimensions  $100 \times 100$  [mm<sup>2</sup>], under pure uniaxial tension. The material properties given in Table 6.3 are assumed, in which all the material parameters in the  $y$  direction are reduced by a factor two (except the fracture energy) to simulate orthotropic behavior. For the fracture energy  $G_{fy}$ , three different values are considered:  $0.3 G_{fx}$  (general case),  $0.5 G_{fx}$  (isotropic softening) and  $+\infty$  (elastic-perfectly-plastic behavior).

Table 6.3 Material properties for uniaxial tension test ( $\alpha = 1.0$ ).

Material properties				
$E_x$	10000 [N/mm <sup>2</sup> ]	$E_y$	5000 [N/mm <sup>2</sup> ]	
$\nu_{xy}$	0.2	$G_{xy}$	3000 [N/mm <sup>2</sup> ]	
$f_{tx}$	1.0 [N/mm <sup>2</sup> ]	$f_{ty}$	0.5 [N/mm <sup>2</sup> ]	
$G_{fx}$	0.02 [Nmm/mm <sup>2</sup> ]	$G_{fy}$	Example 1	0.006 [Nmm/mm <sup>2</sup> ]
			Example 2	0.01 [Nmm/mm <sup>2</sup> ]
			Example 3	$+\infty$ [Nmm/mm <sup>2</sup> ]

The values chosen for the material parameters illustrate the fact that completely different behavior along the two material axes can be reproduced, see Figure 6.13. Further insight into the behavior of the model can be obtained from Figure 6.14, which shows the trace of the tensile criterion in the plane  $\tau_{xy} = 0$  upon increasing softening. In the first example, the material strength in the  $y$  direction degrades at a faster rate than the material strength in the  $x$  direction. The second example yields isotropic softening, which means that degradation of  $f_{tx}$  and  $f_{ty}$  occurs at the same rate, i.e. the ratio of strength along the material axes  $f_{tx} / f_{ty}$  is constant during any load history. In both examples, once the fracture energies are exhausted, a no-tension material is recovered, see Figure 6.14a,b. Finally, the third example yields elastic-perfectly-plastic behavior in the  $y$  direction while softening is allowed to occur in the  $x$  direction. This means that the ratio of strength along the material axes tends to zero and the yield surface is only allowed to shrink along the  $x$  axis, see Figure 6.14c.

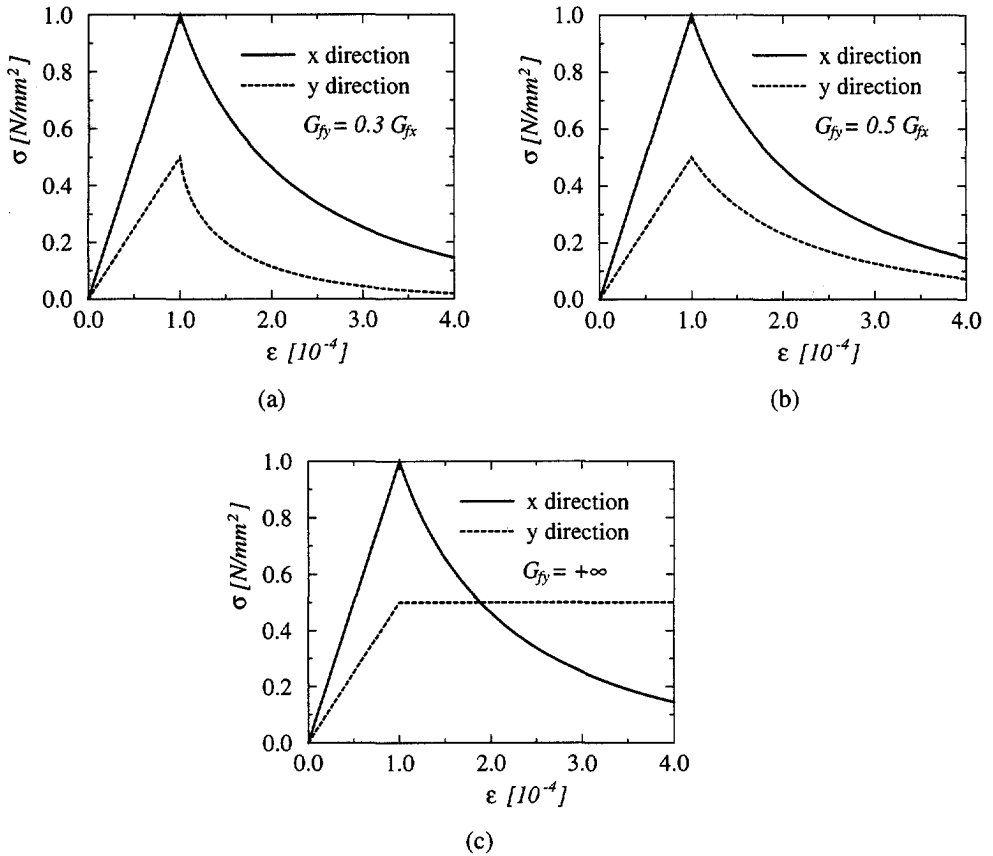


Figure 6.13 Stress - strain response in uniaxial tension along the two material axes: (a) example 1 (general case); (b) example 2 (isotropic softening); (c) example 3 (elastic-perfectly-plastic behavior in y direction).

### 6.3.2 Orthotropic behavior in uniaxial compression

The ability of the proposed model to represent compressive orthotropic behavior is now discussed. For this purpose, we again consider a single element test, with dimensions  $100 \times 100$  [mm<sup>2</sup>], under pure uniaxial compression. The material properties given in Table 6.4 are assumed, in which all the material parameters in the y direction are reduced by a factor two (except the compressive fracture energy) to simulate orthotropic behavior. For the compressive fracture energy  $G_{f_{cy}}$ , three different values are considered:  $0.3 G_{f_{cx}}$  (general case),  $0.5 G_{f_{cx}}$  (isotropic softening) and  $+\infty$  (post-peak perfectly plastic behavior).

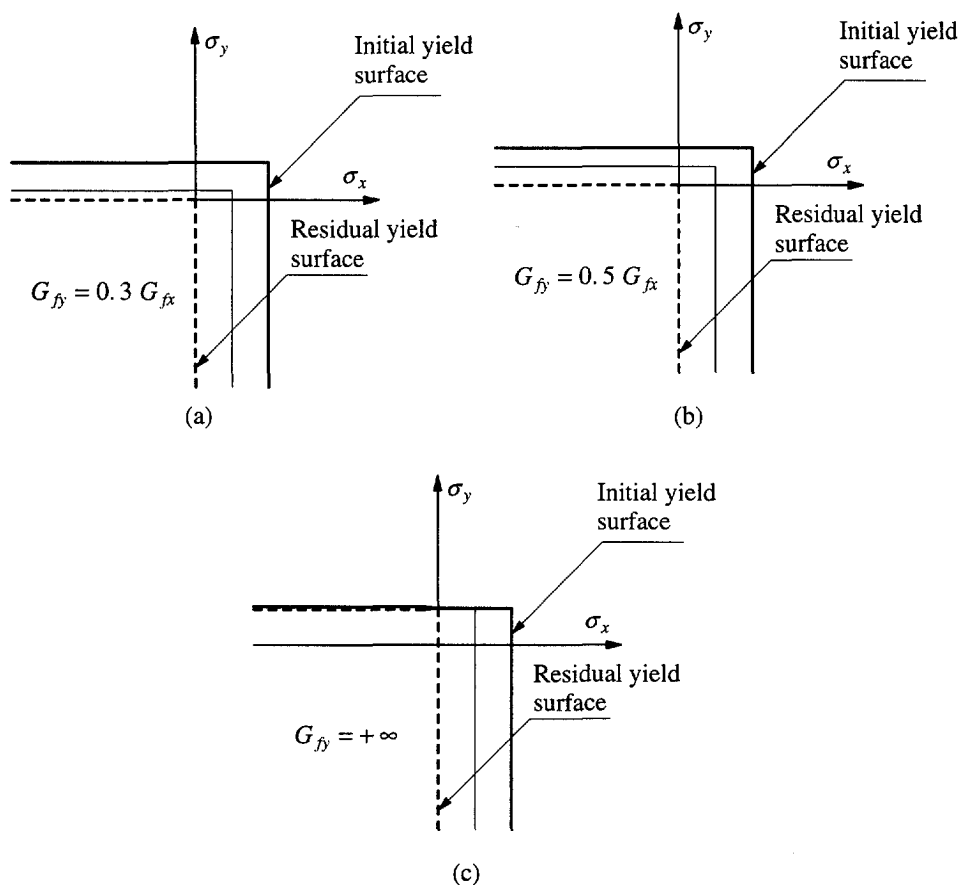


Figure 6.14 Trace of the tensile criterion in the plane  $\tau_{xy} = 0$  upon increasing softening: (a) example 1 (general case); (b) example 2 (isotropic softening); (c) example 3 (elastic-perfectly-plastic behavior in y direction).

Table 6.4 Material properties for uniaxial compression test ( $\beta = -1.0$ ,  $\gamma = 3.0$  and  $\kappa_p = 0.0005$ ).

Material properties				
$E_x$	10000 [N/mm <sup>2</sup> ]	$E_y$	5000 [N/mm <sup>2</sup> ]	
$\nu_{xy}$	0.2	$G_{xy}$	3000 [N/mm <sup>2</sup> ]	
$f_{mx}$	10.0 [N/mm <sup>2</sup> ]	$f_{my}$	5.0 [N/mm <sup>2</sup> ]	
$G_{fcx}$	5.0 [Nmm/mm <sup>2</sup> ]	$G_{fcy}$	Example 1	1.5 [Nmm/mm <sup>2</sup> ]
			Example 2	2.5 [Nmm/mm <sup>2</sup> ]
			Example 3	$+\infty$ [Nmm/mm <sup>2</sup> ]

Again, the values chosen for the material parameters illustrate the fact that completely different behavior along the two material axes can be reproduced, see Figure 6.15. Further insight into the behavior of the model can be obtained from Figure 6.16, which shows the trace of the compressive criterion in the plane  $\tau_{xy} = 0$  upon increasing softening. In the first example, the material strength in the  $y$  direction degrades at a faster rate than the material strength in the  $x$  direction. In the second example, degradation of the material strength in both directions occurs with the same rate and isotropic softening is obtained. In both examples, the residual yield surface, retrieved once the fracture energies are exhausted, is scaled from the peak yield surface keeping the original shape. Finally, in the third example, degradation only occurs for the material strength in the  $x$  direction, while a post-peak perfectly plastic behavior is obtained in the  $y$  direction. This means that the ratio of strength along the material axes tends to a constant quasi-zero value and the residual yield surface has a different shape than the original one.

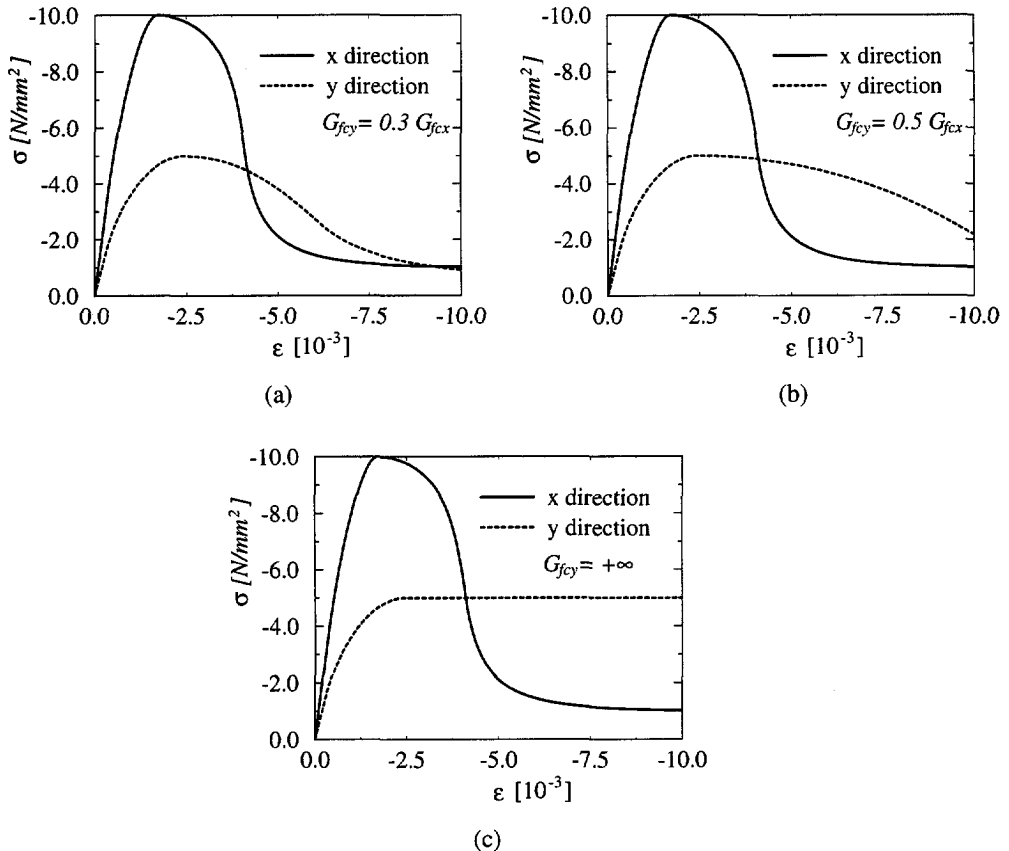


Figure 6.15 Stress - strain response in uniaxial compression along the two material axes: (a) example 1 (general case); (b) example 2 (isotropic softening); (c) example 3 (post-peak perfectly plastic behavior in  $y$  direction).

Note that, in the case of isotropic softening, the post-peak stress-strain diagrams under uniaxial loading conditions along the two material axes, see Figure 6.15b, are not scaled by a factor two. This is solely due to the definition of the softening scalar and the fact that the yield value  $\bar{\sigma}_c$  is not equal to the uniaxial strength along each material axis. This also means that the definition of the “compressive fracture energy” can be questioned because a perfect equivalence in the stress-strain diagram is not obtained. This limitation of the model can be easily solved, for example, if a unit norm is used for the plastic flow vector and a strain softening hypothesis is used for the softening scalar. The additional difficulty introduced in the formulation ( $\dot{\kappa}_c \neq \dot{\lambda}_c$ ) is not particularly difficult to solve but, with the notorious lack of experimental results on the material inelastic behavior, the initial assumptions are advised in order to simplify the implementation.

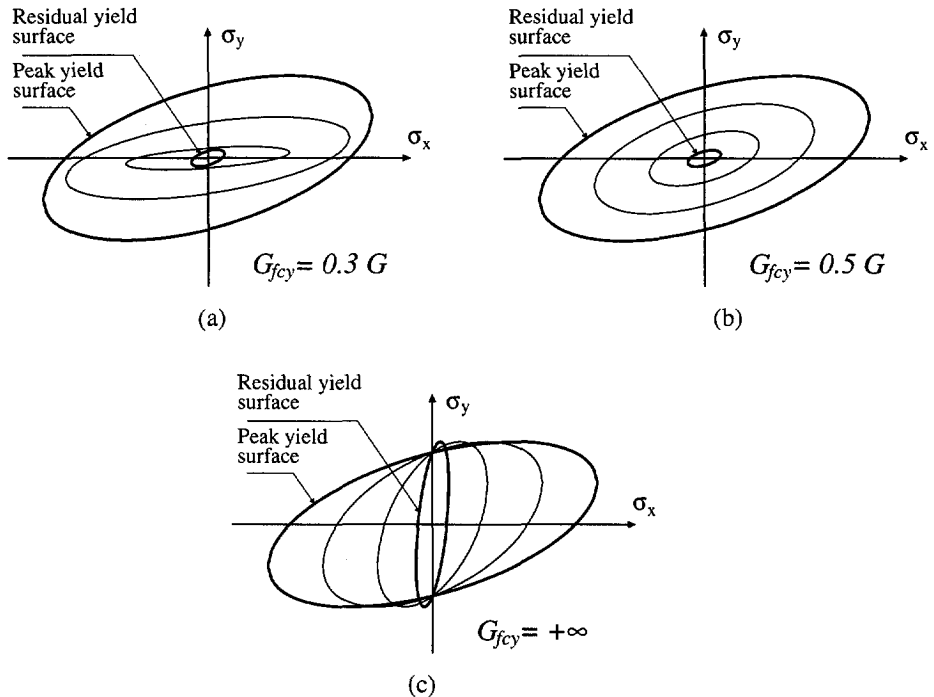


Figure 6.16 Trace of the compressive criterion in the plane  $\tau_{xy} = 0$  upon increasing softening: (a) example 1 (general case); (b) example 2 (isotropic softening); (c) example 3 (post-peak perfectly plastic behavior in y direction).

### 6.3.3 The definition of a mesh independent compressive fracture energy

For strain-softening materials, the need to introduce an equivalent length  $h$  in the stress-strain diagram to obtain analyses which are objective with respect to mesh refinement is a well debated issue since the original work of Bažant and Oh (1983). In the present

work  $h$  is assumed to be related to the area of an element, cf. eq. (6.1). However, this approach is generally used in engineering practice only for modeling tensile behavior with linear elastic pre-peak behavior followed by inelastic softening until total degradation of strength.

The constitutive relation for compression introduced in Figure 6.5 features pre-peak hardening and a residual plateau. Clearly, the hardening branch of the constitutive relation is stable and should not be adjusted as a function of  $h$ . Physically, the hardening behavior is due to bulk material damage which is a nonlocal phenomena. The residual plateau is constant and also independent of the  $h$  value. To demonstrate the veracity of the definition of a mesh independent release of energy upon mesh refinement an example of a simple bar loaded in uniaxial compression is given. The example, introduced by Feenstra and De Borst (1996), is similar to the well-known problem of a simple bar loaded in tension proposed by Crisfield (1982).

Consider the bar shown in Figure 6.17, which is divided in  $n$  elements with  $n = 10, 20$  and  $40$  elements. The length of the bar is  $50$  [mm] and the cross-section of the bar has unit dimensions ( $1.0 \times 1.0$  [mm<sup>2</sup>]). The compressive fracture energies are assumed to equal  $G_{fcx} = 10.0$  [Nmm/mm<sup>2</sup>] and  $G_{fcy} = 5.0$  [Nmm/mm<sup>2</sup>]. For the rest of the material properties the values used in Table 6.4 of the previous section are assumed. One element is slightly imperfect (10%) to trigger the localization:  $f_{mx} = 9.0$  [N/mm<sup>2</sup>],  $f_{my} = 4.5$  [N/mm<sup>2</sup>],  $G_{fcx} = 9.0$  [Nmm/mm<sup>2</sup>] and  $G_{fcy} = 4.5$  [Nmm/mm<sup>2</sup>]. The other material parameters remain the same.

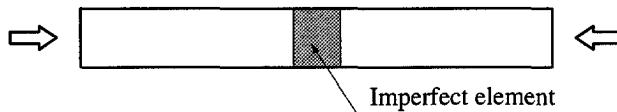


Figure 6.17 Simple bar with imperfect element loaded in compression.

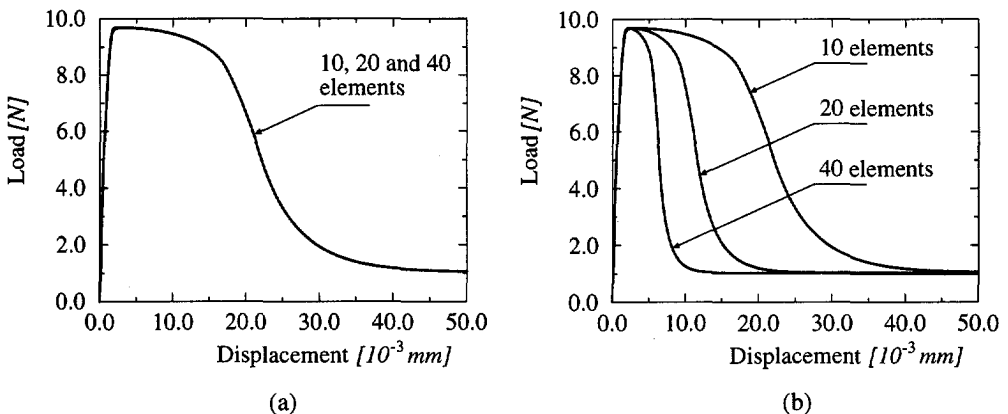


Figure 6.18 Load - displacement diagram for simple bar with imperfect element for: (a) energy-based regularization; (b) no regularization.

The load-displacement response of the bar is depicted in Figure 6.18a for the energy-based regularization method (note that "displacement" is understood as the relative displacement between the ends of the bar). It can be observed that the response is completely independent of the number of elements. The response of the bar with a constitutive model which has not been modified according to the size of the finite element mesh, see Figure 6.18b, shows a dramatic mesh-dependent behavior in the post-peak response (the residual plateau remains of course unchanged). The brittleness of the response increases with an increasing number of elements.

## 6.4 Validation

Any masonry macro-model always includes some degree of approximation because all the different failure mechanisms of masonry, detailed in Chapter 4, cannot be reproduced and must be smeared out in the continuum. The field of applications of macro-models are indeed large structures, subjected to loading and boundary conditions such that the state of stress and strain across a macro-length can be assumed to be uniform.

The use of the anisotropic continuum model for the analysis of masonry structures is validated next by a comparison with experimental results available in the literature. Due to the difficulties and cost of testing large masonry structures, most examples available in the literature are "small" or loaded in such a way that the local behavior of masonry controls the global response of the structure. In this case a macro-modeling strategy cannot be applied and units and joints must be discretized.

It is pointed out in Chapter 4 that, traditionally, experiments in shear walls have been adopted by the masonry community as the most common in-plane large test. In this study, attention is devoted to the tests carried out at ETH Zurich, see Ganz and Thürlimann (1984) and Lurati and Thürlimann (1990). These experiments are well suited for the validation of the model, not only because they are large and feature well distributed cracking, but also because most of the parameters necessary to characterize the model are available from biaxial tests. Figure 6.19 shows the geometry of the walls, which, unless stated otherwise, consist of a masonry panel of  $3600 \times 2000 \times 150$  [ $mm^3$ ] and two flanges of  $150 \times 2000 \times 600$  [ $mm^3$ ]. Additional boundary conditions are given by two concrete slabs placed in the top and bottom of the specimen. Initially, the wall is subjected to a vertical load  $p$  uniformly distributed over the length of the wall with a resultant  $P$ . This is followed by the application of a horizontal force  $F$  on the top slab along a horizontal displacement  $d$ .

For the numerical analyses linear plane stress continuum elements and constant strain triangles in a cross diagonal patch with full Gauss integration are utilized. A regular mesh of  $24 \times 15$  4-noded quadrilaterals is used for the panel and  $2 \times 15$  cross diagonal patches of 3-noded triangles are used for each flange. The analyses are carried out with indirect displacement control with line searches, whereas the snap-backs are traced with COD control over the most active crack. It is noted that the self-weight of the wall and the top slab is also considered in the analyses.

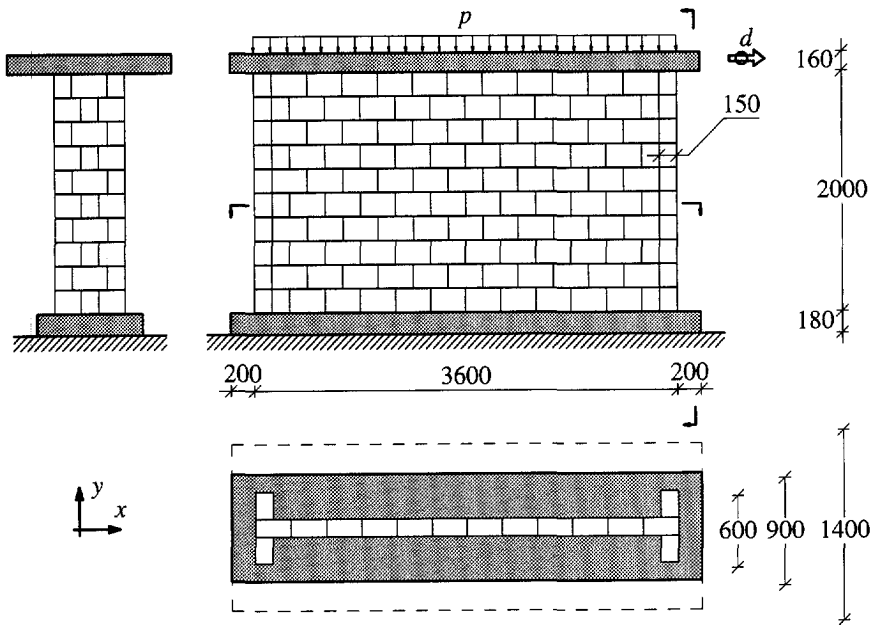


Figure 6.19 Geometry and loads for ETH Zurich shear walls.

#### 6.4.1 ETH Zurich clay brick masonry shear walls

The first series of shear walls analyzed consists of hollow clay brick masonry, see Figure 6.11 on page 143. The tests were carried out by Ganz and Thürlimann (1984) and are denoted by W. Three walls from the experiments, W1, W2 and W4, are analyzed with the composite plasticity model. Wall W3 is outside the scope of the present study because reinforcement is included in the bed joints. The properties of the composite material are obtained from Ganz and Thürlimann (1982), see Table 6.5 and Table 6.6. A low tensile strength value is assumed in the direction normal to the bed joints ( $f_{ty} = 0.05 [N/mm^2]$ ) instead of the no-tension material obtained in Section 6.2.2. It is noted that the flanges have the width of a single unit and the failure in the  $x$  direction (equivalent to the out-of-plane direction of the panel) is determined by the tensile and compressive strength of the clay brick. These new inelastic properties of the flanges read:  $f_{tx} = 0.68 [N/mm^2]$  and  $f_{mx} = 9.5 [N/mm^2]$ .

The first wall analyzed here, denoted by W1, is subjected to an initial vertical load  $P$  of  $415 [kN] \equiv 0.61 [N/mm^2]$  and shows a very ductile response with tensile and shear failure along the diagonal stepped cracks, see Figure 6.20.



(a)



(b)

Figure 6.20 Wall W1. Experimental failure patterns: (a) peak; (b) end stage.

Table 6.5 Walls W. Elastic properties.

$E_x$	$E_y$	$\nu_{xy}$	$G_{xy}$
2460	5460	0.18	1130
[N/mm <sup>2</sup> ]	[N/mm <sup>2</sup> ]		[N/mm <sup>2</sup> ]

Table 6.6 Walls W. Inelastic properties.

Tension regime						
$f_{tx}$	$f_{ty}$	$\alpha$	$G_{fx}$	$G_{fy}$		
0.28	0.05	1.73	0.02	0.02		
[N/mm <sup>2</sup> ]	[N/mm <sup>2</sup> ]		[Nmm/mm <sup>2</sup> ]	[Nmm/mm <sup>2</sup> ]		
Compression regime						
$f_{mx}$	$f_{my}$	$\beta$	$\gamma$	$G_{fex}$	$G_{fey}$	$\kappa_p$
1.87	7.61	-1.05	1.20	5.0	10.0	$8 \times 10^{-4}$
[N/mm <sup>2</sup> ]	[N/mm <sup>2</sup> ]			[Nmm/mm <sup>2</sup> ]	[Nmm/mm <sup>2</sup> ]	

The comparison between numerical and experimental load-displacement diagrams, for wall W1, is given in Figure 6.21. Good agreement is found. The low initial vertical load combined with the confinement provided by the flanges and the top concrete slab yields an extremely ductile behavior. The unloading found at  $d \approx 2.0$  [mm] is due to the mode I crack opening of the left flange.

The behavior of the wall is depicted in Figure 6.22 and Figure 6.23 in terms of deformed meshes, where the center node of the crossed diagonal patch of the flanges is not shown in order to obtain a more legible picture, and cracked Gauss points. Cracks are plotted normal to the tensile principal plastic strain directions with a thickness

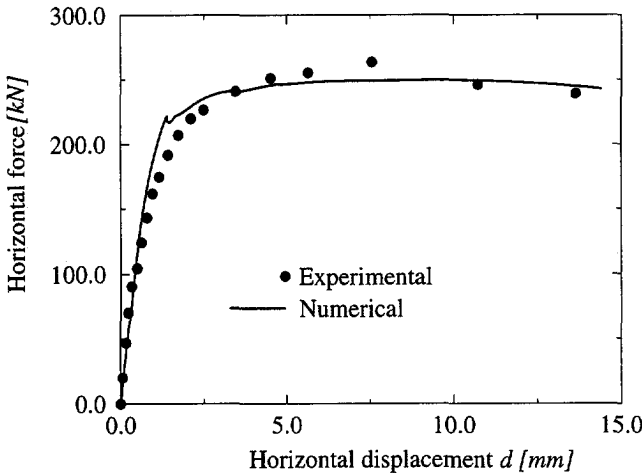


Figure 6.21 Wall W1. Load - displacement diagrams.

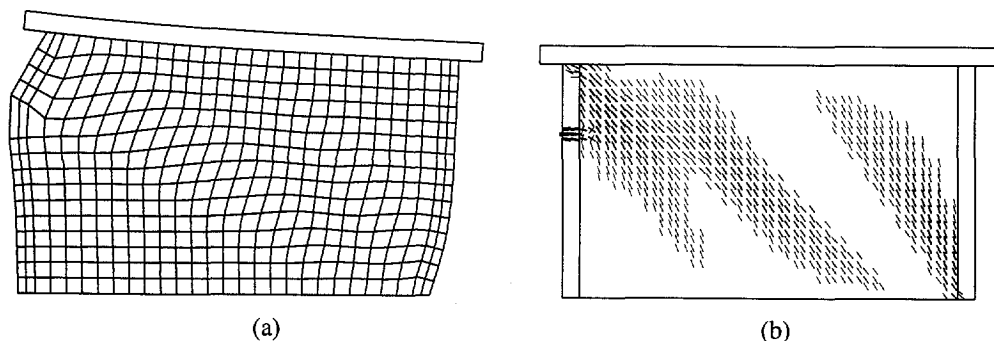


Figure 6.22 Wall W1. Results of the analysis at a displacement of 2.0 [mm]: (a) (incremental) deformed mesh; (b) cracks.

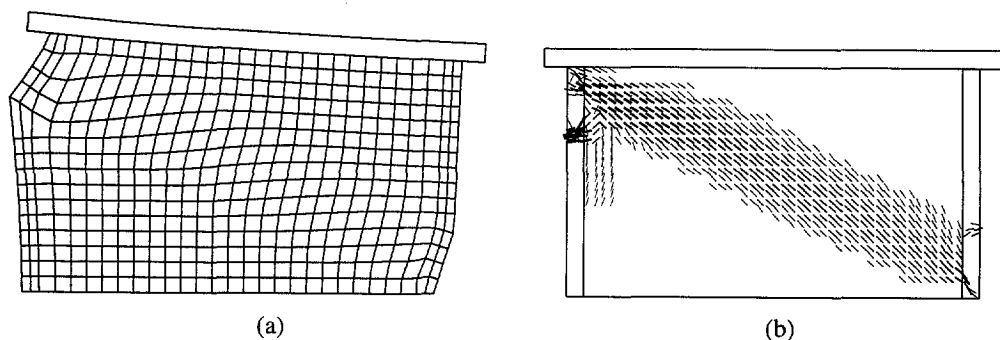


Figure 6.23 Wall W1. Results of the analysis at a displacement of 12.0 [mm]: (a) deformed mesh; (b) cracks.

proportional to the tensile equivalent plastic strain, being the lowest 5% values discarded in order to obtain legible pictures. The comparison between experimental and numerical results is more difficult than in the case of micro-models because units and joints are not modeled. However, reasonable agreement seems to be found. Initially, extensive diagonal cracking of the panel is found, see Figure 6.22b. This is accompanied by flexural cracking of the left flange. At this stage, cracking of the panel is, basically, governed by the Mohr's circle as a relatively uniform state of stress in the panel is found. Upon increasing horizontal loading, cracking tends to concentrate in a large shear band going from one corner of the specimen to the other, which is accompanied by flexural cracking of the right flange, see Figure 6.23. At this ultimate stage, a well defined failure mechanism is formed with a final shear band going from one corner of the specimen to the other and intersecting the flanges. This means that cracks rotate significantly after initiation governed by Mohr's circle to failure in a sort of shear band, which agrees well with the experiments, Figure 6.20.

It is not surprising that the plasticity model can capture the significantly large rotations of cracks because the Rankine yield surface resembles the rotating crack model, see Feenstra (1993) and Lourenço *et al.* (1995). The obtained failure shear mode seems

to be determined by the loading conditions and geometry of the wall and not by the mesh alignment, which is a relevant issue in softening materials and standard continuum.

Figure 6.24 shows the contour of minimum principal stresses at the same stages of the analysis. It is possible to observe the concentration of stresses in a narrower band with peak stresses at the bottom-right corner, upon increasing loading. However, even at the ultimate stage the stress values are considerably below the maximum compressive strength in the vertical direction which confirms the fact that failure is exclusively governed by the tension regime.

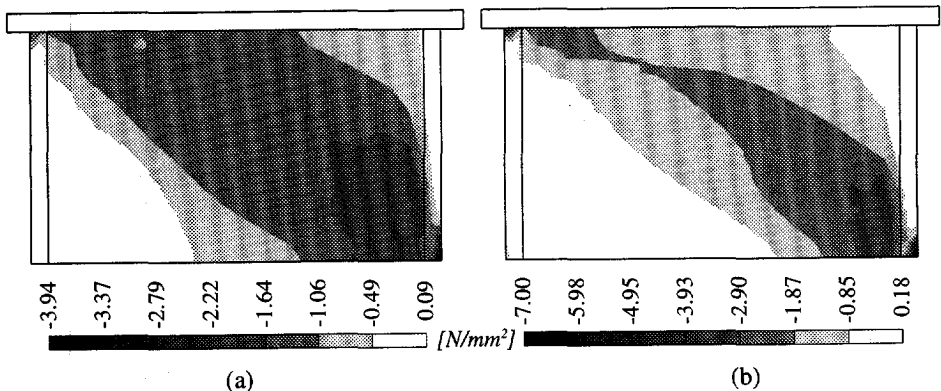
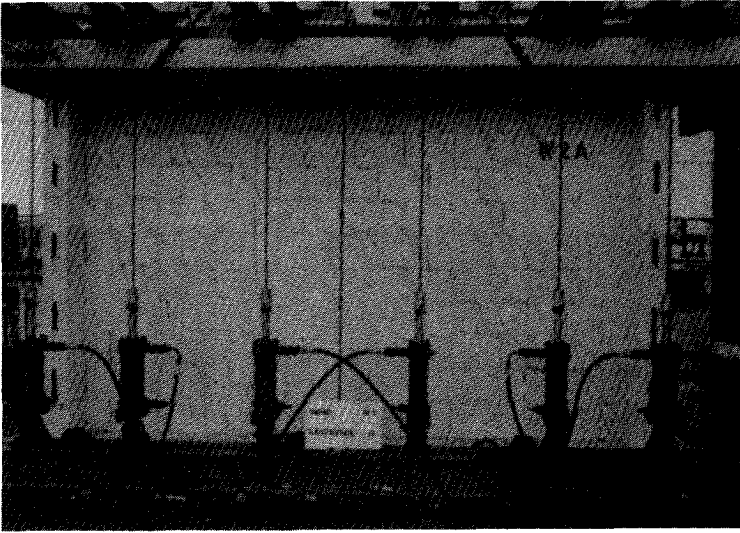


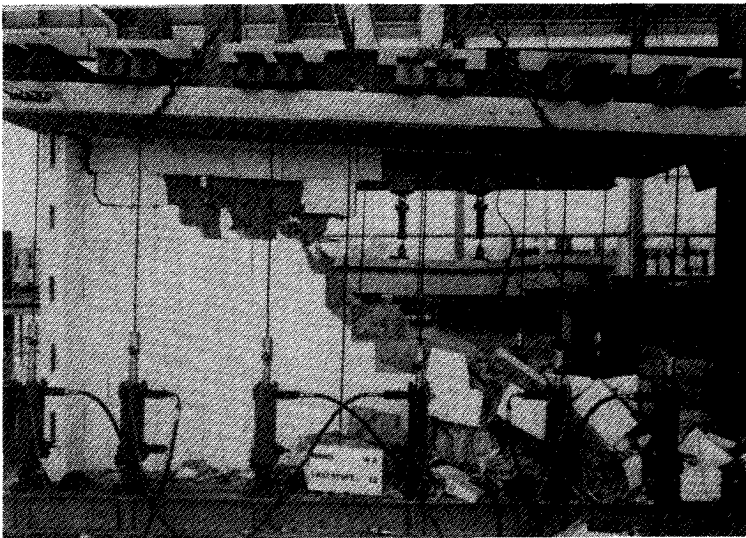
Figure 6.24 Wall W1. Minimum principal stresses at a displacement of (a) 2.0 [mm] and (b) 12.0 [mm].

The wall analyzed next, denoted by wall W2, is subjected to an initial vertical load  $P$  of 1287 [kN]  $\equiv 1.91 [N/mm^2]$  and, initially, shows a relatively ductile behavior, followed by brittle failure with explosive behavior due to crushing of the compressed zone, see Figure 6.25.

The comparison between numerical and experimental load-displacement diagrams, for wall W2, is given in Figure 6.26. From a qualitative perspective good agreement is found because the same trend is observed in both diagrams. In particular, from a displacement of approximately 3.0 [mm] the numerical and experimental load-displacement diagrams are almost perfectly parallel. Remarkably, the explosive type of failure observed in the experiments at a displacement of approximately 8.0 [mm] is also predicted by the analysis. Less good agreement is found with respect to the calculated collapse load value, which is 20 % higher than the experimental value. Even if the sharp reproduction of the collapse load value is not the main issue here, it is likely that the difference can be explained by the variation of the material properties in compression between the biaxial tests and the wall. In Section 6.4.2, good agreement is found for the collapse load even in the case of failure due to masonry crushing.



(a)



(b)

Figure 6.25 Wall W2. Experimental failure patterns: (a) peak; (b) end stage.

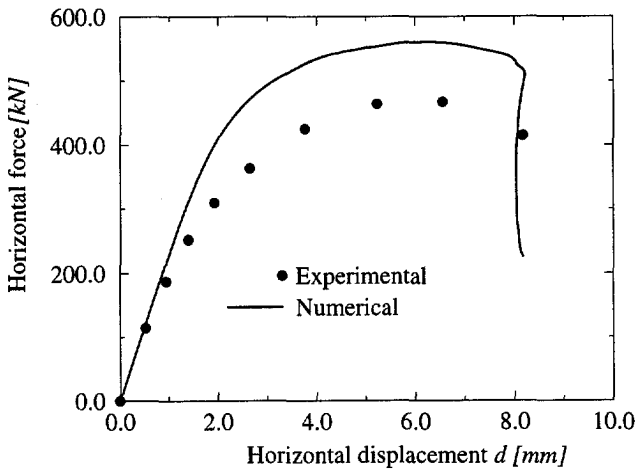


Figure 6.26 Wall W2. Load - displacement diagrams.

The behavior of the wall W2, depicted in Figure 6.27 and Figure 6.28 in terms of deformed meshes and crack patterns, is quite different from the behavior of wall W1. During the entire loading process cracks in the panel built up in two large bands that go

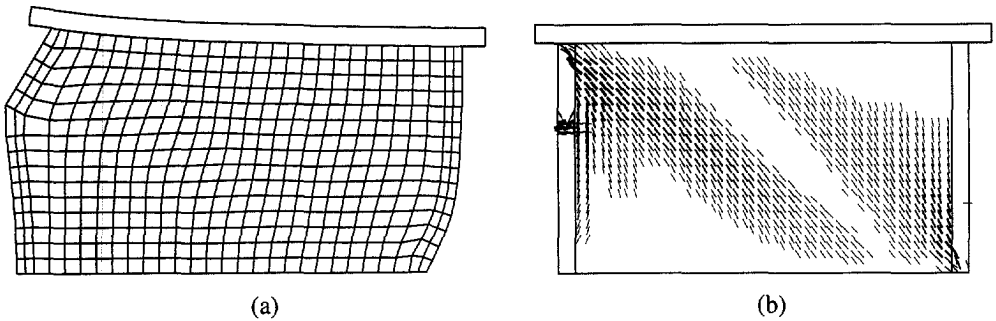


Figure 6.27 Wall W2. Results of the analysis at a displacement of 6.0 [mm] (peak): (a) deformed mesh; (b) cracks.

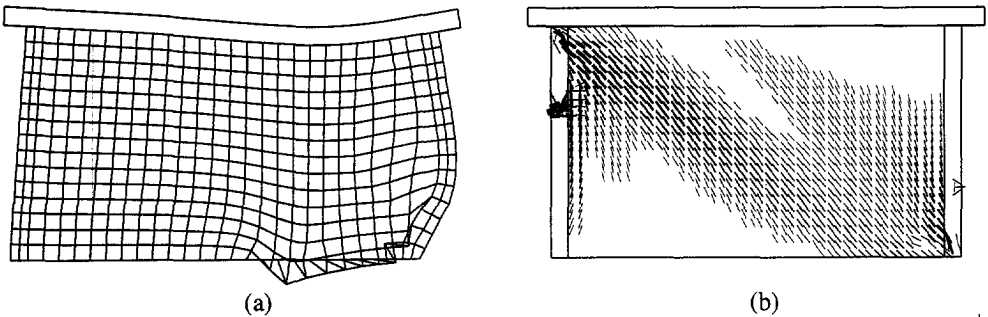


Figure 6.28 Wall W2. Results of the analysis at a displacement of 8.0 [mm] (ultimate): (a) (incremental) deformed mesh; (b) cracks.

through, respectively, the top-left and the bottom-right corners, see Figure 6.27b. This, again, agrees with the experiments, see Figure 6.25a. The difference in stiffness between panel and flanges contributes significantly to the formation of these crack bands. As the flanges bend, see Figure 6.27a, horizontal tensile stresses are induced in the panel. The two crack bands fail to concentrate in a single band because crushing of the bottom-right corner of the structure occurs first, see Figure 6.28. This explosive type of failure, which is also observed in the experiments, has been traced with arc-length control over the nodes in the bottom row of elements of the panel.

Figure 6.29 shows the contour of minimum principal stresses for the same stages of the analysis. It is observed that failure is clearly governed by masonry crushing where, at ultimate stage, the compressive strength of the bottom-right corner of the panel is completely exhausted.

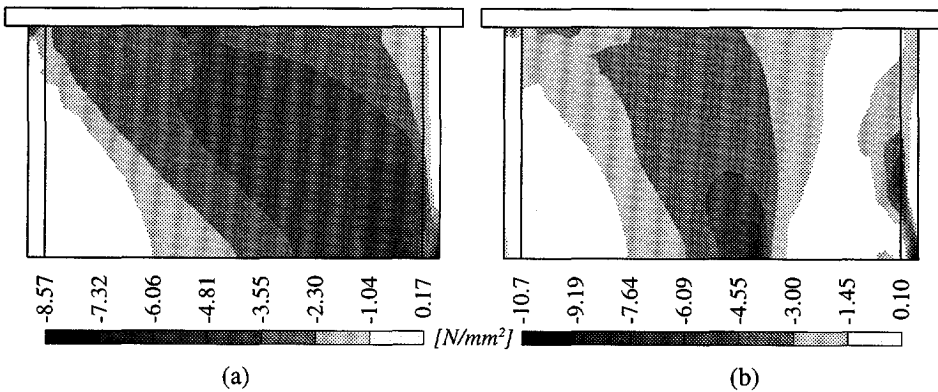


Figure 6.29 Wall W2. Minimum principal stresses at a displacement of (a) 6.0 [mm] (peak) and (b) 8.0 [mm] (ultimate).

Wall W4, which is analyzed next, is subjected to an initial concentrated load  $P$  of 422 [kN] applied with an eccentricity  $e$  equal to 840 [mm], see Figure 6.30. The load is applied via a steel profile over a length of 500 [mm]. The width of the flanges is larger than the width of the previous walls and equals 900 [mm]. The initial vertical load  $P$

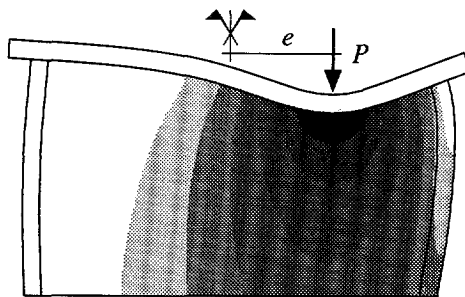
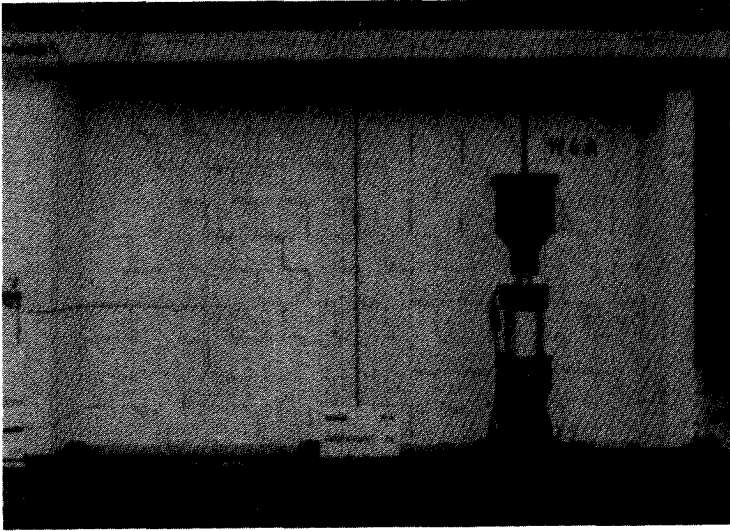
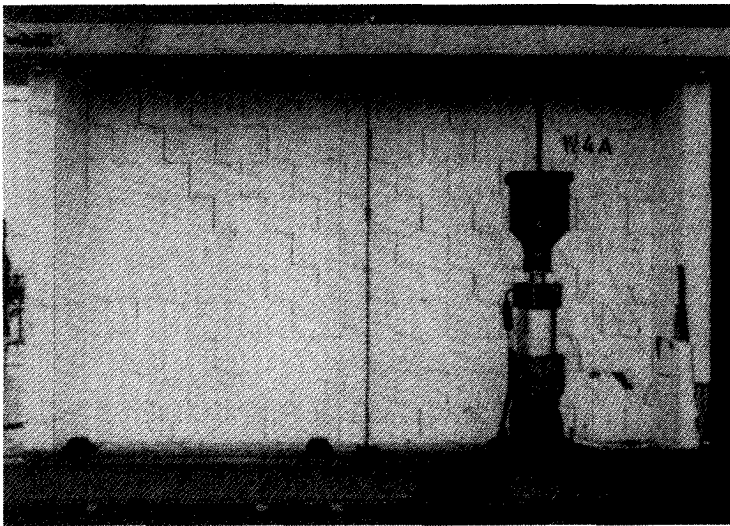


Figure 6.30 Wall W4. Loading with corresponding deformation and stress contour.

has practically the same magnitude as the load applied to wall W1. However, in wall W4, the load is applied concentrated at  $\approx 1/4$  of the wall length. The behavior of the wall is still very ductile even if some crushing is visible in the right flange at ultimate stage, see Figure 6.31.



(a)



(b)

*Figure 6.31* Walls W4. Experimental failure patterns: (a) peak; (b) end stage.

The comparison between numerical and experimental load-displacement diagrams is given in Figure 6.32. Good agreement is found. The unloading found at  $d \approx 1.0$  [mm] is due to the mode I crack opening of the left flange. The behavior of the wall is depicted in Figure 6.33 and Figure 6.34 in terms of deformed meshes and crack patterns. Initially, two crack bands arise from each corner of the panel, see Figure 6.33. The crack band located at the left side arises at approximately  $45^\circ$ , a preferential direction for square elements. However, the right crack band arises at approximately  $65^\circ$ . This gives a good impression about the model and the performance of the elements, namely, it seems to confirm the idea that the results are not solely determined by the mesh alignment. Upon increasing horizontal loading, cracking tends to concentrate in a large shear band going from one corner of the specimen to the other. However, the cracking band is no longer in a straight line as observed in wall W1. The influence of the concentrated

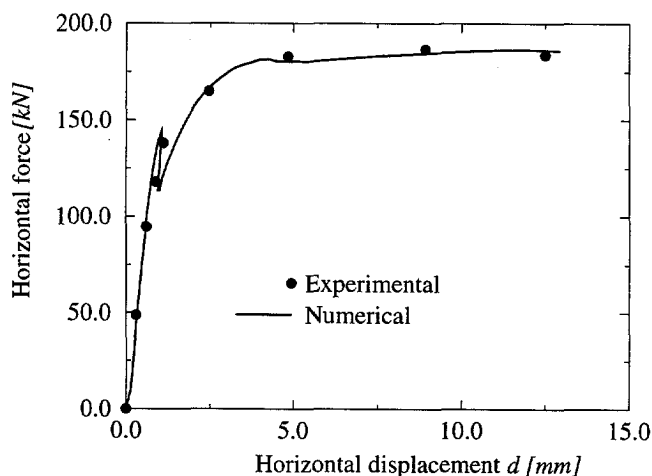


Figure 6.32 Wall W4. Load - displacement diagrams.

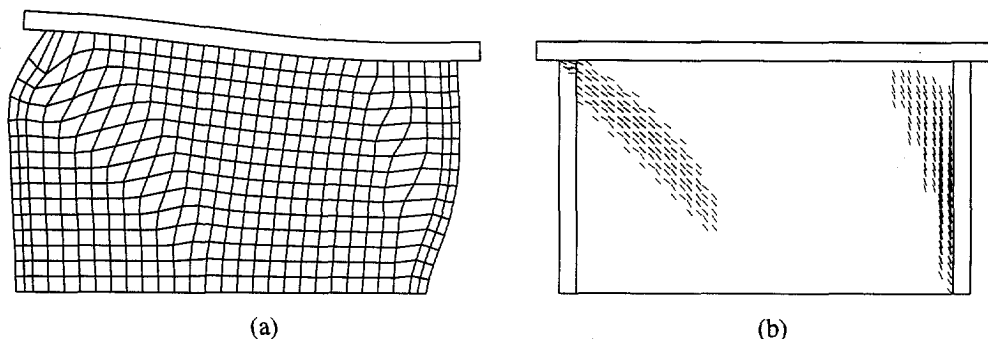


Figure 6.33 Wall W4. Results of the analysis at a displacement of 1.0 [mm]: (a) (incremental) deformed mesh; (b) cracks.

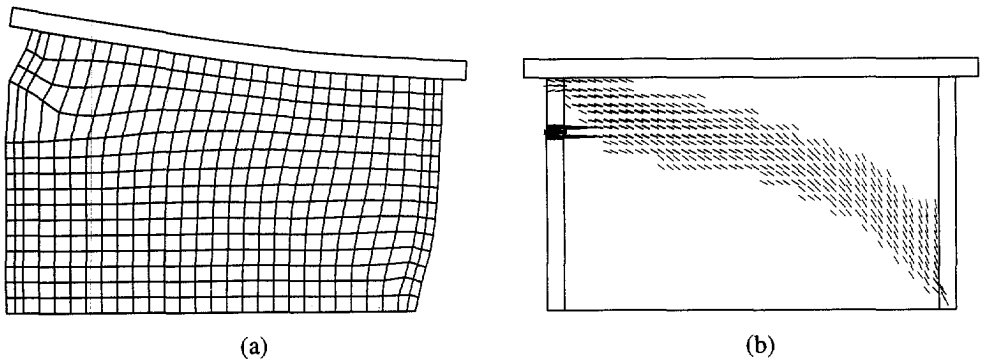


Figure 6.34 Wall W4. Results of the analysis at a displacement of 11.0 [mm]: (a) deformed mesh; (b) cracks.

load leads to diagonal failure of the right part of the wall, whereas the left part fails with a sliding mechanism with approximately horizontal cracking, see Figure 6.34. The predicted failure mode agrees reasonably well with the experiments, see Figure 6.31.

Figure 6.35 illustrates the contour of minimum principal stresses for the stages of the analysis shown previously. Due to the concentrated nature of the initial vertical load, it is possible to observe that the concentration of minimum principal stresses in the right corner of the wall W4 is much larger than wall W1, see Figure 6.24. The panel still features a large reserve of strength but compressive failure has been initiated in the right flange. Crushing at the bottom of the right flange, for an extremely late stage of the analysis, is also confirmed in the experiments, see Figure 6.31b.

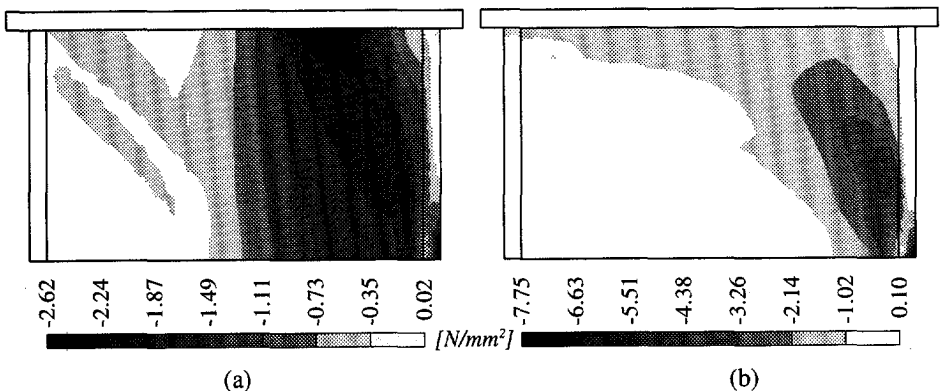


Figure 6.35 Wall W4. Minimum principal stresses at a displacement of (a) 1.0 [mm] and (b) 11.0 [mm].

A comparison between the behavior of all the walls in terms of load-displacement diagrams is shown in Figure 6.36. Walls W1 and W4, with a low confining pressure, exhibit an extremely ductile behavior whereas wall W2, with a high confining pressure, exhibits a relatively small plateau followed by brittle failure. A good impression of the

model is obtained because both types of failure can be described. Another interesting point is the eccentricity of the applied initial vertical load. The difference in collapse load between wall W1 and W4, which amounts to 25%, corresponds to moving the initial vertical load resultant from the middle line of the wall to an eccentricity of  $\approx 1/4$  of the wall length.

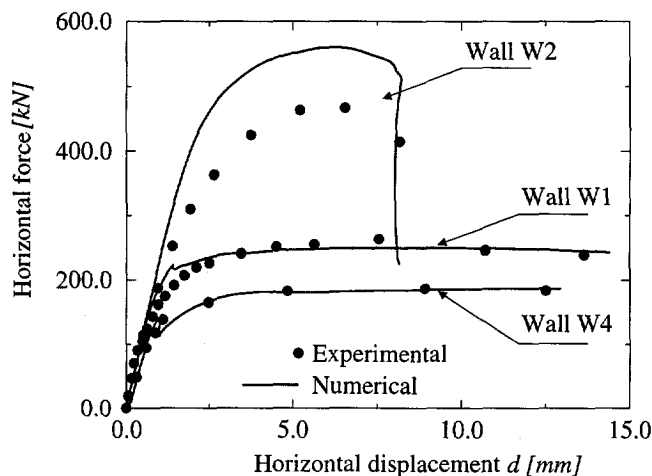


Figure 6.36 Walls W. Comparison between load - displacement diagrams.

#### 6.4.2 ETH Zurich concrete block masonry shear walls

The second series of shear walls analyzed consists of hollow concrete block masonry, see Figure 6.12 on page 144. The tests were carried out by Lurati and Thürliman (1990) and are denoted by ZW. The properties of the composite material are obtained from Lurati *et al.* (1990), see Table 6.7 and Table 6.8. In Section 6.2.2, a no-tension material was obtained according to the least squares method. There, it was also stressed that this result is debatable, especially in the  $x$  direction, see Section 5.3. Here, it is assumed that the tensile strength in the direction parallel to the bed joints is given by  $0.075 f_{mx}$ , according to the experiments reported by Schubert (1994). A low tensile strength value is assumed in the direction normal to the bed joints ( $f_{ty} = 0.05 [N/mm^2]$ ). The inelastic properties of the flanges in the direction parallel to the bed joints are determined by the concrete block behavior and read:  $f_{tx} = 0.83 [N/mm^2]$  and  $f_{mx} = 16.5 [N/mm^2]$ .

Table 6.7 Walls ZW. Elastic properties.

$E_x$	$E_y$	$\nu_{xy}$	$G_{xy}$
3030	11700	0.32	3000
$[N/mm^2]$	$[N/mm^2]$		$[N/mm^2]$

Table 6.8 Walls ZW. Inelastic properties.

Tension regime						
$f_{tx}$	$f_{ty}$	$\alpha$	$G_{fx}$	$G_{fy}$		
0.43	0.05	1.00	0.03	0.02		
[N/mm <sup>2</sup> ]	[N/mm <sup>2</sup> ]		[Nmm/mm <sup>2</sup> ]	[Nmm/mm <sup>2</sup> ]		

Compression regime						
$f_{mx}$	$f_{my}$	$\beta$	$\gamma$	$G_{fex}$	$G_{fey}$	$\kappa_p$
5.78	9.21	-0.97	3.36	5.0	10.0	$1.0 \times 10^{-3}$
[N/mm <sup>2</sup> ]	[N/mm <sup>2</sup> ]			[Nmm/mm <sup>2</sup> ]	[Nmm/mm <sup>2</sup> ]	

The walls analyzed next yield an additional assessment of the ability of the plasticity composite model to reproduce the behavior of structures made of a different masonry type. As shown in Section 6.2.2, the yield criterion obtained with the material properties given above differs substantially from the yield criterion utilized in Section 6.4.1.

Wall ZW1 is subjected to an initial vertical load  $P$  of 419 [kN]  $\equiv$  0.42 [N/mm<sup>2</sup>]. Attention is given exclusively to the load-displacement diagrams shown in Figure 6.37. Good agreement is found. The low initial confining pressure leads to a very ductile response. The behavior of wall ZW1 is similar to the behavior of Wall W1 and will not be detailed here.

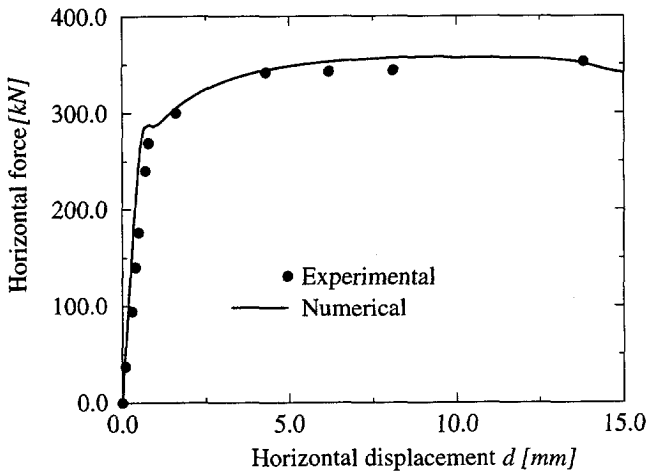


Figure 6.37 Wall ZW1. Load - displacement diagrams.

Wall ZW2 is subjected to an initial vertical load  $P$  of 833 [kN]  $\equiv$  1.23 [N/mm<sup>2</sup>]. Figure 6.38 shows the comparison between the experimental and calculated load-displacement diagrams. Again, good agreement is found. The higher confining pressure yields a higher collapse load but, still, a ductile response as compressive softening followed by explosive crushing did not occur in the ultimate stage. The difference between

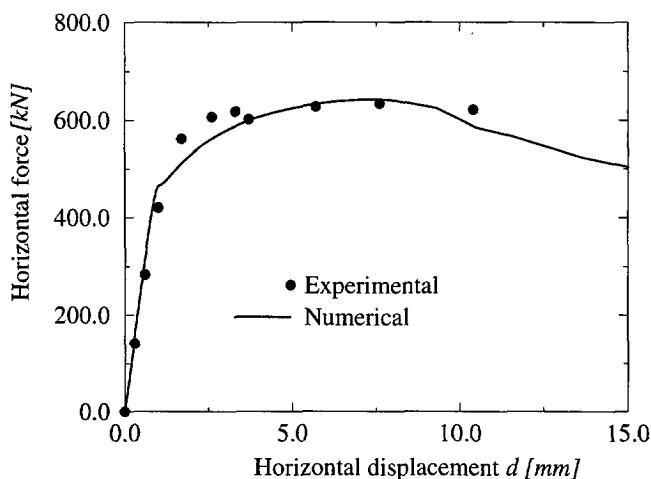


Figure 6.38 Wall ZW2. Load - displacement diagrams.

the ductile failure of wall ZW2 and the brittle failure of wall W2 results from several factors. In particular, the hollow concrete block masonry has more strength than the hollow clay brick masonry and the initial vertical load for wall ZW2 is only 65 % of the load for wall W2.

### 6.4.3 Discussion of the results

A good impression about the adequacy of the composite plasticity criterion to model masonry is obtained from the analyses of the ETH Zurich shear walls. The different failure mechanisms observed in the experiments are well captured by the model, which is the most important validation of any material model. It is striking that such excellent agreement is obtained also in the load-displacement diagrams (with the exception of Figure 6.26). These results are somewhat misleading because the perfect agreement of the experimental and numerical load-displacement diagrams must be regarded as a coincidence and not as an objective of any numerical modeling. An attempt to closely reproduce the experimental load-displacement diagrams was not carried out. In fact, if more than one test of each wall had been carried out the scatter in experimental results would become visible. Two other points of the numerical modeling are also important. Firstly, the model incorporates seven strength parameters and five inelastic parameters. The strength parameters were obtained with the least squares method without further adjustments whereas the inelastic parameters represent reasonable *first* guesses. Therefore, the sensitivity of the model with respect to the parameter estimation is unknown and will be the study of future work. A first impression is that the sensitivity of the results with respect to the estimation of material parameters is small. However, *some* variation on the load-displacement diagrams can be expected if different material parameters are adopted. Secondly, numerical results of softening materials with standard continuum are

(slightly) mesh dependent, see Section 6.5.2, even if an energy-based regularization is adopted. Therefore, a numerical load-displacement diagram is not unique, even if, for practical applications, it can be considered so.

## 6.5 Reflections about the modeling strategy

### 6.5.1 Limitations of macro-models

When using macro-models, it is tacitly assumed that the structure, loading and boundary conditions are such that the discretization of units and mortar can be avoided. Of course, it is not enough to postulate that the structure is large because it is also necessary that a truly composite failure mechanism is obtained. The example presented next demonstrates that unrealistic collapse loads can be found when the above conditions are not met.

The TU Eindhoven shear walls introduced in Section 4.3.1 are again considered. Walls J4D and J5D built of 16 courses of 4  $\frac{1}{2}$  units, with an initial vertical load  $P$  equal to 30 [kN]  $\equiv$  0.30 [N/mm<sup>2</sup>], are selected for an additional analysis with the composite plasticity (macro-)model.

For the numerical analysis, linear plane stress continuum elements with full Gauss integration are utilized. A regular mesh of 15  $\times$  15 elastoplastic elements is used. Two additional rows of linear elastic elements are considered to model the units clamped in the boundary steel beams. The purpose of this study is not a sharp reproduction of the experimental results and the main concern of the author is to reproduce the behavior observed in the experiments. For this purpose the exact knowledge of the macro-material parameters is not capital and, in any case, it is not known for this particular material. It is assumed that the properties of the composite material are given by Table 6.9 and Table 6.10. The elastic properties of the composite are obtained from homogenization as given in Section 5.2. Most of the inelastic parameters are unknown and must be estimated, being the only exceptions, the vertical tensile strength  $f_{ty}$ , the vertical stack bond compressive strength  $f_{my}$  and the vertical fracture energy  $G_{fy}$ .

Table 6.9 Walls J4D and J5D. Elastic properties.

$E_x$	$E_y$	$\nu_{xy}$	$G_{xy}$
7520	3960	0.09	1460
[N/mm <sup>2</sup> ]	[N/mm <sup>2</sup> ]		[N/mm <sup>2</sup> ]

Table 6.10 Walls J4D and J5D. Inelastic properties.

Tension regime						
$f_{tx}$	$f_{ty}$	$\alpha$		$G_{fx}$	$G_{fy}$	
0.35	0.25	1.00		0.05	0.018	
[N/mm <sup>2</sup> ]	[N/mm <sup>2</sup> ]			[Nmm/mm <sup>2</sup> ]	[Nmm/mm <sup>2</sup> ]	

Compression regime						
$f_{mx}$	$f_{my}$	$\beta$	$\gamma$	$G_{fxc}$	$G_{fyc}$	$\kappa_p$
10.0	8.8	-1.0	2.5	20.0	15.0	$1.2 \times 10^{-3}$
[N/mm <sup>2</sup> ]	[N/mm <sup>2</sup> ]			[Nmm/mm <sup>2</sup> ]	[Nmm/mm <sup>2</sup> ]	

Figure 6.39a shows the comparison between the results obtained in Section 4.3.1 with the micro-model (which show good agreement with the experimental results) and the newly calculated results with the macro-model. Figure 6.39b shows the total response of the macro-model and the (dis)agreement found in terms of collapse loads. The macro-model yields an enormous over-prediction of strength. The difference found cannot be explained solely by a possibly erroneous estimation of the material parameters but must be due to some deficiency of the model or modeling strategy. A physical reason for this phenomenon does exist and is given further below in the text.

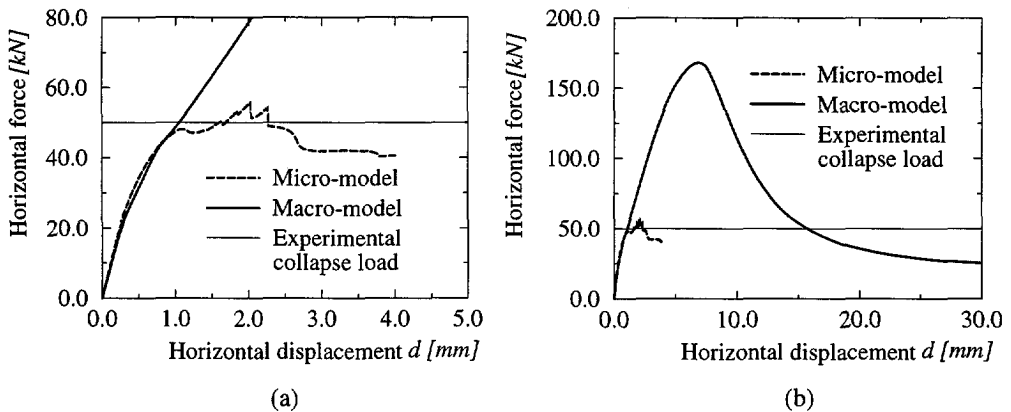


Figure 6.39 Walls J4D and J5D. Load - displacement diagrams: (a) magnified view up to a horizontal displacement of 5.0 [mm]; (b) complete response with macro-model.

The behavior of the wall is depicted in Figure 6.40 and Figure 6.41 in terms of total deformed meshes, incremental deformed meshes, cracked and crushed Gauss points and principal stresses. Masonry crushing is represented by dotted triangles, with a size proportional to the compressive equivalent plastic strain  $\kappa_c$ . Finally, note that the principal stresses in the elastic bricks are not shown. In the elastoplastic elements, the negative

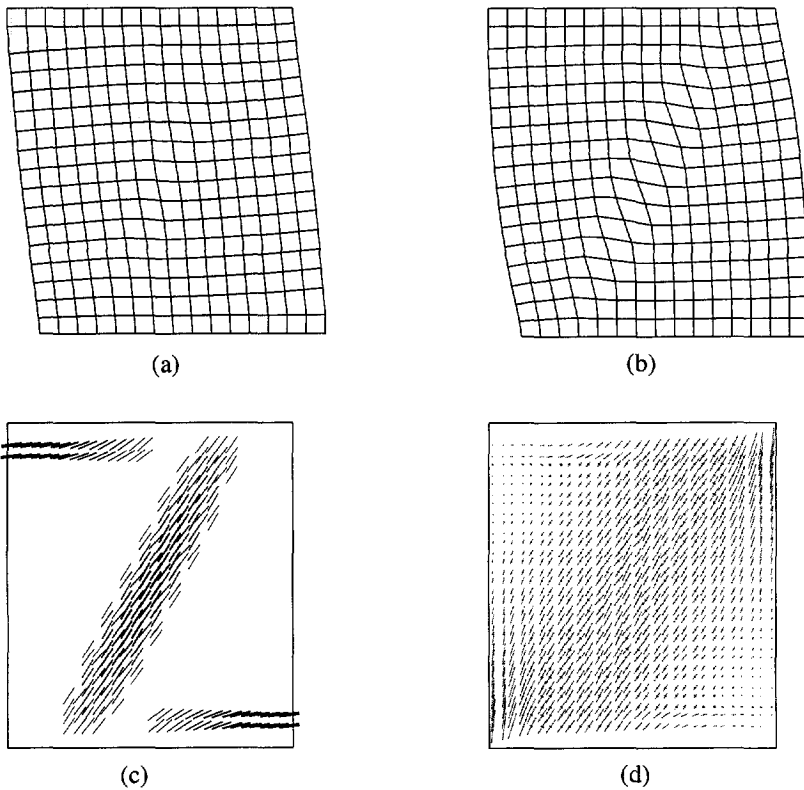


Figure 6.40 Walls J4D and J5D. Results of the analysis at a displacement of 2 [mm]: (a) deformed mesh; (b) incremental deformed mesh; (c) cracks; (d) principal stresses ( $\sigma_{\min} = -3.52$  [N/mm<sup>2</sup>]).

principal values are represented by a dotted line and the positive principal values by a solid line. Figure 6.40 and Figure 6.41 demonstrate that the behavior of the structure is quite well captured by the model. Initially, two horizontal cracks develop at the top and bottom of the wall. Upon increasing deformation, a diagonal crack arises, see Figure 6.40. The diagonal crack progresses in the direction of the compressed corners of the wall, accompanied by crushing of the toes, see Figure 6.41, until total degradation of strength in the compressive strut. This behavior agrees well with the behavior found in the experiments and the micro-analysis, see Section 4.3.1. A good impression about the robustness of the model is obtained because it is possible to follow the complete load path until total degradation of strength.

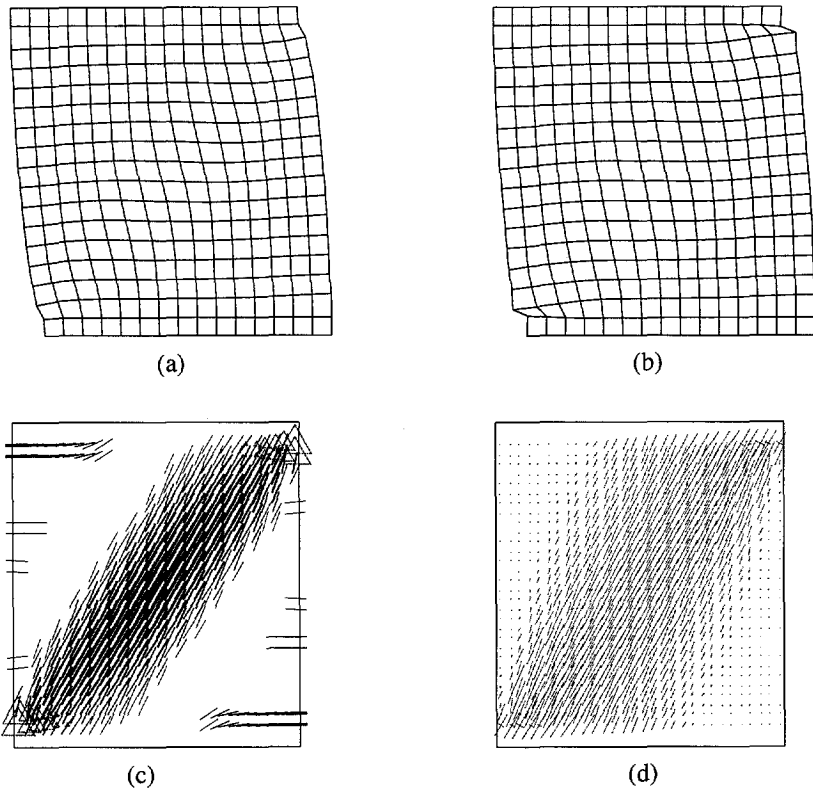


Figure 6.41 Walls J4D and J5D. Results of the analysis at a displacement of 6.9 [mm] (peak): (a) deformed mesh; (b) incremental deformed mesh; (c) cracks and crushing; (d) principal stresses ( $\sigma_{\min} = -10.1$  [N/mm<sup>2</sup>]).

The over-prediction of the collapse load by the macro-model is discussed now. Figure 6.39a shows that the experimental load-displacement diagram is well reproduced until the horizontal displacement  $d$  equals 1.0 [mm], which coincides with the opening of the diagonal shear crack. After this point, it seems that the behavior of the structure is not captured by the model. The crucial question is whether the masonry macro-model here proposed is not acceptable or the modeling strategy is inadequate. It will be shown that the latter is true.

The experimental failure patterns, see Figure 4.15, clearly show an extremely localized diagonal failure type, where all inelastic phenomena concentrate, basically, in a single stepped crack. The internal force distribution calculated with the micro-model, see Figure 4.21, explains the bad performance of a macro-modeling strategy. At an early stage, the direction of the compressive strut is determined by the geometry of the bricks and deviates from the strut direction found in the macro-analysis. The discrepancy between the micro- and macro-model gets only larger under increasing deformation. At ultimate stage, once the diagonal crack is fully open, two independent compressive

struts are found with the micro-model, see Figure 4.21b. A well defined band, with approximately the width of a unit, completely unloads. This behavior cannot be captured by a (smeared) macro-model unless some internal length scale, that reflects the masonry micro-structure, is incorporated in the model. Note that the issue here is compressive failure and the distribution of normal vertical stresses at the supports as discussed in Section 4.3.1 and Section 4.4.3. In particular, a similar increase in the collapse load was found also with the micro-model if the diagonal crack was prevented from opening completely due to a high dilatancy of the joints.

A possible solution for this problem is to introduce coupling in the formulation of the macro-model, in such a way that degradation of tensile strength induces degradation of compressive strength. A simple coupling expression is given by

$$(\bar{\sigma}_{peak})_c = \frac{f_m}{f_t} \bar{\sigma}_t \quad (6.48)$$

where the compressive yield value is made dependent of the current tensile yield value. It is noted that the above equation leads to additional terms in the derivations of the numerical algorithm given in this Chapter. Figure 6.42 demonstrates that then cracking localizes in a single row of elements and the two-strut action can be reproduced.

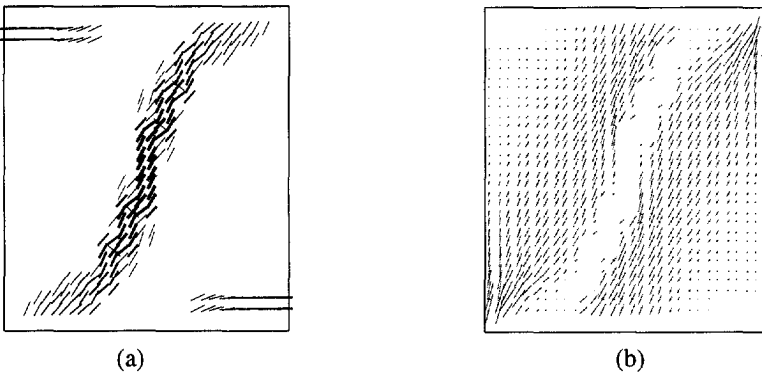


Figure 6.42 Walls J4D and J5D. Results of the new analysis with coupled model at peak: (c) cracks; (d) principal stresses ( $\sigma_{min} = -8.73 [N/mm^2]$ ).

A much better agreement is also found in terms of collapse load. The new collapse load equals 70 [kN] which is just 40 % higher than the experimental value. This should be expected because Figure 6.42b clearly shows that the inactive band (where compressive unloading also occurs) is still too thin, when compared with the results of the micro-model, see Figure 4.21b. The inactive band has the width of one element which means that a coarser mesh must be used to reproduce the correct failure load. Figure 6.43 shows that a coarser mesh (with  $8 \times 8$  elements) can at least reproduce the exact collapse load. Here, the sharp snap-back after the second peak was traced with COD

control over the diagonal crack zone. The first peak in the load-displacement diagram is obtained when the diagonal crack opens. This agrees well with the response obtained with the micro-model.

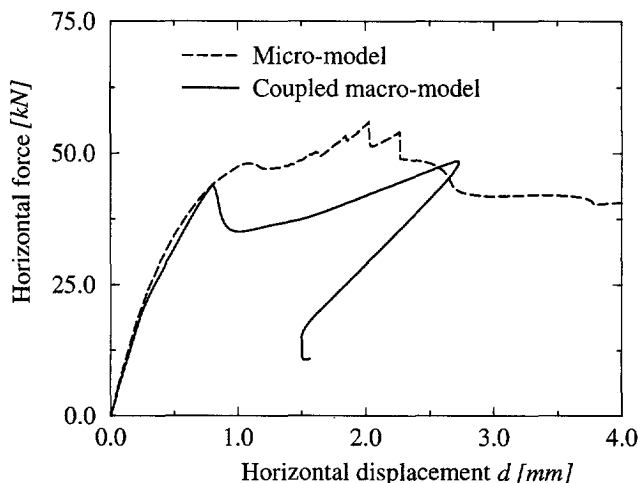


Figure 6.43 Walls J4D and J5D. Load - displacement diagram for analysis with coupled macro-model ( $8 \times 8$  elements).

For this particular structure, with a good estimate of the width of the inactive shear band, it seems possible to reproduce the experimental results, at least to some extent. However, a length scale has been introduced by the finite element mesh which is, in general, not acceptable. A possible direction to remove the mesh dependency of the coupled model is to resort to enhanced continua, see e.g. De Borst *et al.* (1993). However, a complete solution remains quite complex. At the present stage, it is not clear if the above length scale is a geometrical property dependent on the unit size or a structural property that depends on the micro-structure, geometry of the structure and loading conditions. The latter is believed to be true but this problem is outside the scope of the present study and should be the objective of future research.

It is stressed that a conclusion that a macro-modeling strategy is not applicable for structures built of a relatively small number of units *cannot* be made from this single example.

### 6.5.2 Mesh sensitivity of the anisotropic continuum model

A crucial point in the analysis of strain softening materials with standard continuum is the sensitivity of the results with respect to the mesh size. The fracture energy based regularization which has been adopted in this study is widely used in engineering practice to overcome this problem. It suffices to incorporate an equivalent length in the material model which is related to the area of an element, see Section 6.1.

New analyses have been carried out for the structures introduced before with finite element meshes refined by a factor two. Figure 6.44 shows the comparison between the results of the analyses with the coarser and finer meshes. It is observed that, for practical purposes, the results can be considered mesh insensitive. The maximum difference in collapse load is approximately 5% and the predicted failure mechanisms remain unchanged.

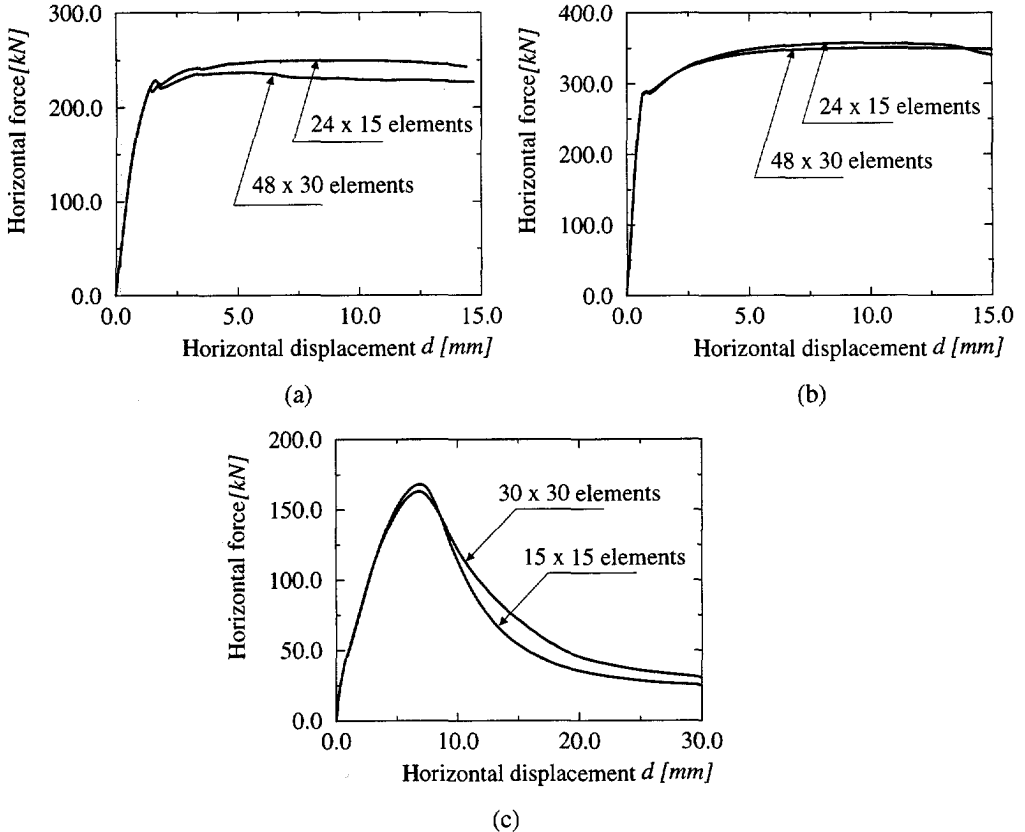


Figure 6.44 Mesh sensitivity of the macro-model analyses. Load-displacement diagrams for: (a) ETH brick masonry wall (wall W1); (b) ETH concrete masonry wall (wall ZW1); (c) TU Eindhoven wall (walls J4D and J5D).

## 6.6 Summary

An anisotropic composite continuum model for the analysis of masonry structures has been formulated in modern plasticity concepts. It is assumed that two failure mechanisms can be distinguished, one associated with localized fracture processes and one associated with a more distributed fracture process which can be termed crushing of the

material. The internal damage due to these failure mechanisms can be represented with two internal parameters  $\kappa_t$  and  $\kappa_c$  for damage in tension and compression respectively, which are related to the inelastic strain. The model is formulated in such a way that each internal parameter is related to two independent fracture energies. Therefore, it is possible to reproduce different inelastic behavior along each material axis.

Orthotropic elasticity is combined with orthotropic plasticity in a frame of reference associated to a set of material axes. The model includes a Rankine type yield criterion for tension and a Hill type yield criterion for compression, which fit well the strength data of biaxially loaded masonry panels. It is shown that the model is flexible enough to accommodate different masonry types, namely solid and hollow masonry or clay and concrete masonry.

A comparison between numerical results and experimental results available in the literature is also given. It is shown that, if a macro-modeling strategy can be applied, the proposed anisotropic model is able to predict well the behavior of masonry structures, with both ductile and brittle failure modes, as well as sufficiently accurate collapse load values.



## 7. APPLICATIONS

In the previous Chapters different modeling strategies for masonry structures have been addressed (micro and macro). For each modeling strategy a numerical model has been introduced and assessed by means of a comparison with experimental results available in the literature. Extensive application of the numerical tools to practice is outside the scope of the present study. In fact, the main objective of the present work is to develop numerical tools suitable for the analysis of masonry structures, which is, in essence, a fundamental goal. However, this study would not be completed without some indication of how the models can be used to solve real engineering problems, in which a premium is put in the predictive capability of the numerical tools.

This Chapter shows examples compatible with two of the different aspects of numerical research, according to the principles reviewed in Chapter 1. A first aspect is the step towards fracture mechanics based design rules in opposition to prevailing rules-of-thumb. The example shown concerns the spacing of movement joints in masonry walls. A second aspect is the assessment/strengthening of existing structures. The examples shown concern the behavior of old masonry buildings in the Netherlands subjected to settlements caused by tunneling and the residual strength of damaged masonry buildings in Italy.

### 7.1 The step towards fracture mechanics based design rules:

#### Movement-joint spacing in masonry walls

Hygral or thermal shrinkage of a wall is often constrained by surrounding building components, like foundations and floors. Figure 7.1 shows that the restraint generates tensile stresses, which may lead to cracking. Cracking might be circumvented by adding movement joints, alternatively denoted expansion joints or construction joints. This type of cracking does not, generally, strongly affect the carrying capacity of the wall. However, the integrity of the wall is damaged which can lead to a dramatic reduction of the water impermeability of the wall, accompanied by a reduction of its thermal and acoustic characteristics. Moreover, from aesthetical and psychological perspectives, extensive cracking is obviously non-acceptable.

Crack formation due to restrained shrinkage is number 1 in the top-10 of damage events in the building industry from the Netherlands, De Jong (1992), which demonstrates the lack of consistent design rules for the spacing and positioning of movement-joints. Typical examples of malfunctioning are given, not only, by incorrect large spacing and positioning of the movement-joints that lead to cracking of the wall at places where joints in fact should have been designed, but also, by sometimes too small spacing that leads to excessive maintenance and bounds the aesthetics. A solution to this problem is not simple due to the large number of influence factors, see e.g. CUR (1994). The experimental and analytical work carried out previously by several authors seems to

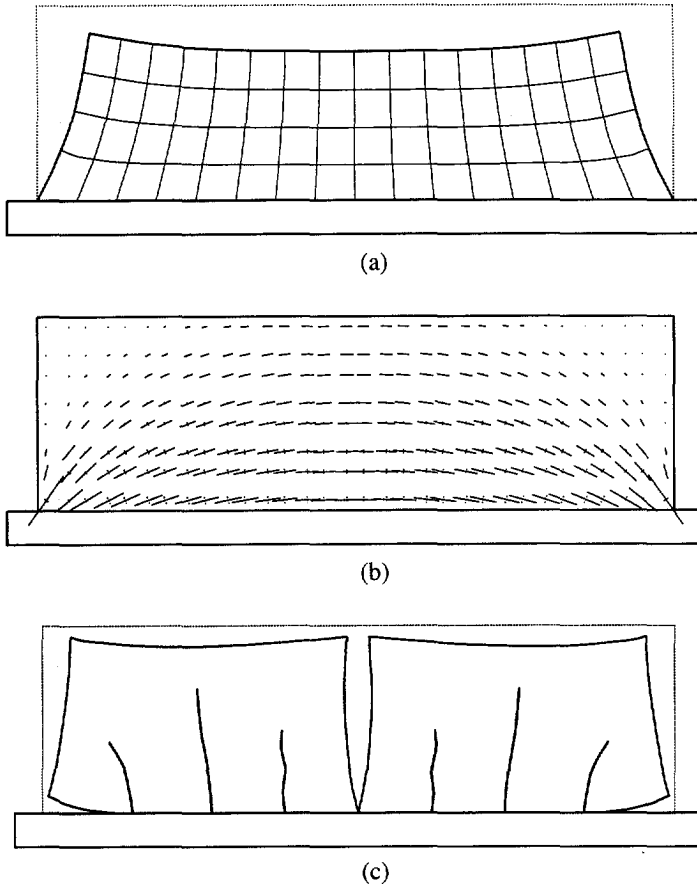


*Figure 7.1* Wall under restrained shrinkage at the bottom: (a) deformation for linear elastic behavior; (b) principal stresses for linear elastic behavior; (c) possible crack pattern.

provide us only with partial understanding of the phenomena involved. Existing rules are strength-based, empirical and show large differences, see e.g. Copeland (1957), Hageman (1968) and Schubert (1988b). Damage is, thus, likely to prevail, particularly for innovative applications of masonry as in the case of new techniques, such as glued masonry joints or mortarless head joints, and different building geometries, such as non-standard openings. The step towards fracture mechanics based design rules was introduced by Rots, see Rots *et al.* (1994) and CUR (1994). Many questions still remain but, in the following, it will be shown that the models developed can be successfully used to rationalize masonry design and provide us with ready-to-use design rules as well as a better understanding of the phenomena involved.

The example adopted in Rots *et al.* (1994) is analyzed next with the (micro-) model developed in Chapter 4. In comparison with the seminal work carried out by Rots, the present work fully includes the masonry joint in the bottom of the wall and adopts a

clear definition of damage based on the maximum crack width. Previous work by Rots *et al.* (1994) did show the importance of the inelastic behavior of the bottom masonry joint but only the Coulomb friction mode was considered in the analyses. Additionally, a lower masonry tensile strength, believed to more in agreement with the values that can be found in site, is adopted. A rectangular wall has been modeled with a predefined vertical crack in the middle and a masonry joint in the connection to the foundation beam, see Figure 7.2. Only half of the wall is modeled due to symmetry conditions. However, to increase the legibility, post-processing of the results includes both halves of the wall. The beam and the wall are assumed to remain linearly elastic. For the wall, this is certainly not true, especially in the case of larger lengths. However, distributed cracking will reduce the maximum crack width in the center of the wall, which means that the assumption of linear elastic behavior of the continuum is conservative. The length  $L$  of the wall is taken as a variable, ranging from 2000 [mm] to 30000 [mm], whereas the height of the wall equals 2400 [mm] and the thickness 100 [mm]. The wall is subjected to a uniform shrinkage which is incremented up to and beyond cracking. The shrinkage is restrained by a non-shrinking concrete foundation beam with a height of 200 [mm] and a thickness of 200 [mm]. The material properties selected are given in Table 7.1 and Table 7.2. Here,  $\gamma$  is the volumetric weight. It is noted that an attempt to model a specific kind of masonry is not carried out. The material properties represent, however, possible data for masonry. The horizontal tensile strength is reduced by a factor two, in comparison with the vertical tensile strength, because the head joints are often improperly filled. However, as discussed in Section 5.3, some ductility can be expected for the post-peak behavior. Therefore, no reduction was made in the fracture energy.

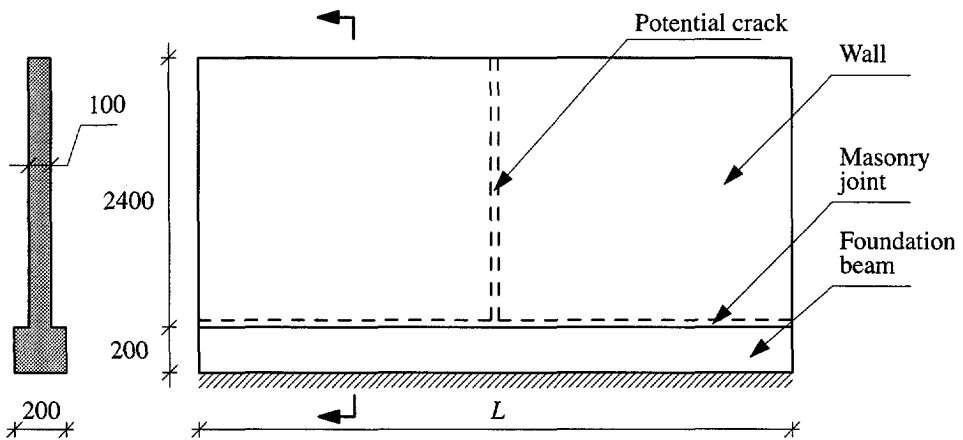


Figure 7.2 Wall under restrained shrinkage at the bottom. Geometry.

A wall with a length of 6000 [mm] is analyzed first. In a preliminary analysis, the bottom joint is not active and the horizontal tensile strength has no strength reduction in order to obtain a better understanding of the mode I behavior of the central crack. Figure

Table 7.1 Wall under restrained shrinkage. Elastic properties.

Masonry			Concrete beam			Bottom joint		Potential crack	
$E$	$\nu$	$\gamma$	$E$	$\nu$	$\gamma$	$k_n$	$k_s$	$k_n$	$k_s$
5000	0.2	$1.8 \times 10^{-5}$	30000	0.2	$2.4 \times 10^{-5}$	333	199	$1.0 \times 10^6$	$1.0 \times 10^6$
[N/mm <sup>2</sup> ]		[N/mm <sup>3</sup> ]	[N/mm <sup>2</sup> ]		[N/mm <sup>3</sup> ]	[N/mm <sup>3</sup> ]	[N/mm <sup>3</sup> ]	[N/mm <sup>3</sup> ]	[N/mm <sup>3</sup> ]

Table 7.2 Wall under restrained shrinkage. Inelastic properties.

Bottom joint						Potential crack	
$f_t$	$G_f^I$	$c$	$\tan \phi$	$\tan \psi$	$G_f^{II}$	$f_t$	$G_f^I$
0.25	0.01	0.4	0.75	0.2	0.1	0.125	0.01
[N/mm <sup>2</sup> ]	[Nmm/mm <sup>2</sup> ]	[N/mm <sup>2</sup> ]			[Nmm/mm <sup>2</sup> ]	[N/mm <sup>2</sup> ]	[Nmm/mm <sup>2</sup> ]

7.3 gives the response in terms of applied shrinkage versus maximum crack width  $w$  at mid-length. The wall remains uncracked up to a shrinkage of about 0.06 [mm/m], see Figure 7.4a. Then, the crack starts to open from the bottom of the wall, Figure 7.4b. Under increasing shrinkage, the crack progresses, Figure 7.4c, and, for a shrinkage of approximately 0.013 [mm/m], snaps through to the top surface, Figure 7.4d. During the analysis, the process could be kept stable by using COD control over the central crack. The wall temporarily swelled, corresponding to the snap-back in Figure 7.3, in order to allow for stable slow crack propagation. In reality, a jump (shown with a dashed line in the graph) would occur. The brittle cracking and explosive type of failure agree with the results of Rots *et al.* (1994) and the experimental observations where noise was reported when walls crack to their free surface, Berkers and Rademaker (1992).

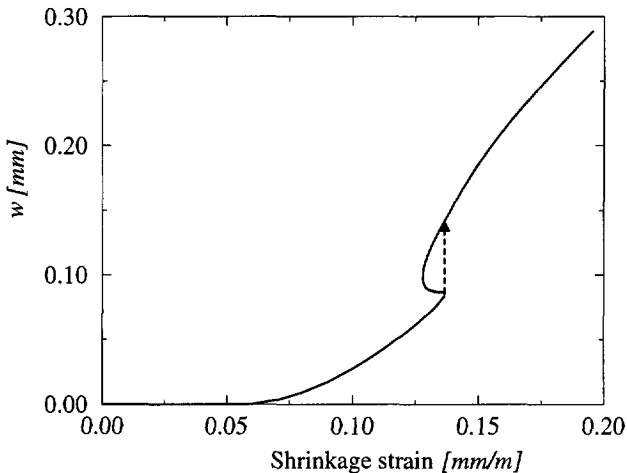
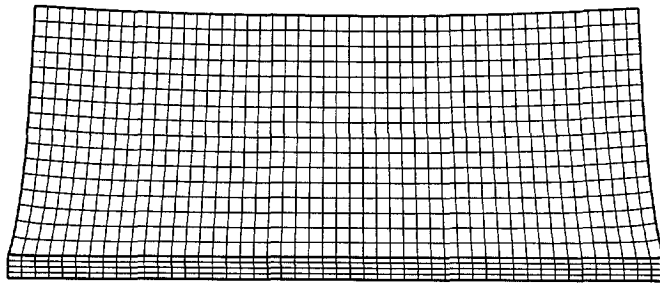
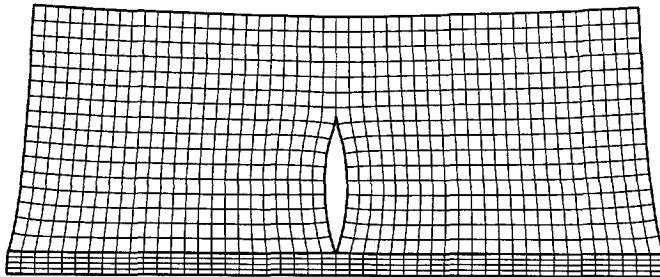


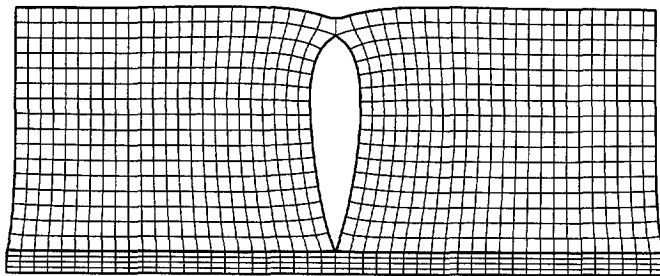
Figure 7.3 Wall under restrained shrinkage. Maximum crack width  $w$  at mid-length versus applied shrinkage strain (bottom masonry joint inactive).



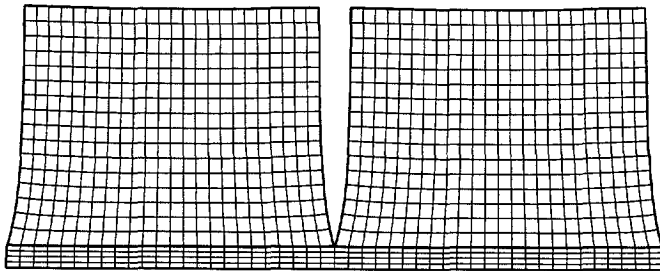
(a)



(b)



(c)



(d)

*Figure 7.4* Wall under restrained shrinkage. Deformation for different stages of the loading process, corresponding to a maximum crack width  $w$  of (a) 0.0 [mm], (b) 0.03 [mm], (c) 0.07 [mm] and (d) 0.25 [mm] (bottom masonry joint inactive).

The length of the wall is varied next in order to investigate the influence of the height/length ratio of the wall in the results. Figure 7.5 illustrates the typical response for a short, medium and long wall with a length  $L$  equal to, respectively, 3000 [mm], 6000 [mm] and 12000 [mm]. The bottom masonry joint is included in the analyses and, in all cases, damage is initiated in the joint, before the onset of cracking in the potential vertical crack (it can be observed in Figure 7.1b that the maximum principal tensile stresses occur indeed in both ends of the wall). The response of the walls differs significantly. For the short wall, the mid-crack stops before reaching the free (top) surface of the wall, see Figure 7.6, and cracking/slipping of the bottom masonry joint becomes predominant. This type of response is obvious and demonstrates that, for sufficiently small lengths, a movement-joint is not necessary independently of the expected value of shrinkage, at least if the main concern of the designer is to preclude vertical shrinkage cracks. For the medium wall, a marked change of slope in the crack-width-

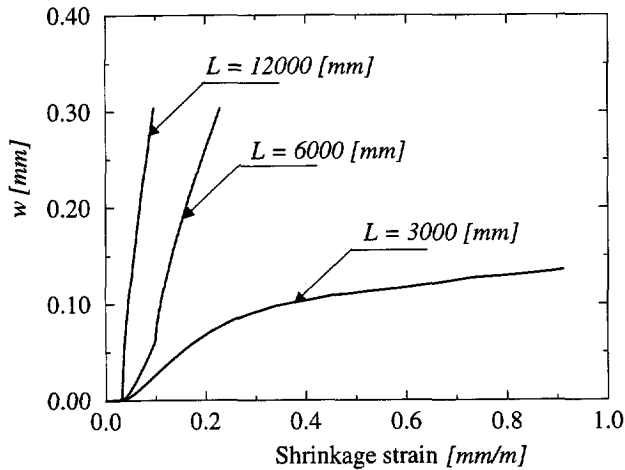


Figure 7.5 Wall under restrained shrinkage. Maximum crack width  $w$  at mid-length versus applied shrinkage strain for different wall lengths.

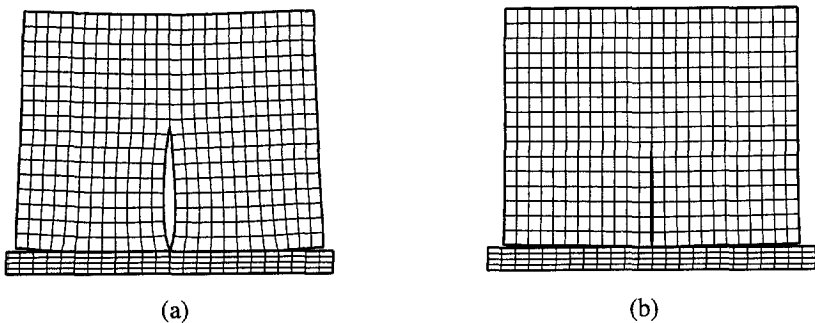
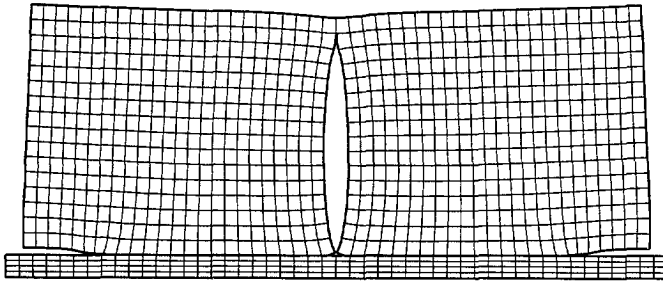
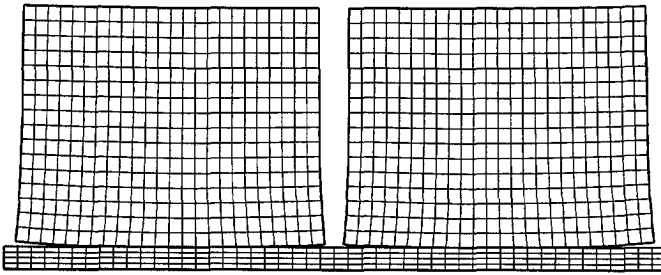


Figure 7.6 Wall with  $L = 3000$  [mm]. Deformation (a) before opening of central crack and (b) at end stage.

shrinkage-strain diagram is obtained. This corresponds to the different deformation modes shown in Figure 7.7. For the long wall, a marked change in slope is not

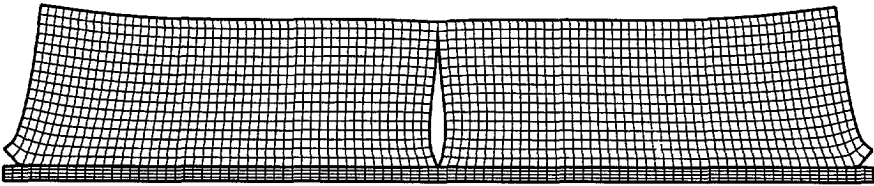


(a)

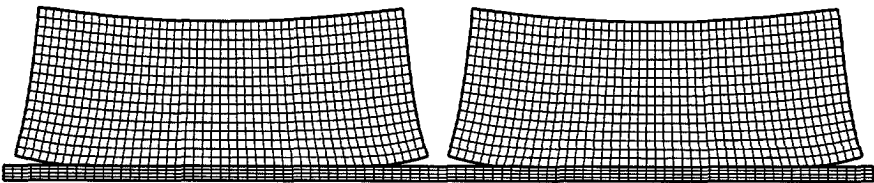


(b)

Figure 7.7 Wall with  $L = 6000$  [mm]. Deformation (a) before opening of central crack and (b) at end stage.



(a)



(b)

Figure 7.8 Wall with  $L = 12000$  [mm]. Deformation (a) before opening of central crack and (b) at end stage.

observed because the vertical mid-crack opens extremely fast. The fracture energy of the mode I crack is practically exhausted in a single load increment and an extremely steep crack-width-shrinkage-strain diagram is found. Cracking/slipping of the bottom joint is now very localized in the ends of the wall, see Figure 7.8, and, most likely, hardly influences the results.

The analyses have been repeated for different wall lengths. Figure 7.9 shows the results for different admissible maximum crack widths. The diagram shows two asymptotes, one horizontal and another vertical. This characteristic is easily explained by the behavior of the walls detailed before. For long walls, the stress distribution at mid-length is practically uniform and a crack immediately snaps to the free surface once it is initiated. For short walls, movement-joints are not necessary because the crack opening at mid-length is prevented by slipping of the bottom masonry joint. Slipping in the bottom joint is a much less severe damage but, still, it is the designer or Codes obligation to ensure that the masonry possesses enough shear bond strength. The wall length obtained from the graph in Figure 7.9 can be denoted as the “crack-free wall length”. It remains for the designer or, preferably, the masonry Codes to stipulate an admissible maximum crack width.

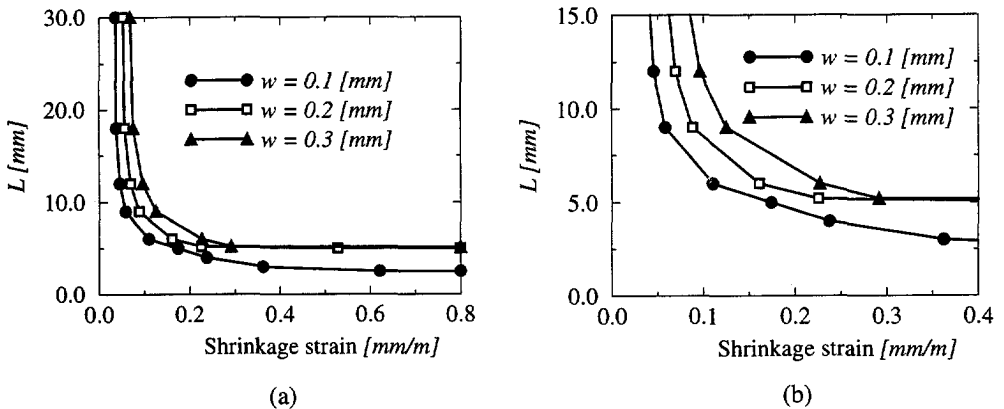


Figure 7.9 Preliminary fracture mechanics based rule for design of movement-joints, according to maximum admissible crack width: (a) complete results; (b) magnified view within practical range.

The results obtained are compared next with three existing strength-based criteria proposed by Copeland (1957), Hageman (1968) and Schubert (1988b), see Figure 7.10. The criteria shown are based in global notions like “the average stress in the wall” calculated with a linear elastic analysis. Clearly, different assumptions have been made, which explain part of the scatter in these results. The trend observed in all criteria is similar to the results of the numerical analyses but, for this particular example, it is shown that one of the criteria (Copeland) can be unconservative, if the maximum admissible crack width is taken equal to 0.1 [mm]. Graphs as shown in Figure 7.10 illustrate

the step towards fracture mechanisms based design rules. A practising engineer makes the design for a certain expected value of shrinkage (depending on hygral and thermal conditions) and can simply consult these graphs to decide whether a movement-joint is needed or not.

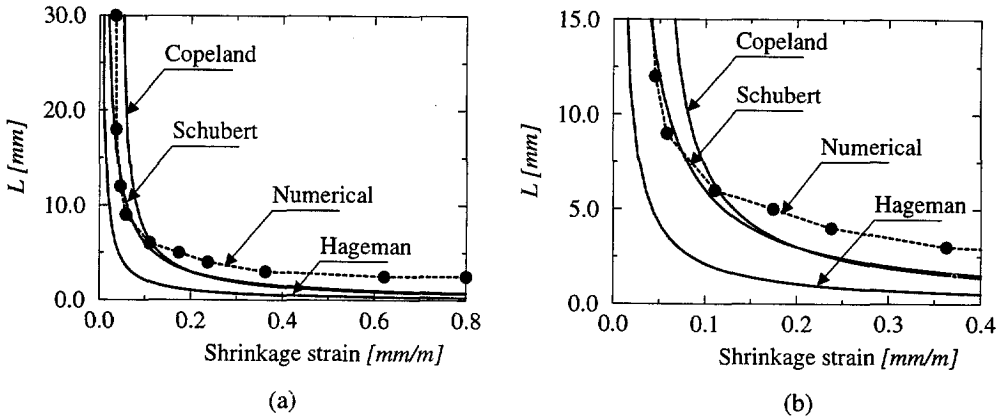


Figure 7.10 Comparison between strength-based rules and a (tentative) fracture mechanics based rule ( $w = 0.1$  [mm]): (a) complete results; (b) magnified view within practical range.

The present results are solely an indication of possible future developments. An integrated numerical/analytical approach is necessary to assess the most determinant influence factors before more rational and more reliable design rules can be obtained. A complete discussion of the behavior of this structure and design criteria can be found in Rots *et al.* (1994) and Berkers and Rademaker (1992).

During the above analyses, full convergence could be obtained, both at local at global level, which demonstrates the robustness and practical applicability of the developed numerical tools. In particular, numerical difficulties to trace the progressive crack growth simultaneously in the middle of the wall and at the bottom masonry joint, which poses high demands in the iterative process to obtain equilibrium, were not encountered.

## 7.2 Assessment of damage in old masonry buildings caused by tunneling induced settlements<sup>†</sup>

Large tunnels are currently being planned in the western part of the Netherlands, which consists of densely populated areas and soft soils. However, in the Netherlands, very

<sup>†</sup> The author gratefully acknowledges TNO Building and Construction Research and its clients for the permission of using this example as a test case for the new anisotropic composite model. The support of dr. ir. M.A.N. Hendriks was highly appreciated.

little practical experience has been gathered about the consequences of soil settlements, caused by tunnels bored in the vicinity of existing buildings. An investigation of the expected damage, associated with crack formation, for old masonry buildings in central Amsterdam has been recently carried out by Hendriks *et al.* (1995).

Figure 7.11 shows a masonry building, representative of the typical architecture in Amsterdam by the late 19<sup>th</sup> and early 20<sup>th</sup> centuries, which is supported by wooden piles of 11.4 [m] length. With the construction of the tunnel, settlements will occur in the soil surface and the first sand layer of the Amsterdam subsoil. The settlements will lead to movement of the foundation piles and, as a consequence, the possibility of damage of the masonry buildings supported by the piles. It is shown next that the models developed in this study can be successfully used to predict the expected settlement damage. A block of ten typical façades is adopted for this purpose, see Figure 7.12. It is noted that a continuous façade is considered, as the objective is not to represent ten individual "houses", that behave independently, but a large structure, where the effects of tunneling will be more severe. The walls are modeled with 8-noded nonlinear plane stress elements with a thickness ranging from 220 [mm] to 440 [mm]. The yield criterion presented in Chapter 6 is adopted to model inelastic behavior even if it is recognized that the small piers are only a few units width. For this large structure, it is only feasible to adopt a macro-modeling strategy. Moreover, this analysis concerns damage due to cracking and the solution with a macro-model seems to be sufficiently accurate in this case, even if the structure is built from a small number of units, see Section 6.5.1. Beam

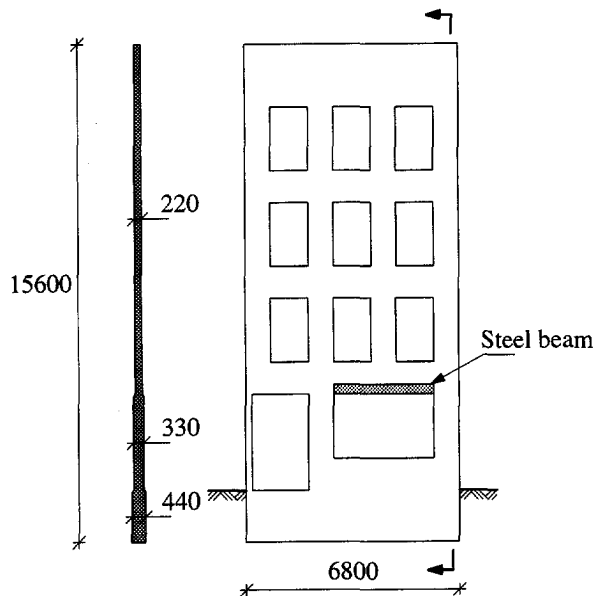


Figure 7.11 Typical Dutch masonry façade in central Amsterdam around the year 1900.

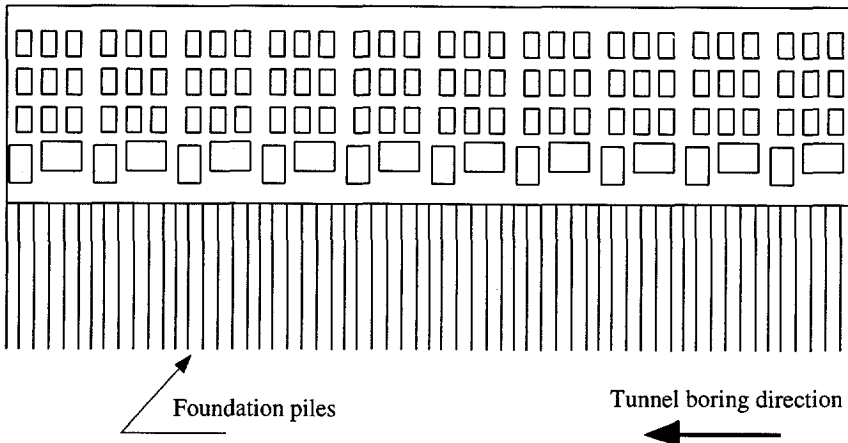


Figure 7.12 Block of ten typical façades adopted for the analysis.

elements, adequately tied to the continuum elements, are included to model the steel profile over the large openings at the ground floor level. The foundation piles are modeled with truss elements, whereas the interaction between the soil and each pile is modeled with two nonlinear springs (one for the tip resistance and another for the skin friction). The applied loads include the self-weight of the structure, dead and live floor loads and the settlements of the piles induced by boring a tunnel parallel to the façade, from right to left. The settlements occur gradually with the construction of the tunnel, starting from the right end of the building. Once the loading process is completed a uniform settlement which amounts to  $12.9 [mm]$  is obtained. The complete description of the finite element model, including geometry, material properties as well as loading and boundary conditions, is given in Hendriks *et al.* (1995) and will not be reviewed here.

The results of the analysis are given in Figures 7.13 to 7.16, in terms of total and incremental deformed meshes, for two stages of the loading process. These stages correspond to a boring front position, with respect to the right end of the structure, of  $0.0 [m]$  and  $34.0 [m]$ , respectively  $0\%$  and  $50\%$  of the structure length. The damage associated with crack formation is illustrated in Figure 7.17. It is noted that *all* cracks are shown in Figure 7.17, independently of the crack width.

It is observed that, during the entire loading process, cracking occurs around the openings due to bending of the beams and the small piers individualized by the geometry. However, these cracks are not the most severe. In a first phase, the structural behavior is, essentially, controlled by the dominant cracks that arise above the top floor windows. These cracks occur in the third and fourth "houses" due to bending of the right end of the structure upon initiation of the tunnel construction, see Figure 7.14 and Figure 7.17a. Once the boring front progresses, the cracks just opened partially close and new bending cracks in the bottom of the structure become predominant. These cracks open in all the next "houses" until the influence of the left end of the structure becomes relevant, see Figure 7.16 and Figure 7.17b. The damage predicted after completing

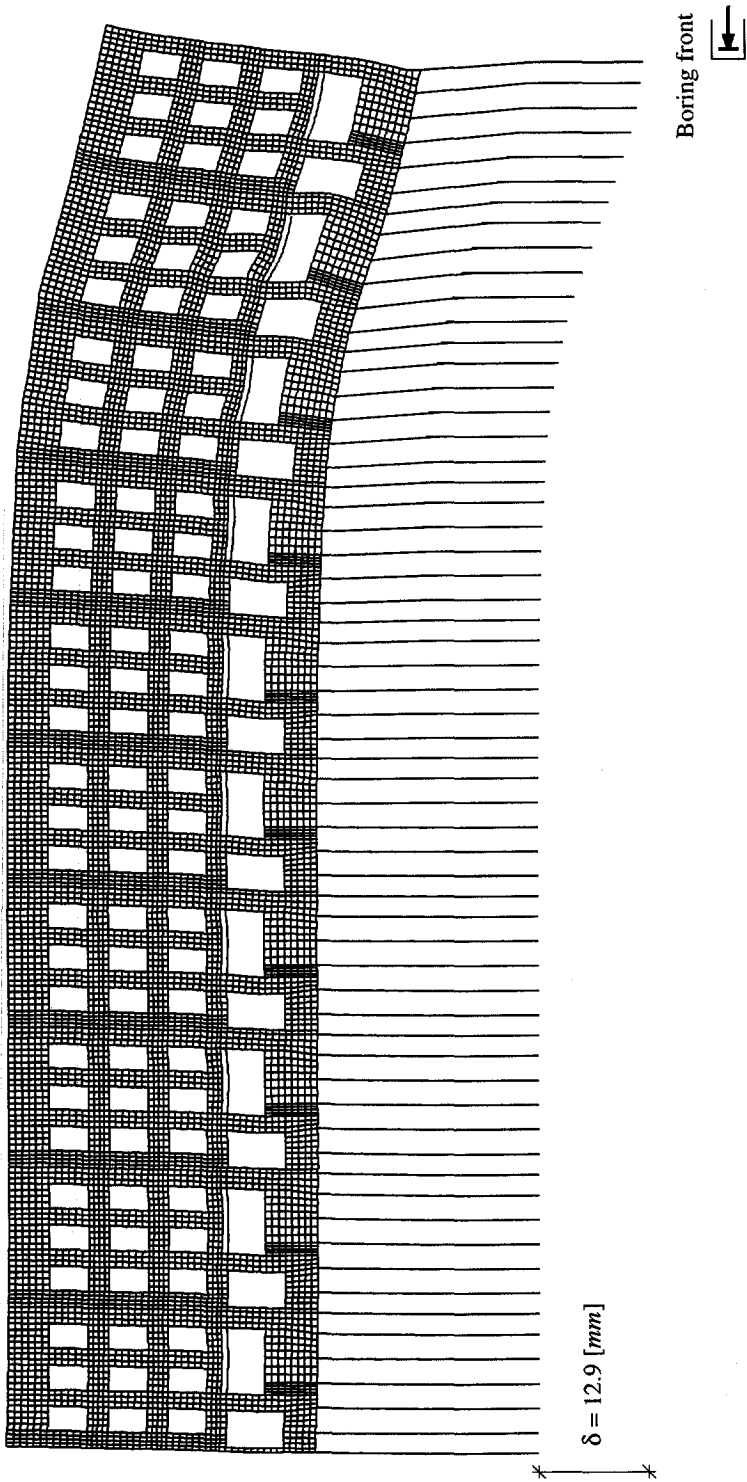


Figure 7.13 Total deformed mesh for settlement analysis. Boring front position in relation to the right end of the structure: 0.0 [m].

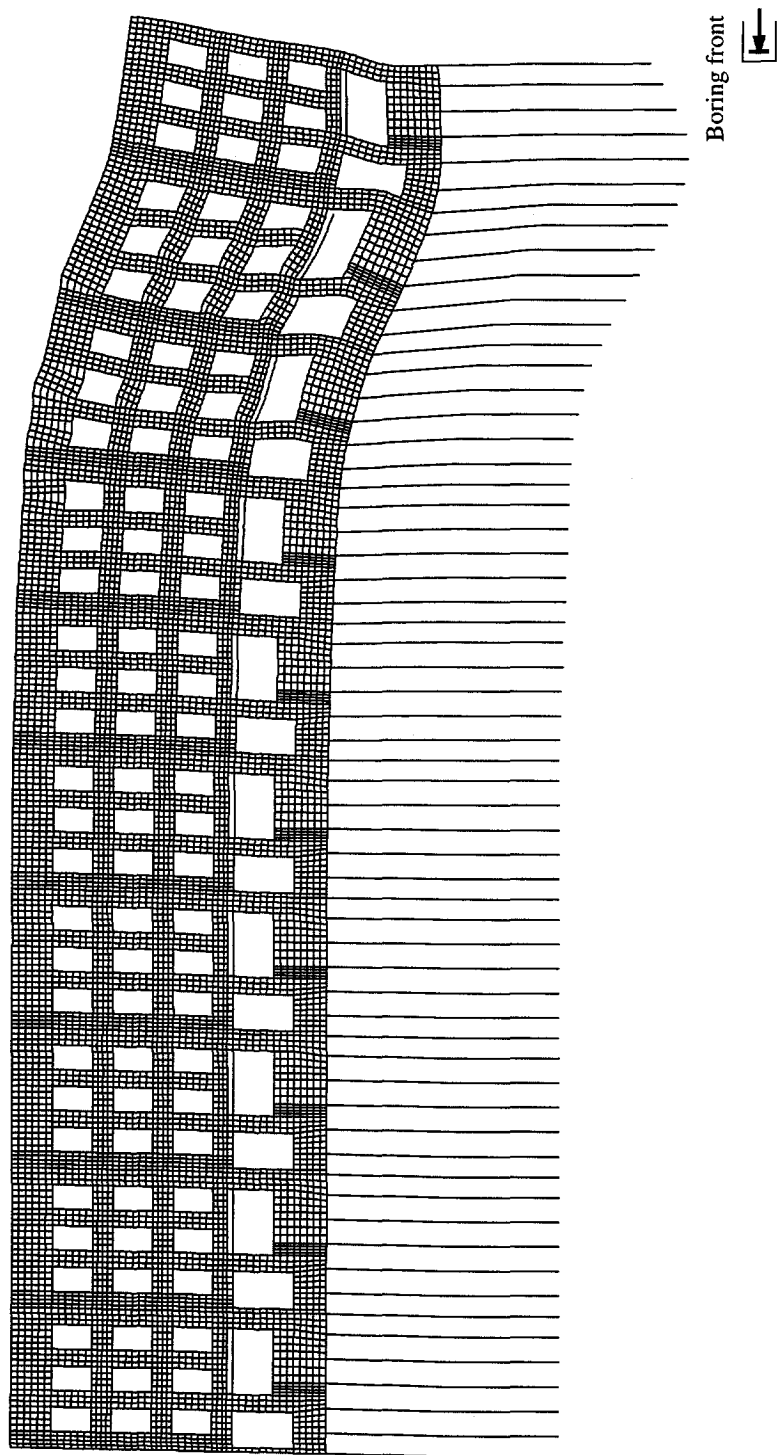


Figure 7.14 Incremental deformed mesh for settlement analysis. Boring front position in relation to the right end of the structure: 0.0 [m].

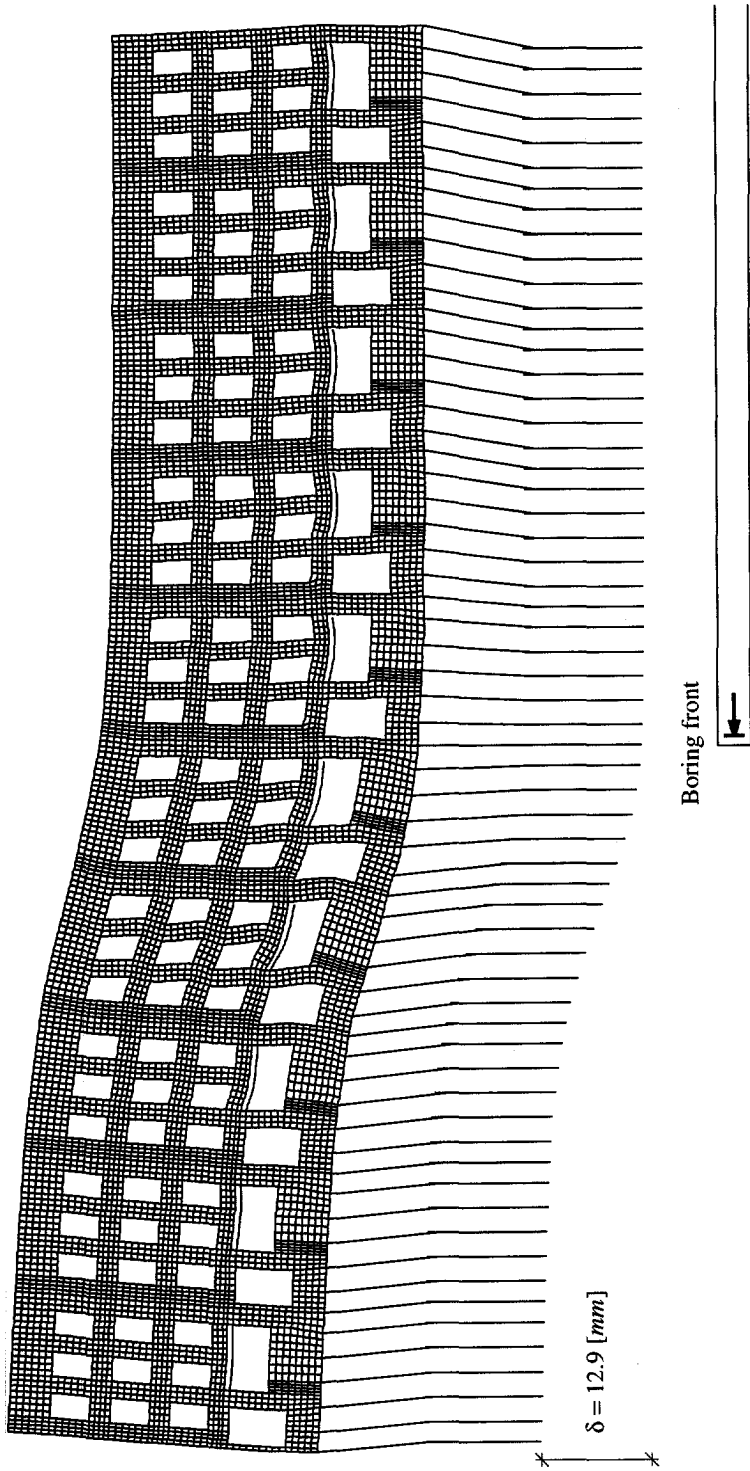


Figure 7.15 Total deformed mesh for settlement analysis. Boring front position in relation to the right end of the structure: 34.0 [m].

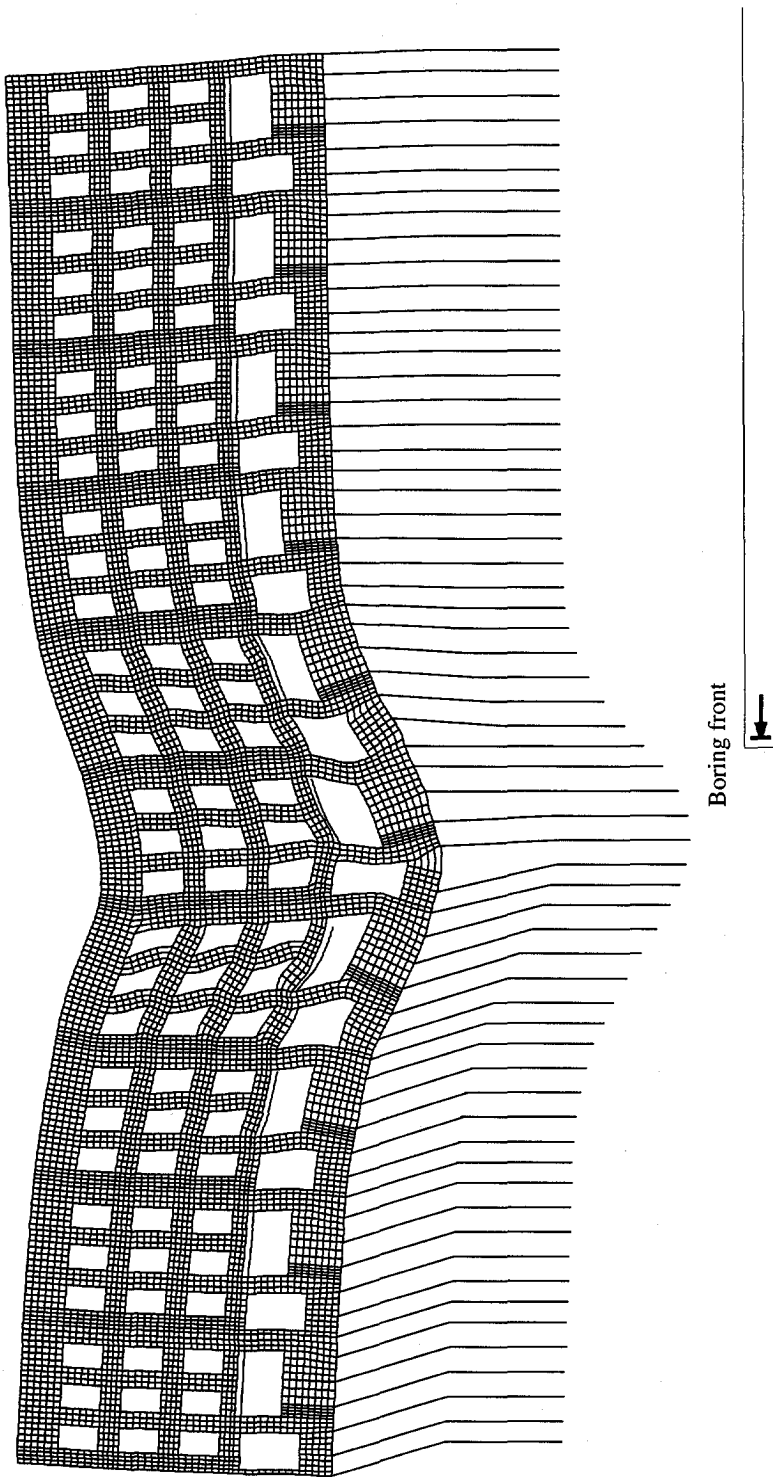


Figure 7.16 Incremental deformed mesh for settlement analysis. Boring front position in relation to the right end of the structure: 34.0 [m].

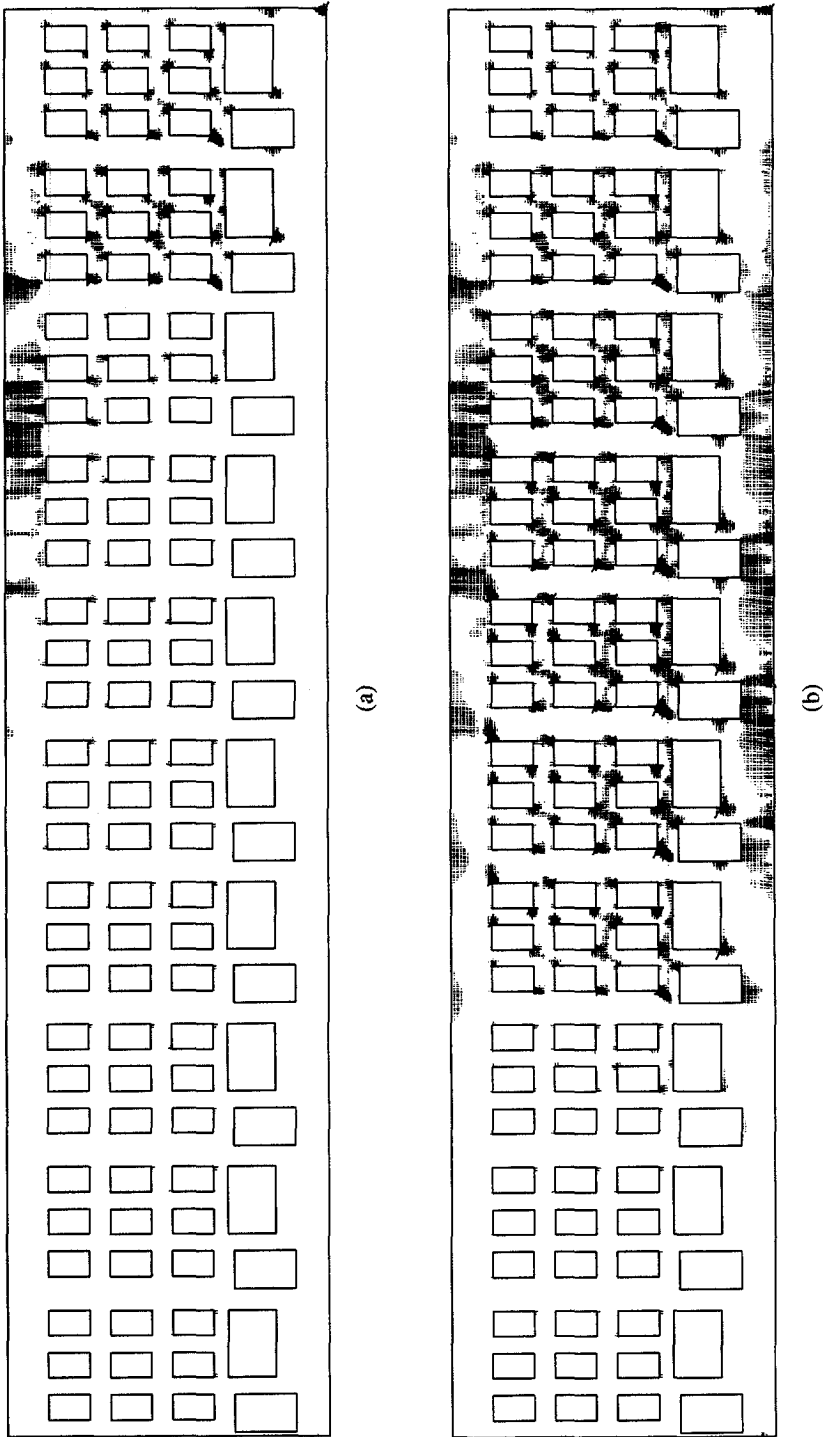
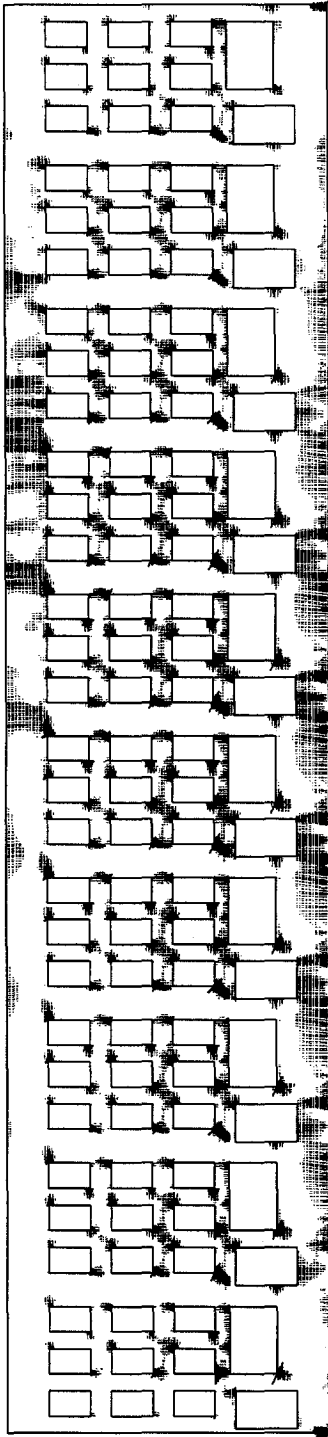
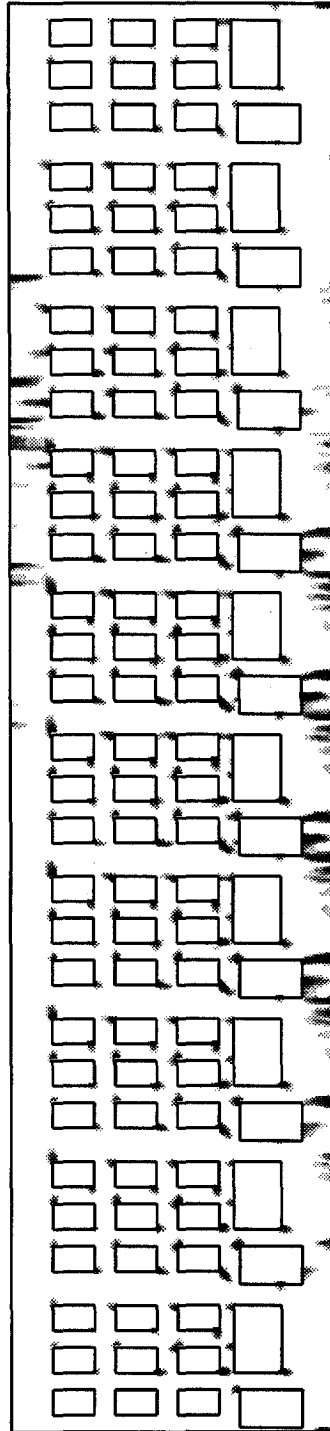


Figure 7.17 Crack patterns for settlement analysis. Boring front position in relation to the right end of the structure: (a) 0.0 [m]; (b) 34.0 [m].



(a)



(b)

Figure 7.18 Results of the settlement analysis at end stage: (a) crack pattern; (b) equivalent plastic strain.

the tunnel construction is shown in Figure 7.18. Assuming that an indication of the crack width can be obtained from the integration of strains over the areas with damage concentration, the maximum crack width amounts to approximately 0.45 [mm]. This value is similar both for the dominant cracks over the top floor windows and the dominant cracks under the (ground floor) doors. Based on this result both the need for repair techniques or the need to reduce the settlement by a better tunneling process can be studied. A complete discussion of the behavior of the structure and criteria for damage acceptance can be found in Hendriks *et al.* (1995).

During the above analysis, full convergence could be obtained, both at local at global level, which demonstrates the robustness and practical applicability of the developed numerical tools.

### 7.3 Assessment of residual strength in damaged structures

After the earthquake of 1980 in Italy, a research program was started in order to assess and strengthen the damaged rich architectural patrimony. The prime objective was to rationalize the techniques of structural rehabilitation.

Experimental tests were carried out in buildings intended to be demolished, at the historical center of Salvitelle, Italy, see Alessandri *et al.* (1983). The stone masonry buildings, selected for testing, dated from *c.* 1600-1700 and were not excessively damaged by the earthquake. The loading conditions consisted of monotonically increasing horizontal forces in the plane of the load-bearing walls, with the objective of modeling future seismic loading. In a first phase, the walls were loaded close to collapse. Afterwards, the loads were removed and the walls were refurbished. This was followed by renewed application of loads in order to evaluate the repair technique and allow for a comparison with the modeling techniques used. It is noted that the only vertical loads acting in the walls were the self-weight because floors and roof had been removed before the application of the horizontal loads.

In the present study, one of the walls, here denoted by façade A, was adopted to show that an indication of the residual strength of damaged structures can be obtained with the help of the developed numerical tools. Based on this information, the designer can decide whether strengthening of the structure is necessary. The numerical analysis was carried out with 4-noded plane stress elements. The material model developed in Chapter 6 is utilized to reproduce a no-tension model, in order to represent the existent damage of the façade in a conservative manner. The adopted Young's modulus equals 5000 [N/mm<sup>2</sup>]. Figure 7.19 shows the geometry of the façade, with a constant thickness of 600 [mm] and the crack pattern after the first loading, *i.e.* with the structure in the original state. Prior to loading, the façade was plastered with a thin gypsum layer and, therefore, the crack pattern shown was, indeed, obtained during loading and does not necessarily refer to previous existing cracks.

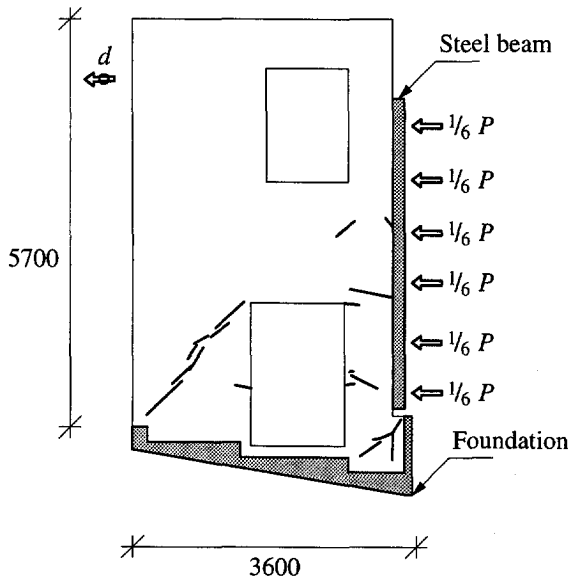


Figure 7.19 Stone masonry façade A. Geometry and experimental crack pattern.

The experimental and calculated load-displacement diagrams are given in Figure 7.20. Here, the displacement  $d$  has been measured in the left side of the façade A, see Figure 7.19. The calculated collapse load is 12 % lower than the value at which the experiment was stopped. The fact that the calculated collapse load is lower than the real collapse load should be expected because a no-tension model has been used, which implies that all the façade is damaged. However, a conservative estimation of the collapse load could be obtained. Moreover, the predicted crack pattern and correspondent structural behavior seems to agree reasonably with the experiments, see Figure 7.21.

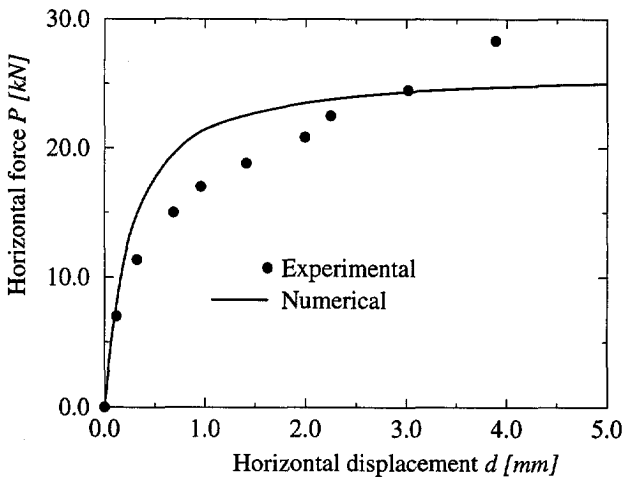


Figure 7.20 Stone masonry façade A. Load - displacement diagrams.

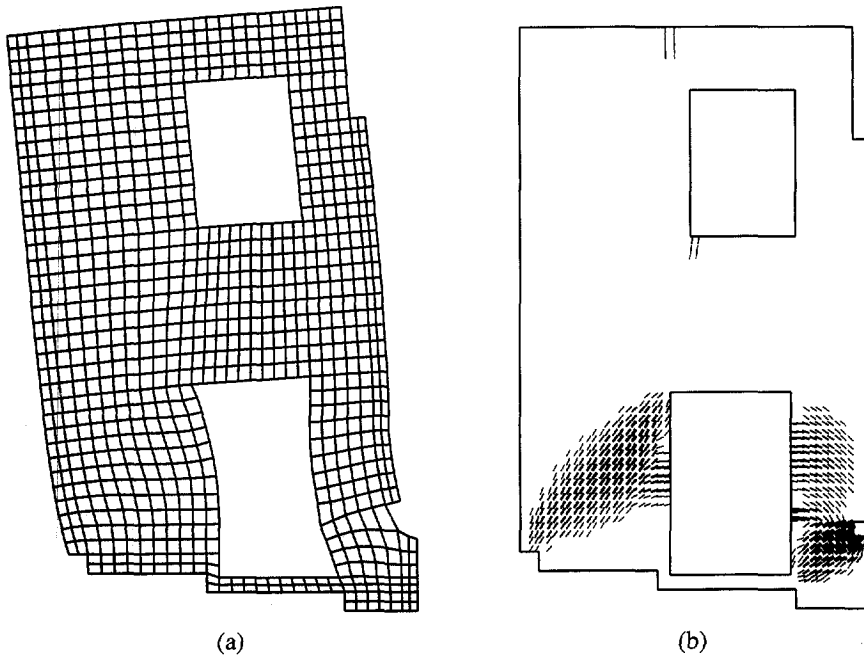


Figure 7.21 Stone masonry façade A. Results of the analysis for a displacement  $d$  of 1.0 [mm]: (a) deformed mesh; (b) cracks pattern.

## 7.4 Summary

The present Chapter shows engineering applications of the models developed in this study. The examples given show an indication, in three different categories, of possible roles for the nonlinear analysis of masonry structures. The first example deals with design rules and how they can be enhanced and rationalized with the help of numerical models. For this purpose, the design of movement-joints in masonry walls is discussed. The second example deals with the analysis of existing (complex) structures subjected to new (complex) loading conditions. For this purpose, the models are used to predict the amount of damage, associated with cracking, for buildings in Amsterdam, the Netherlands, due to settlements caused by tunneling. Finally, the last example, deals with the safety of existing old structures. For this purpose, the residual strength of a 350 years old building damaged by an earthquake, in Salvitelle, Italy, is calculated and compared with the values and behavior obtained experimentally.

It is noted that all the examples presented in this Chapter are mostly associated with tensile failure, which is certainly an important inelastic phenomenon in all masonry structures. However, a conclusion that compression failure is irrelevant for structural masonry would be erroneous. In several other structures and, particularly, in the case of confined masonry, compressive failure cannot be ignored, see e.g. Chapter 4 and Chapter 6.

## 8. SUMMARY AND CONCLUSIONS

Rational, economical and innovative applications of masonry imply advanced and continuous research. To this belongs the development and use of reliable numerical tools. In particular, the tools are of special interest to describe the post-failure behavior of masonry structures in order to assess its safety. Reliable tools consist of accurate material descriptions in combination with robust solution strategies. In this study, an attempt has been made to provide such a set of tools for the analysis of unreinforced masonry structures in plane stress conditions.

### *Numerical Aspects*

The mathematical theory of plasticity has been adopted for the representation of the material behavior. The algorithms have been implemented in modern concepts, including multisurface yield criteria, Euler backward return mappings, consistent tangent operators and a regular Newton-Raphson method to solve the update of the state variables at the integration point level. The fact that the plasticity theory is incapable of modeling crack closure is irrelevant for the analysis of large structures under monotonically increasing loading, as shown by several authors and confirmed by the results obtained in the present study. It is believed that the advantages of using a well established theory and sound numerical algorithms are, by far, more important. Robust material models must be complemented with advanced solution procedures at the structural level. Here, the nonlinear equilibrium problem arising from the finite element discretization has been solved with a constrained Newton-Raphson method with a line-search technique. Non-symmetric tangent stiffness matrices, which arise due to non-associated plastic flow or non-associated hardening/softening, have been utilized in all the analyses. The adopted solution strategy has proven to be satisfactory because the loading paths could be traced completely, ranging from the elastic regime, pre-failure inelastic regime and post-failure inelastic regime until total degradation of strength.

### *Two major modeling strategies*

Masonry is a composite material that consists of units and mortar, normally arranged in a periodic manner. The interface between units and mortar acts as a plane of weakness and is, largely, responsible for the inelastic behavior. A detailed modeling strategy must then include units, mortar and interface. However, such a modeling strategy is unwieldy and the computational inefficiency becomes prohibitive in the analysis of large structures. Simplified approaches are thus preferred in the present study, namely, a *micro-modeling* strategy, where joints are modeled with zero-thickness interface elements, and a *macro-modeling* strategy, where a relation is established between average masonry stresses and average masonry strains, under the assumption of a homogeneous material. Additionally, an investigation about the adequacy of using *homogenization techniques* for masonry structures has been carried out.

### *Micro-modeling*

For the micro-modeling strategy, all inelastic phenomena are lumped in the relatively weak joints via a composite interface model. This (plasticity) model comprehends three different failure mechanisms, namely, a straight tension cut-off for mode I failure, the Coulomb friction model for mode II failure as well as an elliptical cap for compression and combined shear/compression failure. It is assumed that the internal damage associated with each failure mechanism can be modeled using internal parameters which are related to a fracture energy in tension, a fracture energy in shear and a compressive fracture energy. Additional features of the model include coupling between cracking and decohesion as well as softening of the friction and dilatancy angles. Analyses of structures where all the modes of the composite interface model become active show that the strategy results in a stable and accurate algorithm. The entire pre- and post-failure regime can be traced and agrees well with experimental observations. This gives a good impression about the adopted strategy and provides a good understanding of the failure mechanisms involved in the analyzed structures. The (micro-)model is particularly suited for small structures and structural details where the interaction between units and mortar is of primary interest. It is noted that, for large structures, the memory and time requirements become too large and, if a compromise between accuracy and economy is needed, a macro-modeling strategy is likely to be more efficient.

### *Homogenization techniques*

A second aspect of the nonlinear analysis of masonry structures, which has been discussed, is homogenization techniques. The importance of such techniques resides in the fact that, often, the same components, viz. unit and mortar, are used in different geometrical dimensions and arrangements. With adequate homogenization techniques, it would be possible to predict the behavior of the different composites based on the properties of the components. Two different approaches to tackle this problem are touched. The first approach deals with the use of a simplified technique based on a two-step homogenization of layered materials along the masonry material axes. The objective is to obtain a (homogenized) material model for the composite using as input the material properties and geometry of the components, without actual discretization of the components. The result of the homogenization process is, thus, an orthotropic material model in terms of average stresses and average strains. It is concluded that this simplified technique is well suited for elastic behavior, but cannot be used, in the present form, for the nonlinear analysis of masonry because the assumptions fail to accommodate the nonlinear internal force transfer between the components. The second approach deals with the calculation of macro-properties of the composite based on the actual discretization of the components. The macro-parameters can serve as input data for an independent macro-model. Two examples are given, focusing on the homogenization of the elastic characteristics of masonry and the complete (nonlinear) homogenization of the uniaxial tensile response of masonry loaded parallel to the bed joints. This technique seems very promising. It is believed that, once a few additional carefully deformation controlled experiments are

carried out, the numerical laboratory can, in several cases, successfully substitute the costly experimental set-ups for the determination of the composite properties of masonry.

### *Macro-modeling*

For the analysis of large engineering problems, a macro-modeling strategy has been proposed. An orthotropic continuum model has been developed, which consists of a Rankine type yield criterion for tensile failure and a Hill type yield criterion for compressive failure. It is assumed that the failure mechanism of masonry loaded in tension and compression is governed by crack growth at the micro-level. Furthermore it is assumed that the internal damage associated with each failure mechanism can be modeled using internal parameters which are related to a fracture energy in tension and a compressive fracture energy. This energy-based (plasticity) model resorts to the well known crack band theory to obtain objective results with respect to the finite element mesh size. The model is capable of predicting independent, in the sense of completely diverse, behavior along the material axes. The strength parameters involved appear to be enough to reproduce the biaxial behavior of all masonry types, ranging from isotropic behavior to extreme anisotropic behavior. Analyses of structures where both modes of the model become active show that a stable and accurate algorithm has been achieved. The entire pre- and post-failure regime can be traced, which gives a good impression about the model. The well known difficulties in obtaining converged solutions with standard continuum, in the presence of softening behavior, seem to be obviated by selecting lower order elements. A comparison with experimental observations shows good agreement. However, it is further demonstrated that a macro-modeling strategy can perform badly, when used in cases where the failure mode is governed by the interaction of a few units and mortar. The adoption of a macro-modeling strategy must be associated with a composite failure process.

### *Application in engineering practice*

Finally, attention is given to the role of the developed models, and the nonlinear analysis of masonry structures, in engineering practice. Examples have been presented which concern the step towards fracture mechanics based design rules, the analysis of complex existing structures under new complex loading conditions and the safety assessment of old masonry structures. For these three categories it is shown that the models are applicable in engineering practice, which demonstrates the predictive capability of the proposed numerical tools.

### *Suggestions for future work*

In retrospect, the present study successfully achieved the objectives defined in Section 1.4. In particular, robust and accurate numerical tools that can be offered to masonry analysts and designers have been developed, both at the micro- and macro-level.

Further application of the models to a wide range of masonry structures in order to enhance and review current design rules is of primary interest. For this purpose, it is emphasized that the experimental determination of material parameters is necessary. In particular, information about the post-peak material behavior is almost absent from literature.

In a more fundamental perspective, some advances are also important. For micro-modeling, an investigation of refined strategies to model cracks in the units is suggested. Promising strategies seem to be the adoption of a cross triangular interface patch of potential cracks or continuum elements with jump functions, see e.g. Simo *et al.* (1993) and Oliver (1995). For macro-modeling, an investigation about the introduction of an internal length scale related to the micro-structure of units and mortar is suggested. Such an investigation necessarily follows the work developed in enhanced continua, see e.g. De Borst *et al.* (1993). The main difficulties seem to lie in the definition of the length scale and the development of computationally efficient algorithms for use in engineering practice.

**REFERENCES**

- ALESSANDRI, C., BATI, S.B., TEMPESTA, G. and TONIETTI, U. (1983) - *Investigation on the behavior of masonry buildings: the experiments of Salvitelle* (in Italian). Report No. 13/1983, University of Florence, Faculty of Architecture, Florence, Italy.
- ANTHOINE, A. (1992) - *In-plane behavior of masonry: A literature review*. Report EUR 13840 EN, Commission of the European Communities, JRC - Institute for Safety Technology, Ispra, Italy.
- ANTHOINE, A. (1995) - Derivation of the in-plane elastic characteristics of masonry through homogenization theory. *Int. J. Solids Structures*, **32(2)**, p. 137-163.
- ATKINSON, R.H. and YAN, G.G. (1990) - Results of a statistical study of masonry deformability. *The Masonry Society Journal*, **9(1)**, p. 81-94.
- ATKINSON, R.H., AMADEI, B.P., SAEB, S. and STURE, S. (1989) - Response of masonry bed joints in direct shear. *J. Struc. Engrg.*, ASCE, **115(9)**, p. 2276-2296.
- BACKES, H.-P. (1985) - *On the behavior of masonry under tension in the direction of the bed joints* (in German). Dissertation, Aachen University of Technology, Aachen, Germany.
- BAKHVALOV, N. and PANASENKO, G. (1989) - *Homogenization: averaging processes in periodic media*. Studies in mathematics and its applications, Vol. 36, Kluwer Academic Publishers, Dordrecht, The Netherlands.
- BATHE, K.-J. (1982) - *Finite element procedures in engineering analysis*. Prentice-Hall, Englewood Cliffs, New Jersey, USA.
- BATOZ, J.L. and DHATT, G. (1979) - Incremental displacement algorithms for nonlinear problems. *Int. J. Numer. Methods Engrg.*, **14**, p. 1262-1267.
- BAŽANT, Z.P. and OH, B.H. (1983) - Crack band theory for fracture of concrete. *Materials and Structures*, RILEM, **93(16)**, p. 155-177.
- BERKERS, W.G.J. and RADEMAKER, P.D. (1992) - *Cracking in long walls - Final report* (in Dutch). Research Center for Calcium Silicate Industry, Report no. CK015.1, Barneveld, The Netherlands.
- BESSELING, J.F. (1958) - A theory of elastic, plastic and creep deformations of an initially isotropic material showing anisotropic strain-hardening, creep recovery and secondary creep. *J. Appl. Mech.*, **22**, p. 529-536.
- BIERWIRTH, H., STÖCKL, S. and KUPFER, H. (1993) - Triaxial tests on mortar specimens taken from bed joints, in: *Proc. 6<sup>th</sup> North American Masonry Conf.*, eds. A.A. Hamid and H.G. Harris, Drexel University, Philadelphia, Pennsylvania, USA, p. 995-1007.
- BINDA, L., FONTANA, A. and FRIGERIO, G. (1988) - Mechanical behavior of brick masonries derived from unit and mortar characteristics, in: *Proc. 8<sup>th</sup> Int. Brick and Block Masonry Conf.*, eds. J.W. de Courcy, Elsevier Applied Science, London, UK, p. 205-216.
- BORST, R. DE (1986) - *Non-linear analysis of frictional materials*. Dissertation, Delft University of Technology, Delft, The Netherlands.

- BORST, R. DE (1991) - The zero-normal-stress condition in plane-stress and shell elasto-plasticity. *Comm. in Appl. Numer. Methods*, **7**, p. 29-33.
- BORST, R. DE (1993) - A generalization of  $J_2$ -flow theory for polar continua. *Comp. Meth. Appl. Mech. Engrg.*, **103**, p. 347-362.
- BORST, R. DE and FEENSTRA, P.H. (1990) - Studies in anisotropic plasticity with reference to the Hill criterion. *Int. J. Numer. Methods Engrg.*, **29**, p. 315-336.
- BORST, R. DE, SLUYS, L.J., MÜHLHAUS, H.-B. and PAMIN, J. (1993) - Fundamental issues in finite element analyses of localization of deformation. *Engrg. Comput.*, **10**, p. 99-121.
- BORST, R. DE, FEENSTRA, P.H., PAMIN, J. and SLUYS, L.J. (1994) - Some current issues in computational mechanics of concrete, in: *Computational modeling of concrete structures*, eds. H. Mang *et al.*, Pineridge Press, Swansea, UK, p. 283-302.
- CEN (1995) - *Eurocode 6: Design of masonry structures*. ENV 1996-1-1:1995, CEN, Brussels, Belgium.
- CHEN, W.F. and HAN, D.J. (1988) - *Plasticity for structural engineers*. Springer-Verlag, New York, New York, USA.
- CLARKE, M.J. and HANCOCK, G.J. (1990) - A study of incremental-iterative strategies for non-linear analyses. *Int. J. Num. Meth. Engrg.*, **29**, p. 1365-1391.
- COPELAND, R.E. (1957) - Shrinkage and temperature stresses in masonry. *ACI Journal*, **53**, p. 769-780.
- CRISFIELD, M.A. (1981) - A fast incremental/iterative solution procedure that handles 'snap through'. *Comp. Struct.*, **13**, p. 55-62.
- CRISFIELD, M.A. (1982) - Accelerated solution techniques and concrete cracking. *Comp. Meth. Appl. Mech. Engrg.*, **33**, p. 585-607.
- CUR (1994) - *Structural masonry: a experimental/numerical basis for practical design rules* (in Dutch). Report 171, CUR, Gouda, The Netherlands.
- DAJUN, D. (1994) - Masonry structures in China. *Masonry Int.*, **8(1)**, p. 9-15.
- DAVEY, N. (1961) - *A history of building materials*. Phoenix House, London, UK.
- DE BORST, R. - see BORST, R. DE
- DE JONG, P. - see JONG, P. DE
- DENNIS, J.E. and SCHNABEL, R.B. (1983) - *Numerical methods for unconstrained optimization and nonlinear equations*. Prentice-Hall, Englewood Cliffs, New Jersey, USA.
- DETHIER, J. (1982) - *Down to Earth: Mud architecture, an old idea, a new future*. Thames and Hudson, London, UK.
- DHANASEKAR, M. and PAGE, A.W. (1986) - The influence of brick masonry infill properties on the behavior of infilled frames. *Proc. Intsn. Civ. Engrs.*, Part 2, **81**, p. 593-605.
- DHANASEKAR, M., PAGE, A.W. and KLEEMAN, P.W. (1985) - The failure of brick masonry under biaxial stresses. *Proc. Intsn. Civ. Engrs.*, Part 2, **79**, p. 295-313.

- DIALER, C. (1990) - *Failure and deformation behavior of shear stressed masonry panels, biaxial tests in scaled masonry* (in German). Dissertation, Munich University of Technology, Munich, Germany.
- DI MAGGIO, F.L. and SANDLER, I.V. (1971) - Material model for granular soils. *J. Engrg. Mech.*, ASCE, **97**(3), p. 935-950.
- DRUCKER, D.C., GIBSON, R.E. and HENKEL, D.J. (1957) - Soil mechanics and work hardening theories of plasticity. *Trans. ASCE*, **122**, p. 338-346.
- DRYSDALE, R.G., HAMID, A.A. and BAKER, L.R. (1994) - *Masonry structures: Behavior and design*. Prentice-Hall, Englewood Cliffs, New Jersey, USA.
- ELLIOT, C.D. (1992) - *Technics and architecture: The development of materials and systems of buildings*. The MIT Press, Cambridge, Massachusetts, USA.
- FEENSTRA, P.H. (1993) - *Computational aspects of biaxial stress in plain and reinforced concrete*. Dissertation, Delft University of Technology, Delft, The Netherlands.
- FEENSTRA, P.H. and BORST, R. DE (1995) - A plasticity model and algorithm for mode-I cracking in concrete. *Int. J. Numer. Methods Engrg.*, **38**, p. 2509-2529.
- FEENSTRA, P.H. and BORST, R. DE (1996) - A composite plasticity model for concrete. *Int. J. Solids Structures*, **33**(5), p. 707-730.
- GANZ, H.R. (1985) - *Masonry walls under normal force and shear* (in German). Report No. 148, Institute of Structural Engineering, ETH Zurich, Zurich, Switzerland.
- GANZ, H.R. and THÜRLIMANN, B. (1982) - *Tests on the biaxial strength of masonry* (in German). Report No. 7502-3, Institute of Structural Engineering, ETH Zurich, Zurich, Switzerland.
- GANZ, H.R. and THÜRLIMANN, B. (1984) - *Tests on masonry walls under normal and shear loading* (in German). Report No. 7502-4, Institute of Structural Engineering, ETH Zurich, Zurich, Switzerland.
- GENS, A., CAROL, I. and ALONSO, E.E. (1989) - Elasto-plastic model for joints and interfaces, in: *Proc. 2<sup>nd</sup> Int. Conf. Computational Plasticity*, eds. D.R.J. Owen *et al.*, Pineridge Press, Swansea, UK, p. 1251-1264.
- GERRARD, C.M. (1982) - Equivalent elastic moduli of a rock mass consisting of orthorhombic layers. *Int. J. Rock. Mech. Min. Sci. Geomech.*, **19**, p. 9-14.
- GROEN, A.E., SCHELLEKENS, J.C.J. and BORST, R. DE (1994) - Three-dimensional finite element studies of failure in soil bodies using a Cosserat continuum, in: *Computer Methods and Advances in Geomechanics*, eds. H.J. Siriwardane and M.M. Zaman, Balkema, Rotterdam, The Netherlands, p. 581-586.
- GUGGISBERG, R. and THÜRLIMANN, B. (1987) - *Experimental determination of masonry strength parameters* (in German). Report No. 7502-5, Institute of Structural Engineering, ETH Zurich, Zurich, Switzerland.
- HAGEMAN, J.G. (1968) - *Study of shrinkage cracks* (in Dutch). Research Center for Calcium Silicate Industry, Reports no. 189-1-0/189-2-0, Barneveld, The Netherlands.
- HASHIN, Z. and SHTRIKMAN, S. (1962) - On some variational principles in anisotropic and nonhomogeneous elasticity. *J. Mech. Phys. Solids*, **10**, p. 335-342.

- HENDRIKS, M.A.N., ROTS, J.G. and STAALDUINEN, P.C. VAN (1995) - Confidential report (in Dutch). Report no. 95-CON-R0343, TNO-Bouw, Delft, The Netherlands.
- HENDRY, A.W. (1990) - *Structural masonry*. Macmillan Education, London, UK.
- HILSDORF, H.K. (1969) - Investigation into the failure mechanism of brick masonry loaded in axial compression, in: *Designing, engineering and constructing with masonry products*, eds. F.H. Johnson, Gulf Publishing Company, Houston, Texas, USA, p. 34-41.
- HILL, R. (1948) - A theory of the yielding and plastic flow of anisotropic metals. *Proc. Roy. Soc., (London) A*, **193**, p. 281-288.
- HILL, R. (1950) - *The mathematical theory of plasticity*. Oxford University Press, London, UK.
- HILL, R. (1963) - Elastic properties of reinforced solids: Some theoretical principles. *J. Mech. Phys. Solids*, **11**, p. 357-372.
- HOEK, E. (1983) - Strength of jointed rock masses. *Géotechnique*, **33(3)**, p. 187-223.
- HOFFMAN, O. (1967) - The brittle strength of orthotropic materials. *J. Composite Mat.*, **1**, p. 200-206.
- HOFFMANN, G. and SCHUBERT, P. (1994) - Compressive strength of masonry parallel to the bed joints, in: *Proc. 10<sup>th</sup> Int. Brick and Block Masonry Conf.*, eds. N.G. Shrive and A. Huizer, University of Calgary, Calgary, Alberta, Canada, p. 1453-1462.
- HOFSTETTER, G., SIMO, J.C. and TAYLOR, R.L. (1993) - A modified cap model: closest point solution algorithms. *Comp. Struct.*, **46(2)**, p. 203-214.
- HOHBERG, J.-M. (1992) - *A joint element for the nonlinear dynamic analysis of arch dams*. Report No. 186, Institute of Structural Engineering, ETH Zurich, Zurich, Switzerland.
- HORDIJK, D.A. (1991) - *Local approach to fatigue of concrete*. Dissertation, Delft University of Technology, Delft, The Netherlands.
- JONG, P. DE (1992) - Lessons from damage events in the building industry I (in Dutch). *Cement*, **2**, p. 26-28.
- KOITER, W.T. (1953) - Stress-strain relations, uniqueness and variational theorems for elastic-plastic materials with a singular yield surface. *Q. Appl. Math.*, **11(3)**, p. 350-354.
- KOK, A.W.M. (1995) - *Lumped pulses and discrete displacements: A physical way to understand numerical dynamics*. Dissertation, Delft University of Technology, Delft, The Netherlands.
- LI, X., DUXBURY, P.G. and LYONS, P. (1994) - Considerations for the application and numerical implementation of strain hardening with the Hoffman yield criterion. *Comp. Struct.*, **52(4)**, p. 633-644.
- LOURENÇO, P.B. (1994) - *Analysis of masonry structures with interface elements: Theory and applications*. Report 03-21-22-0-01, Delft University of Technology, Delft, The Netherlands.

- LOURENÇO, P.B. (1995a) - *The elastoplastic implementation of homogenization techniques: With an extension to masonry structures*. Report 03-21-1-31-02, Delft University of Technology, Delft, The Netherlands.
- LOURENÇO, P.B. (1995b) - *An orthotropic continuum model for the analysis of masonry structures*. Report 03-21-1-31-27, Delft University of Technology, Delft, The Netherlands.
- LOURENÇO, P.B. and ROTS, J.G. (1993) - On the use of micro-models for the analysis of masonry shear-walls, in: *Computer methods in structural masonry - 2*, eds. G.N. Pande and J. Middleton, Books & Journals International, Swansea, UK, p. 14-26.
- LOURENÇO, P.B., ROTS, J.G. and BLAAUWENDRAAD, J. (1994) - Implementation of an interface cap model for the analysis of masonry structures, in: *Computational modeling of concrete structures*, eds. H. Mang *et al.*, Pineridge Press, Swansea, UK, p. 123-134.
- LOURENÇO, P.B., ROTS, J.G. and FEENSTRA, P.H. (1995) - A 'tensile' Rankine type orthotropic model for masonry, in: *Computer methods in structural masonry - 3*, eds. G.N. Pande and J. Middleton, Books & Journals International, Swansea, UK.
- LURATI, F. and THÜRLIMANN, B. (1990) - *Tests in concrete masonry walls* (in German). Report No. 8401-3, Institute of Structural Engineering, ETH Zurich, Zurich, Switzerland.
- LURATI, F., GRAF, H. and THÜRLIMANN, B. (1990) - *Experimental determination of the strength parameters of concrete masonry* (in German). Report No. 8401-2, Institute of Structural Engineering, ETH Zurich, Zurich, Switzerland.
- MANN, W. and MÜLLER, H. (1982) - Failure of shear-stressed masonry - an enlarged theory, tests and application to shear walls. *Proc. British Ceramic Society*, **30**, p. 223-235.
- MANN, W. and BETZLER, M. (1994) - Investigations on the effect of different forms of test samples to test the compressive strength of masonry, in: *Proc. 10<sup>th</sup> Int. Brick and Block Masonry Conf.*, eds. N.G. Shrive and A. Huizer, University of Calgary, Calgary, Alberta, Canada, p. 1305-1313.
- MARQUES, J.M.M.C. (1984) - Stress computations in elastoplasticity. *Engrg. Comput.*, **1**, p. 42-51.
- MIER, J.G.M. VAN (1984) - *Strain-softening of concrete under multiaxial loading conditions*. Dissertation, Eindhoven University of Technology, Eindhoven, The Netherlands.
- MUSGROVE, J. and FLETCHER, B. (1987) - *Sir Banister Fletcher's: A history of architecture*. Butterworths, London, UK.
- NELISSEN, L.J.M. (1972) - Biaxial testing of normal concrete. *Heron*, **18**, p. 3-90.
- NYSSSEN, C. (1981) - An efficient and accurate iterative method allowing large stress incremental steps, to solve elasto-plastic problems. *Comp. Struct.*, **13(1)**, p. 63-71.
- ORTIZ, M. and POPOV, E.P. (1985) - Accuracy and stability of integration algorithms for elastoplastic constitutive relations. *Int. J. Numer. Methods Engrg.*, **21**, p. 1561-1576.

- OLIVER, J. (1995) - Continuum modeling of strong discontinuities in solid mechanics, in: *Computational Plasticity*, eds. D.R.J. Owen *et al.*, Pineridge Press, Swansea, UK, p. 455-479.
- PAGE, A.W. (1978) - Finite element model for masonry. *J. Struc. Div., ASCE*, **104(8)**, p. 1267-1285.
- PAGE, A.W. (1981) - The biaxial compressive strength of brick masonry. *Proc. Intsn. Civ. Engrs.*, Part 2, **71**, p. 893-906.
- PAGE, A.W. (1983) - The strength of brick masonry under biaxial compression-tension. *Int. J. Masonry Constr.*, **3(1)**, p. 26-31.
- PAIPETIS, S.A., POLYZOS, D. and VALAVANIDIS, M. (1993) - Constitutive relations of periodic laminated composites with anisotropic dissipation. *Arch. Appl. Mech.*, **64**, p. 32-43.
- PANDE, G.N., LIANG, J.X. and MIDDLETON, J. (1989) - Equivalent elastic moduli for brick masonry. *Comp. Geotech.*, **8**, p. 243-265.
- PAPA, E. (1990) - *About damage mechanics with particular reference to masonry* (in Italian). Dissertation, Politecnico di Milano, Milan, Italy.
- PAUL, B. (1960) - Prediction of elastic constants of multiphase materials. *Trans. of AIME*, **218**, p. 36-41.
- PIETRUSZCZAK, S. and NIU, X. (1992) - A mathematical description of macroscopic behavior of brick masonry. *Int. J. Solids Structures*, **29(5)**, p. 531-546.
- PIJAUDIER-CABOT, G., BORDERIE, C. LA and FICHANT, S. (1994) - Damage mechanics for concrete modeling: Applications and comparisons with plasticity and fracture mechanics, in: *Computational modeling of concrete structures*, eds. H. Mang *et al.*, Pineridge Press, Swansea, UK, p. 17-36.
- PLUIJM, R. VAN DER (1992) - Material properties of masonry and its components under tension and shear, in: *Proc. 6<sup>th</sup> Canadian Masonry Symposium*, eds. V.V. Neis, Saskatoon, Saskatchewan, Canada, p. 675-686.
- PLUIJM, R. VAN DER (1993) - Shear behavior of bed joints, in: *Proc. 6<sup>th</sup> North American Masonry Conf.*, eds. A.A. Hamid and H.G. Harris, Drexel University, Philadelphia, Pennsylvania, USA, p. 125-136.
- PLUIJM, R. VAN DER and VERMELTFOORT, A.Th. (1991) - *Deformation controlled tension and compression tests in units, mortar and masonry* (in Dutch). Report B-91-0561, TNO-Bouw, Delft, The Netherlands.
- PRAMONO, E. and WILLAM, K. (1989) - Implicit integration of composite yield surfaces with corners. *Engrg. Comput.*, **6**, p. 186-197.
- RAIJMAKERS, T.M.J. and VERMELTFOORT, A.Th. (1992) - *Deformation controlled tests in masonry shear walls* (in Dutch). Report B-92-1156, TNO-Bouw, Delft, The Netherlands.
- RAMM, E. (1981) - Strategies for tracing the nonlinear response near limit points, in: *Nonlinear Finite Element Analysis in Structural Mechanics*, eds. W. Wunderlich *et al.*, Springer-Verlag, Berlin, Germany, p. 63-89.

- RIGGS, H.R. and POWELL, G.H. (1990) - Tangent constitutive matrices for inelastic finite element analysis. *Int. J. Numer. Methods Engrg.*, **29**, p. 1193-1203.
- RIKS, E. (1970) - *On the numerical solution of snapping problems in the theory of elastic stability*. Dissertation, Stanford University, Stanford, California, USA.
- ROSCOE, K.H. and BURLAND, J.B. (1968) - On the generalized stress-strain behavior of 'wet' clay, in: *Engineering Plasticity*, eds. J. Heyman and F.A. Lekie, Cambridge University Press, London, UK, p. 535-609.
- ROTS, J.G. (1988) - *Computational modeling of concrete fracture*. Dissertation, Delft University of Technology, Delft, The Netherlands.
- ROTS, J.G. (1991) - Numerical simulation of cracking in structural masonry. *Heron*, **36(2)**, p. 49-63.
- ROTS, J.G., BERKERS, W.G.J. and HEUVEL, H.A.J.G. VAN DEN (1994) - Towards fracture mechanics based design rules for movement-joint spacing, in: *Proc. 10<sup>th</sup> Int. Brick and Block Masonry Conf.*, eds. N.G. Shrive and A. Huizer, University of Calgary, Calgary, Alberta, Canada, p. 707-717.
- SALAMON, M.D.G. (1968) - Elastic moduli of stratified rock mass. *Int. J. Rock. Mech. Min. Sci.* **5**, p. 519-527.
- SANCHEZ-PALENCIA, E. (1980) - *Non-homogeneous media and vibration theory*. Lecture notes in physics, No. 127, Springer, Berlin, Germany.
- SANCHEZ-PALENCIA, E. (1987) - *Homogenization techniques for composite media*. Lecture notes in physics, No. 272, Springer, Berlin, Germany.
- SCARPAS, A. and BLAAUWENDRAAD, J. (1993) - Non-local plasticity softening model for brittle materials, in: *Fracture and Damage of Concrete and Rock - FDCR-2*, eds. H.P. Rossmannith, E & FN. Spon., London, UK, pp. 44-53.
- SHELLEKENS, J.C.J. (1992) - *Computational strategies for composite structures*. Dissertation, Delft University of Technology, Delft, The Netherlands.
- SHELLEKENS, J.C.J. and BORST, R. DE (1990) - The use of the Hoffman yield criterion in finite element analysis of anisotropic composites. *Comp. Struct.*, **37(6)**, p. 1087-1096.
- SCHUBERT, P. (1988a) - The influence of mortar on the strength of masonry, in: *Proc. 8<sup>th</sup> Int. Brick and Block Masonry Conf.*, eds. J.W. de Courcy, Elsevier Applied Science, London, UK, p. 162-174.
- SCHUBERT, P. (1988b) - About the crack-free length of non-loadbearing masonry walls (in German). *Mauerwerk-Kalendar*, 1988, p. 473-488.
- SCHUBERT, P. (1994) - Tensile and flexural strength of masonry: influences, test methods, test results, in: *Proc. 10<sup>th</sup> Int. Brick and Block Masonry Conf.*, eds. N.G. Shrive and A. Huizer, University of Calgary, Calgary, Alberta, Canada, p. 895-907.
- SCHUBERT, P. and HOFFMANN (1994) - Compressive strength of mortar in masonry: Significance, influences, test methods, requirements, in: *Proc. 10<sup>th</sup> Int. Brick and Block Masonry Conf.*, eds. N.G. Shrive and A. Huizer, University of Calgary, Calgary, Alberta, Canada, p. 1335-1344.

- SCHWEIZERHOF, K.H. and WRIGGERS, P. (1986) - Consistent linearization for path following methods in nonlinear FE-analysis. *Comp. Meth. Appl. Mech. Engrg.*, **59**, p. 261-279.
- SEIM, W. (1994) - *Numerical modeling of the failure of biaxially loaded masonry walls with consideration of anisotropy* (in German). Dissertation, University of Karlsruhe, Karlsruhe, Germany.
- SIMO, J.C. and TAYLOR, R.L. (1985) - Consistent tangent operators for rate-independent elastoplasticity. *Comp. Meth. Appl. Mech. Engrg.*, **48**, p. 101-118.
- SIMO, J.C. and TAYLOR, R.L. (1986) - A return mapping algorithm for plane stress elastoplasticity. *Int. J. Numer. Methods Engrg.*, **22**, p. 649-670.
- SIMO, J.C., JU, J.-W., PISTER, K.S. and TAYLOR, R.L. (1988a) - Assessment of cap model: Consistent return algorithms and rate-dependent extension. *J. Engrg. Mech.*, ASCE, **114(2)**, p. 191-218.
- SIMO, J.C., KENNEDY, J.G. and GOVINDJEE, S. (1988b) - Non-smooth multisurface plasticity and viscoplasticity. Loading/unloading conditions and numerical algorithms. *Int. J. Numer. Methods Engrg.*, **26**, p. 2161-2185.
- SIMO, J.C., OLIVER, J. and ARMERO, F. (1993) - An analysis of strong discontinuities by strain-softening in rate-independent inelastic solids. *Comp. Mech.*, **12**, p. 277-296.
- SPENCER, A.J. (1979) - *Brick architecture in ancient Egypt*. Aris & Philipps, Warminster, Wilts, UK.
- STÖCKL, S., BIERWIRTH, H. and KUPFER, H. (1994) - The influence of test method on the results of compression tests on mortar, in: *Proc. 10<sup>th</sup> Int. Brick and Block Masonry Conf.*, eds. N.G. Shrive and A. Huizer, University of Calgary, Calgary, Alberta, Canada, p. 1397-1406.
- SUQUET, P.M. (1985) - Approach by homogenization of some linear and nonlinear problems in solid mechanics, in: *Plastic behavior of anisotropic solids*, CNRS Int. Colloquium, No. 319, CNRS, Paris, France, p. 77-117.
- SUTER, G.T. (1982) - The unique adaptability of brick: A personal viewpoint based on a study trip to India, in: *Proc. 2<sup>nd</sup> North American Masonry Conf.*, eds. D.W. Vannoy and J. Colville, University of Maryland, Maryland, USA, p. 20.2-20.13.
- SWAN, C.C. and CAKMAK, A.S. (1994) - A hardening orthotropic plasticity model for non-frictional composites: Rate formulation and integration algorithm. *Int. J. Numer. Methods Engrg.*, **37**, p. 839-860.
- TSAI, S.W. and WU, E.M. (1971) - A general theory of strength of anisotropic materials, *J. Composite Mat.*, **5**, p. 58-80.
- URBANSKI, A., SZARLINSKI, J. and KORDECKI, Z. (1995) - Finite element modeling of the behavior of the masonry walls and columns by homogenization approach, in: *Computer methods in structural masonry - 3*, eds. G.N. Pande and J. Middleton, Books & Journals International, Swansea, UK.
- VAN DER PLUIJM, R. - see PLUIJM, R. VAN DER
- VAN MIER, J.G.M. - see MIER, J.G.M. VAN

- VERMELTFOORT, A.Th. and RAUWMAKERS, T.M.J. (1993) - *Deformation controlled tests in masonry shear walls, Part 2* (in Dutch). Report TUE/BKO/93.08, Eindhoven University of Technology, Eindhoven, The Netherlands.
- VONK, R.A. (1992) - *Softening of concrete loaded in compression*. Dissertation, Eindhoven University of Technology, Eindhoven, The Netherlands.
- WATT, J.P. and O'CONNELL, R.J. (1980) - An experimental investigation of the Hashin-Shtrikman bounds on two-phase aggregate elastic properties. *Phys. Earth Planetary Interiors*, **21**, p. 359-370.
- WEMPNER, G.A. (1971) - Discrete approximations related to nonlinear theories of solids. *Int. J. Solids Structures*, **7**, p. 1581-1599.
- WESCHE, K. and ILANTZIS, A. (1980) - General recommendations for methods of testing load bearing walls. *Materials and Structures*, RILEM, **13(78)**, p. 433-445.
- ZIENKIEWICZ, O.C. and TAYLOR, R.L. (1989) - *The finite element method (4<sup>th</sup> ed.): Volume 1, Basic formulation and linear problems*. Mc-Graw Hill, Berkshire, England, UK.
- ZIENKIEWICZ, O.C. and TAYLOR, R.L. (1991) - *The finite element method (4<sup>th</sup> ed.): Volume 2, Solid and fluid mechanics, Dynamics and non-linearity*. Mc-Graw Hill, Berkshire, England, UK.



# SAMENVATTING

## REKENSTRATEGIEËN VOOR METSELWERKCONSTRUCTIES

Rationeel, economisch en vernieuwend gebruik van metselwerk vraagt om geavanceerd en doorlopend onderzoek. Hierbij hoort de ontwikkeling en het gebruik van betrouwbaar numeriek gereedschap. Dit gereedschap is met name van belang voor de beschrijving van het bezwijk- en na-bezwijkgedrag van metselwerk om hiermee de veiligheid te voorspellen. Betrouwbaar numeriek gereedschap bestaat uit nauwkeurige materiaalbeschrijvingen gecombineerd met robuuste oplostechnieken. In deze studie is een poging gedaan om dergelijk gereedschap voor de analyse van ongewapende metselwerkconstructies in een vlakke spanningstoestand te ontwikkelen.

### *Numerieke aspecten*

De plasticiteitstheorie is aangewend voor de beschrijving van het materiaalgedrag. De hieruit voortkomende algoritmes zijn in computerprogrammatuur geïmplementeerd, gebruikmakende van moderne numerieke concepten. Samengestelde vloeioppervlakken, volledig impliciete integratie van de vloe- en versterkingsregels, consistente tangentoperatoren en een Newton-Raphson methode voor het oplossen van de toestandvariabelen op integratiepuntniveau zijn toegepast. Deze robuuste materiaalmodellen dienen te worden gecombineerd met geavanceerde oplosprocedures op constructieniveau. De uit de eindige-elementendiscretisatie volgende evenwichtsvergelijkingen zijn opgelost met een Newton-Raphson methode met nevenvoorwaarden inclusief een 'line-search' techniek. De aangewende oplosmethodiek is succesvol gebleken aangezien de oplossingspaden volledig gevolgd konden worden vanaf het elastische stadium, via het inelastische gedrag tot bezwijken met volledige afname van de sterkte.

### *Twee hoofdmodelleringsstechnieken*

Metselwerk is een composiet materiaal bestaande uit stenen en mortel, gestapeld volgens een bepaald metselwerkverband. In deze studie zijn vereenvoudigde modelleringsstechnieken toegepast. Een *micro-modellering*, waarbij de voeg is vereenvoudigd tot interface-elementen zonder dikte, en een *macro-modellering*, waarbij steen en voeg uitgesmeerd worden over een homogeen continuüm. Ook is de bruikbaarheid van *homogenisatietechnieken* voor metselwerkconstructies onderzocht.

### *Micro-modellering*

In de micro-modellering worden alle niet-lineaire verschijnselen geconcentreerd gedacht in de relatief zwakke voegen met behulp van een samengesteld interface-model. Het model omvat drie verschillende bezwijkmechanismen: een rechte 'tension cut-off' voor mode I bezwijken op trek, een Coulombs wrijvingsmodel voor mode II bezwijken op afschuiving en een elliptische kap voor bezwijken op druk en druk/afschuiving. Validatie van het model aan de hand van experimenten op afschuifwanden en een hogewandligger waren succesvol en leverde bijkomende kennis op over metselwerk-

constructies. De micro-modellering is in het bijzonder geschikt voor kleine constructies en metselwerkdetails waarbij de modellering van interactie tussen steen en mortel voorop staat. Voor grote constructies worden de geheugen- en CPU-eisen voor de huidige computerapparatuur te groot. Als een compromis tussen nauwkeurigheid en efficiëntie nodig is, wordt een macro-modellering waarschijnlijk aantrekkelijker.

#### *Homogenisatietechnieken*

Het belang van homogenisatie-technieken vloeit voort uit het feit dat dezelfde componenten, t.w. steen en mortel, worden gebruikt in verschillende geometrische afmetingen en stapelpatronen. Het zou met homogenisatietechnieken mogelijk moeten zijn het gedrag van verschillende composieten te voorspellen op grond van de eigenschappen van de afzonderlijke componenten. Twee verschillende benaderingen voor dit probleem zijn toegepast. De eerste benadering gebruikt een vereenvoudigde techniek om een materiaalmodel voor het composiet te verkrijgen uitgaande van de materiaalgegevens van de afzonderlijke componenten, zonder dat deze componenten daadwerkelijk gediscretiseerd worden. In de tweede benadering worden door discretisatie van de componenten de macro-parameters berekend die gebruikt kunnen worden als invoer voor een onafhankelijk macro-model.

#### *Macro-modellering*

Een macro-modelleringstechniek voor de analyse van grote constructieproblemen wordt voorgesteld. Een orthotroop continuümmodel is ontwikkeld bestaande uit een Rankine-achtig vloeicriterium voor bezwijken op trek en een Hill-achtig vloeicriterium voor bezwijken op druk. Dit op energie gebaseerde plasticiteitsmodel maakt gebruik van de bekende scheurbandtheorie om objectieve resultaten met betrekking tot de elementgrootte te verkrijgen. Het model is in staat om onafhankelijk, dat wil zeggen volledig verschillend, gedrag voor verschillende materiaalassen te voorspellen. De hierin gebruikte sterkte-parameters blijken voldoende in staat het gedrag van verschillende soorten metselwerk te beschrijven, reikend van isotroop tot extreem anisotroop gedrag. Een vergelijking met experimentele observaties van afschuifwanden toont goede overeenstemming. Echter ook wordt gedemonstreerd dat een macro-modelleringsstrategie slechte resultaten kan geven zodra een bezwijkmechanisme beheerst wordt door locale interactie van een paar stenen en mortel. Het gebruik van een macro-modelleringsstrategie is daarom alleen gerechtvaardigd bij diffuus bezwijken.

#### *Toepassing in de ingenieurspraktijk*

Uiteindelijk wordt aandacht geschonken aan de rol van de ontwikkelde modellen en niet-lineaire analyse van metselwerkconstructies in de ingenieurspraktijk. Voorbeelden worden gepresenteerd die een stap betekenen in de richting van ontwerpregels gebaseerd op breukmechanica, analyse van complexe constructies onder nieuwe complexe belastingen en veiligheidsbeoordeling van oude metselwerkconstructies. Voor deze drie categorieën wordt de toepasbaarheid en de voorspellende waarde van de ontwikkelde modellen aangetoond.

## CURRICULUM VITAE

Paulo José Brandão Barbosa Lourenço was born in Porto, Portugal, on March, 24 1967. He attended the Faculty of Engineering, University of Porto, Portugal, from 1985 to 1990 where he completed his Civil Engineering degree in the Structures Division. In 1989 and 1990, he spent two months in traineeships at the structural department of CowiConsult, A/S in Virum, Denmark and at the laboratory of Norsk Leca, A/S in Oslo, Norway, respectively. In the last year of his study he received a research grant from the Portuguese National Institute of Scientific Research (INIC) for the development of a computer program to integrate the design of reinforced concrete frame structures. For his graduation, he received two awards: the Eng. António de Almeida Foundation award for the best student in the Civil Engineering Department, University of Porto, as well as the Portuguese Society of Engineers award for the best student in the Faculty of Engineering, University of Porto.

In September, 1990, he started working as an assistant lecturer at the Structures Division of the Civil Engineering Department, University of Minho, Portugal, teaching the courses of "strength of materials", "theory of structures" and "reinforced concrete". In October, 1992, he became a lecturer (on leave) on basis of the research work "New methodologies for the design of reinforced concrete structures". In November, 1992, he started working as a research assistant at the Mechanics and Structures Division, Faculty of Civil Engineering, Delft University of Technology. He is author of 20 scientific publications in the fields of structural concrete and masonry research.